CHARLES UNIVERSITY PRAGUE

faculty of mathematics and physics

Doctoral Thesis

Ultra-high Energy Cosmic Rays and Theirs Detection in AUGER Project

Michael Prouza

Supervisor of the Thesis RNDr. Jiří Grygar, CSc.

Study Program: Physics F1 — Theoretical Physics, Astronomy and Astrophysics

Prague 2005

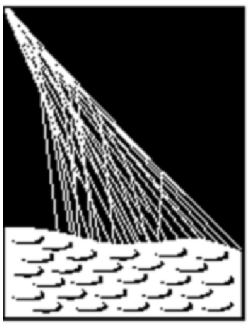

PIERRE
AUGER
OBSERVATORY

I declare that I have worked out this doctoral thesis myself using only the literature stated. I agree with being it used for educational purposes.

Prague, November 24th, 2005

Acknowledgment

It is a pleasure to acknowledge the invaluable help I have received in writing of this thesis from my supervisor Jiří Grygar. His guidance and friendly advice have made good use in the final form of the text.

I was very excited by the inspiring atmosphere between all of my colleagues within the Czech Group of Auger Collaboration. While writing the thesis, I was fortunate enough to receive a valuable feedback namely from Jan Řídký, Petr Trávníček and Radomír Šmída. They read the manuscript very carefully and offered numerous insigthful suggestions that substantially enhanced both clarity and accuracy of this text.

My first springlets of cosmic-ray physics interest were awakened by my astronomy and astrophysics lecturers at the Charles University. I owe them all a special debt of gratitude. I would like to thank here especially to Petr Harmanec who provided me the program HEC22 for photometric data processing and gave me an important introductory information about its applications.

My thanks go out also to my friends, who helped me in many different ways. Especially, I would like to thank to David Ondřich for proof-reading of the manuscript and for his expert advice about thesis typography, to Radka Flašarová and to my brother Pavel Prouza for moral and technical support.

Finally, I'm deeply obliged to my parents for providing of peaceful background.

Contents

Chapter 1

Introduction

How do cosmic accelerators work and what are they accelerating?

This is one of the eleven questions, which were raised by a group of elite U.S. scientists from the National Research Council. This set of fundamentally important questions for the 21^{st} century [77] was completed in 2001 and later published as an influential book. Authors have clearly shown that two separated realms — the realm of vast distances and empty spaces, the realm of huge bodies and almost infinite time scales — the realm of astronomy — and the realm of tiny particles, the world of instant swarm and flash interactions — the realm of particle physics — start to join their powers, start to share their different views, start to accelerate their common progress under a new, unified name.

The new science branch has emerged recently, *astroparticle physics* was born. Such birth could be well mapped by the existence of new scientific journals. The journal holding this particular name — *Astroparticle Physics* [137], commenced its publication in 1993 within the Elsevier group. Since then it reached an impressive Impact Factor of 3.610 for the year 2004 [139]. More recently, in 2003, American Institute of Physics started issuing of *Journal of Cosmology and Astroparticle Physics* [141], an electronic-only journal created by the International School of Advanced Studies (SISSA). This journal received its first Impact Factor in 2004 — 7.914 and so confirmed still growing importance of this scientific field.

An experimental part of astroparticle physics deals mostly with the detection of cosmic rays and γ-rays. Scientists who build and maintain cosmic ray detectors are recruited especially from particle physics community. This fact is even more stressed during the interim after the cease of LEP work and before LHC start. The Pierre Auger Collaboration, of which the author of this work is a member, could serve as a typical example. Astrophysicists and astronomers constitute only small minority there, taking just few percent of the total number of involved scientists.

Therefore, not very surprisingly, the role of astrophysics within astroparticle physics is generally somewhat supressed only to theoretical field. Pure astrophysical knowledge base is used for explanation of the nature of particle sources or it determines the conditions for particle propagation. The experimental part of the field is dominated by particle physics

approach, what is actually quite natural, because the whole one-hundred-year long history of cosmic ray detection has particle physics roots and more specifically — the methods of detection of Ultra High Energy Cosmic Rays (UHECR)[1] evolved in close interaction with genuine particle physics.

Within this work the author provides a description of function, performance, calibration and monitoring of the Fluorescence Detector (FD) of the southern site of the Pierre Auger Observatory (PAO) as well as the introductory overview of the current status of UHECR theory and experiments. The first part also contains a more detailed discussion of the influence of the Galactic magnetic field on particle propagation based mainly on author's own research. These original results [193, 194] could serve as a humble example how growing richness and explorative potential of the astroparticle physics profits from typical astrophysical backgrounds.

In the latter part, dedicated to FD part of the Auger Observatory, the stress is given to author's original contributions which illustrate that astronomical and astrophysical methods can also be successfully used in the midst of an experimental work, namely for the improvement of data acquisition effectiveness [71], for the fluorescence telescope pointing calculations [85, 195] and for the construction of innovative robotic photometric atmospheric monitor [74, 196].

In the great scale of the cosmic ray physics and also in the much smaller scale of this thesis it is confirmed again that the symbiosis of different scientific fields is indeed very fruitful.

[1]The definition of this widely used term is somewhat vague. Within this work we will use the term 'UHECR' for particles with energy above 10^{19} eV and the term 'EHECR' — Extremely High Energy Cosmic Rays — for particles with energies above 10^{20} eV.

Chapter 2

Ultra High Energy Cosmic Rays

2.1 Spectrum of Cosmic Rays

We know today that the energy range of cosmic rays extends from 10^8 eV to 10^{20} eV[1]. Two basic types of cosmic rays introduced above are still distinguished — primary and secondary cosmic rays. Generally, primary cosmic rays consist mainly from protons ($\sim$ 90%) and He nuclei ($\sim$ 9%). The remaining 1% is composed of heavier nuclei with proton numbers up to 92. Only very small fraction of the primaries should be ascribed to electrons, photons and neutrinos.[2]

The energy flux of cosmic rays is rapidly decreasing with their growing energy. We observe one particle per m^2 per second with the energy of about 10^{11} eV, but only one particle per m^2 per year at the energies of about 10^{16} eV and in the EHECR range (around 10^{20} eV it is just one particle per km^2 per century (see Fig. 2.1). In this region ($10^{11} \div 10^{20}$ eV) the energy spectrum approximately fulfils simple power law:

$$F(E)\mathrm{d}E = CE^{-x}\mathrm{d}E, \tag{2.1}$$

where F is the energy flux, E the energy, C is the constant of proportionality and x is characterizing the slope of the curve and in the first approximation is equal to 3. In the detailed view we can see that x isn't a constant, but it varies slightly — the two most important regions of change were named *knee* (about $10^{15.5}$ eV; spectrum becomes steeper) and *ankle* (about $10^{18.8}$ eV; spectrum becomes flatter) in the analogy with features of human leg. The basic form of the spectrum curve is associated with the effectivity of the most common acceleration mechanism in the variable magnetic fields[3], but these slope changes are very puzzling. The existence of the knee was in the last years somehow acceptably explained but the question about the ankle remains unanswered. Of course, some hypotheses were presented and we will discuss them later.

[1] The 10^{20} eV limit is not rigid at all. Maybe there are also particles with energies 10^{21} eV or 10^{22} eV, but were not detected yet. See discussion namely in section 2.6.

[2] We have to emphasize that in the region of UHECRs and EHECRs the composition is unknown and probably very different from this general view, see section 2.6.

[3] The so-called Fermi acceleration will be discussed in the paragraph 2.6.1.

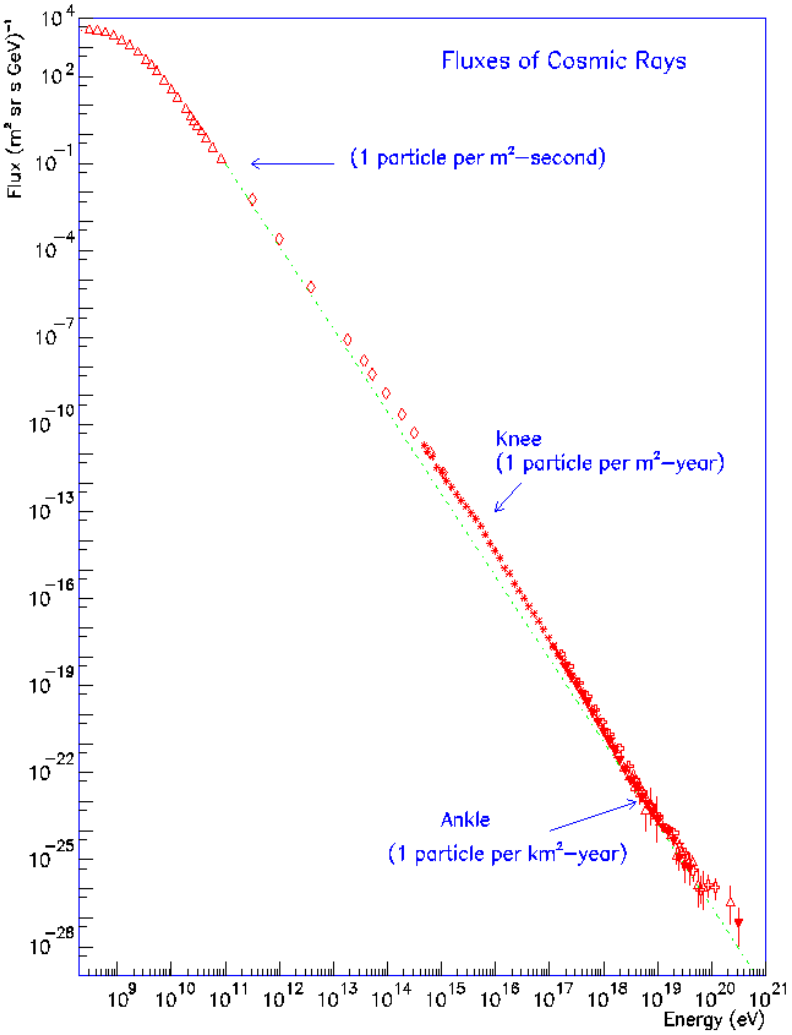

Figure 2.1: *Observed energy spectrum of cosmic rays with energies greater than 100 MeV. The spectrum should be expressed in the form of a power law from* 10^{11} *eV to* 10^{20} *eV. There are slight changes of slope about* $10^{15.5}$ *(called knee), about* $10^{17.8}$ *eV (called second knee) and finally about* $10^{18.8}$ *eV (called ankle). The dotted line shows* E^{-3} *power-law for comparison. Details for "ankle region", interesting for UHECRs, will be given in following figures. This figure was taken from [219], and it is a compilation of the published results from LEAP, Proton, Akeno, AGASA, Fly's Eye, Haverah Park and Yakutsk experiments.*

Observations of primary cosmic rays are carried above the Earth atmosphere and orbital probes, rockets and high-altitude balloons are used for the detection. For the "knee" energies and above are detector surfaces at these devices too small for any valuable particle detection rate and the use of ground arrays of detectors is necessary. This group of detectors

analyses the properties of secondary cosmic ray particle showers and reconstructs from it the parameters of primaries using of Monte Carlo computer models of hadronic interactions. Actual methods of detection of CRs using ground detectors will be analysed in the next chapter.

The spatial distribution of CRs is almost isotropic. Only in the lowest energy region ($10^8 \div 10^{11}$ eV) we observe an excess in the direction of the Sun. This part of spectrum shows also the 11-year variability in flux and is clearly associated with solar activity. The energetic part of cosmic ray spectrum owes its isotropy to influence of magnetic fields. The well known Lorentz force is acting on every charged particle moving in any magnetic field and its influence is often characterized by the so called Larmor radius, what is the radius of the trajectory of particle with given energy in the given magnetic field:

$$r_L[kpc] \approx \frac{E[10^{18}eV]}{ZB[\mu G]}, \tag{2.2}$$

where r_L is the Larmor radius in kiloparsecs, E is the energy of the particle in 10^{18} eV, Z is the proton number and B is the intensity of magnetic field, expressed in microgausses[4].

The typical magnetic field strength in the Galaxy is in the order of μG and so the Larmor radius e.g. for proton with energy 10^{15} eV is only about 0.5 pc. This leads to simple deduction that particles are moving through the variable magnetic field in the Galaxy along very complicated trajectories and it is impossible to trace the point of their origin. The only exception is in the highest energy ranges (above 10^{19} eV) — for these particles is the Larmor radius reaches an order of kiloparsecs. But no anisotropy (with respect to Galactic plane) is observed even at these energies and so it is generally assumed that particles at highest energies have extragalactic origin. Some recent theories are challenging this statement and we will discuss it in detail in chapter 2.6. Sources of CRs with Galactic origin (so mainly in the range $10^{11} - 10^{18}$ eV) should be searched near supernovae and their relics. Potential sources of UHECRs and EHECRs are more rare and will be discussed in next section.

[4]The unit gauss (G) or microgauss (μG; $1\mu G = 10^{-6}G$) is generally used in the astroparticle physics. So, we follow this usage and use this unit in the whole work instead of tesla (T) from SI system ($1T = 10^4 G$). The *CGS* system is used also elsewhere in this thesis, where it is common within astroparticle physics.

2.2 Ultrahigh Energy Cosmic Rays (UHECRs)

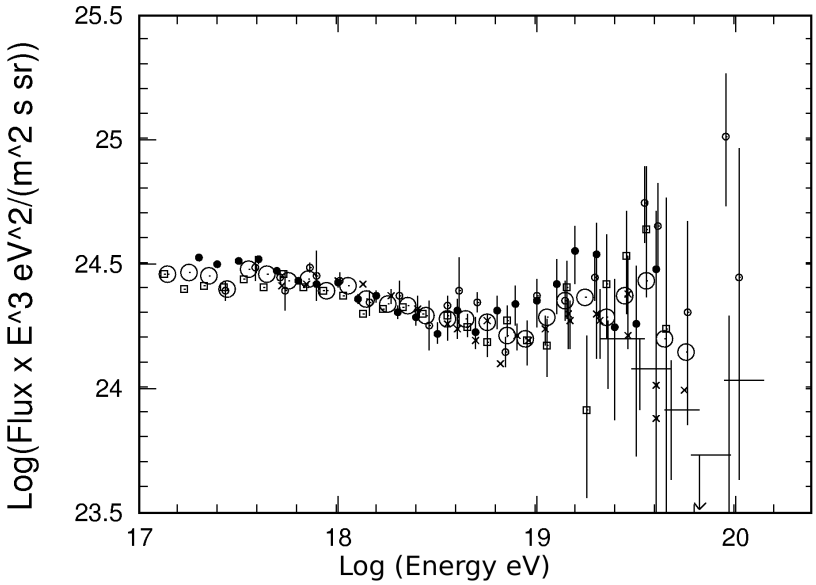

Figure 2.2: *Most energetic part (> 100 PeV) of cosmic ray spectrum. On the vertical scale is the product of energy flux of CRs and of the third power of energy ($Flux \times E^3$; this or similar scales are commonly being used). The ankle around $10^{18.8}$ eV is clearly visible, a growing uncertainty in the measurements around 10^{20} eV is also easily recognizable. Taken from [51], compiled by M. Nagano.*

The cosmic ray particles with energies (approximately) above 4×10^{19} eV have unique position. As we have introduced in the previous section, they are obviously taken as having an extragalactic origin, because of their isotropical spatial distribution and because of non-existence of suitable sources inside our Galaxy. Furthermore, these extreme energies, about eight orders above man-made accelerators, require extreme intensities of magnetic fields or extreme sizes of this acceleration regions for known methods of acceleration. Such conditions are hardly available at any places in the universe; maybe the most promising are large radio lobes in active radio galaxies. But even these need to have all conditions finely tuned and only in such a case the theoretically derived maximum attainable energy is achieving 10^{21} eV.

But there is another hitch. The suitable sources are relatively far from Earth and relatively rare. The nearest one is the active radio galaxy M87, which is about 20 Mpc from Earth and the next one is radio galaxy NGC 315, which is separated by 50 Mpc from Earth. Farther galaxies are not so suitable candidates because of the existence of Greisen-Zatsepin-Kuzmin (GZK) cutoff. In 1966, very shortly after discovery of cosmic

microwave background radiation (CMBR) [185], Greisen [116] and independently Zatsepin and Kuzmin [244] published articles, where they evaluate the effects of interactions with CMBR. They concluded, that CMBR quite effectively degrades the energy of most energetic CRs — protons are undergoing the photopion production, nuclei are photodisintegrated and photons are creating pairs. The critical threshold for effectivity of these processes is different for individual types of cosmic rays, but in this introduction we can summarize, that it is positioned around the energy of photopion resonance, around 4×10^{19} eV and so around energy, which defines the membership in UHECRs. For probably dominant component, protons, the attenuation length is about 6 Mpc and the mean energy loss is about 20% per interaction. The nuclei and photons are generally lossing energy on shorter distance and more effectively. So, the critical distance for particles with energies above 10^{20} eV lies around 50 Mpc (or 100 Mpc when we use less strict criteria for acceleration sites conditions). Furthermore, observed UHECRs and EHECRs are rather isotropic (but the statistics is very poor) and so e.g. the M87 as the single point source is very improbable[5].

The solution of this puzzle is still unknown. Many hypotheses were proposed, but we are now waiting for further data, mainly from built Project Auger. These hypotheses are ranging from simple solutions in which the M87 is a single source indeed, and the trajectories are isotropised by the strong magnetic field in the Galactic halo, to fundamental ones, which are introducing Lorentz-transformation violation or decay of GUT particles originated shortly after the Big Bang.

We can conclude, that all these fascinating problems and themes, which were only shortly touched in this section, will be subsequently worked through in the rest of this work.

2.3 History of Cosmic Ray Research

The research of cosmic rays started several years after the beginning of the 20^{th} century. The physicists were detecting some strange new type of penetrating radiation even with shielded electroscopes. Some measurements were done also out on sea, far away from any radioactive material. First man, who was speculating about cosmic origin of this radiation, was Theodor Wulf in 1910 — he realized several experiments on Eiffel Tower and found much slower decrease of ray flux with the increasing height above the ground level than was expected. After him came more widely cited Victor Hess in 1912 [128] with his balloon experiments — he proved the Wulf's conclusions and furthermore — he found that the radiation level actually rose with height. After that it was quite clear that radiation was coming from outer space.

Quite shortly after discovery of cosmic rays the first hypotheses about its origin were formulated. For example, a famous physicist Robert Millikan [175] thought in 1928 that cosmic ray are originating as energetic gamma photons during creations of heavier nuclei from primary protons and electrons[6]. His hypothesis was overturned by Arthur Compton

[5]But not completely excluded — due to the influence of different magnetic fields. See mainly 2.10.

[6]Neutron wasn't discovered yet.

[78] in 1933, who discovered the dependence of cosmic ray intensity on the magnetic latitude and concluded that cosmic rays are made predominantly from charged particles.

This first very important experimental result was followed by another one in five years. In 1938 Pierre Auger and Roland Maze [31] showed that cosmic rays separated by the distance around 20 meters are still coming in time coincidence. Subsequent experiments found time coincidences even at distances around 200 meters. Their proposed explanation is now well justified — detected particles are only secondaries from a common source. Particles detected on the ground are products from cascading process, when from one primary cosmic ray particle the so-called extensive air showers (EAS) are originating. Auger and his colleagues used newly developed theory and were fascinated by computed results — according to them the observed initiating primary cosmic ray particles had energies up to 10^{15} eV — in time, when products of natural radioactivity or artificial acceleration were reaching energies only several MeV.

Like Auger and collaborators several other groups were continuing their experiments with Geiger-Müller counters used in continually growing arrays. The energy of detected events rose up to 10^{17} eV, but the handicap of unability of the direction detection was again and again more evident. This limitation was overcome by MIT group in 1953 [38], which developed a technique of reconstructing the arrival direction by measuring of arrival times of signals in scintillation counters separated by a few tens of meters. The MIT group also operated 15-counter array, called Harvard Agassiz Station, between 1954 and 1957. This array was used to derive energy spectrum of cosmic rays from 10^{15} eV to 10^{18}.

From this array was the only step to the first giant array — Volcano Ranch[7] array located in New Mexico. John Linsley [161] observed with this array first EHECR — extremely energetic particle with energy above 10^{20} eV in 1962.

Alternative methods of detection were searched from early sixties. Suga and Chudakov in 1962 pointed out the possibility of using the Earth's atmosphere as a huge scintillator. In 1968 Tanahashi and his group [121] finally succeeded in detecting fluorescence light from 10^{19} eV shower at Mt. Dodaira in Japan. This new technique was further tested in climatically more suitable Volcano Ranch and after that in Utah, where the very successful experiment Fly's Eye was developed[8].

[7]More details will be given in section 2.5.1.

[8]As in foregoing case, the more detailed description will be given — in 2.5.6.

2.4 Methods of Detection of UHECR

As was already mentioned in 2.3, there are two basic methods of detection of ultra-high energy cosmic rays — or more generally of detection of extensive air showers.

Earth atmosphere is acting as a large calorimeter on an incident cosmic ray and it has a vertical thickness of 26 radiation lengths and about 11 interaction lengths, which are acting in the development of extensive air shower.

Auger's original idea was to distribute a sufficient number of particle counters across a large area and detect the densities of particles which are arriving to a detection level.

Second method exploits the excitation of nitrogen molecules by particles during evolution of the shower and uses the observation of fluorescence light in the $300 \div 400$ nm band. The light is detected by photomultipliers and the profile of the shower in the atmosphere is observed rather directly.

2.4.1 Ground Arrays of Detectors

Pioneering research of Auger and his team showed that there is a relation between energy of primary particle and between the size of surface, where we are able to detect secondary particles. Quite in accordance with our intuition, the surface is larger when the primary energy is bigger. So also the separation distance d of individual detectors is proportional to the energy of particles that the detector is aiming to measure. For UHECRs d is generally in range of hundreds of meters. The detectors are deployed often in regular grid; total surface covered by detectors for UHECR detection should be at least several square kilometers (see e.g. Figs. 2.1 & 2.5.1.) The density of at least one charged particle type and/or muons and/or air Čerenkov photons, is measured at each detector location. Sizes of individual detector is ranging from 1 to 20 m^2 with the exception of muon detectors, which should be optimally much larger. Scintillation and water Čerenkov detectors are used as individual detectors.

2.4.2 Extensive Air Showers

The properties of extensive air showers (EAS) are simulated using of Monte Carlo programs, cf. AIRES [209], CORSIKA [68] or MOCCA [133]. At energy ranges of UHECRs simulation is a bit delicate, because the interaction energies are several orders higher, than those attainable in man-made accelerators. Generally, the models are cross-checked at lower energies and then extrapolated only to higher energy ranges. The most commonly used models for high energy hadronic interactions are SIBYLL [104], NEXUS [89] and QGSJet [149] or DPMJet [200]. These models were recently analyzed by KASCADE group [154] and this study indicates that QGSJet is reproducing the measured data in the best way. However, when simulating a shower, these above-mentioned models are used only for high-energy interactions interactions and for further development of hadronic showers lower-energy ($\sim$ GeV range) models as FLUKA [97, 98] or GHEISHA [101] are used. Due to this initial extrapolation and non-availability of direct comparison there remains still some

uncertainty for evaluation of fundamental shower parameters, for example there still could remain the uncertainty of $\sim 20\%$ for the energy of primary particle of the shower.

However, we are able to introduce [51] typical parameters of EAS, which are obtained from simulations, e.g. for vertical EAS initiated by 10 EeV proton: At sea level, where the atmospheric thickness is 1033 g/cm^2, the number of secondaries (with energies above 200 keV) is about 3×10^{10}. 99% of these are photons and electrons or positrons in a ratio 6:1. Their energies are mostly in the range from 1 to 10 MeV and they transport 85% of the total shower energy. The remaining 1% of total number of particles is shared between muons with an average energy 1 GeV (muons are carrying about 10% of energy), pions with a few GeV energies (carrying 4% of total energy), and, in smaller proportions, contains also some neutrinos and baryons. The lateral development of the shower is represented by Molière radius (or the distance within which 90% of the total energy of the shower is contained), that in the average is about 70 meters. Actual extension of the whole shower is, of course, much larger, e.g. at a distance 1 km from shower core the average densities of photons/electrons/muons are 30/2/1 per m^2. The maximum size of shower is reached at an atmospheric depth of about 830 g/cm^2 (or at an altitude of 1800 meters), where it contains about 7×10^9 electrons and emits fluorescence light detected with fluorescence detectors.

Showers initiated by heavier nuclei with mass number A and energy E could be roughly approximated as a superposition of A showers initiated by nucleons with energy E/A. Therefore for the same energy these showers are less penetrating, e.g. iron is reaching its maximum size at depths roughly 100 g/cm^2 higher than proton. This feature is generally used in the analysis of fluorescence detector events to distinguish individual components (see section 2.4.3 & Fig. 2.3).

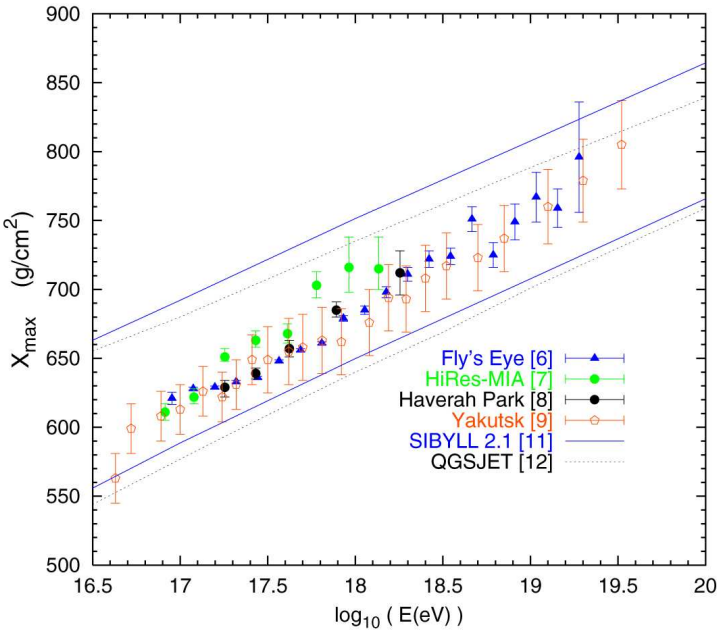

Figure 2.3: *Average depth of shower maximum (X_{max}) vs. energy (E) compared to the calculated values for protons (upper curves) and Fe primaries (lower curves)). From [106].*

Nuclei are distinguished from nucleons (or from the ultra-high energy photons) on the ground detector arrays using two basic criteria: the proportion of muons compared to the electromagnetic component of the shower and the rise time of the detected signal. The muons in shower are coming form the decay of charged pions when they reach energy low enough that their decay length becomes smaller than their interaction length. This happens earlier for heavier nuclei and thus the resulting shower is richer in muons than a proton shower. And, since muons are produced earlier in the shower development, they reach ground also earlier, in comparison to the electromagnetic component, that exhibits a greater delay generated in many interactions.

Detector Signal Analysis

First basic information, which is necessary to be obtained from raw data, is the arrival direction of the primary ray, and hence the direction of the shower axis. This parameter is computed from the relative arrival times from at least three individual noncollinear detectors. As a first approximation, the front shower disc is assumed to be planar and sweeping across the array with the velocity of light. Two factors are limiting the accuracy of positioning — the accuracy of timing and synchronization of time measurements at individual detectors and the range of the whole giant array. The shower disc has generally the thickness of about several nanoseconds close to the shower core and this thickness

is growing to a several microseconds at separations in order of kilometers from the core. So the large detectors have advantage in the determination of front reconstruction. The angular accuracy of giant arrays installed around the world are spread from 1° to 5°.

Second key parameter of the primary particle is its energy, but here its determination is much more difficult. First step in its evaluation is the determination of core position at the ground. For this reason the lateral distribution function is used, e.g. for scintillation detectors the so called Nishimura-Kamata-Greisen function proposed in [114]:

$$S(r) = k \left(\frac{r}{r_0}\right)^{-\alpha} \left(1 + \frac{r}{r_0}\right)^{-(\eta-\alpha)}, \tag{2.3}$$

where $S(r)$ is the density of particles hitting a scintillator at distance r, r_0 is the Molière unit (the product of one radiation length and the rms deflection of a particle of critical energy traversing one radiation length), and α and η are determined empirically from the data; k is proportional to the shower size.

The trial core position is set and then the algorithms based on chi-square minimization or maximum-likelihood procedure are processed; the goal is to find the best fit for a new core position between computed and measured data. After the core position is found, planar description of UHECR shower is modified to more realistic spherical one, with curvature in order of kilometers [164]. In principle, the shower size and energy, should be determined using the lateral distribution function. However, especially, for large arrays $d \gg r_0$, and it is extremely unlikely that any density will be measured at $r < r_0$. Furthermore, as was early recognized, shower sizes for particular energy are stochastically fluctuating, depending on the individual shower development. So, these considerations led Hillas [131] to conclusion, that the more appropriate quantity is the density of the shower at large distances from the core.

In the Haverah Park experiment (see section 2.5.3) the first conversion from $\rho(600)$ (density in the distance 600 meters from the shower core per m^2) to primary energy E_0 was evaluated [132]:

$$E_0[eV] = 7.04 \times 10^{17} \times \rho(600)^{1.018} \tag{2.4}$$

For the purposes of Pierre Auger Observatory this equation was reevaluated [33] using MOCCA code with SIBYLL hadronic model[9]:

$$E_0[eV] = 5.25 \times 10^{17} \times \rho(600)^{1.023}, \tag{2.5}$$

so the Haverah Park energies are probably overestimated by 25%.

Another important equation comes from AGASA [180], where instead of $\rho(600)$ factor $S(600)$ is used. Parameter $S(600)$ is determined by energy losses in a scintillator of 50-mm thickness at 600 meters, in units of vertically penetrating particles:

$$E_0[eV] = 2.15 \times 10^{17} \times S(600)^{1.015} \tag{2.6}$$

[9] And it is now not used on any spectrum evaluations, because these are based on hybrid events, see 3.3

The comparison between these two last equations is quite good — within 15 %, what was experimentally tested at AGASA [206]. For the extremely situated detectors as in Yakutsk, it is also quite important to follow specific factors as temperature, which also influences the sensitivity of the detector.

Scintillation Detectors

Scintillation detectors are historic devices, e.g. already Rutherford used a scintillating zinc sulphide screen to count α-particles in his famous experiment, in which he discovered the existence of atomic nucleus. Rutheford was observing the scintillation by naked eye, nowadays we rather use a photomultiplier to produce large number of secondary electrons and then we record the resulting electric current.

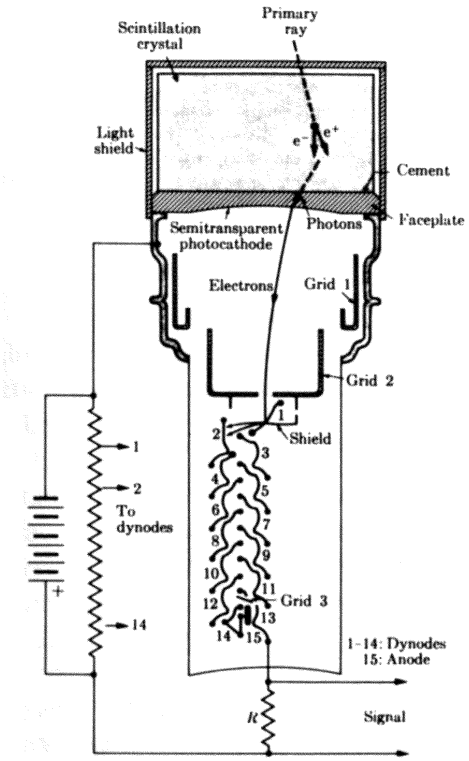

Figure 2.4: *A scintillation detector showing the large scintillation crystal and the photomultiplier tube (type RCA 7046). From [93].*

The scheme, illustrated on 2.4 is the following: electrons, liberated by cosmic-ray particle, produce photons inside the crystal and these photons hit the semitransparent photocathode which again liberates photoelectrons. These are accelerated and focused onto multiplier arrangement. The result is a large pulse arriving at the anode, which size is pro-

portional to the total energy dE liberated in the scintillation crystal. There are two main disadvantages of this system — first, the scintillation material converts only about 3 % of the liberated electron energy into useable optical photons; second, the cathode efficiency is only about $10 \div 20$ %, so only one of $5 \div 10$ photons arriving at the photocathode initiate the cascade in dynodes.

The materials used in scintillation detectors are sodium iodide, which has maximum photon emission at -188 °C. Sodium iodide is doped with thallium, which has higher efficiency at the room temperature, or replaced by caesium iodide. Organic scintillators as liquid *p*-terphenyl or anthracene and trans-stiblene are also used.

Water Čerenkov Detectors

When a fast particle moves through a medium at velocity v, greater than the velocity of light in that medium (so $v > c/n$; c is speed of light, n is a refractive index of given medium), it emits the so-called Čerenkov radiation.

The physical principle of this effect rests in a polarization of medium by the relativistically moving particle. A charged particle moving slowly through a transparent material will polarize the medium along its trajectory. The atoms around the particle are transformed into a little dipoles. When the particle moves to another point, they relax to their normal state. Owing to complete symmetry of this effect no resulting field reaching larger distances is produced. However, the situation differs qualitatively, when particle is moving relativistically. The field is no longer symmetrical along the path of flight and each element of the track is radiating. However, the elementary waves generally interfere destructively and there is then no visible effect at large distances. Only when the velocity of the particle is higher than the phase velocity of the light in that medium it will produce field detectable at distant point. Waves from the different points of the track combine to form a plane wavefront.

The wavefronts only add up to produce coherent radiation in a particular direction θ with respect to the velocity vector of the particle, so the radiation should be observed only in a narrow cone along the track. The apex angle of this cone θ is given by formula $\cos\theta = c/vn$. The intensity of radiation is given by [166]:

$$I(\nu) = \frac{\nu Q^2 v}{4\pi\varepsilon_0 c^3}\left(1 - \frac{c^2}{n^2 v^2}\right), \tag{2.7}$$

where ν is the frequency of the emitted radiation, Q is the charge of a particle in coulombs and ε_0 is the permitivity of vacuum. It should be noticed, that refractive index n depends on the frequency of emitted radiation ν.

In practice, no measurements of the wavefront are realized in arrays of surface detectors, although this can be achieved in dedicated experiments (neutrino experiments as KAMIOKANDE or imaging Čerenkov telescopes as HESS or MAGIC). In high-energy cosmic ray detectors we measure only the total amount of light emitted. The medium determines threshold velocity for detection; in UHECR experiments pure water is mainly

used. The principal problem of these detectors is very low light yield and sensitive photomultipliers should be used to produce a measurable signal.

2.4.3 Fluorescence Detectors

Fluorescence detectors are detecting mainly the UV light ($300 \div 400$ nm) emitted by nitrogen molecules in the air. Instead of sampling a shower with many detectors on a ground grid, the fluorescence detector follows the trajectory of the shower. For this reason, the whole observed sky is segmented, and each segment (typically $\sim 1^\circ$) is observed by its own photomultiplier. The emission efficiency (ratio of emitted energy in fluorescence light to the deposited one) of the emission is poor (about 1%), the detector sees the shower as a variable light bulb moving at the speed of light along the shower axis. A rule of thumb of the equivalent radiated power is $3 \times E[10^{18}\text{eV}]$ watts at shower maximum. For this reason, observation should be made only during clear moonless nights, thus the duty cycle is only about 10%. Under favorable conditions EHECR showers could be detected at the distances as large as 20 km — for Fly's Eye or HiRes detectors (see sections 2.5.6 & 2.5.7). The fluorescence yield [51] is 4 photons per electron per meter at ground level.

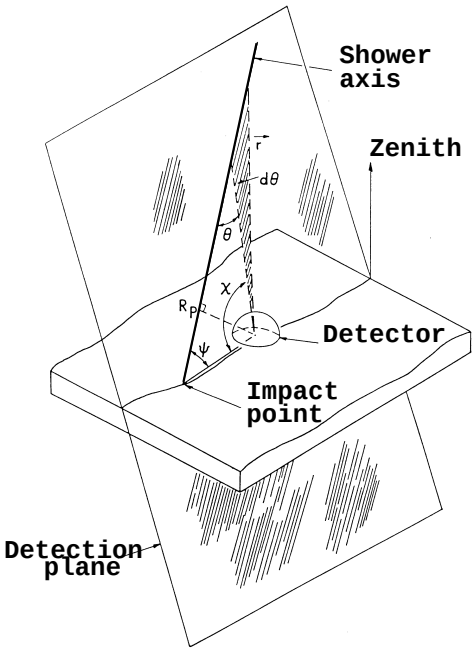

Figure 2.5: *A sketch of fluorescence detector. In the figure the geometry of extensive air shower is visible as seen with any ground fluorescence detector (this scheme was created particularly for Fly's Eye detector). The detection plane is specified by the air shower (approximated as a line) and by the center of detector (point). This plane is reconstructed as a fit to the spatial patterns of triggered photomultiplier tubes, which must lie along a great circle on the celestial sphere. The angle ψ and impact parameter R_p are obtained by fits to observation angles χ_i vs time of observation. Figure taken from [37].*

A fit on the pattern of the hit photomultiplier tubes determines the plane containing detector and the shower axis with precision better than 1° (see Fig. 2.5). In the so-called stereo mode, when the EAS is observed by at least two fluorescence detectors separated at least by few kilometers, two planes are reconstructed and their intersection gives incident direction with a quite good precision. In mono mode, when only one detectors observes EAS, it is necessary to reconstruct the angle ψ (see Fig. 2.5) by using of arrival times on individual photomultipliers. At least the same level of precision will reach the hybrid measurement (for the first time being realized at the Pierre Auger Observatory), when the information from ground array will be combined with information about detection plane from fluorescence measurement.

The fluorescence technique is the most appropriate for energy measurements — atmosphere acts like large calorimeter and thus the emitted energy is proportional to a number of charged particles in the shower. The longitudinal development of the shower is parameterized by the analytical Gaisser-Hillas function [51] giving the size of shower N_e (the

number of electrons in the shower) as the function of atmospheric depth x (in g/cm^2):

$$N_e(x) = N_{max} \left(\frac{x - x_0}{X_{max} - x_0} \right)^{(X_{max}-x_0)/\lambda} e^{(X_{max}-x)/\lambda}, \tag{2.8}$$

where λ is a constant equal to 70 g/cm^2, x_0 is the depth at which the first interaction occurs, and X_{max} is the position of the shower maximum. The total energy of the shower (or the energy of the primary, E_0) is then proportional to the integral of this function, knowing that the average energy of one created particle is 2.2 MeV/(g.cm^{-2}) and that the energy fraction of this electromagnetic component is about 90 % [179]:

$$E_0[eV] = 2.65 \times 10^6 \times \int_0^\infty N_e dx \tag{2.9}$$

In practice several additional effects should be taken in account, which are complicating the evaluation and raising the uncertainty of the result. These are subtraction of the direct and diffused Čerenkov light, the wavelength-dependent Rayleigh and Mie scatterings and the dependence of the attenuation on the altitude. The overall systematic error of fluorescence measurements is currently estimated to be around 25 % [1].

2.5 Existing Experiments and Future Projects

Five ground giant arrays successfully measured (or still measure) the flux of UHECRs up to now — in chronological order of its start date of operation it was Volcano Ranch, SUGAR, Haverah Park, Yakutsk and AGASA. Furthermore, two fluorescence detectors have functioned for detection of UHECRs — pioneering detector Fly's Eye and its successor HiRes. The properties and specialties of these observatories will be discussed in following sections.

The most important or the most innovative projects in construction or in advanced phase of preparation will be mentioned too — Pierre Auger Observatory (PAO), Telescope Array (TA), ASHRA and orbital EUSO project. This thesis was created within the Auger Collaboration and therefore the description of the PAO is the most detailed. The general description of PAO has a dedicated chapter 3, special thesis themes are discussed within chapters 4 & 5.

For quicker discrimination the letters in parentheses are added to the headlines of sections of individual observatories, where *S — stands for 'stopped operation', O — still in operation, C — in construction and P — in planning.*

Experiment	Detector Types	Surface Size	Number of detectors	Covered area [km^2]	Notes
Volcano Ranch	scintillators	3.3 m^2	19	8	
(New Mexico, USA)	muon detectors (>220 MeV)	3.3 m^2	19		
SUGAR	muon detectors (>0.75 GeV)	2 × 6 m^2	54	60	
(Australia)					
Haverah Park	water Čerenkov	34 m^2	4	12	
(UK)	water Čerenkov	2.25 ∼ 54 m^2	28		
	water Čerenkov	1 m^2	30	0.3	by the array center
Yakutsk	scintillators	2 ∼ 4 m^2	58	18	up to 1995
(Russia)	muon detectors (>1 GeV)	20 m^2	5	10	from 1996
	muon detector (>0.5 GeV)	192 m^2	1		
	air Čerenkov phototube	5" ∼ 15"	45		
AGASA	scintillators	2.2 m^2	111	100	
(Japan)	muon detectors (>0.5 GeV)	2.4 ∼ 10 m^2	29	50	
	scintillators	1 m^2	159	1	1-km^2 array
	muon detectors	25 m^2	9	1	

Table 2.1: *Parameters of detectors at existing surface arrays, adapted from [179].*

2.5.1 Volcano Ranch (S)

As first giant ground array for detection of cosmic rays was constructed at Volcano Ranch site in New Mexico, USA [165]. It has been located at 35°09' northern latitude and 106°47' western longitude, 1770 meters above sea level (atmospheric depth 834 g/cm^2). The array consisted of 19 3.3-m^2 plastic scintillators, each viewed with a 5-inch photomultiplier. The regular pattern of the detector is visible on Fig. 2.6, the array spacing d was 884 m during approx. 650 days of operation between years 1959 and 1963. Furthermore, there was added one more scintillation detector, shielded with 10 cm lead plate, for muon detection $E_\mu > 220$ MeV.

From Volcano Ranch came our first information about cosmic ray spectrum above 10^{18} eV and also the first about the spectrum flattening in this region, in other words about the existence of an ankle. The project leader, Linsley made also the first rough analysis of the direction distribution and wrote a paper about first EHECR particle [161] ever detected. This particle was detected in February 1962 and after corrections in the following years it has the assigned energy of about 1.4×10^{20} eV [161]. This event is actually (and a bit surprisingly) fifth largest event ever detected and was reported two years before discovery of the CMBR and three years before the forecast of the GZK cutoff.

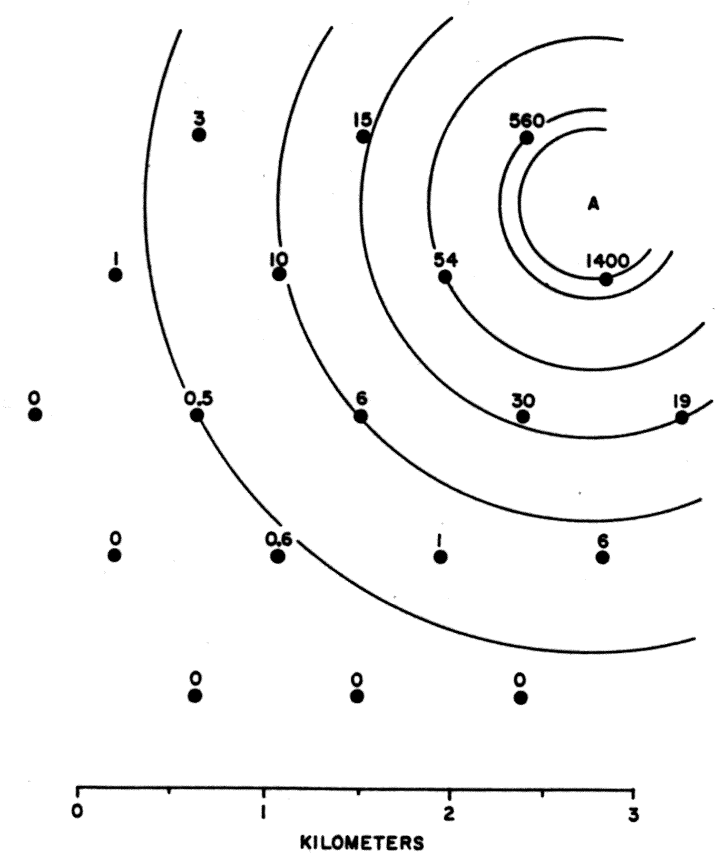

Figure 2.6: *Plan of Volcano Ranch array in February 1962. The circles represents 3.3 m^2 scintillation detectors. The numbers near the circles are the shower densities (particles/m^2) registered in this event (No. 2-4834). Point A is the estimated location of the shower core. The circular contours about that point aid in verifying the core location by inspection. Adapted from [161].*

2.5.2 SUGAR (S)

The Sydney University Giant ARray (SUGAR) was the only one which until now operated in the southern hemisphere (before start of AUGER construction) at Narrabri, New South Wales, Australia [240]. It was located at 30°32' southern latitude and 149°36' eastern longitude, just 250 meters above sea level (atmospheric depth 1015 g/cm^2). This array consisted of 54 detector stations spread on the surface about 54 km^2 and was functioning from 1968 to 1979. Stations were autonomous, with local power sources. Detectors were deployed in pairs — each two 6-m^2 scintillation detectors were buried about 1.7 m below ground and thus responding to penetrating muons ($E_\mu > 0.75 \sec\theta$ GeV, where θ is zenith angle).

The spacing between detectors d was generally about one mile (1610 m) and proved to be too large. Detected densities were generally very small and the number of hit individual stations too. Even at largest detected events this situation sustained. For the ten largest events the mean number of stations struck was only 4.7 and the position of core has an error in excess of 100 m.

Each detector had 7-inch photomultiplier, timing was driven by radio signal across the array, data were logged onto audio tapes — these tapes were collected once a week and taken to Sydney for analysis. Another serious problem connected with photomultipliers was theirs after-pulsing, because logarithmic time to height converters were used. So the accuracy of energy estimation was very poor, in dependence on the used model of evaluation the estimates vary with a factor of $2 \div 3$[10]. So the SUGAR events reported as above 4×10^{19} eV should be further analyzed with great awareness of discussed error.

More useful are arrival directions of detected particles (used e.g. in [153]) and the novel method of data recording, which is used similarly also in its successor on the southern hemisphere — in southern PAO in Argentina, accounting, of course, for the 30 years of progress in technology.

[10]Two models were used for energy estimates — so called Hillas E model (from [130]) and SUGAR researchers' own model — so called Sydney model. From Hillas E model follows formula for primary energy E_0: $E_0[eV] = 1.64 \times 10^{18}(N_\nu \times 10^{-7})^{1.075}$, where N_ν is the showers' equivalent verical muon number. For Sydney model similar equation is valid: $E_0[eV] = 6.75 \times 10^{17}(N_\nu \times 10^{-7})^{1.11}$. From comparison analysis it seems that more suitable and precise is Hillas E model, which attains the greater accordance [240] namely with Haverah Park data. So for these reasons we use the energy data from Hillas E model in the following chapter.

2.5.3 Haverah Park (S)

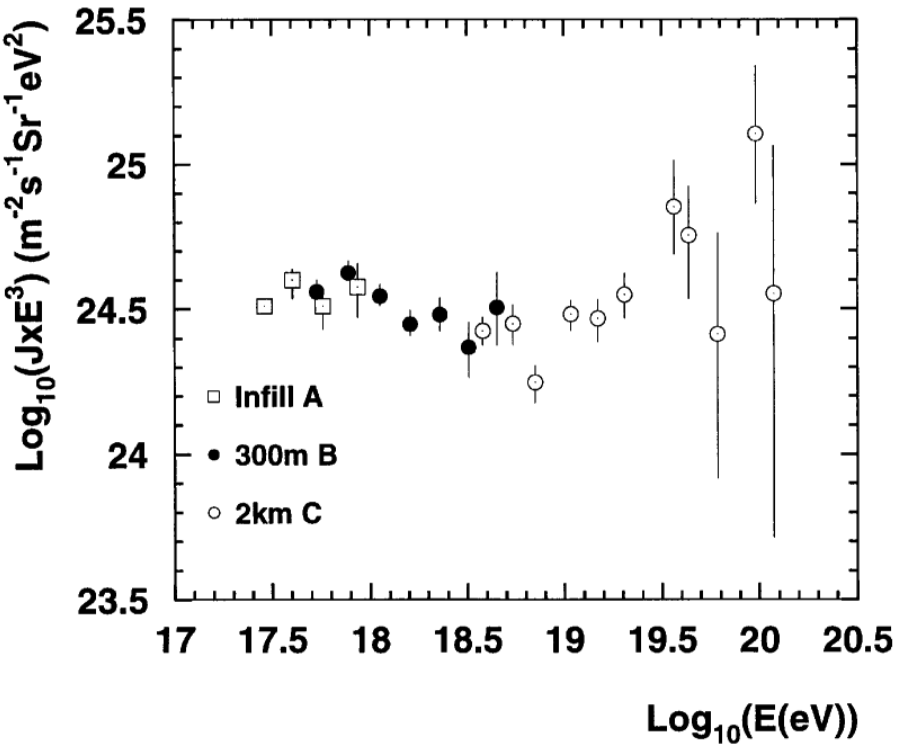

Figure 2.7: *Energy spectrum above 100 PeV from Haverah Park. For the description of the detector structure (infill, 300 m, 2 km) see the text below. Taken from [243].*

First use of more effective water Čerenkov detector arrays was realized at Haverah Park, UK from 1968 to 1987 [157]. Haverah park is located at 53°58' northern latitude and 1°38' western longitude, 200 meters above sea level (atmospheric depth 1016 g/cm^2). Detectors weren't positioned on a uniform grid. Four detectors with 300-m spacing and 34 m^2 surface created the basis of the array (300 mB in the graph), which was extended with six 50-m and 150-m spaced subarrays in distances of about 2 km from the array core (2 km C in the graph of the spectrum). Finally, a *infill (A) array* composed of 30 small detectors (surface area of each detector of about 1 m^2) was created around the center of the array.

Water Čerenkov detectors respond to photons in a very efficient way (not like scintillators[11]). The low energy photons (10 MeV) are almost totally absorbed and similarly at the distances > 100 m, which is most important for large showers, also electrons are almost completely absorbed. So, the detectors measured the flow of energy in the shower

[11]See paragraph 2.4.2.

rather well. For comparison with e.g. SUGAR array there was up to 50 measured nonzero densities in the largest events (ranging form 100 m to 2500 m).

During the last years of the project an array of eight scintillators was also operated within 150 m of the array center for the cross-calibration with other giant arrays.

2.5.4 Yakutsk (O)

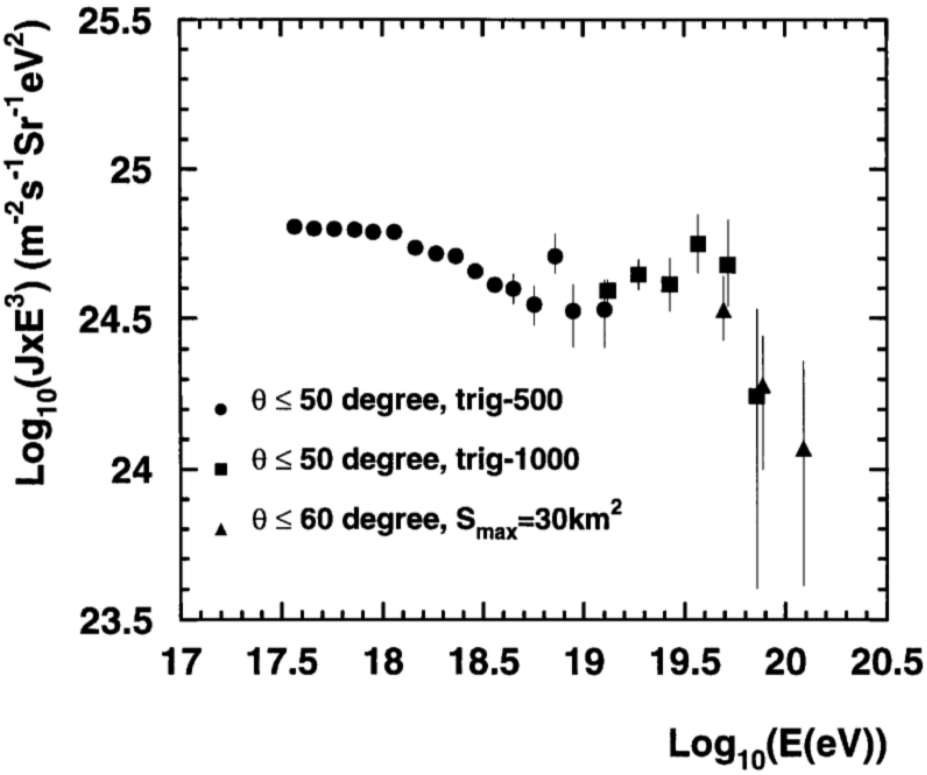

Figure 2.8: *The Yakutsk energy spectrum above 100 PeV. Different trigger criteria were used for different parts of the spectrum (trig-500, trig-1000 and S_{max} = 30 km^2). For details see [243].*

The very sophisticated scheme of scintillator and muon detector array was developed in Yakutsk, Siberia, Russia [5]. Yakutsk is situated at 61°36' northern latitude and 129°24' western longitude, only 105 meters above sea level (atmospheric depth 1020 g/cm^2), began taking data in 1970, from 1974 is covering an area of 18 km^2 and is still in operation[12].

[12]But from 1995 in contracted area about 10 km^2, which is more suitable for study of air showers around 10^{19} eV, where they reported the qualitative change of shower characteristics.

There are three nested arrays. The inner-most is covering area about 0.0026 km^2 and consisting from 19 0.25-m^2 scintillation detectors. The next is surrounding the first one, composed form 43 2.0-m^2 scintillation detectors on the 500-m grid, covering totally 10 km^2, replenished with further 17 2.0-m^2 scintillation detectors around them with spacing 1 km. Muon detectors are situated within 1 km around array center. Seven muon 20-m^2 detectors have energy threshold about 1 GeV, one 192-m^2 detector have threshold about 0.5 GeV.

Data from individual stations are collected via coaxial cable, timing signal is distributed via microwave broadcasting and the time resolution $\sim$ 100 ns is achieved. Other important feature of this array is the presence of 35 air Čerenkov radiation phototubes, which allows an indirect information about longitudinal development of shower and about energy evaluations (the precision of energy measurement for vertical showers is about 20% using Čerenkov detector information).

2.5.5 AGASA (S)

The largest finished ground array constructed so far — Akeno Giant Air Shower Array — was located at Akeno, Japan, at 35°47' northern latitude and 138°30' eastern longitude, 700 meters above sea level (atmospheric depth 920 g/cm^2) [178]. The site is equipped with 111 scintillation detectors, covers 100 km^2 and was in operation from 1990 up to 2004. 2.2-m^2 scintillation detectors have spacing about 1 km. Each detector has its detector control unit (DCU), which records the arrival time and density of every incident signals. Several DCUs are connected in series to a common communication string consisting of two optical fibres. One fibre is used for signal sending, the another one for data acquisition. There exists also the dense array (at the southeast corner of array) covering 1 km^2 with spacing 3, 15, 30, 60 and 120 meters, which has been operated since 1979. The whole array has 27 added muon detectors, which were installed on chosen scintillator sites and their sizes are ranging from 2.4 m^2 to 10 m^2. Furthermore, as tests for the prepared experiments, there are also two scintillators with a sandwiching 1-cm lead plate[13] and two prototype water Čerenkov detectors for the Auger Project.

The most recently assigned energies [225] of AGASA events have an accuracy of $\pm$18% in systematic errors around 10^{20}eV. This systematic uncertainty is independent of primary energy above 10^{19}eV and the largest contribution to this error is equal to $\pm$12% and is due to uncertainty of the conversion formula that transforms parameter S(600) to the energy of primary particel, which represents errors of interaction models, not known chemical composition, height correction, etc. Other systematic error contribution are assigned to the detector properties ($\pm$8%) and air shower phenomenology ($\pm$11%). Based on the energy spectrum from $10^{14.5}$eV to a few times 10^{20}eV determined at Akeno, there are surely events above 10^{20}eV and the energy spectrum extends up to a few times 10^{20}eV without a observable GZK-cutoff.

[13]For the investigation of relative proportions of electrons and muons in the same shower.

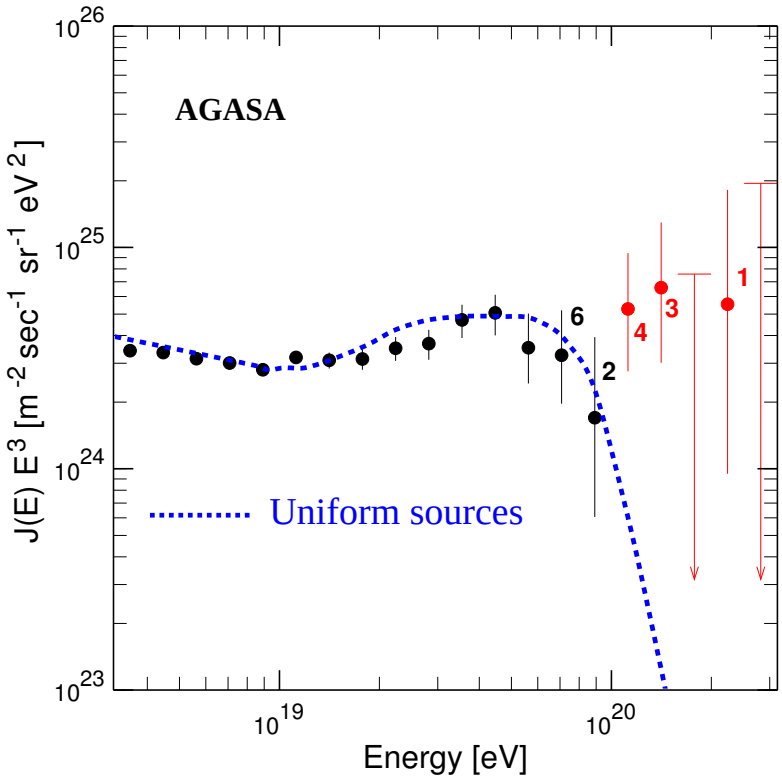

Figure 2.9: *Energy spectrum determined by AGASA and the exposure with zenith angles smaller than 45° up until July 2002. (Open circles: well contained events; Closed circles: all events) The vertical axis is multiplied by E^3. Error bars represent the Poisson upper and lower limits at 68% confidence limit and arrows are 90% C.L. upper limits. Numbers attached to the points show the number of events in each energy bin. The dashed curve represents the spectrum expected for extragalactic sources distributed uniformly in the Universe, taking account of the energy determination error. The uncertainty in the exposure is shown by the shaded region. From [225].*

2.5.6 Fly's Eye (S)

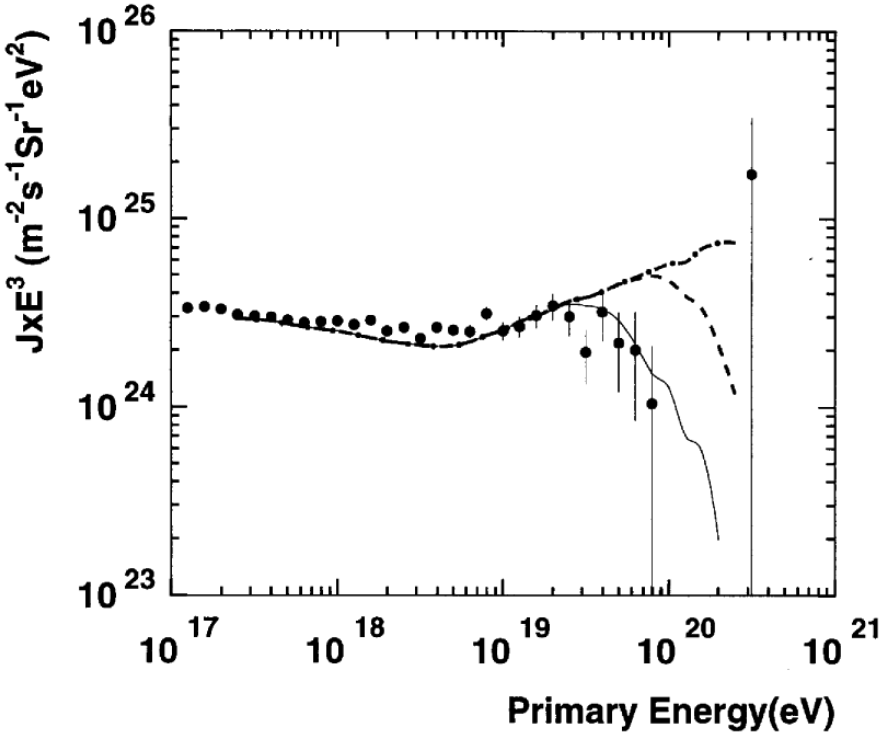

Figure 2.10: *Spectrum of CR events above 100 PeV from monocular Fly's Eye. Big dots are representing data and lines are showing predicted spectra for source energy cutoff at different energies. Solid line is for cutoff at* $10^{19.6}$ *eV, dashed line is for cutoff at* 10^{20} *eV and chain line is for cutoff at* 10^{21} *eV. From [243].*

The first realized fluorescence detector (or detectors) was situated at Dugway, Utah, USA at 40° northern latitude and 113° western longitude, about 1400 meters above sea level (atmospheric depth 869 g/cm^2) [54]. The detector was in operation from 1981 to 1992 and has two stations — Fly's Eye I and Fly's Eye II. Fly's Eye I began full operation in 1981, consisted from 67 spherical mirrors of 1.5-m diameter, each with 12 or 14 photomultipliers at the focus. Each tube viewed a 5.5°-diameter hexagonal area of the sky, in total 880 photomultipliers covered the whole sky. Fly's Eye II was completed 3.4 km from first station and began operation in 1986. Fly's Eye II consisted of 36 mirrors of the same design as No. I and its 464 photomultipliers was covering the half of sky in the direction of Fly's Eye I. Both stations should operate in stand alone mode or in stereo mode. The integrated monocular exposition time is about seven times larger than the stereo exposition [37].

Nitrogen lasers were used for the calibration of the system and for checking of the light scattering around station, vertical flashers for monitoring of atmospheric conditions and pulsing diodes in each mirror system for the determination of relative efficiency of whole detector.

The only one EHECR event was ascribed to this detector, but it was the largest cosmic ray event ever detected. It was on October 15th 1991, when Fly's Eye measured the profile of this giant event with energy 3.2×10^{20} eV (51 J).

2.5.7 HiRes (O)

Because of the great success of the Fly's Eye, the next generation detector is starting its career at the same place — the so called High Resolution Fly's Eye or more frequently just HiRes. The detector is again displaced at two sites, which are separated by 12.5 km.

HiRes started data acquisition in June 1997 in monocular mode and in December 1999 in stereo mode. Since then, the largest sample of UHECR data so far was obtained and therefore it also has the best statistical power for determining features in the spectrum [50]. Despite this fact, only two monocular (for HiRes-I station and HiRes-II station, as described below) spectra were published, the Hires stereo spectrum is still being analyzed and will appear publicly probably during the next year (2006) [1].

The HiRes-I detector is located atop Little Granite Mountain on the U.S. Army Dugway Proving Ground in west-central Utah. It consists of 21 mirrors, and their associated phototube arrays, arranged in one ring, observing from 3 degrees to 17 degrees in elevation and providing almost complete coverage in azimuthal angle. The detector uses a sample-and-hold readout system which integrates phototube pulses for 5.6 μs. This is long enough to collect the signal from all cosmic ray showers of interest.

The HiRes-II detector is located on Camel's Back Ridge, also on Dugway Proving Ground, about 12.6 km SW of HiRes-I. It consists of 42 mirrors, arranged in two rings, covering from 3 to 31 degrees in elevation and almost the whole azimuthal angle range. This detector uses a flash ADC (FADC) readout system with a 100 ns sampling time.

The diameter of each detector mirror is about 2 m, and 256 photomultipliers attached to each mirror are observing $1^\circ \times 1^\circ$ segment of the sky.

For both Hires-I and HiRes-II stations is the expected time averaged aperture (10% duty cycle) of about 1000 km^{2}sr at 10^{20} eV. HiRes-II detector (because of its two-ring arrangement) is able to detect also showers of substantially lower energies (down to $E \sim 10^{17.4}$ eV) in comparison with HiRes-I, which goes down only to $E \sim 10^{18.5}$ eV. Two times larger extent in elevation angles of HiRes-II enables to observe also the development of these less energetic showers with smaller X_{max} in higher layers of atmosphere. Furthermore, two-ring mirror arangement contributes to generally longer shower tracks over telescope cameras and therefore improves the time-fitting and so the geometrical reconstruction of detected shower.

According to [1] the overall systematic uncertainty is of about 31%, where the largest contribution comes from modelling of the atmosphere (15%), absolute calibration of the phototubes (10%), fluorescence yield (10%) and correction for unobserved energy (5%).

As we will discuss in greater detail later (in chapter 3), the final combined HiRes monocular spectrum (see Figure 2.11) is quite in disagreement with latest AGASA spectrum, because it well presents the GZK suppression, confirmed to 4.8σ level.

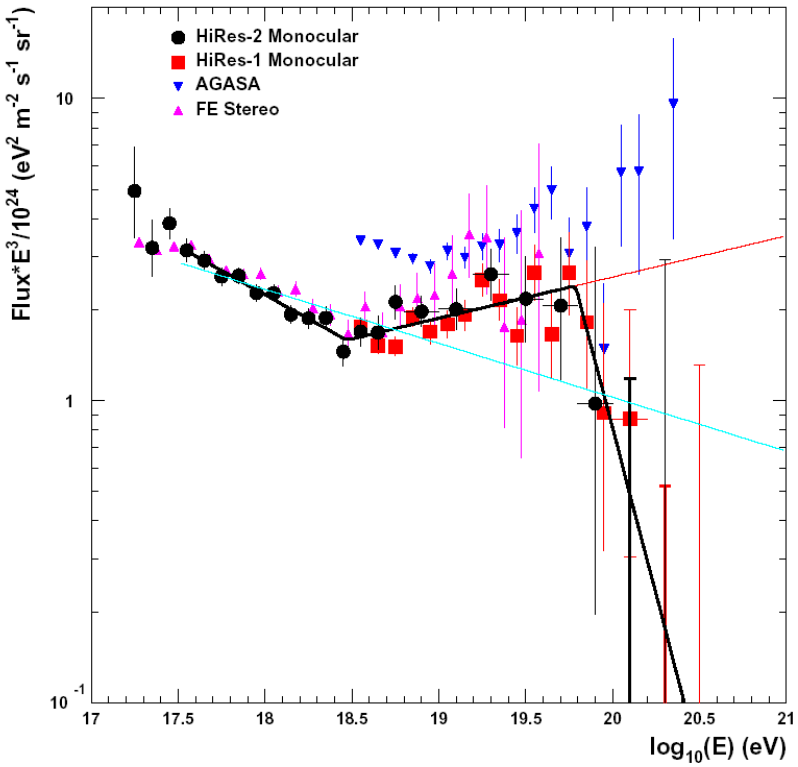

Figure 2.11: *E^3 times the UHECR Flux of HiRes. Results from the HiRes-I (red squares) and HiRes-II (black circles) detectors, the AGASA experiment (blue down-triangles) and the Fl's Eye experiment (in stereo mode; magenta up-triangles) are shown. The Fly's Eye points have been shifted to the right by one quarter bin ($\Delta log_{10}E = 0.025$) for clarity. Also shown are two possible spectral law fits to the HiRes-I and HiRes-II spectra. The 1σ upper limits for two empty bins of each HiRes spectra are also shown. Figure from [1].*

2.5.8 AUGER (C)

Detailed description of Pierre Auger Observatory (PAO), especially of its southern part and of its fluorescence detector system, is one of the aims of this work and will follow later. The chapter 3 and following are dedicated to this subject.

2.5.9 Telescope Array (C)

Another important project currently under construction is Telescope Array (TA). This common project of more than twenty institutions from Japan and USA is being built in

familiar Dugway Proving Ground in Millard County, Utah, USA — where HiRes is already in operation.

The configuration of hybrid TA is shown in Figure 2.12. The ground detector consists of an array of 576 plastic scintillators with an area of 3 m^2 deployed in a grid of 1.2 km spacing covering the ground area of 760 km^2. The surface detector aperture should be approximately 9 times that of AGASA. The detection efficiency is planned to reach 100% for cosmic rays with energies above $10^{19.5}$ eV and with zenith angles less than 45°. The fluorescence measurement is made at 3 stations surrounding the ground array. The stations form a triangle with a separation of 30–40 km. Twelve reflecting telescopes will be installed at each station and cover the sky of $3° \div 34°$ in elevation and 108° in azimuth looking toward the center of the ground array. The diameter of the telescope mirror is ∼3.3 m and the pixel resolution is approximately $1° \times 1°$. The stereo aperture will be of about 670 km^2.sr for $E > 10^{20}$ eV by requiring at least one station is within 45 km from the shower center. The fluorescence acceptance is 4 times that of AGASA assuming 10% duty factor for the observations.

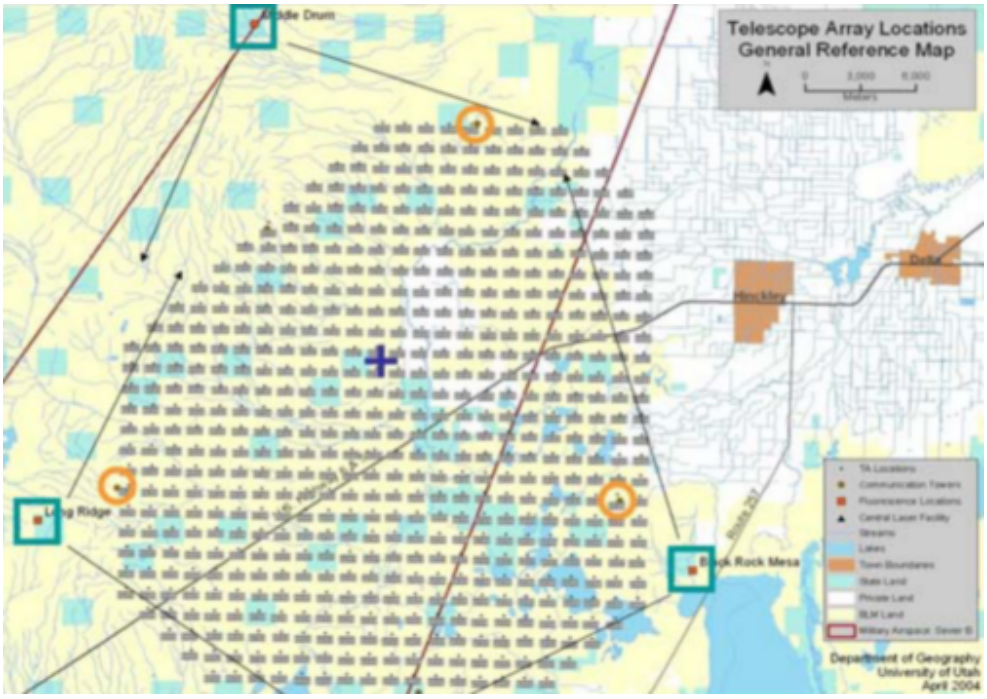

Figure 2.12: *Detector Arrangement of Telescope Array. Three square boxes indicate the location of fluorescence telescope stations overlooking a scintillation counter array at the center. The circles indicate the locations of communication tower, by which all the controls and data acquisition are relayed to the operation center in the nearby town of Delta. Figure from [151].*

The experimental part of ground array consisting of 18 scintillators was already working during summer 2005. These plastic scintillators are sensitive to the charged particles

in the air shower. Since electrons and positrons outnumber muons by an order of magnitude, the thin ($\sim$ 12 mm) plastic scintillator array of TA is sensitive in effect only to the electromagnetic component of the air shower. By this reason, the energy measurement of TA is less affected by the difference of the primary composition and the detail of unknown hadronic interactions at studied extremely-high energies. This should be the advantage with respect to the use of water Cherenkov detectors, which are equally sensitive to the high energy muons and soft gamma rays. The expected uncertainty of the absolute energy scale can be cut down to below 10% by carefully analyzing the simultaneously measured events for $E > 10^{19}$ eV according to TA collaboration [151].

2.5.10 Ashra (C)

The very novel design presents ASHRA (All-Sky Survey High Resolution Air shower detector; or Ashra — the capitalization is not generally used by members of Ashra Collaboration) [207]. It will comprise three stations on Hawaii Big Island, which are being built by Japanese-USA-Taiwan Collaboration of 17 institutes. The prototype station (downscaled to 2/3 of final size) is working since Fall 2004 on the Haleakala mountain, the first station is under construction on the Mauna Loa mountain and has to be completed in 2006.

Figure 2.13: *Locations of three proposed Ashra stations at Hawaii. Figure from [20].*

Ashra will consist of three high-altitude ($\sim$ 3 km) stations to be incrementally installed at Mauna Loa, Hualalai, and Mauna Kea. Each station, separated by 30–40 km, will

observe the entire moonless night sky with 12 detectors. In the Ashra optics, UV photons from air showers and directly from gamma ray bursts (GRBs) are collected using modified Baker-Nunn optics. Each one of twelve detectors utilizes three or four 2.2 m spherical reflectors for viewing a 0.5 sr region of sky. Detector images pass through a photoelectric pipeline for trigger processing and recording on 4 megapixel CMOS sensors. Covering the sky with 48 megapixels, roughly a thousand-fold improvement over presently employed technology of photomultipliers, represents resolution measured in arc minutes rather than degrees.

The most unique feature of Ashra however is the ability to serve as simultaneous detector for both the long duration (100 μs) fluorescent events and short (few ns) air Cherenkov events, not possible with earlier instruments. The problem of integrating background light over long times is solved by an image delay system to the CMOS sensors, and a moving electronic shutter driven from a parallel multi-anode photomultiplier trigger. The major gain here is the ability to monitor the whole sky continuously for extended (dark) periods, making an unprecedented search for new point (and time varying) sources such as the numerous gamma ray bursts, soft gamma ray repeaters, unidentified EGRET sources and so on.

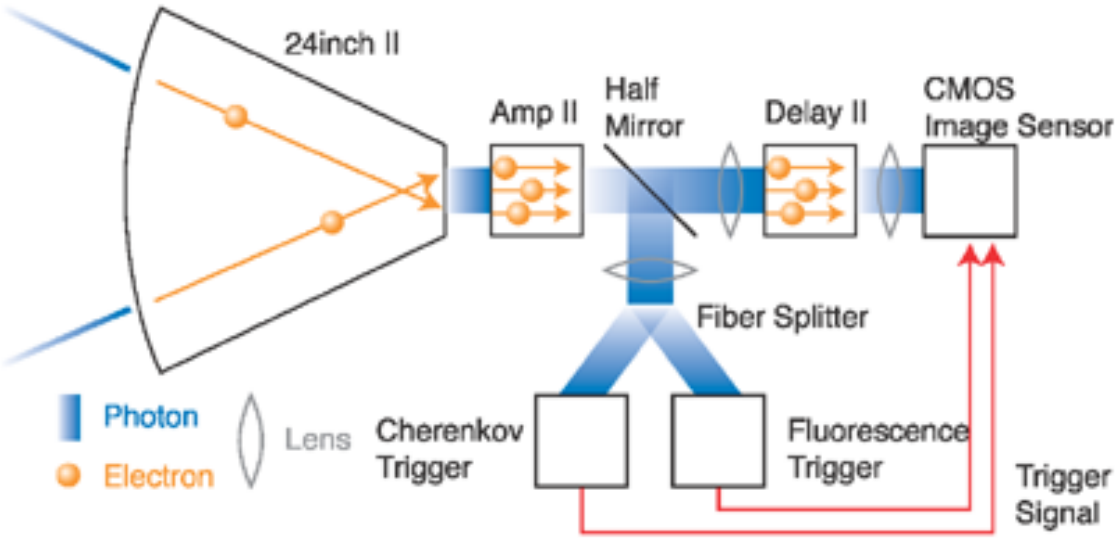

Figure 2.14: *Ashra image pipeline. The optical system consists of three corrector normal lenses made of acrylic resin, spherical reflector and focal sphere image intensifier (FIIT). The photoelectric image pipeline consists of FIIT, light guide, self-triggered IIT (STIIT) providing the functions of splitting light and making optical delay, trigger image sensor, and high resolution CMOS image sensor. Figure from [20].*

2.5.11 EUSO (P)

The challenge of overcoming of capabilities of PAO and of TA is very inspiring, but quite difficult to fulfill. Any ground array, covering significantly greater surface or air volume, will be too expensive for realization in the following decades. However, Linsley [162] pointed out already in 1979 that the solution should be in space observation of fluorescence emissions (concept of satellite SOCRAS). Clear major advantage is huge observable air-volume. Complications should be hidden in correct filtering of lightnings, lights from cities, oceanic biofluorescence or in high altitude clouds.

The Extreme-Universe Space Observatory (EUSO) is a European Space Agency (ESA) mission [47] to investigate the nature and origin of UHECRs. EUSO is successor of previously planned mission OWL (USA project) nad AIRWATCH (European Union) and will pioneer measurements of UHECR-induced extensive air showers from space. It will make measurements of the primary energy, arrival direction, and composition using a target volume far greater than is possible from the ground.

EUSO is a wide angle high resolution telescope, which has a field of view of $\sim 30^\circ$ with a 0.1° resolution. It will be accommodated in the International Space Station (ISS) and look down the earth atmosphere from a 400km height ISS orbit. The full aperture for UHECRs is estimated to be 500 000 km^{2}sr. Even with conservative assumption of observational duty cycle of 10 % , one obtains an effective time averaged aperture of 50 000 km^{2}sr. This aperture is ~ 300 times larger than the one of AGASA and ~ 7 times larger than southern site of Auger Observatory, which is now under construction in Argentina.

If event clusters observed by AGASA are real, it is expected from Monte Carlo simulation that EUSO will see ~ 100 particles from individual brightest sources and will give us a good opportunity to test the possible violation of the Lorentz invarian as proposed by one of the hypotheses which we discuss below in 2.6.3.

The EUSO mission has to be included as a external payload for the ESA Columbus module. The Phase A study was successfully completed in 2004, however ESA executive has put on hold succession of EUSO to Phase B because of recent reconsiderations of the whole ESA space program [208]. If the results of these changes will be positive for EUSO, then the current most probable date for mission launch is the year 2012.

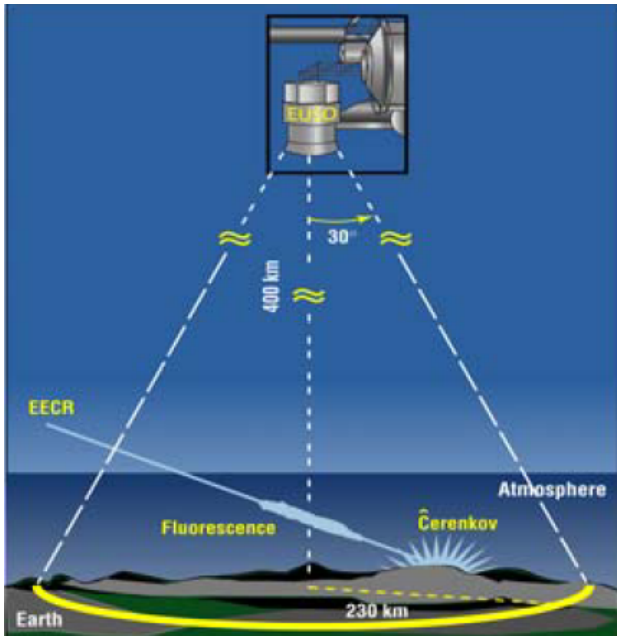

Figure 2.15: *Scheme of EUSO orbital detector at ISS. From [208].*

2.6 Possible Sources & Mechanisms of UHECR Generation

2.6.1 Fermi Acceleration

The basic mechanism of the very high energy particle acceleration was first proposed by Fermi [100] in 1949. He obtained that for stochastic particle acceleration by electric fields induced by the motion of magnetic fields B, the rate of energy gain by relativistic particles of charge Ze can be written:

$$\left(\frac{\mathrm{d}E}{\mathrm{d}t}\right)_{acc} = \xi Z\, ec^2 B, \tag{2.10}$$

where $\xi < 1$ and depends on the acceleration mechanism. This was equation used by Hillas [130] in 1968 for the construction of his already classical diagram, where the suitable acceleration sites are shown and the maximum achievable energy for given proton number Z could be derived (see Fig. 2.16). On one axis is the characteristic size of the object (proportional to the mean total acceleration time) and on the other is its characteristic magnetic field strength. Generally, this diagram is still valid and suitable for first orientation at the field of possible acceleration sites.

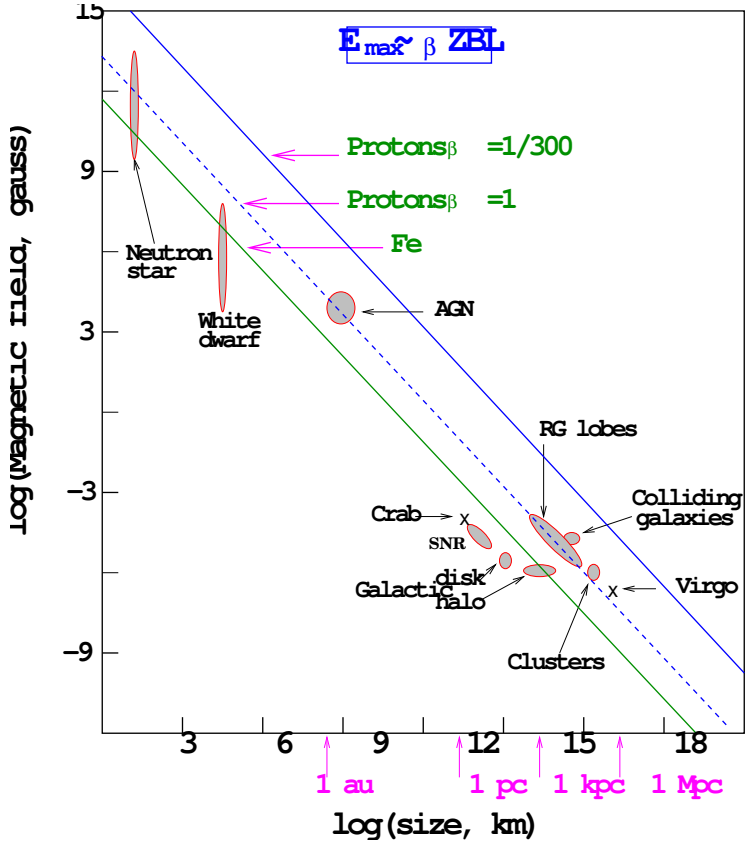

Figure 2.16: *Classical "Hillas Diagram". Size and magnetic field strength of some possible acceleration sites. Objects below the diagonal lines cannot accelerate the corresponding elements above* 10^{20} *eV or* 10^{21} *eV. SNR is abbreviation for supernovae remnants, RG lobes is for radiogalaxy lobes,* β *is the factor of efficiency of acceleration mechanism. Adapted from [130].*

Today two modifications of Fermi acceleration are distinguished — Fermi's original theory (the so-called second order Fermi acceleration) and a more efficient first-order Fermi acceleration, developed in late 70s [36]. In the text below simplified explanation of both theories given by Protheroe [191] in 1998 is followed.

Fermi's Original Theory

Gas clouds in the interstellar medium have random velocities of $\sim 15\ \mathrm{km\,s^{-1}}$ superimposed on their regular motion in the galaxy. Cosmic rays gain energy on average when scattering on these magnetized clouds. A cosmic ray enters a cloud and scatters off irregularities in the magnetic field which is tied to the cloud because it is partly ionized.

In the frame of the cloud no change in energy occurs because the scattering is collisionless and so the elastic scattering between the ray and the cloud as a whole materialises,

because the cloud is much more massive than the cosmic ray. Also, cosmic ray's direction is randomized by the described scatterings.

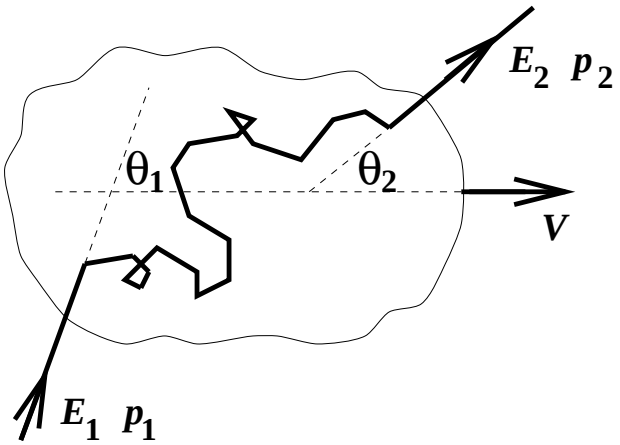

Figure 2.17: *Fermi acceleration—interaction of cosmic ray of energy E_1 with "cloud" moving with speed V. From [191].*

We can ascribe velocity V to the cloud, initial energy E_1 and initial momentum p_1, and also final energy E_2 and final momentum p_2 to the particle. The particle enters the cloud in the direction θ_1 with respect to the cloud's velocity V and leaves it in the direction θ_2. The energy is obtained by applying the Lorentz transformation between the laboratory frame and the cloud frame. Transforming to the cloud frame gives :

$$E_1' = \gamma E_1(1 - \beta \cos\theta_1), \tag{2.11}$$

where $\beta = V/c$ and $\gamma = 1/\sqrt{1-\beta^2}$. Returning back to the laboratory frame we get:

$$E_2 = \gamma E_2'(1 + \beta \cos\theta_2'), \tag{2.12}$$

Because the scattering is collisionless, the magnetic field is tied to the cloud and the cloud is very massive, in the cloud's rest frame there is no change of energy $E_2' = E_1'$ and hence we obtain the fractional change in the laboratory frame :

$$\frac{E_2 - E_1}{E_1} = \frac{\Delta E}{E} = \frac{1 - \beta\cos\theta_1 + \beta\cos\theta_2' - \beta^2\cos\theta_1\cos\theta_2'}{1-\beta^2} - 1. \tag{2.13}$$

For the evaluation of the mean value of the energy value we need to obtain average values of $\cos\theta_1$ and $\cos\theta_2'$ (we will denote them as $\langle\cos\theta_1\rangle$ or $\langle\cos\theta_2'\rangle$). Inside the cloud, the cosmic ray direction is randomized after many scatterings:

$$\langle\cos\theta_2'\rangle = 0 \tag{2.14}$$

The average value of $\cos\theta_1$ depends on the rate at which cosmic rate collide with clouds at different angles. The rate of collision is proportional to th relative velocity between the cloud and the particle so that the probability P per unit solid angle Ω_1 of having a collision at angle θ_1 is proportional to $(v - V\ \cos\theta_1)$, where v is the velocity of the particle, and for the ultrarelativistic particles $v \simeq c$. Thus we can write:

$$\frac{\mathrm{d}P}{\mathrm{d}\Omega_1} \propto (1 - \beta cos\theta_1) \tag{2.15}$$

By integration we obtain:

$$\langle \cos\theta_1 \rangle = \int \frac{\cos\theta_1 \frac{\mathrm{d}P}{\mathrm{d}\Omega_1}\mathrm{d}\Omega_1}{\int \frac{\mathrm{d}P}{\mathrm{d}\Omega_1}\mathrm{d}\Omega_1} = -\frac{\beta}{3} \tag{2.16}$$

And finally giving for the mean energy change $\langle \Delta E \rangle$:

$$\frac{\langle \Delta E \rangle}{E} = \frac{1 + \beta^2/3}{1 - \beta^2} - 1 \simeq \frac{4}{3}\beta^2 \tag{2.17}$$

because $\beta \ll 1$.

As $\langle \Delta E \rangle / E \propto \beta^2$ must be positive, this process leads to energy gain, but because $\beta \ll 1$ the average energy gain is very small.

First Order Fermi Acceleration

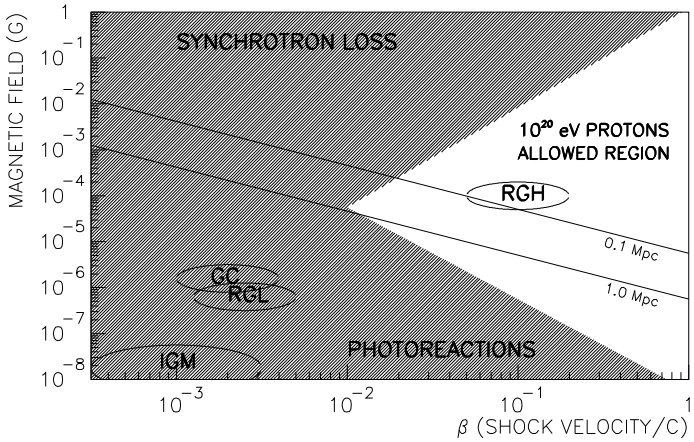

Figure 2.18: *Magnetic field strength and shock velocity of possible acceleration sites. GC refers to Galactic Cluster (accretion shocks), IGM to Inter Galactic medium, RGL to Radio Galaxy Lobes and RGH to Radio Galaxy Hot spots (subclass of RGL). From [33].*

Fermi's original theory modification was developed to the more effective acceleration (first order in β) taking place at supernova shocks but it is generally applicable to strong shocks in other astrophysical contexts. Our discussion of shock acceleration will be of necessity brief and omit a number of details. For simplicity we will consider the test particle approach, adopt a plane geometry and consider only non-relativistic shocks.

We will take the classic example of a SN shock, although the discussion applies equally to other shocks. During the supernova explosion several solar masses of material is ejected at a speed of $\sim 10^4$ km.s^{-1} that is much faster than the speed of sound in the interstellar medium (ISM) which is $\sim 10\,\mathrm{km\,s^{-1}}$. A strong shock wave propagates radially up in front of the supernova ejecta. The velocity of the shock V_S depends on the velocity of the ejecta V_P and on the ratio of specific heats κ through the compression ratio R:

$$\frac{V_S}{V_P} \simeq \frac{R}{R-1} \tag{2.18}$$

For SN shocks the SN will ionize the surrounding gas which will therefore be monoatomic ($\kappa = 5/3$) and the theory of the shock hydrodynamics than gives $R = 4$.

In order to work out the energy gain per shock crossing, we can imagine magnetic irregularities on both sides of the shock as clouds of magnetized plasma in Fermi's original theory. By considering the rate at which cosmic rays cross the shock from downstream to upstream, and upstream to downstream one finds that $\langle \cos\theta_1 \rangle = -2/3$ and $\langle \cos\theta_2' \rangle = 2/3$, giving:

$$\frac{\Delta}{E} \simeq \frac{4}{3}\beta \simeq \frac{4}{3}\frac{V_P}{c} \simeq \frac{4}{3}\frac{(R-1)}{R}\frac{V_S}{c} \tag{2.19}$$

Note that $\beta = V_P/c \propto \Delta E/E$, so basically β influences the resulting energy change in its first order, so the whole theory of Fermi shock acceleration and therefore is called the *first order* Fermi theory. We can conclude, that first order Fermi acceleration is much more efficient than previously discussed theory.

To obtain the energy spectrum we need to find out the probability of a cosmic ray encountering this shock once, twice, three times etc. We need to take into account the flow rate downstream and the flow rate upstream, and then to evaluate the probability of escape. From simple arguments which can be found e.g. in [191] we arrive to a power-law spectrum, where for the exponent Γ it holds:

$$\Gamma = 1 - \frac{\ln(1 - P_{escape})}{\ln(1 + \Delta E/E)} \approx \frac{R+2}{R-1}, \tag{2.20}$$

where P_{escape} is the probability of escaping from the shock. Hence we get for $R = 4$ to the differential spectrum Q of cosmic-ray acceleration:

$$Q(E) \propto E^{-\Gamma} = E^{-2} \tag{2.21}$$

The observed cosmic ray spectrum is generally steepened, what is in first approximation attributed to energy-dependent escape from the Galaxy.

2.6.2 Classical accelerators

Several surveys of possible accelerator sites were recently published, namely [179], [243], [82] and [183].

Origin in the vicinity of neutron stars in our Galaxy

The nearest suitable UHECR sources should be represented by neutron stars. These source type is not consistent with the assumption of extragalactic origin of UHECRs and have to explain the observed isotropic distribution[14] and no confinement with Galactic plane. One possible explanation will also be given in this work, actually in paragraph 2.10.3.

According to the presented *Hillas plot* the typical surface strength of magnetic field on young neutron stars is sufficient ($\sim 10^{13}$ G) for the acceleration up to EHECR scale ($\approx 10^{20}$ eV for protons). However, the plasma that expands beyond the light cylinder is free from the main loss processes and may be accelerated to ultra-high energies. In particular, newly formed, rapidly rotating neutron stars may accelerate iron nuclei to ultra-high energies through relativistic magnetohydronamic (MHD) winds [56]. These Galactic sources need the magnetic field efficient enough to isotropize the directions of UHECRs, because no observable correlation with Galactic plane was found[15].

Origin in radio galaxy hot spots

The hot spots are interpreted as a gigantic shock waves emanating from from a central active galactic nucleus at relativistic speeds. Typical size of the hot spot is about few kiloparsec and the magnetic field within is several hundred μG. The maximum energy attainable is $(1-10)\times 10^{20}$ eV, dependent on actual parameters of the spot. The acceleration is classically due to the first-order Fermi acceleration.

Origin in cosmologically nearby galaxies

It is generally agreed that our Galaxy is producing cosmic rays up to 10^{18} eV, with a luminosity 10^{30} J.s^{-1}. for a confinement time 10^{11} s. It is possible that in more active galaxies [220], with higher rate of star formation, the magnetic field may be higher. The requirement for 10^{20} eV protons exceeds 3×10^{15} G.m (magnetic field $\times$ characteristic size). Such not common units illustrate the fact that we need either extremely large acceleration sites or extremely strong magnetic fields. Acceleration to extremely high energies near the horizons of supermassive black holes in the galactic centers has also been suggested [59].

[14] See section 2.8.
[15] See section 2.8.

Origin in active galactic nuclei — in BL Lac objects (blazars)

The origin of UHECRs in the vicinity of active galactic nuclei (AGNs) should be included into previous paragraph. However, we decided to stress the importance of these particular objects by presenting it separately.

Theories, explaining the observed flux of UHECRs by their generation in AGNs, were presented recently e.g. by [48]. Especially the special type of AGNs, which is historically called 'BL Lac' has recently attracted the attention of cosmic ray community, because of significant correlation between positions of subset of BL Lac objects and positions of UHECRs found in the data of AGASA, Yakutsk and Hires experiments [227, 112].

BL Lac objects, named after first discovered object of their type, are of course not variable stars as the name suggests. Simply stated, BL Lac are AGNs with jets oriented in the direction of observer, where the particle accleeration has to occur within the jet. The estimated maximum energy of accelerated particles could reach up to the order of 10^{20} eV, maybe sufficiently enough to explain the observed UHECR flux. Moreover, the local emissivity of AGNs is in agreement of required emissivity of cosmic rays ($L \sim 10^{47}$ ergs/Mpc^3 yr).

Origin in gamma ray bursts

According to hypotheses presented e.g. in [235] gamma ray bursts (GRBs) may also be a source of ultra-high energy cosmic rays. Both phenomena have still unknown origins and also other similarities that may point for a common source. UHECRs and GRBs are distributed isotropically, the average rate of γ-ray energy emitted by GRBs is comparable to the energy generation rate of UHECRs of energy $> 10^{19}$ eV in a redshift independent cosmological distribution of sources, both have energy $\approx 10^{37}$ J.Mpc^{-3}.yr^{-1}.

However, the recent observations of GRBs counterparts leads us to really cosmological distance of UHECRs and so the UHECR flux from the nearby GRBs (which are not so extremely losing initial energy during propagation[16]) is too low. Furthermore, this limitation to a "GZK sphere"[17] would change also the spatial distribution of the UHECRs, because such near GRB is expected to occur less than once over a period of 100 years. Extragalactic magnetic fields[18] are then generally expected to be too low to affect the trajectories of UHECRs significantly and so the final distribution will not be isotropic, but in a form of a "hot spot" (covering only a small fraction of the sky as a small spherical cap).

The general problem of all described processes up to this point is that the generated particles loss have the significant energy losses in the vicinity of all these discussed active environments. Maybe the most important loss channels are due to synchrotron radiation emissions and pair production in the dense surroundings of these objects.

[16] See next section.
[17] Sphere with the 50 Mpc radius around the Earth.
[18] See next chapter.

2.6.3 "New physics" theories

Origin in interactions with neutrinos

The first presented acceleration mechanism in this group, which is often labeled as *top-down* acceleration, is represented by the neutrino — neutrino interactions. According to this scenario, the extreme energetic neutrino ($\sim 10^{22}$ eV) accelerated in any cosmologically distant source interacts with background relic neutrino (with temperature about 1.9 K) and produces Z^0 boson. The resonance energy for this energy is of about 4×10^{21} eV. This Z boson decays and produces ~ 2 nucleons, ~ 20 γ-rays and ~ 50 neutrinos. *Z-bursts* are taking place in the relative vicinity ($\sim$ Mpc) to the Earth and we observe the arriving nucleons, which are products of Z decay.

Other possibility is that the cross-section of neutrino-nucleon interaction rises rapidly in the investigated energy region and this extreme energy neutrinos from the unknown cosmological sources are interacting directly with nucleons in the Earth's atmosphere [214].

Decay of relic superheavy particles

According to this theory cold dark matter in the galactic halo is supposed to contain a small admixture of long-lived superheavy particles with mass $> 10^{21}$ eV with a lifetime greater than the age of universe [49]. Such particles have to be created during reheating following the inflation or through the decay of hybrid topological defects[19]. The decay products are nucleons, electrons, photons and neutrinos, which are arriving to the Earth and initiating showers with common properties.

Origin in topological defects

Topological defects, cf. monopoles, cosmic strings or superconducting strings could be also the sources of UHECRs [49]. These defects has to be left from the phase transitions in the early universe. The UHECRs are originated during the collapse, the annihilation or when such formations cross each other.

New hadrons

The suggestion has also been made that new neutral particles could be producing the trans-GZK events [95]. This particle have to be stable and with lower cross-sections for the interactions during propagation. Such a particles are called *uhecrons*. Similarly *vortons* (superconducting cosmic strings stabilized by a current) present a solution that is limited to the very highest energies.

Magnetic monopoles

The accelerated monopoles with mass $< 10^{10}$ GeV could be the sources of UHECRs too [187]. These monopoles should be accelerated in the Galactic magnetic field and then hit

[19] See the next topic.

the Earth's atmosphere. But according to the simulations the produced showers then have special properties, which are not observed. Also the correlation with the Galactic plane is not observed.

Violation of Lorentz symmetry

Last idea presented here is the possible departure from the strict Lorentz invariance [76]. The proposed departure is too small to be detected by the man-made accelerators, but large enough to affect the particle kinematics in ultra-high energy region and so to suppress or completely forbid the interactions of UHECRs with CMBR. Therefore the predicted cutoff in the spectrum is at least shifted by one order of magnitude to higher energies and the origin of the observed high-energetic particles is possible also in the cosmological distances.

2.7 Propagation and Interactions

As we have noticed in section 2.2, for a proper identification of a suitable source the determination of the distance of the investigated object is also very important. It stems from the fact that UHECRs are efficiently losing significant fraction of theirs energy during propagation. For the range of ultra-high energies, the most important processes are pion photoproduction (affecting nucleons), Bethe-Heitler pair production and photodisentegration of nuclei.

The mean interaction length $x_{p\gamma}$ of a proton of energy E is given by [191]:

$$\frac{1}{x_{p\gamma}} = \frac{1}{8\beta E^2} \int_{\varepsilon_{min}(E)}^{\infty} \frac{n(\varepsilon)}{\varepsilon^2} \int_{s_{min}}^{s_{max}(\varepsilon,E)} \sigma(s)(s - m_p^2 c^4) \mathrm{d}s \mathrm{d}\varepsilon, \tag{2.22}$$

where $n(\varepsilon)$ is the differential photon number density of photons of energy ε, and $\sigma(s)$ is the appropriate total cross section for the process in question, for a centre of momentum (CM) frame energy squared s, which is given by:

$$s \ = m_p^2 c^4 + 2\varepsilon E(1 - \beta \cos\theta), \tag{2.23}$$

where θ is the angle between the directions of the proton and photon and βc is the proton's velocity.

For pion photoproduction (index π is for pion) we get:

$$s_{min} = (m_p c^2 + m_\pi c^2) \approx 1.16\mathrm{GeV}^2 \tag{2.24}$$

and

$$\varepsilon_{min} = \frac{m_\pi c^2 (m_\pi c^2 + 2 m_p c^2)}{2E(1+\beta)} \approx \frac{m_\pi c^2 (m_\pi c^2 + 2 m_p c^2)}{4E} \tag{2.25}$$

For photon-pion pair-production the threshold is somewhat lower:

$$s_{min} = (m_p c^2 + 2 m_e c^2)^2 \approx 0.882\mathrm{GeV}^2 \tag{2.26}$$

and

$$\varepsilon_{min} \approx \frac{m_e c^2 (m_e c^2 + m_p c^2)}{E} \tag{2.27}$$

For both processes is valid:

$$s_{max}(\varepsilon, E) = m_p^2 c^4 + 2\varepsilon E(1+\beta) \approx m_p^2 c^4 + 4\varepsilon E. \tag{2.28}$$

$s_{max(\varepsilon,E)}$ corresponds to a head-on collision of a proton of energy E and a photon of energy ε.

Examination of the integrand in equation 2.22 shows that the energy of the soft photon interacting with a proton of energy E is distributed as:

$$p(\varepsilon) = \frac{x_{p\gamma}(E) n(\varepsilon)}{8\beta E^2 \varepsilon^2} \Phi(s_{max}(\varepsilon, E)), \tag{2.29}$$

where in the range $\varepsilon_{min} \leq \varepsilon \leq \infty$ is valid:

$$\Phi(s_{max}) = \int_{s_{min}}^{s_{max}} \sigma(s)(s - m_p^2 c^4) \mathrm{d}s \tag{2.30}$$

Now we are able to derive the mean interaction length from equation (2.22). Dividing by the inelasticity $\kappa(E) = \Delta E/E$, one obtains the energy-loss distances for the two discussed processes:

$$\frac{E}{\mathrm{d}E/\mathrm{d}x} = \frac{x_{p\gamma}(E)}{\kappa(E)} \tag{2.31}$$

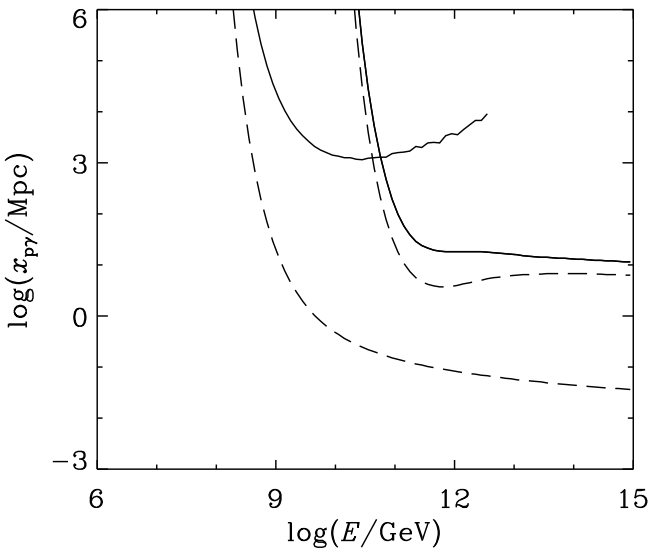

Figure 2.19: *Mean interaction length (dashed lines) and energy-loss distance (solid lines; $E/(dE/dx)$) for proton-photon pair-production (lower curves) and pion-production (higher curves) in the microwave background. From [191].*

Numeric values for the mean interaction lengths and energy losses are shown on Fig. 2.19. Very illustrative is also the resulting dependence of the energy of proton on the travelled distance, which is showed in Fig. 2.20.

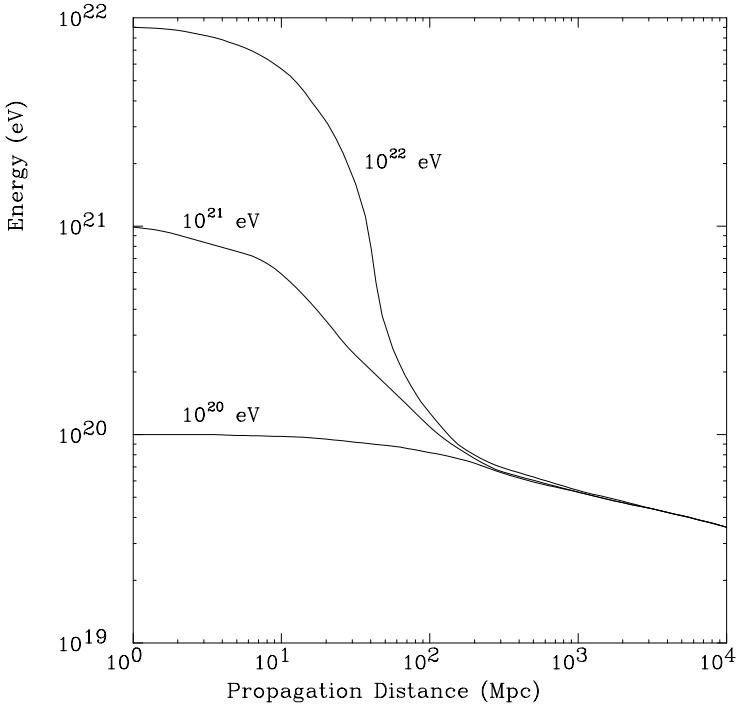

Figure 2.20: *Energy of a proton as a function of the propagation distance through the 2.7 K cosmic background radiation for various initial energies. The energy loss is computed only due to photopion production. From [33].*

In the case of nuclei the situation is a little more complicated. The threshold condition for Bethe-Heitler pair production can be expressed as (γ is here given by $\gamma = E/A\ m_p c^2$):

$$\gamma > \frac{m_e c^2}{\varepsilon}\left(1 + \frac{m_e}{A m_p}\right), \tag{2.32}$$

and the threshold condition for pion photoproduction can be expressed as:

$$\gamma > \frac{m_\pi c^2}{2\varepsilon}\left(1 + \frac{m_\pi}{A m_p}\right), \tag{2.33}$$

where A is the atomic mass number. Because the gamma factor γ is divided by A in the case of nuclei against the case of proton, the pair production starts for nuclei in lower energy region.

The energy loss for the pair production by a nucleus in each collision near threshold is approximately $\Delta E \approx \gamma 2 m_e c^2$. Hence the inelasticity is

$$\kappa = \frac{\Delta E}{E} \approx \frac{2m_e}{Am_p}, \tag{2.34}$$

what is a factor of A lower than for protons. On the other hand, the cross section of each interaction rises by a factor Z^2, so the overall energy loss distance is for pair production reduced by a factor Z^2/A, e.g. for iron $26^2/56 \approx 12.1$.

For pion production the energy loss by a nucleus in each collision is given by $\Delta E \approx \gamma m_\pi c^2$, so the inelasticity is also lower by a factor A. However, the cross section in this case rises only as $A^{0.9}$ and the overall energy loss distance increases by a factor 1.5 for iron nuclei.

In the case of heavy nuclei (mass number A) we have to take into account also other important process — the photodisintegration (first evaluated in 1976 by [198]): $A + \gamma \rightarrow (A\ -1) + N$ or $\rightarrow (A\ -2) + 2N$, where A is here for nuclei with mass number A and N for nucleon. The energy loss from photodisintegration is not only due to CMBR photons but also due to photons from the IR background flux[20] The energy loss due to IR photons is only effective below 5×10^{19} eV, while the energy loss in interactions with microwave background dominates above 2×10^{20} eV [213].

The gamma photons are losing their energy mainly through the pair creation in interactions with the CMBR. It takes place in the wide energy region above the threshold at 4×10^{14} eV: $\gamma + \gamma_{CMBR} \rightarrow e^+ + e^-$. Also in this case the attenuation due to IR background radiation is important, and becomes dominating above 2×10^{19} eV.

The last non-negligible effect arises from the omnipresent cosmological redshift. All particles lose energy due to the general expansion of the universe. The time scale over which a particle would suffer complete energy loss due to this effect is of the order

$$\tau_H = \left(\frac{1}{E} \frac{\mathrm{d}E}{dt} \right)^{-1} \approx H^{-1}, \tag{2.35}$$

where H is the Hubble constant. Then the constant $c\tau_H$ is representing the absolute upper limit on the distance a particle can travel before expiring. This limit and also the net effects for the attenuation lengths of protons, iron nuclei and photons is plotted in Fig. 2.21.

[20] Estimated empirically from the observations of 3000 galaxies in the IRAS catalogue.

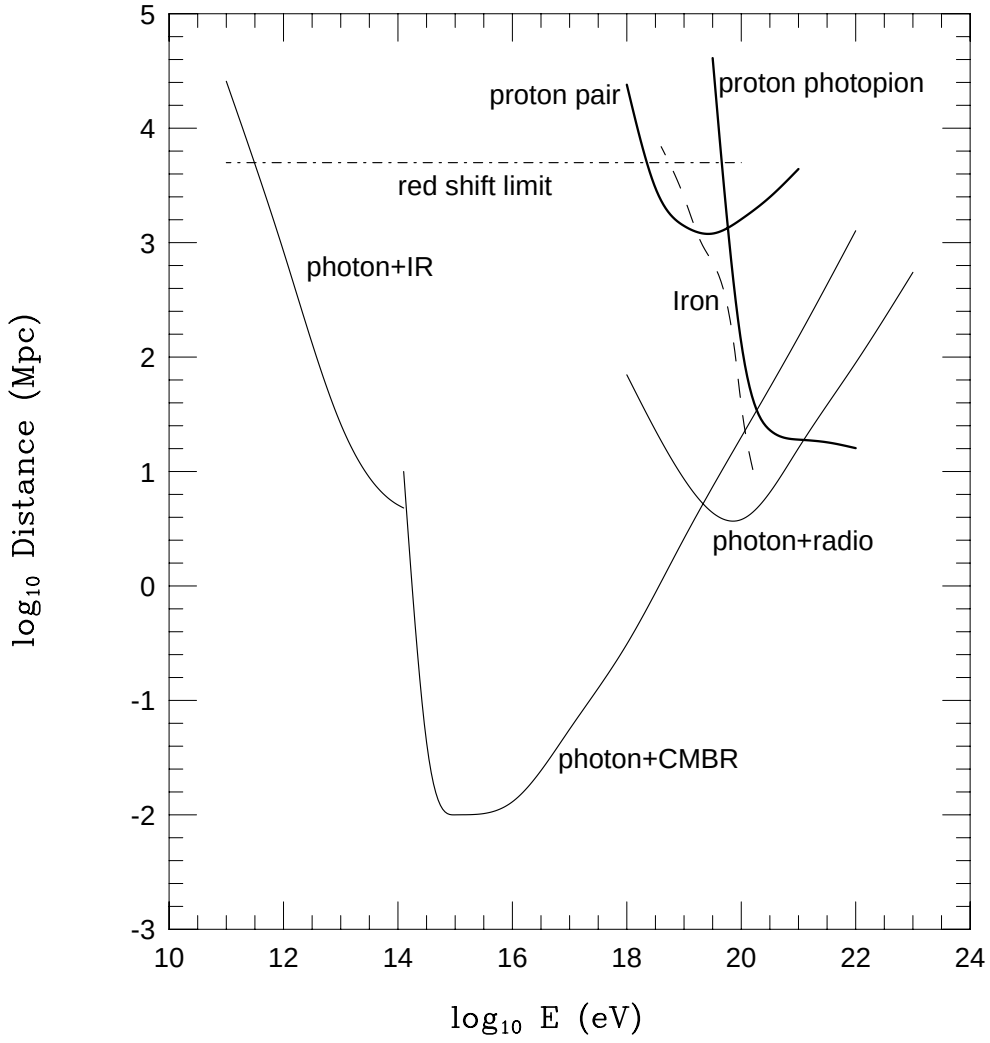

Figure 2.21: *Attenuation length of photons, protons and iron in various background radiations as a function of energy. Double pair production, which is not shown, limits the photon attenuation length to about 100 Mpc above* 10^{22} *eV. The dot-dashed line represents the absolute upper limit on the distance a particle can travel toward Earth, regardless of its initial energy. From [33].*

2.7.1 The GZK effect and the GZK cutoff

Some ambiguity exists between two following terms that are heavily used within CR-physicists community:

The GZK effect (or the GZK mechanism) was first described independently by Greisen [116] and Zatsepin and Kuzmin [244] in 1966 (quantitatively for proton interaction with CMBR) and currently this term is understood as the set of possible cosmic ray interactions

mostly with cosmic microwave background photons. These interactions were described above in section 2.7 and all have well defined thresholds for given type of cosmic ray particles. If the UHECR are dominated by protons, then the most important interaction remains proton photopion production described at first, which has the threshold of 4×10^{19} eV for proton energy.

On the other hand, different authors propose slightly different definitions of *GZK cutoff*. Here we will follow the definition described by [46] and its expansion by [243]:

The position of the GZK cutoff in CR spectrum is given by the decrease to one half of the expected flux. This expected flux is first evaluated as non-attenuated — without accounting of all attenuation processes during the propagation of cosmic ray particle.

Therefore, we are actually looking for the energy, where the set of attenuation processes is effective enough to suppress the flux to the one half of its original value.

From this statement it is clear that position of the GZK cutoff is dependent on the type of CR and on our expectations about the non-attenuated flux. Furthermore, our expectations about flux are just hypothetical, because we still do not know neither the spatial distribution nor the nature of sources of UHECRs. For example, if all the UHECR sources are of Galactic origin, then there is almost no cutoff at all, because the typical distance of such type of source is much smaller than the typical interaction length of GZK effect processes. Or, for the different cosmological distributions of radio galaxies and for proton-dominated composition of CR spectrum is the resulting GZK cutoff varying in the range $(5 \div 6) \times 10^{19}$ eV.

The cutoffs for nuclei and photons are in general lower by several orders of magnitude; only the neutrinos have this cutoff around 10^{22} eV.

Therefore, the knowledge of the actual GZK cutoff value (steming from the above-mentioned definition) is not critical; more substantial is the knowledge of the energy losses and interaction lengths or cross-sections for a given acceleration process. Generally, under the term *GZK cutoff* is understood the energy range about $(5 \div 6) \times 10^{19}$ eV, the energy of proton cutoff assuming the cosmologically distributed sources. If we are refering to any particle as to *super-GZK* particle, it is meant that this particle is well above the GZK cutoff and then it is generally considered that its energy is above 10^{20} eV.

2.8 Spatial Distribution of UHECRs

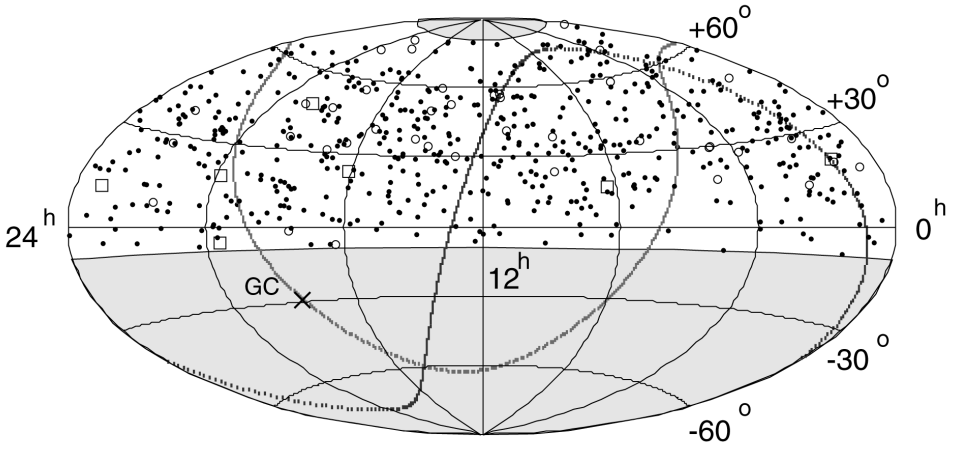

Figure 2.22: *AGASA arrival directions of cosmic rays with energies above* $10^{19.0}$ *in equatorial coordinates. Dots, open circles, and open squares represent cosmic rays with energies* $(1-4)\times 10^{19} eV$, $(4-10)\times 10^{19}$ eV *and* $\geq 10^{20}$ eV, *respectively. The Galactic and supergalactic planes are shown by the dotted curves, "GC" designates Galactic center — on the Galactic plane. From [223].*

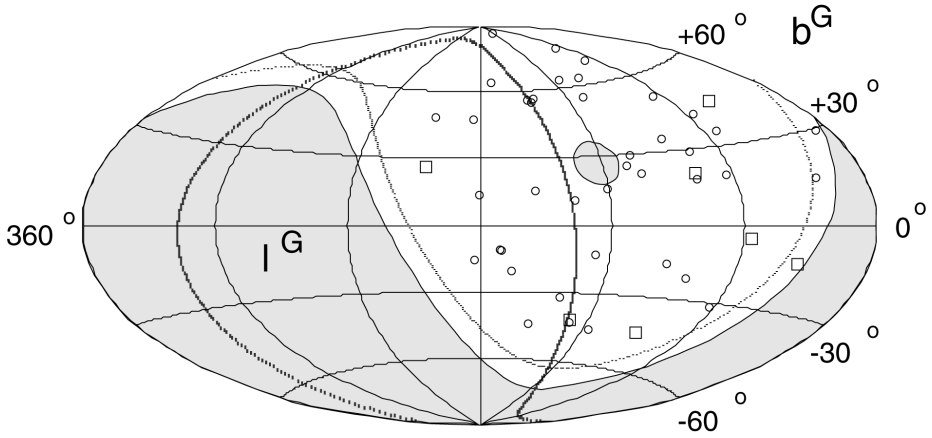

Figure 2.23: *The same as on Fig. 2.22, but in galactic coordinates and only for AGASA particles above* $4 \times 10^{19} eV$. *Also from [223].*

The essential importance for the discrimination of the real source(s) of UHECRs has their observed spatial distribution. Many analysis were done in the lower energy regions and are summarized in [234]. Because of the existence of the magnetic field, which effects will be discussed in detail in next section, the arrival directions are very accurately isotropic. The individual experiments are unable to observe the whole sky and so the analysis where the declination is a studied parameter is rather complicated and not straightforward. Therefore the harmonic analysis is applied obviously in the right ascension. The method is to fit the observed distribution to a sine wave with period $2\pi/m$ (mth harmonic) and to derive the maximum amplitude and the phase of anisotropy.

Some signs of slight anisotropy were observed in the energy region, where the Larmor radius (equation 2.2) is growing above the kiloparsec order, above 10^{17} eV. In the data from Haverah Park it was found the amplitude with an excess of about 2 % at right ascension $212^\circ \pm 17^\circ$ in energy region about 10^{17} eV. 1.4 % excess at the very different right ascension 123° in the energy region $3 \times 10^{16} - 3 \times 10^{17}$ eV in Yakutsk data. So, even in this regions, where the data volumes are very large (about millions of detected events around 10^{17} eV), the observed departures from the anisotropy are not statistically very significant.

Other interesting sign of anisotropy was found in the AGASA data between $8 \times 10^{17} - 2 \times 10^{18}$ eV (4.3×10^4 events), where the first harmonic amplitude of 4 % was found in the direction to the Galactic center and to anticenter.

As we have seen in section 2.5, the statistics in the UHECR region is very poor. Only about 200 particles with energies above 4×10^{19} eV could be analyzed. However, several works dealing with such analysis were published. The first one [211], which we will

discuss here, found the slight correlation with the direction of the supergalactic plane[21], the observed excess is $\sim 2.5 - 2.8\sigma$ in terms of Gaussian probabilities. This claim was challenged indirectly by the work [170], where the authors found no correlation with the distribution of nearby galaxies with EGMF[22] taken into account. Also the recent special analysis of the data from AGASA [223] found no correlation with supergalactic plane and no large-scale anisotropy at all. However, the small-angle clustering was found. Actually, one triplet and three doublets int the energy region above 4×10^{19} eV were found. This analysis was further expanded in the paper [231], where authors used UHECR data from Volcano Ranch, Haverah Park, Yakutsk and AGASA (total number is 92 events). Within this work [231] were presented also two triplets and twelve doublets (with space angle separation $< 3.0^{\circ}$). Both triplets and eight doublets are within $\pm 10^{\circ}$ from the supergalactic plane. The probability that this effect will be observed by chance is less than 1 % [102]. However, the correlation with supergalactic plane should not be significant and the small angle clustering should be accounted to another set of point sources of UHECRs. According to recent studies [102] the significance of such small-scale clustering is smaller than it was claimed previously. In fact, it it is consistent with the null hypothesis of isotropically distributed arrival directions at the 8 % level.

The very recent work of the HiRes Collaboration [237] found no significant clustering and the evidence for the point sources within combined data above 10^{19} eV of HiRes experiment (271 events) and AGASA (57 events above 4×10^{19} eV) experiment. Actually, the chance probability of appearance of a source is 43 %, therefore no evidence for clustering consistent with point source was found. Also AUGER first anisotropy studies [23] show no statistically significant clustering of events consistent with a point source.

Finally, some quite significant correlations between subsets of BL Lac objects and cosmic rays observed by AGASA and Yakutsk [227] were found. These correlations were partially confirmed by the HiRes collaboration [103]. The probabilities that such correlations will appear by chance is in order of 10^{-4} and therefore rather significant. However, some special cuts for BL Lac objects selection were made as well as some not really straightforward cuts on data itself. Therefore these identified correlations have to be confirmed not only by the new data from HiRes, but also independently from Auger experiment.

Studying the spatial distribution of cosmic rays and possible departures from their isotropy we definitely cannot neglect the influence of the magnetic fields onto their trajectories. The detailed knowledge of magnetic fields is of essential importance also for UHECRs, which are the main subject of this thesis. These descriptions of magnetic fields and the propagation of UHECR particles in these fields is provided within following section.

[21] Defined by the higher concentration of bright galaxies in our local supercluster.

[22] Extragalactic magnetic field; see section 2.9.

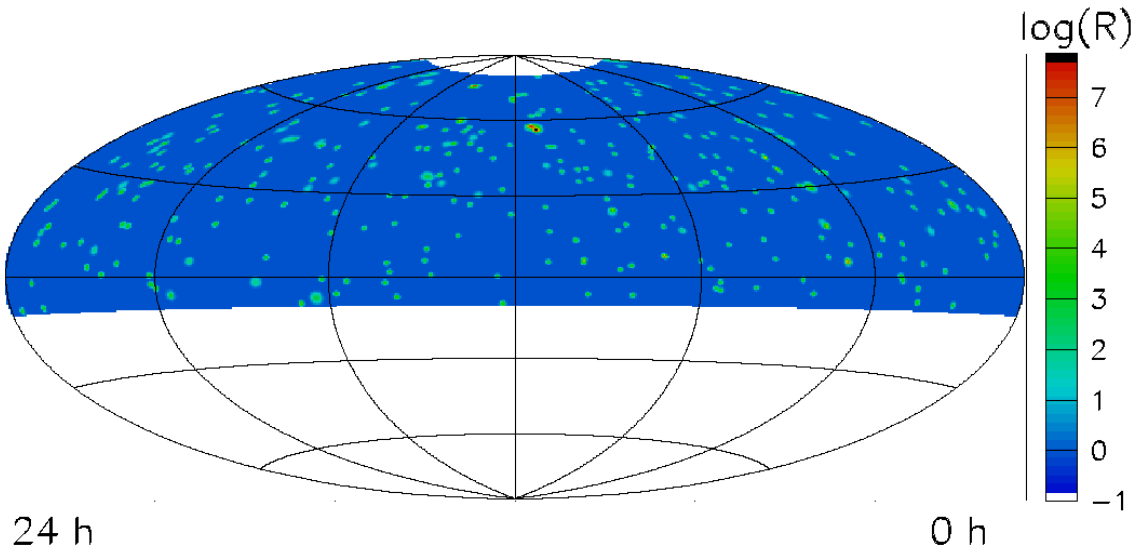

Figure 2.24: *Likelihood ratio ln R , maximized with respect to n_S, as a function of right ascension and declination for the combined set of HiRes events above 1×10^{19} eV and AGASA events above 4×10^{19} eV. From [237], where the detailed description of the method as well as the definition of likelihood ratio R is also available.*

2.9 Extragalactic Magnetic Fields

While the first measurements of interstellar magnetic fields are older than a half of the century[23], the large-scale structures are still known very poorly. From the Faraday rotation measures of the extragalactic objects we are able to derive only the upper limits ([156] or [160]) for the field strengths. Actually, Faraday rotation measures from the distant powerful radio sources give $B\sqrt{l_c} < 10^{-9}$ G Mpc$^{1/2}$ for the magnetic field strengths, where the l_c denotes the reversal length of the field. So any modelling of this field is just very speculative.

This pure experimental approach is quite often challenged by ambitious theoreticians, who expect some magnetic field anomalies in the form of (primordial) large-scale curved strings or planes [205], in which the magnetic field is reasonably stronger than the above-mentioned upper limits — ranging from 10^{-6} G up to 10^{-3} G or the intensive magnetic field ($\sim 10^{-6}$ G) in very extensive galactic halo (reaching several Mpc) [124] or in the local galactic cluster [96] (with the same strength $\sim 10^{-6}$ G). These claims are further challenged

[23]See next section for short survey of used methods of magnetic fields measurements in the Galaxy.

by [83], giving a basic argument that the presence of such a strong magnetic field in the surroundings of our Galaxy would confine the bulk of cosmic rays for a time comparable to a Hubble time and turn the ratios of observed radioactive nuclei (Al^{26}/Al^{27} or Be^{10}/Be^{9}) in cosmic radiation into contradiction with observations. The case of intensive field in the large galactic halo will be also discussed in the next section.

Generally, the magnetic field simulations are also limited by the fact that the mechanism of the origin of extragalactic field is still unknown. Up to now is not possible to decide whether these fields are generated by the local fields of the galaxies or whether they are primordial and were originated in some phase transitions shortly after big bang.

2.10 Galactic magnetic field

The text of this section outgoes from author's original articles [193] & [194]. This work started as the part of author's diploma thesis [192], however it was largely expanded and re-worked using more effective computational approach and finished for publication during author's doctoral study.

2.10.1 Experimental evidence

The first evidence for the existence of a Galactic magnetic field (GMF) was derived from the observation of linear polarization of starlight by [134]. Many new measurements have been done since using of Zeeman spectral-line splitting (gaseous clouds, central region of the Galaxy), optical polarization data (large-scale structures of the magnetic field in the local spiral arm) and the Faraday rotation measurements in the radio continuum emission of pulsars and of the extragalactic sources. The last mentioned method is probably also the most reliable for the large scale structure. This method is also used for the determination of the global structure of the magnetic fields in the external galaxies. From these measurements it follows that the Galactic magnetic field has two components — regular and turbulent ([199]).

Random fields appear to have a length scale $50 \div 150$ pc and they are about two or three times stronger than the regular field. These random field cells have such a small scale (in comparison with kiloparsec scale of Larmor radii of UHECRs) that they are not modelled within global GMF models. However, it follows from recent work of [124] or [11] that turbulent field really plays a key role in the clustering, magnification or multiplying of the source images. Therefore we introduced random fields into our simulations, respecting the fact that such fields are very strong, especially in Galactic arm regions.

We are able to summarize our direct experimental knowledge about the Galactic magnetic field in several statements (according to [40], [238] and [119]):

- The strength of the *total* magnetic field in the Galaxy is (6 ± 2) μG in the disk and about (10 ± 3) μG within 3 kpc from the Galactic center.

- The strength of the local regular field is (4 ± 1) μG. This value is based on optical and synchrotron polarization measurements. Pulsar rotation measures give more conservative and approximately half the value. These rotation measures are probably underestimated due to anticorrelated fluctuations of regular field strength and of thermal electron intensity. On the other hand, optical and synchrotron polarization observations could be overestimated due to presence of anisotropic fields.

- The local regular field may be a part of a Galactic magnetic spiral arm, which lies between the optical arms.

- The global structure of the Galactic field remains uncertain. However, an established conservative model, which has prevailed in the last years, is the two-arm logarithmic spiral model (see below).

- Existence of two reversals in the direction towards Galactic center was confirmed recently. The first reversal is between the Local and Sagittarius arm, at ~ 0.6 kpc from the Sun, the second one is at ~ 3 kpc from the Sun. Some of the Galactic reversals may be due to large-scale anisotropic field loops.

- As expected from the beginning of the 1990s and also recently confirmed, the Galactic center region contains highly regular magnetic fields with strengths up to 1 mG. This extremely intensive field is concentrated in thin filaments oriented perpendicularly to the Galactic plane. The characteristic length of these filaments is about 0.5 kpc.

- The local Galactic field is oriented mainly parallel to the plane, with a vertical component of only $B_z \simeq (0.2 \div 0.3)$ μG in the vicinity of the Sun. The recent explanation is that this component is present due to existence of a poloidal magnetic field (see theoretical global field model below) — a poloidal field naturally originates within a dynamo model of GMF generation.

- The Galaxy is surrounded by a thick radio disk (height of about 1.5 kpc above and under the Galactic plane, half-width of 300 pc) similar to that of the edge-on spiral galaxies. The field strength in this thick disk is estimated to be around 1 μG. As in the case of the vertical field component discussed above (poloidal field), the most common explanation of the existence of such a thick disc is that this field is toroidal originating through the dynamo effect.

- The local Galactic field in the standard thin disk has an even symmetry with respect to the plane (it is a quadrupole). This is in agreement with the galactic dynamo model, which is briefly discussed in the next paragraph.

Other facts used in modeling of the GMF have an indirect character — they are usually derived from the observations of the other spiral galaxies and of the structure of their magnetic fields or from existing hypotheses of the mechanisms of magnetic field generation. In general, it is expected that the Galactic magnetic field encompasses the entire Galactic

disk and shows some spiral structure. Further research and measurements in this field have vital importance not only for the observations of UHECRs, but also for cosmic-ray physics and for other astronomical applications, e.g. for Galactic dynamics.

Theoretical global models of GMF

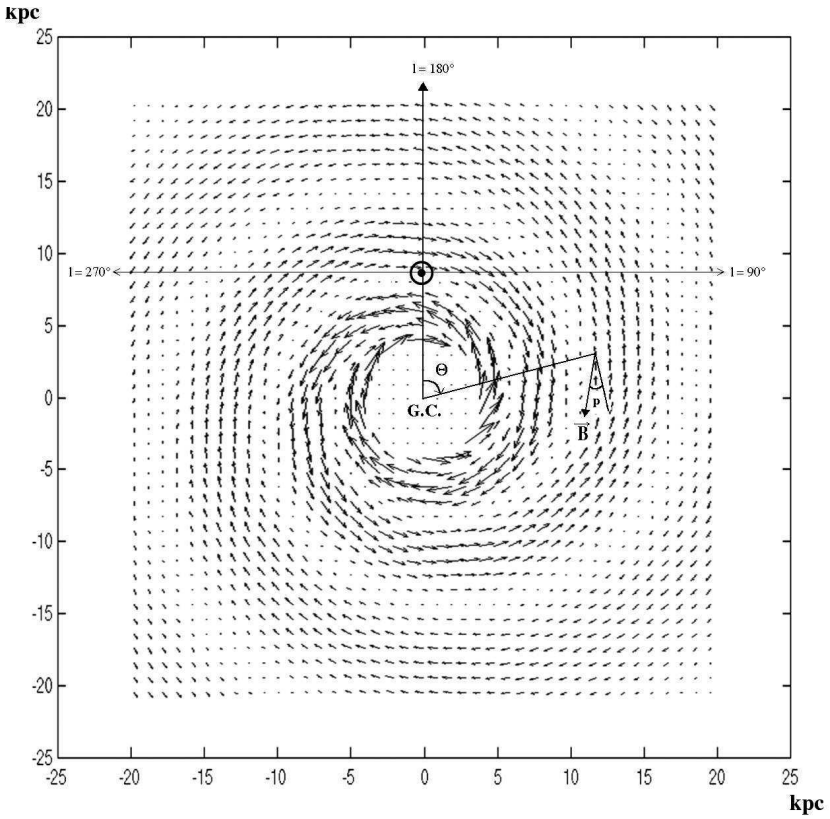

Figure 2.25: *Direction and strength of the regular magnetic field in the Galactic plane is represented by the length and direction of the arrows. The field inside the Galactocentric circle of radius 4 kpc is taken as constant, 6.4 μG. The model was constructed using parameters from [212] and [117], which are in detail described in the text. The sense and orientation of the field and of the angles Θ and p follows from the figure. G.C. denotes the Galactic center (at $l = 0°$).*

The global models omit the presence of turbulent fields and are trying to model just the regular component. The basic conservative model of the global Galactic plane was established by [117], based on the Faraday-rotation measurements of 134 pulsars. The model assumes a two-arm logarithmic spiral with the constant pitch angle[24] p and it shows

[24]The pitch angle determines the orientation of the local regular magnetic field. Its sense is clear from Fig. 2.25. The precise definition of pitch angle is not unique, in this work we used the definition proposed

π-symmetry, so that it is a bisymmetric (BSS) magnetic field model. More exactly, it has also a dipole character (it has field reversals and odd parity with respect to the Galactic plane), so it is called the BSS-A model.

The discussed model employs cylindrical coordinates — the radial distance r, the position angle Θ and the vertical height z. The radial B_r and azimuthal B_Θ components at the plane position (r, Θ) can be given by the following equations:

$$B_\Theta = B_0(r) \cos\left(\Theta - \beta \ln \frac{r}{r_0}\right) \cos p, \tag{2.37}$$

$$B_r = B_0(r) \cos\left(\Theta - \beta \ln \frac{r}{r_0}\right) \sin p. \tag{2.38}$$

where p denotes the pitch angle and according to [212] and [119] it is about $-10°$, $\beta = 1/\tan p \doteq -5.67$, r_0 is the Galactocentric distance of the maximum field strength at $l = 0°$ (in the discussed model it has a value $r_0 = 9.0$ kpc) and for $B_0(r)$ it holds:

$$B_0(r) = 3\frac{R}{r}, \tag{2.39}$$

where R is the Galactocentric distance of the Sun, taken as 8.5 kpc.

The vertical (z) component of the field is taken as zero in approximate agreement with observations. Results of this model are depicted in Fig. 2.25 and the orientation of the whole system is also clear from this Figure.

The size and field strength in the Galactic halo is extremely important for the cosmic-ray trajectories, but it is very poorly known. An obvious approach to this problem is represented by the work [212], where the field above and under the Galactic plane is taken as exponentially decreasing:

$$|B(r, \Theta, z)| = |B(r, \Theta)| e^{(-|z|/z_0)}, \tag{2.40}$$

where $|B(r, \Theta)|$ is the vector sum of magnitudes of B_r and B_Θ with the $z_0 = 1$ kpc[25].

We used this described model of the GMF as the basis for our simulations. Strictly speaking, we simply add toroidal and poloidal field components to this model, as is detailed in the next subsection.

Alternative models with other field configurations were also proposed. Another possible but according to recent observations a bit less probable configuration is the so-called ASS-S

by [117]: The galactic azimuthal angle Θ is defined to be increasing in the direction of galactic rotation. Logarithmic spirals are then defined by:

$$R = R_0 e^{k\Theta}, \tag{2.36}$$

where R is the radial distance and R_0 is the scale radius. The pitch angle is then $p = \arctan(k)$. This angle is negative for trailing spirals such as in our Galaxy, where R increases with decreasing azimuthal angle Θ. For our Galaxy, the galactic angular momentum vector points toward the south Galactic pole, and Θ increases in a clockwise direction when viewed from the north Galactic pole.

[25]There is a slight difference in comparison with [212], he used two-scale model — with the $z_0 = 1$ kpc for $|z| < 0.5$ kpc and $z_0 = 4$ kpc for $|z| > 0.5$ kpc.

configuration, axisymmetric configuration without reversals and with even parity ([212]). However, this configuration has one advantage. It could be much more easily modelled using the very popular dynamo model of magnetic field generation ([92]). The bisymmetric mode can also be obtained from the dynamo model, but in such case the use of strong non-axisymmetric perturbations is necessary. The other two possibilities of magnetic field configurations — bisymmetric dipole type (BSS-S) and axisymmetric quadrupole type (ASS-A) are also not completely observationally excluded yet ([41]).

Poloidal and toroidal regular field components

The dynamo model has one very interesting consequence for the propagation of CRs — namely that except for a relatively flat field in the galactic disc it contains also quite strong toroidal fields above and under the galactic plane. Motions of these fields and their superpositions generate the net field in the Galaxy. The existence of such a field is indirectly supported by the existence of a radio thick disc mentioned above in the review of observation results. Such a field could change the CR trajectories quite essentially, furthermore this type of model was not yet used for UHECR propagation simulation, therefore we decided to add these components in our simulations. We take advantage of the fact that only recently some first quantitative estimates of strengths of such fields were proposed by [119].

For toroidal fields we choose the model with simple geometry (circular discs above and under the Galactic plane with a Lorentzian profile in z-axis). For Cartesian components of the toroidal field it holds[26]:

$$B_x = -B_T \sin(\phi) \tag{2.41}$$

$$B_y = B_T \cos(\phi) \tag{2.42}$$

For the value of B_T we have:

$$B_T = B_{max} \frac{1}{1 + (\frac{z-H}{P})^2} \quad \text{for } x^2 + y^2 < R^2 \text{ and} \tag{2.43}$$

$$B_T = B_{max} \frac{1}{1 + (\frac{z-H}{P})^2} \exp\left(-\frac{(x^2+y^2)^{1/2}}{R}\right) \quad \text{for } x^2 + y^2 > R^2 \tag{2.44}$$

where x and y are positions in the Galactic plane. It has the radius of a circle with toroidal field $R = 15$ kpc, height above Galactic plane $H = 1.5$ kpc, half-width of Lorentzian distribution $P = 0.3$ kpc, and maximal value of toroidal magnetic field $B_{max} = 1\mu$G.

As a consequence of the existence of the poloidal field (dipole field) we probably observe a vertical component of 0.2μG in the Earth vicinity and intensive filaments near Galactic

[26]The equations above are valid only in the northern Galactic hemisphere, in the southern hemisphere the field has the opposite direction, so B_x and B_y will change their sign there.

center. Appropriate equations, which we used for the description of poloidal fields, are the same as the equations for a magnetic dipole. The field is symmetrical around the Galactic axis. For the total poloidal field strength it is then valid (in xz-plane) in polar coordinates (θ ranges from 0 to π and it goes from north to south pole):

$$B = \frac{K}{R^3}\sqrt{3\cos^2(\theta) + 1.} \tag{2.45}$$

rom this, it follows that in spherical coordinates we then have these Cartesian field components:

$$B_x = -\frac{3K}{2R^3}\sin 2\theta \cos\phi \tag{2.46}$$

$$B_y = -\frac{3K}{2R^3}\sin 2\theta \sin\phi \tag{2.47}$$

$$B_z = -\frac{K}{R^3}(3\cos^2\theta - 1) \tag{2.48}$$

A cylinder (height 300 pc, diameter 100 pc) with a constant strength of the magnetic field equal to 2 mG was put into the Galactic center instead of the field resulting from the equations above[27]. The main motivation for such an arrangement was to avoid a problem with a too strong field near this center ($R \sim 0$) and so to keep the total field strength in observed bounds and to describe the character of observed filaments.

The constant K was selected as follows: $K = 10^5$ G.pc^3 for outer regions ($R > 5$ kpc) and $K = 200$ G.pc^3 for the central region ($R < 2$ kpc). For the intermediate region (2 kpc $< R <$ 5 kpc) we used a constant absolute field strength 10^{-6} G. These values correspond to observed features of the Galactic magnetic field: a milligauss field is restricted only to the central cylinder and the vertical magnetic field is equal to 0.2 μG at the Sun's distance (see also Fig. 2.26).

[27] Orientation of this field is in accordance with the general description, only the strength is constant.

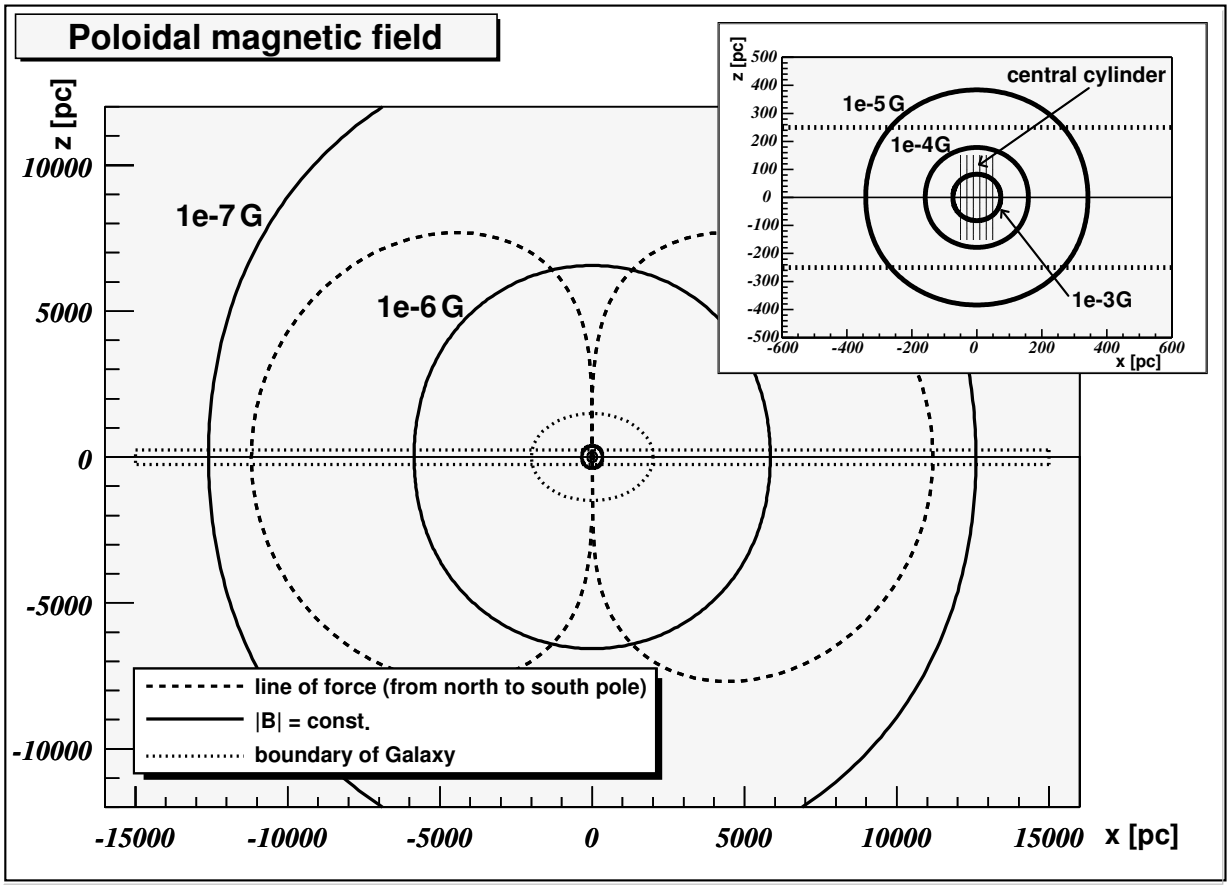

Figure 2.26: *The resulting model of poloidal magnetic field. The central region is enlarged in the upper right corner.*

Turbulent fields and Galactic arms

We introduce also the influence of random fields in our simulations. Cells with a characteristic size of 50 pc with random field orientation and with maximum field strength $|B| = 10\mu$G were added to regular, poloidal and toroidal field components.

In the two following examples we used two different approaches for the introduction of turbulent fields. For the study of the chemical composition of CR (Example No. 2) various configurations (cell frequency, cell size) were used and are described in detail below. However, for directional analysis (Example No. 1) we respect the fact that turbulent fields are common especially within spiral arms of Galaxy. Therefore we expect that 80% of the volume inside spiral arm regions contains turbulent field components, while outside these arm regions (but within the surroundings of the Galactic plane[28]) 20% of the total simulated volume has a nonzero turbulent field. Finally, in other outer regions of the Galaxy we suppose that only 1% of the volume has a nonzero turbulent component.

[28]More precisely: For the distance $r < 20$ kpc and $|z| < 1.5$ kpc, where r and z are components of cylindrical Galactic coordinates.

As a model of spiral arms we used the model by [233], which is a simple four-plus-local arm model. Parameters of this particular model are described in detail in Fig. 2.27.

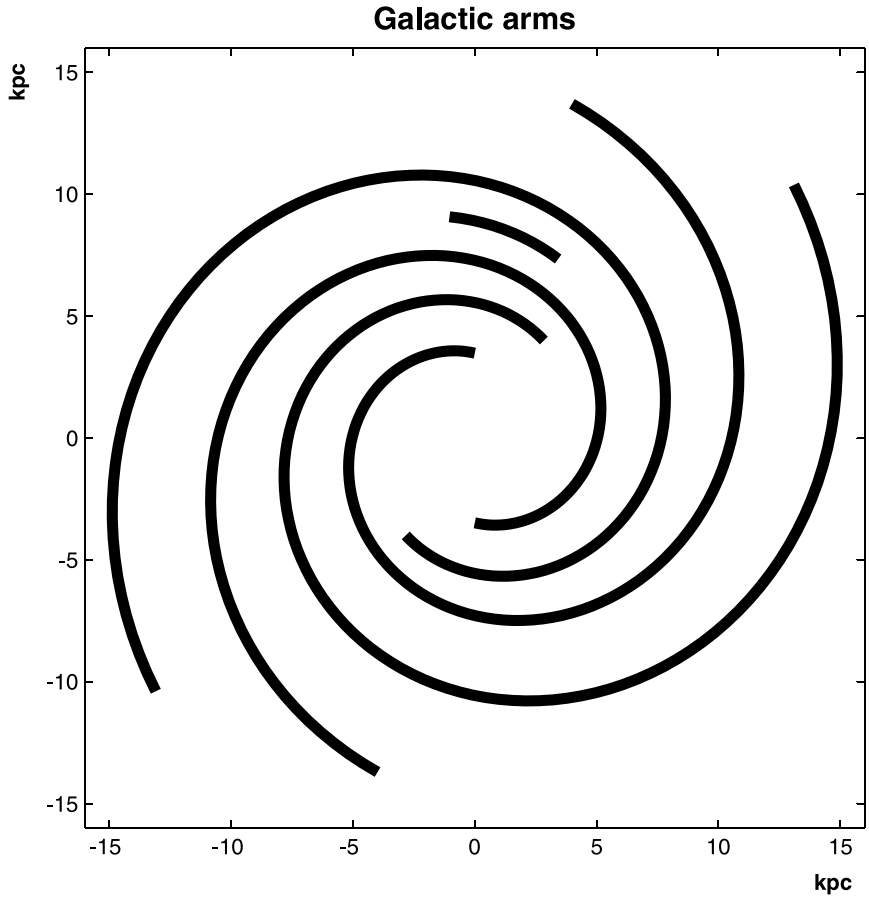

Figure 2.27: *Model of Galactic arms by [233] has a 4-arm pattern and it also includes a so called Local arm. Equation for individual arms is:* $\Theta(R) = \alpha \log(R/R_{min}) + \Theta_{min}$*, where* Θ *grows counterclockwise and* $\Theta = 0$ *at positive part of x-axis,* α *is the winding constant,* R_{min} *is inner radius and* Θ_{min} *angle at inner radius (Sun is positioned on y-axis.). Width of each arm is 750 pc, height 500 pc (centered on the Galactic plane). Arms are truncated at a distance 15 kpc from the Galactic center. Parameters for individual arms follow: (Arm No.,* α *[rad],* R_{min} *[kpc],* Θ_{min}*, angular extent* $(\Theta_{max} - \Theta_{min})$ *[rad]): (1, 4.25, 3.48, 1.571, 6.0); (1', 4.25, 3.48, 4.712, 6.0); (2, 4.89, 4.90, 4.096, 6.0); (2', 4.89, 4.90, 0.953, 6.0); (Local, 4.57, 8.10, 1.158, 0.55).*

2.10.2 Propagation of UHECRs in GMF

In the next sections we describe two simple analyses of cosmic ray propagation in GMF. These analyses are done in different energy ranges for derivation of different conclusions, but they involve the same principles of particle motion in magnetic fields:

The propagation of the main part of UHECR (or more generally of cosmic rays) candidates (charged particles like protons, nuclei, electrons, ...) is of course influenced by the magnetic fields. This influence is given simply by the well-known Lorentz equation. The term with the electric field in this equation can be neglected, because there is no evidence for large-scale electric fields in the Galaxy. For the acceleration $\vec{a}$ we then get:

$$\vec{a} = \frac{q}{m}(\vec{v} \times \vec{B}), \tag{2.49}$$

where q is the charge of the particle, m is its relativistic mass, v its velocity[29] and B is the magnetic field strength.

Taking $\vec{B}$ as constant in suitably small volumes the trajectory of a particle is followed and the resulting deflection is examined.

2.10.3 Directional analysis of UHECR

"Antiparticle tracing" method and recent works

Some computer simulations in the UHECR range were treated for this purpose recently and the effects, especially on the changes in spatial distribution, were studied.

The method of "antiparticle tracing" is used in all these models. The particle carrying the opposite charge starts its propagation at the position of the Earth in the Galaxy. Its initial velocity vector has spherical coordinates $\sim c, b, l$, where c is the velocity of light and b and l are the galactic coordinates of the detected particle. Because of the opposite charge such a particle traces backwards the trajectory of original detected particle. When the particle leaves the sphere of influence of the Galactic magnetic field, we are able to evaluate its new galactic coordinates and thus its initial direction before the entrance into the GMF.

The first work published was [212]. Authors of this paper analyzed the motion of UHECRs in conservative models of BSS-A and ASS-S GMF with similar parameters as given above. They examined the shifts for protons with energies ranging from $(2 \div 10) \times 10^{19}$ eV. The second article is by [171]. Particles with energy equal to 4×10^{19} eV are analyzed in this paper. The changes in regular distributions are followed for the ASS-S model of GMF and for the particles supposed to be either protons or Fe nuclei. The basic results of both models (magnitudes of deflections) are in good agreement with our model.

Two other papers appeared recently. In these papers the GMF model of [212] was employed to support specific arguments. Firstly, [184] assumed iron nuclei as the only component of UHECRs and the authors try to identify the sources as very young pulsars. Secondly, [227] investigated correlation between the positions of UHECRs propagated from outside the Galaxy and of positions of specific types of blazars. They focused on possible identification of these blazars as UHECR sources and significant attention was paid also to analysis of clustered UHECR events.

[29] Almost equal to the velocity of light c; UHECRs reach the highest known relativistic γ-factors, about 10^{11}.

Two other works propose a large Galactic magnetic halo with very intensive fields. The first article was published by [7], they speculate about large and intensive purely azimuthal magnetic fields in the Galactic halo. This field should exist as an analogy to a solar wind and should extend to about 1.5 Mpc. In spherical coordinates r, θ, ϕ it holds then

$$B_\phi = B_S R \frac{\sin\theta}{r}, \tag{2.50}$$

where $B_S R$ is the normalization factor derived from the values in the solar surroundings, which is equal to 70 μG.kpc. If such a field is introduced, the positions of 11 out of 13 EHECRs from Haverah Park, Volcano Ranch, Fly's Eye and AGASA should fall within a 20° spherical cap around M87. This hypothesis was challenged shortly after its publication by [53]. They proved that this is simply based on the fundamental property of the magnetic field model used in halo. The model of an azimuthal field used is simply focusing all positions into the direction of the Galactic north pole and M87 lies near to this pole, and so the small angular distance between computed EHECR positions and between M87 is probably just an interesting coincidence without fundamental physical importance. Furthermore, such a strong magnetic halo is in contradiction with recent observations.

The second work was published by [123] and it proposes a Galactic magnetic wind extending to 1.5 Mpc. The model examines focusing abilities of the magnetic wind. The model of the magnetic wind used in this work is purely azimuthal:

$$B = B_7 \frac{r_0}{r} \sin\theta \tanh\left(\frac{r}{r_s}\right), \tag{2.51}$$

It describes B as a function of the radial spherical coordinate r and the angle to the north galactic pole θ. The term r_0 in this equation is the distance from the Earth to the Galactic center (equal to 8.5 kpc), the factor r/r_s was introduced to smooth out the field at small radii (r_s was taken as 5 kpc). B_7 is the normalization factor (the strength of the field in [7 μG] units) and so in conservative models of GMF B_7 should be $\sim 0.3 \div 0.4$. As it is shown in our combined Fig. 2.28, such a magnetic field has to sweep out some fraction of the southern Galactic hemisphere. However, using the data from SUGAR[30] which are also plotted in this figure, we are able to show that such a model could not be completely correct. This is due to the fact that these regions with proposed zero particle flux — contrary to the theoretical expectations — contain several SUGAR events.

[30]We note that the SUGAR direction measurements are generally significantly more trustworthy than their energy estimates.

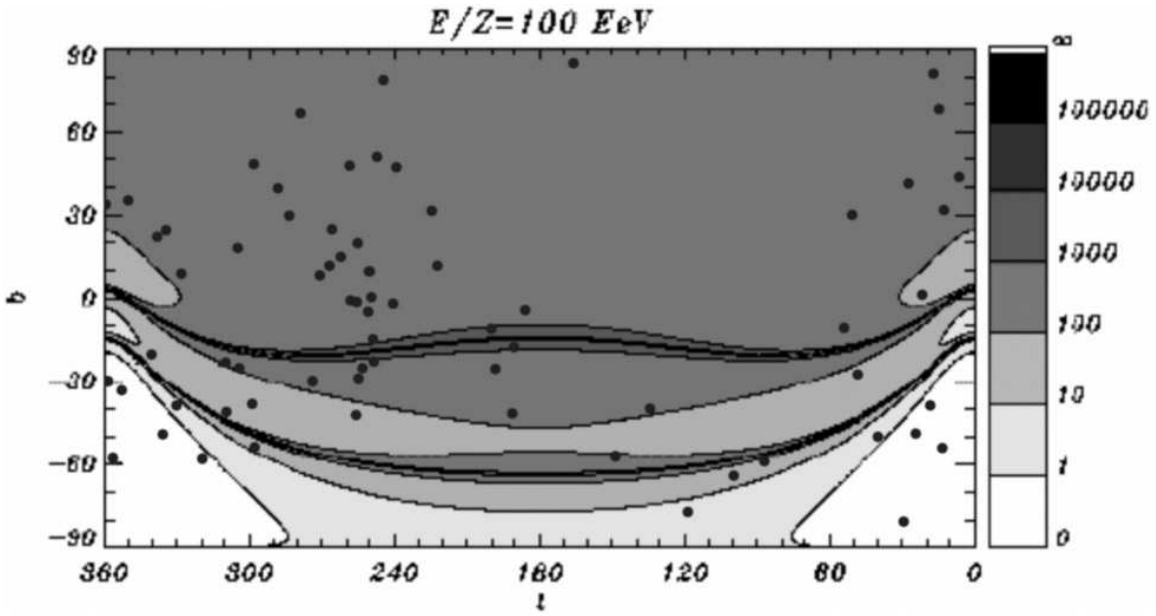

Figure 2.28: *Contour plots of the amplification of cosmic-ray flux by the Galactic wind (according to [123]). The plotted dependance of the flux on arrival directions to the Earth was computed for initial isotropic distribution of point sources (outside of the Galaxy) and for* $\bar{E} = 10^{20}$ *eV. Figure was superposed with coordinates of SUGAR events* (black dots) *of the arrivals of most energetic particles (*$\geq 4 \times 10^{19}$ *eV according to Hillas E model of energy estimation of SUGAR events). There are some SUGAR events inside of the white triangle-shaped areas (bottom corners), where the zero cosmic-ray flux is expected.*

Finally, two interesting works treating the turbulent fields appeared recently. [11] carefully analyzed the influence of turbulent fields on possible clustering of UHECRs and [124] made a large study of properties of typical turbulent fields with respect to amplification and multiplication of source images.

Computer Model

In our simulation we have supposed the conservative Galactic magnetic field model by [117], which was amended with toroidal and poloidal field components and with turbulent fields linked to spiral arms; this complete configuration of the magnetic field was discussed in detail above.

Despite having used various types of initial data, we present here only the results for real data. Namely, even such a constrained set of data can sufficiently demonstrate all important changes of features of particle flux. These real data[31] were taken from our catalogue of UHECRs[32]. We propagate these particles through the Galactic magnetic field assuming

[31]The arrival direction (b, l) and energy E was used for each detected particle.

[32]This catalogue was created using available data from several various experiments: Data from all UHECR experiments with energies above 10^{20} eV, data from the AGASA experiment and data from the

various charges — starting as protons (proton number $Z = 1$), continuing as oxygen nuclei ($Z = 8$) and ending with iron nuclei ($Z = 26$). All particles were traced back off the influence of the Galactic field. The final distance of each particle was assumed to be 40 kpc from the Earth. We present here (Figure 2.29) the results of simulations corresponding the real UHECR data (145 UHECR positions and energies) taken successively as protons, oxygen and iron nuclei.

SUGAR experiment for particles with energies above 4×10^{19} eV were used. The catalogue is available on-line (http://www-hep2.fzu.cz/Auger/catalogue.html).

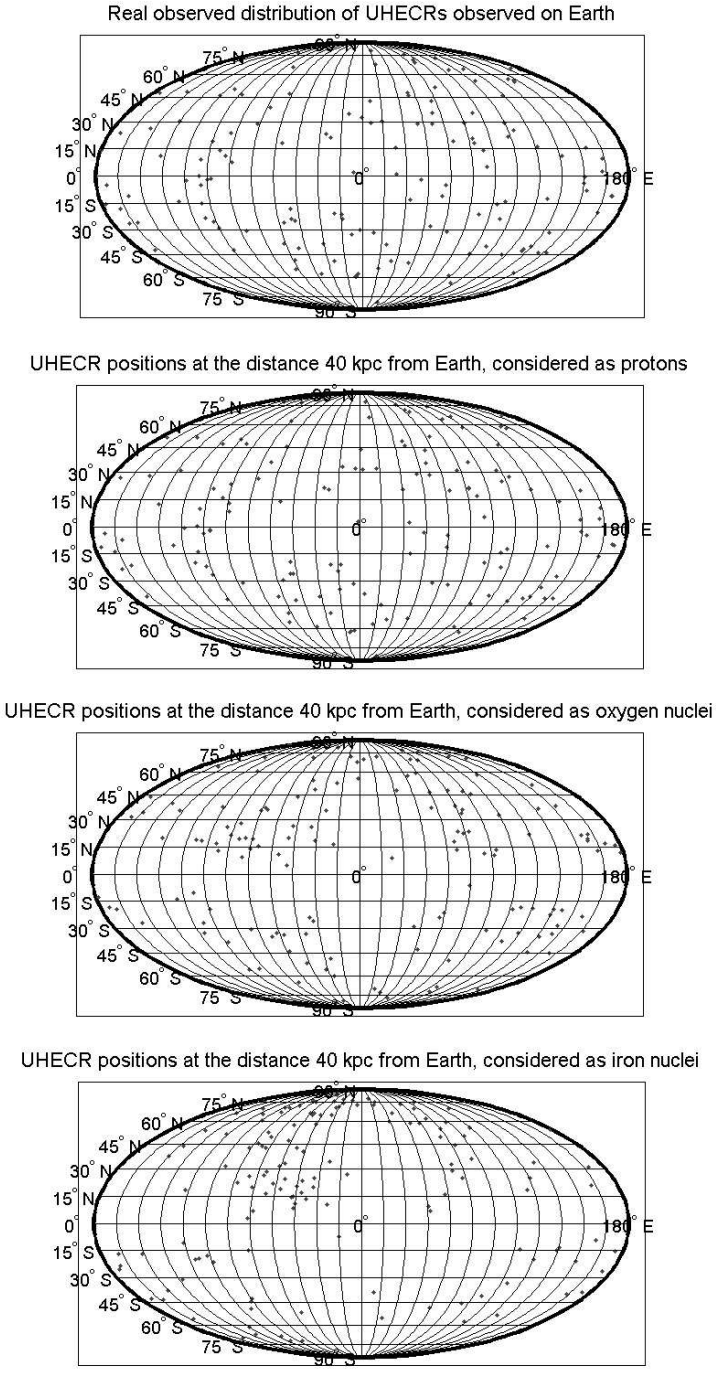

Figure 2.29: *The original arrival directions (in galactic coordinates) of 145 UHECRs are shown in the uppermost part of the Figure. The other three sky-maps (all in galactic coordinates) show the final positions of cosmic ray particles which were propagated to the distance 40 kpc from the Earth. The second map from the top shows final positions of protons (the average angle between the initial and final position of individual particle is* $2.9^\circ \pm 1.6^\circ$ *[s.e.]). The third map shows final positions of oxygen nuclei (average angle* $23^\circ \pm 12^\circ$ *[s.e.]) and the fourth map shows positions of iron nuclei (average angle* $72^\circ \pm 38^\circ$ *[s.e.]).*

2.10.4 Results of simulations

Results of particle tracking

We can state that the given deflection ranges (Fig. 2.29) are in good agreement with previous models ([212], [171] or [184]) of propagation of UHECRs through the Galactic magnetic field. Hence we can formulate the following conclusions:

- As we already stressed above, the detail of global structure of the GMF is still uncertain, but despite that its influence is non-negligible for protons and essential for Fe nuclei.

- The simulations of particles with higher charges (e.g. oxygen or iron nuclei) are transforming the isotropic distribution to structures which show some regularities. The actual forms of these regular structures are as well as the global model of the GMF rather uncertain, but their existence is clear and it is independent of the specific parameters of given magnetic field model[33]. In accordance with [124] we observe especially for oxygen and iron nuclei (Fig. 2.29) that at some places the initial flux is amplified, in other areas it is strongly suppressed (see e.g. overdensity in region to the north-west of the Galactic center ($270^\circ < l < 360^\circ$ and $b > 0$) for both oxygen and iron nuclei or the almost empty region along the Galactic plane again for both type of nuclei).

- The GMF is very important also for protons, because it is able to affect the small-angle clustering (as one can see on the second upper part of Fig. 2.29, where some initial small clusters were transformed into other ones). Small-angle clustering is today lively discussed and it is one of the key features in discrimination between some models of sources ([11]).

- That the UHECRs originate in the Galaxy (e.g. near the young neutron stars in the form of iron nuclei) is not probable, but not completely excluded (see the bottom part of Fig. 2.29). Furthermore, such UHECRs should originate only in several point sources in our Galaxy, again in accordance with the existence of pseudo-regular structures after propagation through the GMF (see also [184] or [124]).

The theory of Galactic origin of UHECRs could be also combined with the above discussed fact that also relatively strong (~ 1 mG) fields exist in the form of filaments near the Galactic center. In such fields the Larmor radius of a 10^{19} eV UHECR proton is only about 4 pc.

[33] Of course, our simulation does not completely exclude the possibility that also the initial directions of particles before they enter into the Galaxy are isotropic. Our conclusions were derived only in one direction — the observed isotropic distribution doesn't necessarily require the initial isotropic distribution for oxygen and iron nuclei. For a test of the opposite direction of we have to make another type of simulation — we have to inject huge numbers of particles isotropically distributed on a spherical surface around the Galaxy and then detect them on some tiny sphere (or other shape) around the Earth's position. This problem was partially treated by [184].

Results of statistical analysis

In our work we first analyzed the available real data from UHECR experiments. We used the data for particles with energy $> 4 \times 10^{19}$ eV from Volcano Ranch, Haverah Park, Yakutsk and AGASA (all these four experiments were situated on the northern hemisphere) and for SUGAR experiment, the only pre-Auger experiment situated on the southern hemisphere.

We performed the tests of particle behavior in GMF in dependence on their charge, starting with protons (charge $Z = 1$), up to iron nuclei, which is carrying $26\times$ elementary charge ($Z = 26$). Our choice had two following main reasons: (1) There still exists quite huge uncertainty in determination of chemical composition of UHECRs [228]. (2) Particles, carrying a larger charge behave in GMF like the particles with smaller charge and with proportionally smaller energy. For example, the iron nuclei with energy 10^{20} eV follow in the Galaxy the same trajectories as protons with energy 4×10^{18} eV.

Our tests were performed for individual experiments and for all experiments combined together. Our main results for all experiments combined together are summarized in Figure 2.30.

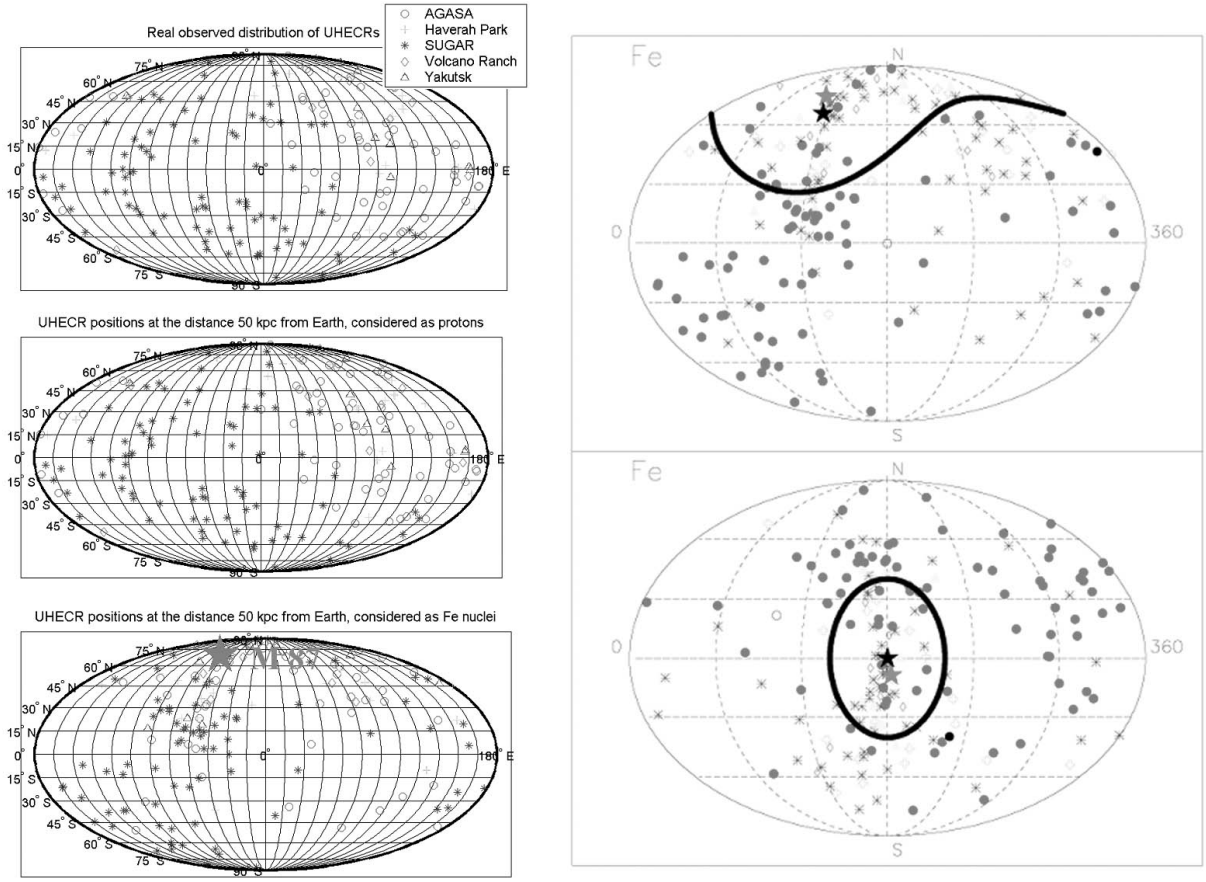

Figure 2.30: *Results of statistical analysis.* Left: *Top figure is the distribution of events as observed on the Earth; middle one is a result of antiparticle propagation to the distance 50 kpc from the Earth, when particles are considered as protons (we can observe that directional changes are only small, in order of degrees, only the small-angle clustering could be different); bottom one is for the case of iron nuclei – the position of radiogalaxy M 87 is indicated. It is clear that directional changes are very significant and that such final distribution is not isotropic (see right part of figure), we can easily find empty regions or (on the other hand) strong overdensities.* Right: *Statistical analysis – search for potential single source (propagation to 50 kpc, particles are iron nuclei); we compute mean value on the sphere and its variance and we get result for the position of the mean value: [283°; 67°] with variance: 41.6°. The position of radiogalaxy M 87 is [284°; 75°], what is at least very interesting similarity. The grey star indicates the position of M 87 and black star is the position of mean value. Top figure is drawn in galactic coordinates, bottom one is with the mean value rotated to the image center.*

Chapter 3

Concept of the Pierre Auger Observatory

The Pierre Auger Observatory (PAO) [33] should consist of two sites — the first one will be situated on the southern hemisphere, the second one on the northern hemisphere. The main aim of PAO is to enlarge existing UHECR and EHECR data sets by at least one order of magnitude.

This project is realized by a large collaboration of 369 scientists and 63 institutions from 16 countries[1], when the Czech Republic also participates. The activities of the Czech Republic, represented by scientists and technicians from Institute of Physics of the Academy of Sciences of the Czech Republic, from the Charles University in Prague and from the Palacký University in Olomouc is concentrated in following areas: The primary contribution is the development and the construction of the fluorescence detectors, where Czech working group has the responsibility to produce mirror segments for 12 (of 24 total) fluorescence detector mirrors. As it is described within chapter 5, we have taken part also in the atmospheric monitoring program. Moreover, we are involved in rather independent experiment AIRFLY [16], which will serve not only to the Auger project by providing very precise measurement of fluorescence atmospheric yield and its dependence on various possible conditions (pressure, temperature, chemical composition).

Each Auger site has to be a hybrid detector, where the advantages of ground arrays and fluorescence detectors will be combined (see section 3.1). The both sites together will cover whole sky and will enable us to provide a solid statistical analysis of the spatial distribution of UHECRs and EHECRs. The northern site is expected to be in Colorado, USA and its realization will start after the successfull completion of the southern site. Southern site is already being built in Argentina, in Mendoza province, near the city of Malargüe [34].

[1] This status as in the official author list for the year 2005.

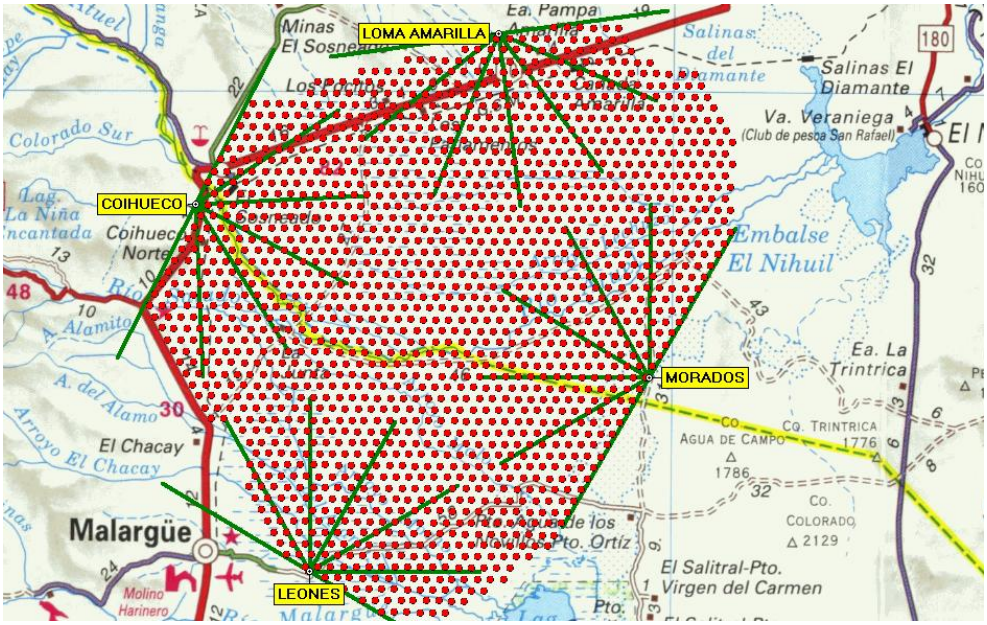

Figure 3.1: *The final scheme of the southern PAO. Small red dots indicate all 1600 positions of Čerenkov detectors; yellow flags with names show positions of four fluorescence detector sites. The green rays then show the field of view of six individual telescopes at each fluorescence site. From [33].*

Each site should consist of 1600 ground particle detectors and four fluorescence detectors. Ground detectors will be spread over the enormous area of 3 000 km^2 arranged in the triangular grid with separation distance $d = 1.5$ km. The exact scheme of final southern PAO ground detector distribution is available on the Fig. 3.1. Water Čerenkov detectors will be used as these ground detectors.

During clear moonless[2] nights this ground array information will be enriched by the measurements by the fluorescence detectors. It is expected that at least about 10 % events will be recorded simultaneously by the groun and atmopsheric detectors.

The current situation is depicted at the Fig. 3.2. Three of four fluorescence sites are fully operational and more than half of the surface detectors is also regularly taking data. Southern site of PAO has to be completed before the end of 2006.

[2]See detailed discussion in 4.3.

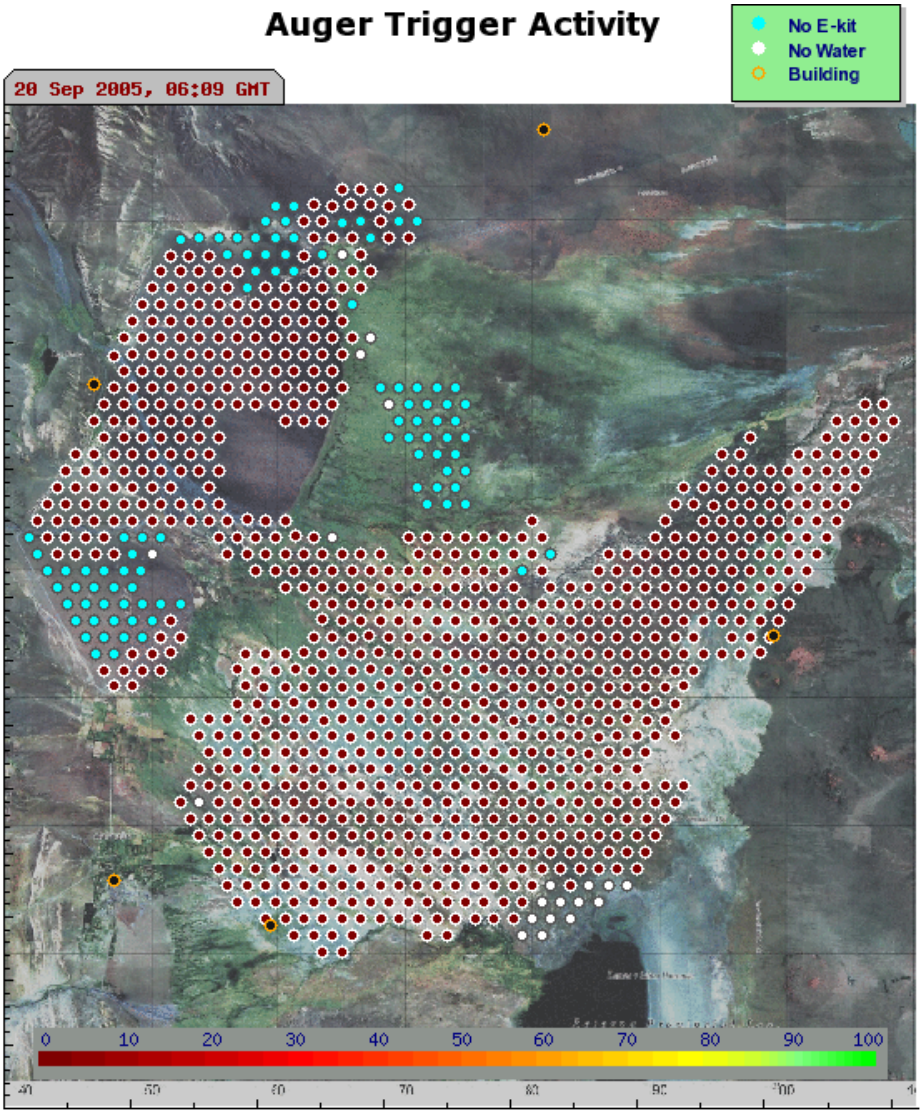

Figure 3.2: *Current status (September 20th 2005) of the Pierre Auger Observatory. The surface array has already 863 of planned 1600 Cherenkov detectors operational and three of four planned fluorescence telescope sites take data. This figure was taken from Auger on-line performance monitoring program, called Big Brother.*

As it is given in [26], *a hybrid event* is an air shower that is *simultaneously detected by the fluorescence detector and the ground array.* The Observatory was originally designed and is currently being built to operate in such hybrid mode of observation. Data are recovered from both parts of this complex detector whenever either system is triggered. If an air shower independently triggers both types of detectors the event is tagged accordingly in a database. There are cases where the fluorescence detector, having a lower energy

threshold, promotes a sub-threshold array trigger. Surface stations are mutually matched by timing and location. Using a information from the fluorescence detector reconstruction the position of the shower core is determined and signals from the appropriate surface detectors are read-out. This is an important capability because these sub-threshold hybrid events would not have triggered the array otherwise.

However, it is not simply a dual experiment. Apart from important cross-checks and measurement redundancy, the two techniques see air showers in complementary ways. The ground array measures the lateral structure of the shower at ground level, with some ability to separate the electromagnetic and muon components. On the other hand, the fluorescence detector records the longitudinal profile of the shower during its development through the atmosphere.

3.1 Advantages of hybrid detector

The Observatory started operation in hybrid production mode in January, 2004. Surface stations have an almost 100% duty cycle, while fluorescence eyes can only operate on clear (more or less moonless) nights. Both surface and fluorescence detectors have been running simultaneously for 14% of the time. The number of hybrid events represents 10% the statistics of the surface array data. These numbers are in good agreement with the design specifications of the observatory.

A hybrid detector has many advantages for studying the highest energy cosmic ray air showers. Much of these advantages stem from the characteristic accurate geometric reconstructions. Timing information from even one surface station can significantly improve the geometrical reconstruction of a shower over that achieved using only fluorescence detector information. The axis of the air shower is determined by minimizing a function involving data from both detector components — all triggered elements in the fluorescence site (in the *eye*) and as well as from the ground are used.

It was shown [27, 28] that the reconstruction accuracy of a hybrid event is better than what the ground array or the single eye could achieve independently. Using the timing information from the individual camera pixels of fluorescence telescope together with the surface stations, a core location resolution of 50 m is achieved. The final current resolution for the arrival direction of cosmic rays is 0.6°, in comparison with more than 1.4° resolution[3] for surface-detector-only events [28].

Due to this improved angular accuracy, the hybrid data sample is ideal for anisotropy studies and, in particular, for point source searches. Many ground parameters, like the shower front curvature and thickness, have always been difficult to measure experimentally, and were usually determined from Monte Carlo simulations. The hybrid sample provides a unique opportunity in this respect. The geometrical reconstruction can be done using only one ground station, thus all the remaining detectors can be used to measure the shower characteristics.

[3]The angular resolution for surface-detector-only hits is energy dependent. It decreases from 2.2° for energies $E < 4$ EeV through 1.8° for energies $3 < E < 10$ EeV to 1.4° for energy > 8 EeV.

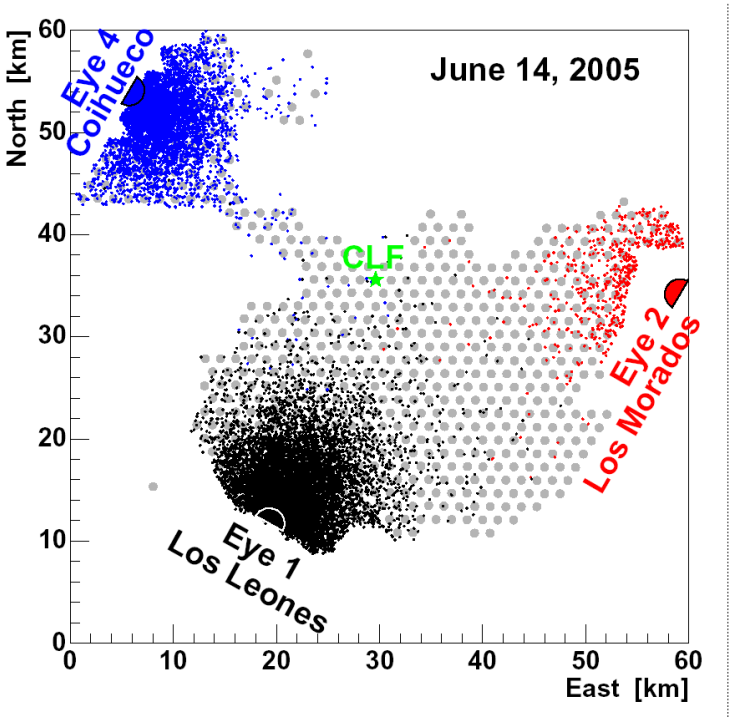

Figure 3.3: *Status of the hybrid detections at the Pierre Auger Observatory on June 14, 2005. Each gray full circle represents a surface station, each color dot is the core location of a reconstructed air shower (where the color indicates which eye saw that event), and each fluorescence site is shown as a colored semi-circle. The Central Laser Facility is shown as a green full star. From [26].*

The combination of the air fluorescence measurements and particle detections on the ground provides an energy measurement almost independent of air shower simulations. The fluorescence measurements determine the longitudinal development of the shower, whose integral is proportional to the total energy of the electromagnetic particle cascade. At the same time, the particle density at any given distance from the core can be evaluated with the ground array. The conversion from particle density to the energy of the shower is where the fluorescence measurements become important. Hybrid events that can be independently reconstructed with both techniques are used to establish an empirical rule for the energy conversion. The procedure to determine the energy of each event is explained in detail below in section 3.3, which again illustrates the advantages of hybrid mode measurements. The hybrid analysis benefits from the calorimetry of the fluorescence technique and the uniformity of the surface detector aperture.

The hybrid detector is sensitive to the showers with energies above 10^{17} eV. As it follows from careful simulations [44], for the final southern PAO configuration its aperture grows with the energy up to 7000 km^2 sr. For monocular mode the aperture grows quicker and flattens at its maximum already for the energy 10^{19} eV, than for the sterero or 3-FD or

even 4-FD events. The present average rate is 50 hybrid events per night per fluorescence detector site (per eye), for a total of 16090 events up to June 14, 2005. At this rate, 4000 hybrid events per month are expected when the PAO will be completed.

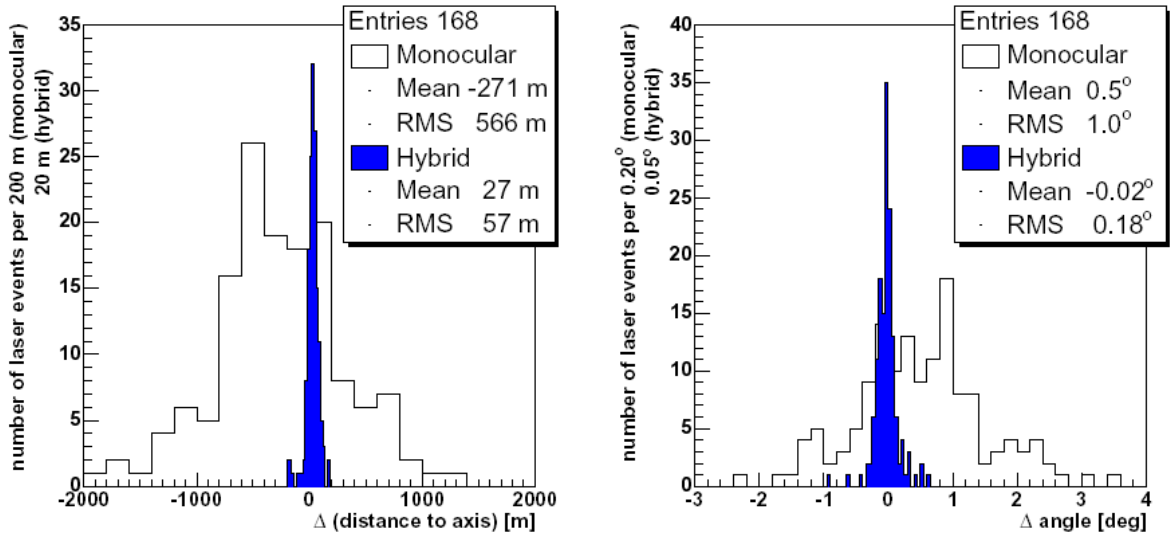

Figure 3.4: Left: *Difference between the reconstructed and true distance from the eye to the vertical laser beam from Central Laser Facility (CLF) using the monocular and hybrid techniques. The location of the laser is known to* ± 5 *m precision.* Right: *Angular difference between reconstructed and true direction of the laser beam from CLF using the monocular and hybrid techniques. The laser beam is vertical within* 0.01°.

3.2 Surface Detector

An Auger Surface Detector (SD) station [22] is a 10m^2 base, 1.5m tall cylindrical roto-molded plastic tank. It encloses a Tyvek liner filled with purified water up to a 1.2m level. Three 9-inch Photonis XP1805 photomultiplier tubes are used to collect the Čerenkov light emitted by particles crossing the tank. Signal is extracted both from the anode and the last dynode, the latter being amplified to achieve a larger final dynamic range extending from a few to about 105 photoelectrons. All channels are connected to a 5 pole anti-aliasing filter with a cutoff at 20 MHz, digitized at 40 MHz by 10 bit FADC, a digital trigger is operated by a local CPU. Timing is obtained by a GPS Motorola unit, and communication to the Central Data Acquisition System (CDAS) is done via a custom built wireless communication system. Two solar panels charging two 12 V batteries provide the 10 W used by the electronics. Each detector is therefore independent and can start operating upon installation, independently of other detectors in the array.

Since January 2004, the surface detector array has been in stable operation and has grown at a steady rate of about 9 tanks per week. Figure 3.2 shows the status in September 2005. Each tank is deployed and its position is verified with differential GPS technique. Even if the landscape sometimes forces some displacements from the perfect triangular geometry, 50 % of the tanks are at less than 5 m from the theoretical position, and 90 % at less than 20 m. The exact position is used to operate the GPS in 'position hold' mode, achieving better than 20 ns time resolution.

3.2.1 SD calibration — weather and environment influence

The environment to which an Auger Surface Detector is exposed is somewhat hostile for the electronics. At 1400 m a.s.l. and with clear skies, day-night temperature variations are of the order of 20 °C. The terrain properties vary significantly on the 3000 km^2 of the array, and some detectors have to face high salinity corrosive air, while others face dusty air from sandy ground. Humidity is present both in the ground (rivers, groundwater) and in the tank due to condensation.

To monitor the whole array accurately various sensors are installed in each tank. This information is sent to the CDAS every 6 minutes. Temperature is measured on each PMT base, on the electronics board, and on each battery. PMT voltage and current are also monitored, as well as solar panel voltages, individual battery voltage, and charge current. These data are used to detect a wide range of failures, from broken solar panels to discharging batteries, and correlations like unstable PMT behavior related to temperature. Weather stations[4] reporting temperature, pressure, humidity, wind speed and direction are installed at each fluorescence site and in the center of the array, to complete the environmental monitoring. These data allow extra checks such as the influence of the pressure on the calibration.

The calibration is operated online every minute, and — as was mentioned above — sent to CDAS every 6 minutes for monitoring. A number of quantities are available to check the behavior of the tank: baseline values, single muon peak signal, single muon average charge, dynode/anode ratio, and PMT stability. In addition, high statistics histograms of the charge distribution from muons (150 000 counts) and average pulse shapes are sent every time a station records an event.

3.2.2 Central data acquisition

The last step monitored to ensure the quality of the Auger SD data set is done at the system acquisition level. The second level trigger[5] rate for each station are registered every second allowing a precise knowledge of the dead time of the detectors. The acquisition is fully automated and no operator is needed for data taking. A watchdog restarts the system in case of failure and an UPS guarantees operation in case of power cut. Information from

[4]See also chapter 5.

[5]See below for the explanation of trigger hierarchy.

the CDAS processes are kept to diagnose possible crashes. Simple quantities such as the number of stations in operation and the event rate, and more complex ones such as the rate of physics events are checked daily to validate the data acquisition period.

Over 2004, the total on-time of the system has been 94%, including all kinds of dead time (individual detectors down, general power cuts, software upgrades, etc.). It should be noted that this on-time was obtained while priority was being given to the building of the Observatory (deploying new detectors) over its operation (repairing failures), and with evolving software for the detectors, the communication system, and the CDAS. It seems very probable that once the Observatory is completed and the software stabilized, an on-time will be above 95 %.

3.2.3 Trigger system

The trigger system has been designed to allow the SD of Auger to operate at a wide range of primary energies, for both vertical and very inclined showers with full efficiency for cosmic rays above 10^{19} eV. Its hierarchy is described here as in [8].

In general, trigger system should select events of interest and reject background or fake events, while keeping the rate constraints imposed by the communication and data acquisition system. The trigger for the Surface Detector is hierarchical with local triggers at levels 1 and 2 (called T1 and T2), whereas level 3 (T3) is formed at the observatory campus based upon the spatial and temporal correlation of the level 2 triggers. All data satisfying the T3 trigger are stored. Additional level of triggers are implemented offline in order to select physical events (T4 physics trigger) and accurate events (T5 quality trigger), with the core inside the array.

Two different trigger modes are currently implemented at the T1 level. The first uses a Time over Threshold (ToT) trigger, requiring that 13 bins in a 120 bins window are above a threshold of 0.2 I^{est}_{VEM} in coincidence on two PMTs. The estimated current for a Vertical Equivalent Muon[6] (I^{est}_{VEM}) is the reference unit for the calibration of FADC traces signals. This trigger has a relatively low rate of about 1.6 Hz, which is the expected rate for double muons for an Auger tank. It is extremely efficient for selecting small but spread signals, typical for high energy distant EAS or for low energy showers, while ignoring single muons background. The second trigger is a 3-fold coincidence of a simple 1.75 I^{est}_{VEM} threshold. This trigger is more noisy, with a rate of about 100 Hz, but it is needed to detect fast signals (< 200 ns) corresponding to the muon component generated by horizontal showers.

The T2 trigger is applied in the station controller to select from the T1 signals those likely to have come from EAS and to reduce to about 20 Hz the rate of events to be sent to the central station. All ToT triggers are directly promoted T2 whereas T1 threshold triggers are requested to pass a higher threshold of 3.2 I^{est}_{VEM} in coincidence for 3 PMTs[7].

Only T2 triggers are used for the definition of a T3. Two independent methods are used for detemination of a trigger probability. First method is based on the existence of

[6]Vertical Equivalent Muon (VEM) is defined as the average energy deposited by vertically penetrating muon, going through the center of the SD tank.

[7]Such higher threshold is necessary for the trigger rate reduction.

two pairs of detectors separated by 11 m from each other. The double sampling of signals in near locations provides a way to estimate the number of signals that did not cause a trigger. the second method uses this result and assumes that a such single probability measurement can describe the behavior of all the stations in the surface array. For each event a Lateral Distribution Function (LDF) is fitted to all the stations that have signal. Here the LDF used is a parabola on a log-log scale. The LDF is assumed to be cylindrically symmetric so for each event there are regions of constant signal. In each event the stations that did and did not trigger in a given constant signal region can be identified and the final triggering probability can be computed. Generally, such correct knowledge of the trigger probability is needed for the reliable acceptance estimation.

Furthermore, the stability of the trigger rates is of great importance for a good estimation of the acceptance of the array. The threshold T2 rates are uniform over the present array within a few percent. The ToT T2 rates are more spread, since they are sensitive to the charge of the signal that depends on the characteristics of the water in the tank. The decay time of the pulses is a good estimator of the water quality in the tank. Each tank needs a few months after installation where this decay time slowly decreases then stabilizes to an average value around 65 ns. Once the tanks are stable, the average ToT rate over the array is 1.6 ± 1 Hz.

The main Auger T3 trigger requires the coincidence of 3 tanks which have passed the ToT conditions and meeting the requirement of a minimum of compactness (one of the tanks must have one of its closest neighbors and one of its second closest neighbors triggered). Since the ToT as a local trigger has already very low background (mainly double muons), this so-called 3ToT trigger selects mostly physical events. The rate of this T3 with the present number of working detectors in the array is around 600 events per day, or 1.3 events per triangle of 3 neighboring working stations. This trigger is extremely relevant since 90 % of the selected events are showers and is mostly efficient for vertical showers. The other implemented trigger is more permissive. It requires a four-fold coincidence of any T2 with a moderate compactness requirement (among the 4 fired tanks, one can be as far as 6 km away from others within appropriate time window). Such a trigger is absolutely needed to allow for the detection of horizontal showers that generate fast signals and have wide-spread topological patterns. This trigger selects about 400 events per day, but only 2 % are real showers.

A physical trigger (T4) is needed to select only showers from the set of stored T3 data. An official physical trigger is applied offline to select events for zenith angles below 60 degrees. The chosen criteria use two main characteristics of vertical showers. The first one is the compactness of the triggered tanks, the second one is the fact that most FADC traces are spread enough in time to satisfy a ToT condition. It was shown that requiring a 3ToT compact configuration in an event ensures that more than 99 % are showers. The present physics trigger is dual and requires either a compact 3ToT or a compact configuration of any local trigger called 4C1 (at least one fired station has 3 triggered tanks out of its 6 nearest neighbors). The tanks satisfying the 3 ToT or 4C1 condition must have their trigger time compatible with the speed of light (with a tolerance of 200 ns to keep very horizontal rare events). With the 3ToT T4 trigger, less than 5 % of showers below 60

degrees are lost. The 4C1 trigger , whose event rate is about 2 % of the previous one, ensures to keep the 5 % of the showers below 60 degrees lost by the other T4 and also selects low energy events above 60 degrees.

Between somewhat problematic issues which have to be mentioned, we can include that in most selected events a number of accidental tanks needs to be removed and that the definition of a T4 for horizontal showers is more challenging and is still under study. Also we have to add that the effect of the temperature on the T4 rate is not negligible. The number of T4 events per day divided by the number of active triangles of stations has a dependence on temperature of about 1 % per degree. This has to be taken into account for the estimation of the acceptance of the array when it is not saturated .

Finally, the adopted T5 — quality trigger — requires that the tank with highest signal must have at least 5 working tanks among its 6 closest neighbors at the time of the event and more over, the reconstructed core must be inside an equilateral triangle of working stations. This represents an efficient quality cut by guaranteeing that no crucial information is missed for the shower reconstruction.

3.2.4 SD aperture

For the hybrid detector, we are able to estimate three different detector apertures — the hybrid aperture, the fluorescence detector aperture and surface detector aperture. The SD aperture is currently the most important one, because it was used for the first estimate of PAO energy spectrum (see below 3.3).

Outgoing from current definition of T5 *quality trigger*, the SD aperture is computed on the basis of *an elementary hexagon*. Such hexagon is defined as one central tank, which is surrounded by six nearest neighbors. Second important term, which has to be defined is *LTP — Lateral Trigger Probability function* — showing the dependence that the individual tank will trigger (ToT trigger) on the radial distance from the shower core (or more precisely from the point where shower axis will cross the earth surface). LTP is dependent on the energy of given particle, as well as on the zenith angle θ and on the type of the primary particle (proton, heavier nucleus, photon, ...). Currently, LTP is estimated on the basis of extensive simulations. It is obtained from a set of Monte-Carlo simulations of the primary CR interaction, shower development and tank response, as the fraction of tanks that pass the trigger in different bins of distance, r_{sf} , from a large number of showers with given parameters: *Probability of triggering (E, θ, particle type) = (No. of stations passing the trigger at r_{sf})/(total No. of stations at distance r_{sf}).*

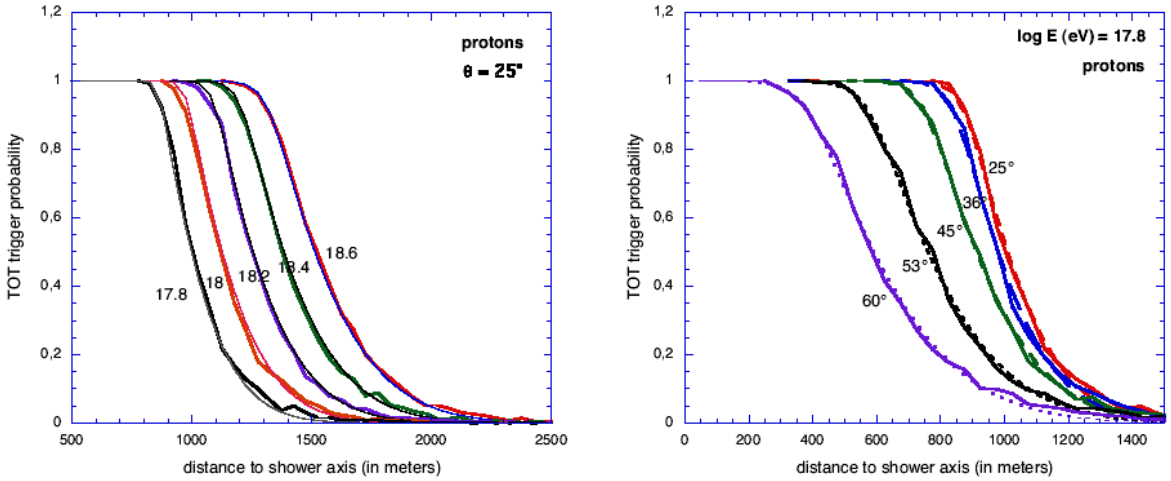

Figure 3.5: *Examples of LTP functions for proton-induced showers at a zenith angle* $\theta = 25°$ *for different energies labeled by* $log_{10}(E)$*, where* E *is in eV (left) and at energy* $E = 10^{17.8}$ *eV for different zenith angles (right). From [9].*

It is worth emphasizing that the LTP functions gather all the information relevant to aperture and exposure calculations, summarizing the properties of the shower development, tank response and trigger definition. To each choice of simulation codes and local trigger definition corresponds a set of LTPs from which the PAO detection efficiency can be computed straightforwardly. When we have larger statistics, the LTPs will be derived directly from the data using hybrid events to measure the SD trigger probability, so that it will be possible to correct for the partial efficiency at low energy in a model-independent way.

The probability to pass the global T4 trigger then follows from a simple probability combination of these local LTP values. This allows us then to calculate the T4 trigger probability for showers of any energy, mass, and angle as a function of the core position.

The *global shower detection efficiency within one elementary hexagon* is then obtained by averaging over all the allowed shower core positions, i.e. satisfying the T5 condition. They are shown as light blue area in Fig. 3.6. On the left, where all 7 tanks are present, the allowed core positions are such that the closest tank (which is bound to record the largest signal) is the central one, since all the others do not satisfy the requirement of having 5 neighbours. On the right, the rightmost tank is missing and shower core positions in the two concerned triangles are excluded.

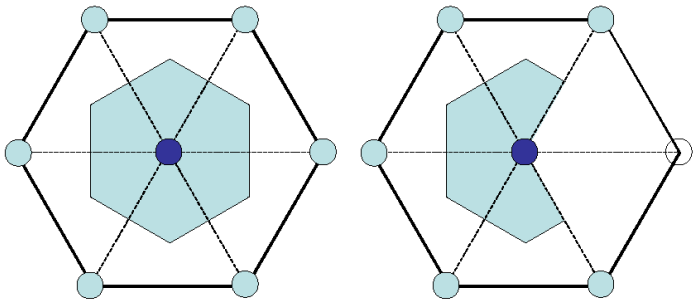

Figure 3.6: *Schematic view of the area (light blue region) where the shower core must be located inside an elementary hexagonal cell in order to pass the T5 trigger (left: full hexagon; right: hexagon with a missing vertex). From [9].*

It is very important for the current spectrum evaluation that this *detection efficiency* saturates (is equal to one) for all showers above $\sim$ 3 EeV with zenith angles θ between $0^\circ - 60^\circ$. The aperture of one internal tank of any elementary hexagon is then geometrically given as:

$$a_{cell} = \int_{\theta \leq 60^\circ} \mathrm{d}S \times \cos\theta \, \sin\theta \, \mathrm{d}\phi \, \mathrm{d}\theta = \mathrm{d}S \times \frac{3}{4}\pi, \tag{3.1}$$

where $\mathrm{d}S$ is the allowed region of an elementary hexagon (see Fig. 3.6), θ zenith angle and ϕ azimuthal angle.

At full efficiency, i.e. above 3 EeV, the detection area per such internal tank (with 6 neighbors) is given as the surface of 6 elementary triangles:

$$\mathrm{d}S = 6 \times \frac{3}{4}\frac{\sqrt{3}}{4} = \frac{9\sqrt{3}}{8} = 1.95 \text{ km}^2. \tag{3.2}$$

Then the corresponding aperture for showers with $\theta < 60^\circ$ is $a_{cell} = 1.95 \times 2.35$ km^{2}sr $=$ 4.59 km^{2}sr.

Finally, to calculate the integrated exposure of the SD over a given period of time, one has to count the number of cell-seconds corresponding to that period. The array configuration changes occasionally when new tanks are deployed or when stations experience failures (e.g. electronics, power supply, communications, ...) and thus get temporarily out of the array (or back in). These changes in the array configuration are monitored through the local trigger rate with a time resolution of one second.

For each new configuration, the number of elementary cells, N_{cell}, is computed and the exposure is incremented by:

$$\text{Exposure} = N_{cell} \times a_{cell} \times t, \tag{3.3}$$

where t is the duration of the configuration. For the period from January 1st, 2004 to June 5th, 2005, we obtained 1.21×10^{10} cell-seconds, which corresponds to 1750 $\mathrm{km}^2\,\mathrm{sr}\,\mathrm{yr}$.[8] Full details about SD aperture calculations may be found in [9].

3.2.5 Current status

The surface array of the Pierre Auger Observatory has been in operation for more than a year and half and has shown very stable behaviour. On-time for 2004 is above 94 %. During this initial phase detectors have been shown to be able to compensate important daily temperature fluctuations. A small number of poorly performing stations have been identified, and most failures appear in the first days of operation. Fraction of stable detectors is increasing and reached 97 % in July 2005 [22].

Up to June 2005, more than 180 000 events were recorded with an average rate of about 0.9 per station per day. Once the array is completed, a rate of about 1500 physics events per day is expected. A significant number of very horizontal events are detected, offering a novel view of EAS. For events above 10^{19} eV, reconstruction accuracy is around 1.4 degree for direction [28] and around 10 % for the SD energy estimator $S(1000)$ (signal at 1000m from the core). The SD array has shown its potential in the period from January 2004 to June 2005, achieving below 60 degrees of zenith angle a total exposure of 1750 $\mathrm{km}^2\,\mathrm{sr}\,\mathrm{yr}$. It will reach its full size, and gain one order of magnitude exposure within the next two years.

3.3 Auger spectrum

Only the first estimate of the spectrum of PAO was published very recently [24]. However, it uses well all above mentioned advantages of first hybrid cosmic ray detector. We will follow the procedures given within this paper [24] in our description below.

Hybrid air shower measurements are utilized in this analysis to avoid dependence on specific numerical simulations of air showers and detector responses to them. The analysis is also fre of assumptions about the primary nuclear masses. The fluorescence detector provides a nearly calorimetric measurement with only minimal model dependency: fluorescence light is produced in proportion to energy dissipation by a shower in the atmosphere. Hybrid data establish the relation of shower energy to the ground parameter $S(1000)$, which is the water Cherenkov signal in the SD at a distance of 1000 meters from the shower axis.

Moreover, hybrid data determine the trigger probability for individual tanks as a function of core distance and energy, from which it is found that the SD event trigger is fully efficient above 3 EeV for zenith angles less than 60°, as it was described above. The SD exposure is then calculated simply by integrating the geometric aperture over time. It is the continuously operating surface array which provides the high statistics with unambiguous exposure. The methods adopted for this first analysis were chosen to be robust and simple.

[8] At low energy, this number must be scaled according to the relative aperture.

The data for the presented analysis are from 1 January, 2004 through 5 June, 2005 for events with zenith angles 0°–60°, and the results are reported for energies above 3 EeV (3525 events). The array is fully efficient for detecting such showers, so the acceptance at any time is the simple geometric aperture. The cumulative exposure adds up to 1750 $\mathrm{km}^2\,\mathrm{sr}\,\mathrm{yr}$ which is 7 % greater than the total exposure obtained by AGASA. The average array size during the time of this exposure was 22 % of what will be available when the southern site of the Observatory will be completed.

Assigning energies to the SD event set is a two-step process. The first step is to assign an energy parameter S_{38} to each event. Then the hybrid events are used to establish the rule for converting S_{38} to energy.

3.3.1 Significance of S_{38} and energy conversion

The energy parameter S_{38} for each shower comes from its experimentally measured S(1000), which is the time-integrated water Cherenkov signal S(1000) that would be measured by a tank 1000 meters from the core. This ground parameter is determined accurately by non-linear interpolation even when there is no tank at that particular core distance.

The slant depth of the surface array varies from 870 $\mathrm{g.cm}^{-2}$ for vertical showers to 1740 $\mathrm{g.cm}^{-2}$ for showers at zenith angle $\theta = 60°$. We know that the signal S(1000) for the given energy E of cosmic ray particle is dependent on θ and attenuated at large slant depths. This dependence on zenith angle θ is derived empirically using the fact that the distribution incoming directions of cosmic rays is expected to be isotropic. The so-called constant intensity cut (CIC) curve is then identified by having the same number of events in each θ-bin. The actual CIC curve for PAO observatory is in Fig. 3.7:

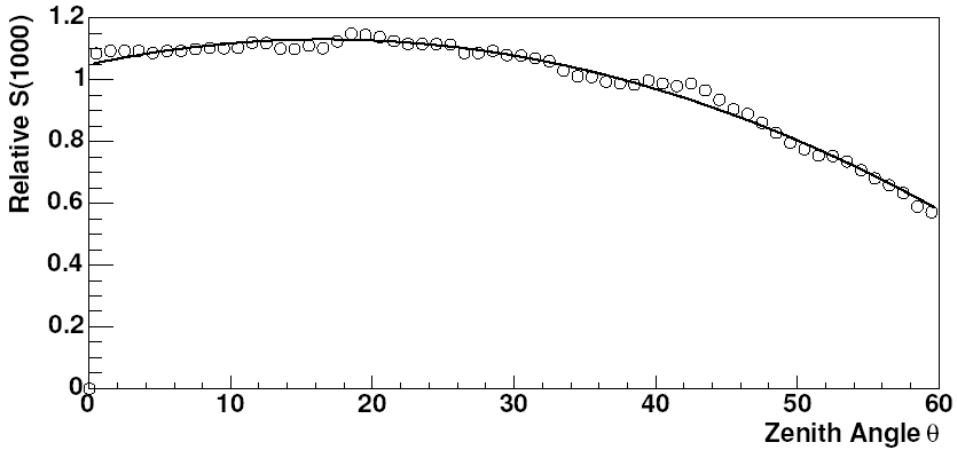

Figure 3.7: *The constant intensity cut (CIC) curve. Values are relative to S(1000) at the median angle value of 38°. The approximating quadratic curve is also shown (solid line). From [24].*

It is then possible to find the analytic aprroximation of resulting curve, currently used for PAO [24] is:

$$CIC(\theta) = 1.049 + 0.00974\theta - 0.000029\theta^2 \tag{3.4}$$

The $CIC(\theta)$ value is then relative to the S(1000) at the median zenith angle 38° and so we can define S_{38}, which is not dependent on the zenith angle θ of incoming shower:

$$S_{38} = \frac{S(1000)}{CIC(\theta)} \tag{3.5}$$

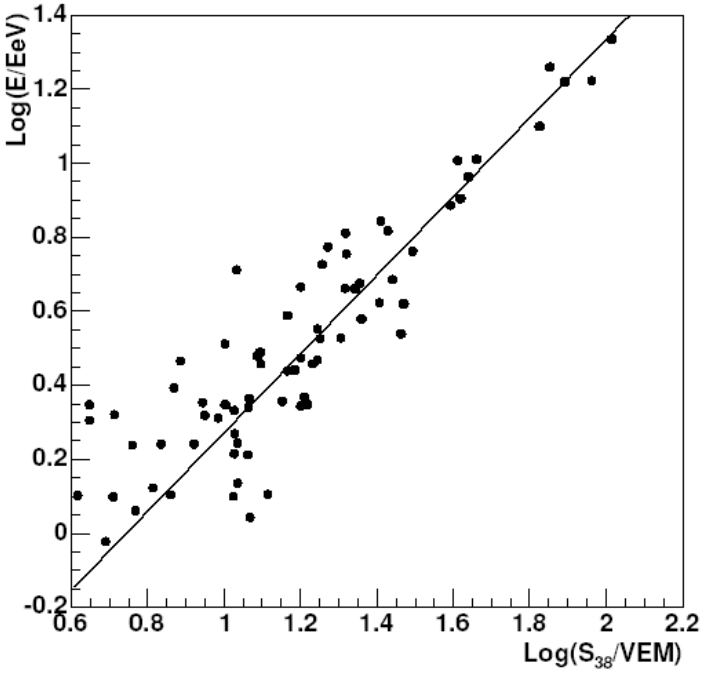

Figure 3.8: *FD energy vs. ground parameter* S_{38} *. These are hybrid events that were recorded when there were contemporaneous aerosol measurements, whose FD longitudinal profiles include shower maximum in a measured range of at least 350* $g.cm^{-2}$ *, and in which there is less than 10% Cherenkov contamination. The solid line is* $\log(E) = -0.79 + 1.06\log(S_{38})$*. From [24].*

The S_{38} parameter is then well correlated with the FD energy measurements of hybrid events, which we can independently analyze by using separately FD and SD data. See Figure 3.8. The fitted line gives than the final formula for energy E (in EeV) and links it to S_{38} (in VEM; vertical equivalent muons):

$$E = 0.16 \times S_{38}^{1.06} \tag{3.6}$$

The distribution over $\ln(E)$ obtained by this two-step process is then divided by the total exposure during analyzed time interval and directly from it we can obtain the spectrum, as it is shown in Fig. 3.9.

The statistical uncertainties in S(1000) are of about 10 % and systematic uncertainties are < 4 % [30]. There is larger systematic uncertainty in the conversion of S_{38} to energy. Part of that comes from the FD energies themselves. Laboratory measurements of the fluorescence yield are still uncertain by about 15 %, and the absolute calibration of the FD telescopes is presently uncertain by 12 %. Together with other smaller FD uncertainties, the total systematic uncertainty in the FD energy measurements is estimated to be 25 %. Another part of the systematic energy uncertainty in this analysis comes from quantifying the correlation between S_{38} parameter and FD energy.

The overall accuracy of the spectrum is limited by the available statistics, and the uncertainty grows with energy. Combining in quadrature the FD systematic uncertainty and this correlation uncertainty, the total systematic energy uncertainty grows from 30 % at 3 EeV to 50 % at 100 EeV. This uncertainty is indicated by horizontal double arrows in Fig. 3.9, and a 10 % systematic uncertainty in the exposure is indicated by vertical arrows.

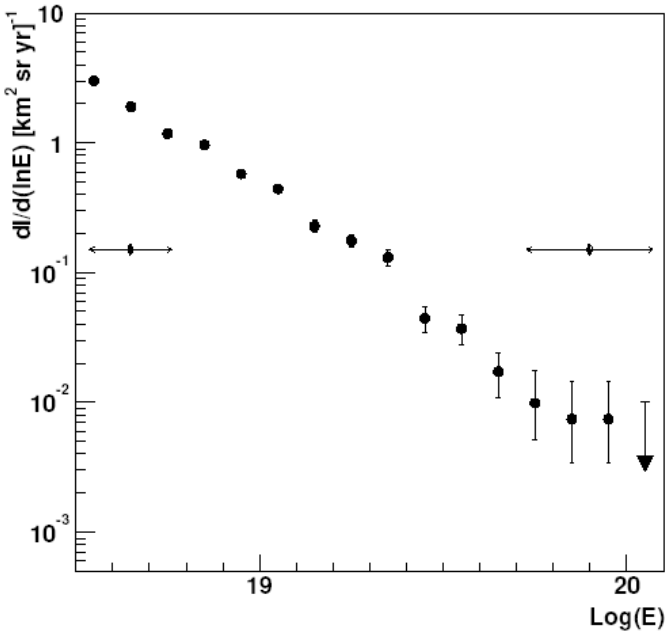

Figure 3.9: *Estimated spectrum. Plotted on the vertical axis is the differential intensity* $\frac{dI}{d\ln E} \equiv E\frac{dI}{dE}$ *. Error bars on points indicate statistical uncertainty (or 95 % CL upper limit). Systematic uncertainty is indicated by double arrows at two different energies. From [24].*

No study dealing with possible chemical composition of primary particles detected by PAO was published up to now, the only exception is the estimate of upper limit on the photon fraction for the energies above 10^{19} eV. Because quite strict criteria [25] on event selection were applied[9] only 16 events survived these cuts and were analyzed. The resulting upper photon limit is 26 % (at 95 % confidence level), what is about a half of the value, which was recently published for AGASA [203]. Furthermore, additional observables recorded with the surface detector array [25], available for a sub-set of the data sample, support the conclusion that a photon origin of the observed events is not favoured.

3.4 Anisotropy searches

The first results of blind searches for overdensities using the data of PAO surface detector were recently published [23]. The data were divided into two energy bands ($10^{18}\text{eV} \leq E_1 \leq 5 \times 10^{18}$ eV and $E_2 \geq 5 \times 10^{18}$ eV) and then again to two angular scales (5° and 15°). This analysis gave results which are compatible with isotropy. Before the start of regular PAO operation also the list of specific targets and conditions (so-called *prescription*) was given, including Galactic center, AGASA-SUGAR excess location and three nearest active extragalactic objects — NGC 253, NGC 3256 and Centaurus A. Also for this set of targets the results are compatible with isotropy, no excess was found or confirmed. However, the number of detected particles is still quite low, so the results could differ after analysis of larger data set.

Special attention was devoted to the search for excesses of events near the direction of the Galactic center [29] in several energy ranges around EeV energies. Taking advantage of its southern hemisphere location, in this region the number of events accumulated by PAO is already larger than that of any previous experiment. Using both the data sets from the surface detector and hybrid data set no significant excess was found. The published results [29] do not support the excesses reported by AGASA and SUGAR experiments.

Finally, the study [29] also presented results for correlations of cosmic ray arrival directions with the Galactic plane and with the super-galactic plane at energies in the range 1 – 5 EeV and above 5 EeV and again have found no significant excess.

[9] Only hybrid events, geometry and profile fits succeeded, X_{max} observed, FD track length in the field of view > 400 g cm^{-2}; to achieve comparable detector acceptance for photon and nuclear primaries only azimuth angle $> 35°$ and distance $< 24km + f(E)$ from telescope to shower axis, where $f(E) = 12\text{km}(\log E[eV] - 19.0)$.

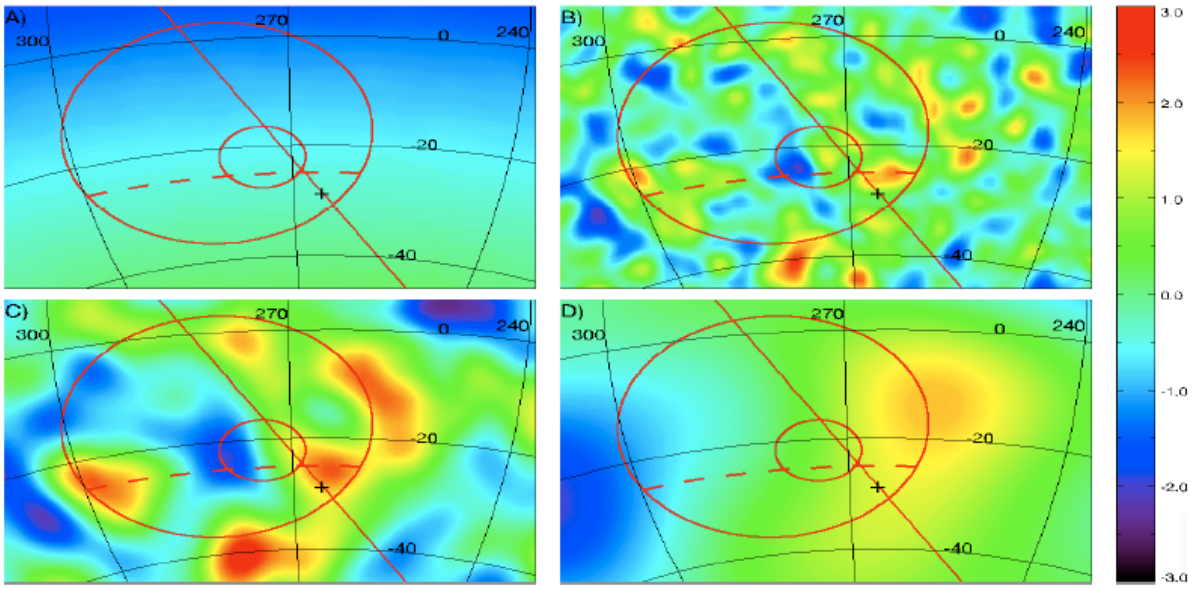

Figure 3.10: *Lambert projections of the Galactic center region, GC (cross), Galactic plane (solid line), regions of excess of AGASA and SUGAR (circles), AGASA field of view limit (dashed line). A) coverage map (same color scale as the significance maps, but in a range [0-1.0]). B) significance map in the range [0.8-3.2] EeV smoothed using the individual pointing resolution of the events and a 1.5° filter (Auger like excess), C) same smoothed at 3.7° (SUGAR like excess), D) in the range [1.0-2.5] EeV smoothed at 13.3° (AGASA like excess). AGASA/SUGAR excess was not confirmed in any of these images. From [29].*

3.5 Offline software framework

A full software framework was designed and developed for the purpose of complex offline data analysis. This framework is implemented in C++ and takes advantage of object oriented design and common open source tools. It consists of three principal parts:

- A collection of processing *modules* which can be assembled and sequenced through the instructions provided in an XML file (*run controller*). The XML language was chosen because it is very easy to learn and use, however still grammatically rich enough even to accomodate very complex and detailed analysis applications.
- An *event* structure through which modules can relay data to one another and which accumulates all simulation and reconstruction information.
- A *detector description* which provides a gateway to data describing the configuration and preformance of the observatory as well as the atmospheric conditions as a function of time.

The modular character of the framework easily allows to prepare and change various partial data processing algorihms, which then can be inserted into the framework by adding a registration macro. Such approach very easily allows that any individual member of Auger collaboration is able to develop his specific part of analysis code and then test it within existing framework, having the rest of it unchanged. Therefore, whole analysis is naturally subdivided to these modules and could be improved much more effectively and simultaneously by many different experts in many different fields.

The *event* data structure contains all raw, calibrated, reconstructed and Monte Carlo data and acts as the principal backbone for communication between modules. The event representation in memory is decoupled from the representation on disk. Currently, these transfers between memory and disk event representations are implemented using the standard ROOT toolkit, developed at CERN. A set of input/output utilities allow user to transfer part or all of the event from memmory to a file at any stage in the processing and to reload the event to continue processing from any point onward. These utilities support multi-format reading and writing to deal with different event and monitoring formats as well as the formats used by AIRES, CONEX and CORSIKA air shower simulation packages.

The *detector description* provide an interface from which mdule authors may retrieve information about the detector configuration and performance. The interface is organized folloowing the hierarchy normally associated with the observatory instruments. Requests for data are passed by this interface to a registry of so-called *managers*, each of which is capable of extracting a particular information from a particular data source. In this way, the user sees only a single interface even though the data sought may reside in any number of different sources. Generally, static detector information is stored within XML files and time-varying monitoring and calibration data are in MySQL databases.

The detailed information about the framework design and functions, as well as further references are available in [18].

Chapter 4

Fluorescence Detector

4.1 General Description

The Auger Fluorescence Detector (FD) measures the longitudinal development of the cosmic ray shower in the atmosphere above the earth through the detection of the fluorescence photons emitted isotropically by the nitrogen molecules excited by the shower's secondary particles propagating in the atmosphere.

Most of the fluorescence photons are emitted in the wavelength range between $300 - 400$ nm for which the atmosphere is quite transparent, corresponding to an attenuation length of ≈ 15 km for a vertical beam of light. The fluorescence yield is ≈ 4 photons per electron traversing one meter of atmosphere, with known dependence on altitude and atmospheric temperature. The pioneering measurements of fluorescence yield were made by Bunner [64]. More recently appeared works [148, 181], which tried to explore more carefully the dependencies of fluorescence yield on specific atmospheric condition (temperature, pressure, composition). The above mentioned experiment AIRFLY [16] with strong Czech participation is trying to push the precision limits of fluorescence yields measurements even further.

The FD of the Pierre Auger Observatory comprises four optical stations located at the periphery of the site overlooking the SD array. Each station consists of a building with six bays, each one containing a telescope sensitive to the UV photons. The focal surface of the telescopes consists of a rigid and spherical aluminum piece (the camera) in which there are installed 440 photomultiplier tubes (PMTs)[1] arranged in a 22×20 array [12].

The PMTs have a semitransparent bialcaline (SbKCs) photocatode of hexagonal shape and a quantum efficiency $QE > 25\%$ in the spectral band 350–450 nm [169].
An UV trasmitting filter (M-UG6 glass sheets) installed at the 2.2 m diameter aperture improves the signal-to-noise ratio [60].

A spherical mirror with an area of 3.5 m $\times$ 3.5 m, a radius of curvature of 3.4 m and 1.743 m detection surface distance, as well as a corrector ring installed in the periphery of the aperture, complete the optical components. Each FD telescope has a field of view of

[1] Manufactured by Photonis, type XP3062.

30° in azimuth and 28.6° in elevation. The main elements of the telescopes are shown in Fig. 4.1.

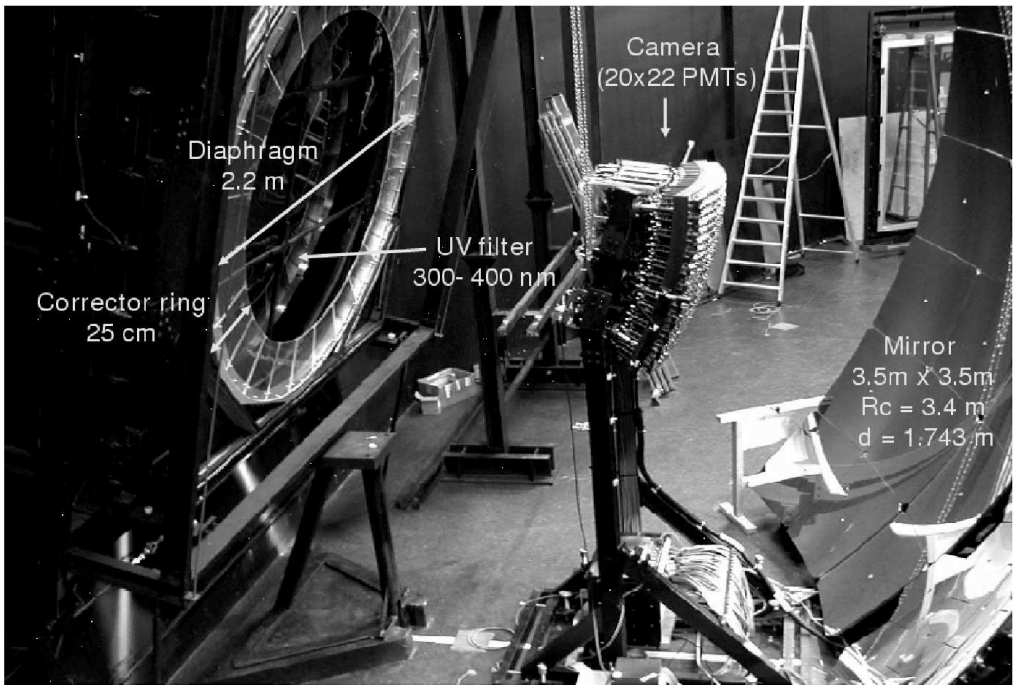

Figure 4.1: *Structure of a FD telescope. The aperture system consists on a diaphragm, a corrector ring and a UV filter. The other optical components are the mirror and the camera, this one comprising an array of* 20×22 *PMTs. From [21].*

The telescope incorporates Schmidt optics to reduce the optical aberrations, where the aperture is defined by the circular diaphragm in the plane perpendicular to the optical axis with its center placed at the center of curvature of the spherical mirror. The great advantage of the optical system is the elimination of coma aberration thanks to the corrector ring, keeping the light spot reflected on the camera at an angular size of 0.5° [79, 142].

Each PMT is equipped with a Head Electronics unit (HE) which provides active bias. This active component improves linearity over the whole dynamic range compared to a standard passive base that should pass a current 2× larger. The PMT signal is sent to the Front-End Board (FEB) in differential mode where it is filtered and digitized at 10 MHz sample rate while keeping a 15 bit dynamic range.

At the present time three of the four fluorescence sites have been completed and are in operation. Two of them, Los Leones and Coihueco, have been collecting data since January 2004, with Los Morados beginning regular data taking in April 2005. The fourth site at Loma Amarilla will be in operation in the second half of 2006.

One of the goals of the FD is to measure air shower energies with an uncertainty smaller than 15 %. In order to achieve this goal the fluorescence detectors have to be calibrated with overall error less than 8 % [27] and the calibration stability needs to be monitored on

a regular basis. An absolute calibration of each telescope is performed three or four times a year, and relative calibrations are performed every night during detector operation. The detailed description of calibration procedures follows in 4.6.

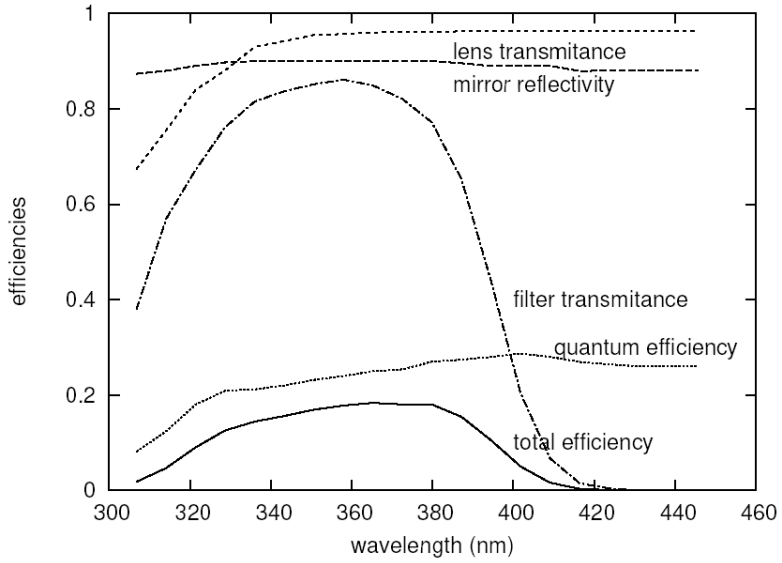

Figure 4.2: *Transmitance, reflectivity and efficiency of the FD telescope components as the function of the wavelength. From [188].*

4.2 Observations

4.2.1 FD trigger

First level trigger

The photomultiplier signals are received by a set of 20 front end boards (FEBs) hosted in a crate placed on the floor below the camera. Each FEB, serving 22 pixels of a camera column, provides proper treatment of the analog signal from the PMTs with a differential line receiver, individual gain control and anti-aliasing active filter. The signals are then digitised continuously by 10 MHz 12 bit ADCs. Digitizing two additional virtual channels, which are the analog sum of the 11 odd and 11 even channel numbers at a lower gain, allowes a dynamic range of 15 bits to be obtained.

The digital part of the FEB is used to implement all functions of the First Level Trigger (FLT) with reprogrammable FPGA[2] logic. While the ADC values are continuously written to memory, the running sum of the last 10 samples is calculated. A pixel is marked as

[2]FPGA = field-programmable gate array. FPGAs have generally wider spectrum of possible applications, but are somewhat slower then specially designes AICs (application integrated circuits).

triggered, whenever the running sum exceeds an adjustable threshold. When the running sum again falls below the threshold, the pixel trigger is extended to a time of 20 μs, which is the overlap coincidence time common to all pixels. The trigger rate of individual pixels is measured continuously and kept close to a reference value of 100 Hz by automatic adjustment of the threshold. In this way, the random coincidence rate of the Second Level Trigger (SLT) remains constant under variable light background conditions.

The trigger FPGA also implements the calculation of the pixel ADC variance, which is proportional to the background light, as we discuss it below in 4.4.

Second level trigger

The Second Level Trigger (SLT) FPGA logic is implemented on a separate board, which is used to read the pixel triggers generated for each channel in the 20 FLT boards. The SLT algorithm is used to search for patterns of 5 pixels consistent with a track segment, and to generate an internal trigger for data readout. Synchronisation with the front-end board is provided by a GPS clock. The algorithm makes use of the fundamental patterns shown in Fig. 4.3, as well as those corresponding to rotation and mirror reflection of these segments.

The algorithm requires only 4 triggered pixels out of the 5 pixel track segment, allowing for possible faulty PMTs or small signals below the FLT threshold. The total number of different pattern classes is 108.

The SLT FPGA is used to read the pixel trigger of a camera column into a pipeline of 5 stages every 50 ns. The pipeline holds the image of a 22×5 submatrix of the camera. A pattern algorithm uses coincidence logic to search for the allowed patterns inside this submatrix while the image is shifted, column-by-column, over the full camera. The full camera image is scanned by the SLT module in 1 μs. If the coincidence condition is fulfilled for any of the pattern classes, the recording of ADC data is continued in the next free circular buffer, and the Mirror PC is informed. Typical SLT random coincidence rates of a few tenths of Hz per telescope.

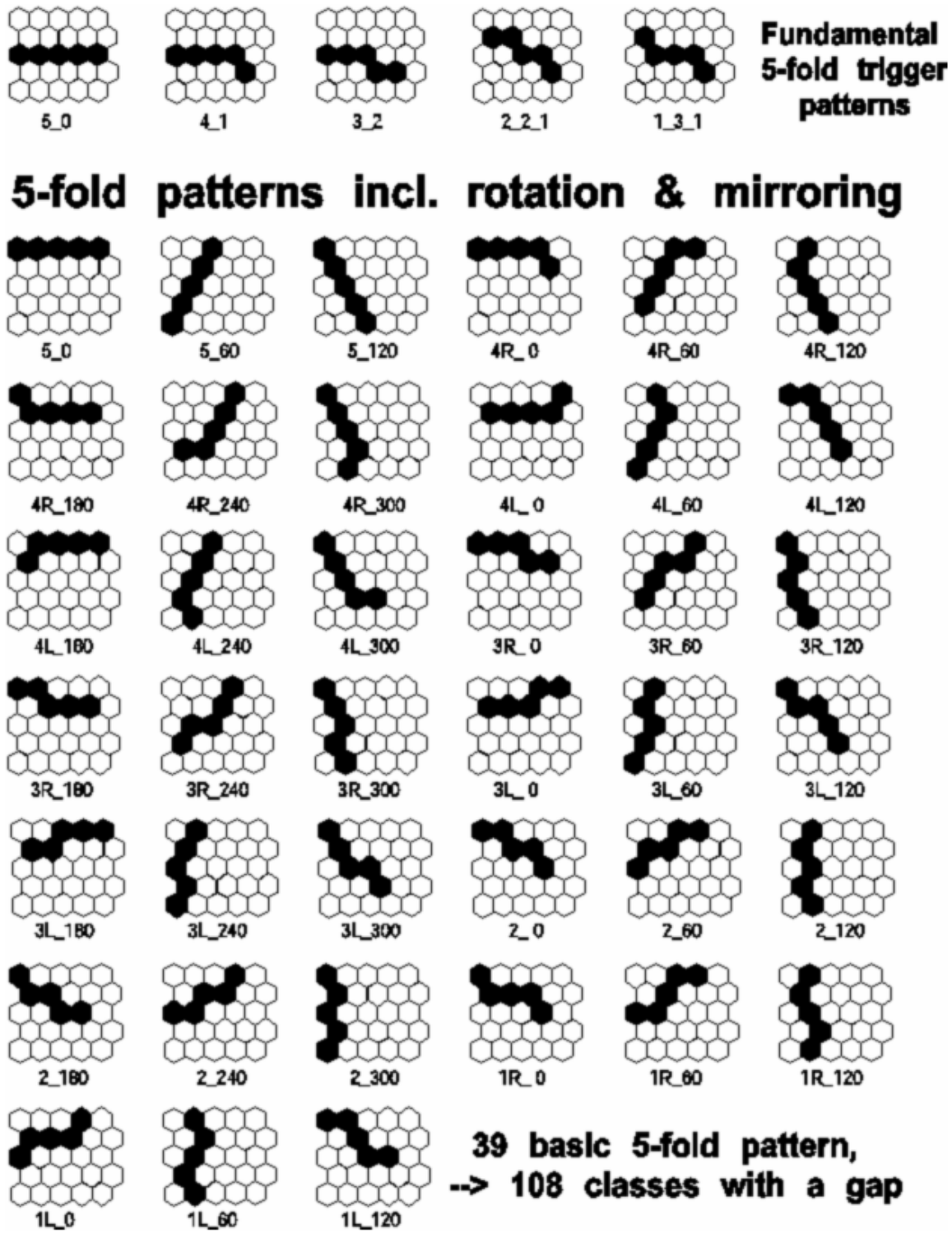

Figure 4.3: *Fundamental types of 5-fold pattern (top part of the figure) and all 39 basic patterns after rotation and mirror reflection (lower part). From [21].*

Third level trigger — T3

The Mirror PC, a robust, diskless, industry PC associated with each telescope, is used to perform the data readout and a simple software, third level trigger selection, based on track length and space-time compatibility requirements. In fact, a more sophisticated T3 algorithm is also implemented, which selects shower candidates and performs a fast reconstruction of the shower geometry, as it is described below.

All pixels that are part of a SLT of the event are selected. A fast search for a maximum of the ADC trace around the FLT time of each pixel is performed. A large part of the background, which is due to cosmic rays passing through the PMTs of the camera, is rejected by requiring that the selected pixels do not fire at the same time. Fits of the pixels to the elevation angle vs azimuthal angle and time are performed, and pixels with a large contribution to the χ^2 fit are removed. After this procedure, candidates with more than 4 pixels are considered good showers, and the azimuth of the shower impact on ground, as well its time of arrival, are calculated.

For good showers, a T3 signal is sent to the central data acquisition system (CDAS), together with information on the shower-detector plane and the time of the shower arrival at ground. These data are then used to form *the hybrid trigger* (see 4.2.2).

4.2.2 FD aperture

We discussed SD aperture in previous chapter and we also mentioned there, that also fluorescence detector aperture and hybrid detector aperture could be defined. In fact, taking into account the $\sim 100\%$ duty cycle of SD then for the fully built observatory the fluorescence and hybrid aperture is pretty much the same. In general, for showers close to the FD detectors the FD energy threshold is lower than SD threshold, but all FD T3 triggers cause also readout of T2 signals from all SD stations nearby shower core (also so-called hybrid trigger). Then, during offline analysis, the SD sub-threshold information could be obtained and successfull hybrid reconstruction could be finished.

As it was also already mentioned, with the current level of statistics, only the SD aperture is used for the spectrum evaluation. Therefore we will limit here ourselves only to illustrate basic energy dependence of hybrid aperture, which is following:

For a fully built detector, the hybrid apertures for cosmic rays with energies of $10^{17.5}$ eV, 10^{18} eV, $10^{18.5}$ eV and greater than 10^{19} eV are approximately 900, 3200, 6400 and 7400 km^2.sr respectively. For comparison, the aperture of HiRes fluorescence detector is 2250 km^2.sr.

Of course, the fluorescence and hybrid apertures (and their difference) were also already studied using detailed simulations, the results are available in [44].

4.2.3 FD operations and data taking

Every synodic month (every lunation), during the period around the new moon, a group of physicists from within the Auger collaboration takes care of the so-called FD data taking

shift. They are first instructed by the appointed person (Scientific Operations Coordinator — SOC) how to operate the data acquisition system and then supervised until they get fully familiar with the procedure. All the information that the operators might need during the shift is contained in manual available from an internal web page. The web page contains not only the basic hardware and software manuals, however also additional information about the Moon fraction, twilight times and weather forecast links.

The basic facts about system calibration or about proper data taking (e.g. the start and end times), as well as all the problems occuring during the shift are reported in the FD electronic log (*e-log*), which is again accessible from the FD web page. A template is provided to unify the way of reporting different events.

The usual number of the physicists in the data taking group is 4, who make pairs and then each of this sub-groups takes data during each odd or even night during given lunation. Two operators are not really necessary, only one experienced operator is able to handle the whole system, however it is much more convenient to work in pairs. In such a case first physicist is responsible for DAQ itself (see below) on Linux system and the second physicist operates the hardware control console (*slow control*) with Windows operating system and writes all the necessary records into e-log.

As it was just mentioned, the DAQ system for FD was developed under the Linux operating system in the C++ language. An event display and online histograms are available to monitor data quality.

Then the slow control system is used to guarantee that the FD operates only under safe conditions. Opening of the external shutters of individual FD bays is prevented during daylight or during windy weather. To avoid direct exposure of the PMT cameras to sunlight in the case of shutter failure, a fail-safe curtains are installed at the apertures. The high voltage of the camera PMTs is shut down when any high light level is detected inside the bay. An uninterruptible power supply (UPS) protects the operation of the computers and shutter should there be a failure of mains power.

4.3 Performance Monitoring and Optimization

4.3.1 FD observation time

Basic parameter describing the FD performance is its observation or run time.

The total available dark time is defined [71] as the time between the end of the astronomical twilight at the beginning of the night and between the start of the dawn at the following day (Sun $> 18°$ below horizon). Everything that prevents the measurement to be as long as this period is considered dead time. The main source of this dead time is the presence of the Moon close to or inside the field of view (FOV) of a telescope. However, also bad weather, hardware or software problems can decrease the measurement time.

The different types of down (or dead) times are then defined as follows:

- **Moon:** this is calculated using a program written by the author of this thesis. The time when the Moon is closer than $5°$ to the FOV of each telescope is used to calculate

the period when that telescope is not able to take data. The operators are requested to close the corresponding shutter at the reported time. This subject of observation under Moon is dicussed in detail below in 4.3.2.

- **DAQ/Hardware:** it is defined as the time between runs in the same night. Takes care of the fact that some runs are stopped due to a problem with the hardware or software and a new run is started as soon as the problem is solved. The assigned time could be modified later if the information in the e-log shows evidence against this assumption.

- **Weather/other:** the down time that cannot be classified as any of the previous cases is attributed to the weather or unknown causes. The real cause is later deduced from the e-log entries.

There is another source of dead time, related to the normal operation of the DAQ software and hardware. As any other system, it has internal delays that can lead to loss of measurement time. This dead time is calculated by the system itself. It is not yet taken into account in the reports, but will be in a near future [71]. For each run, the measurement time is calculated as the time difference between the start and end times, multiplied by the telescope fraction. The telescope fraction is calculated as the number of mirrors used in the run times 1/6. This is useful when some mirrors are not present in the DAQ (for example, they are taken out because the Moon is in their field of view). Run measurement times are added to obtain the total measurement time of the night. Runs shorter than one minute are discarded.

Currently, the number of stereo or triple events is calculated by comparing the GPS times and visually discarding those that could be chance coincidences between two eyes. The automatic distinction of these is planned for future versions of analysis software.

4.3.2 Observation under Moon

As was mentioned above, the FD detector operators are currently running the system also with the Moon above the horizon, closed are only the shutters of the bays which are directly illuminated by Moon or very nearby (the Moon angular distance $< 5°$. The bay shutters are opened or closed by the human operators themselves. Doing so, they are using the output of the *moonfilter* program which was developed by the author of this thesis especially for the PAO southern sites.

Our program is checking the field of views of the actual bays and in the printout for the whole duration of one FD shift (the part of one synodic month around new Moon) are shown only the times, when some shutter operation is needed or when the astronomical night starts/ends or when the Moon rises/sets. For each such (local) time is shown the Moon elevation and azimuth, its illuminated fraction in percents, its visual magnitude and expect background night-sky brightness due to the Moon. The example of such table for one period of FD shift is available as Appendix B of this thesis.

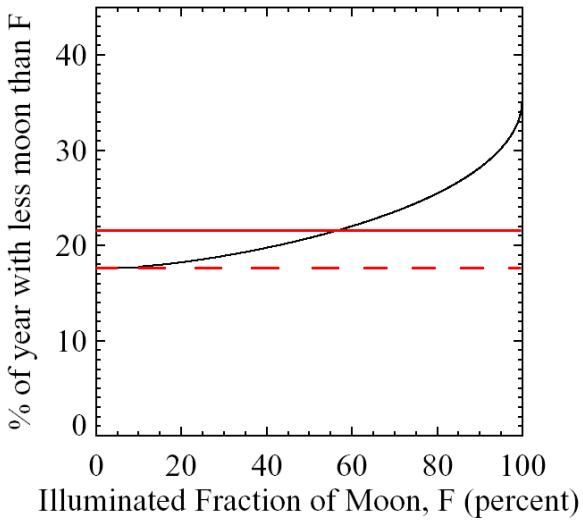

Figure 4.4: *Available hybrid duty cycle as a function of illuminated fraction of the Moon. Astronomical twilight conditions are assumed. The graph was created for the Dugway Proving ground site, where the HiRes detector is located and which northern latitude is* $\sim 40°$. *The PAO southern site lies at* $\sim 36°$ *southern latitude and therefore the difference is negligible for our purposes. To show the magnitude of the time difference with observations under Moon we added red lines. The solid line shows the currently used level of maximum illuminated Moon fraction allowed and the dashed line is for the observations with the Moon under horizon only. From [84].*

The program itself is very straightforward and simple application of Moon ephemeris calculation, which is e.g. incorporated into *libnova* astronomical library [111]. Only the evaluation of the background light level is based on the empirical correlation between computed Moon illumination of the earth surface and real observed background variance levels. However, even such almost elementary application of astronomical knowledge has great impact on increase of the total FD observation time, as we will show below precisely for the year 2005. Such increase of data taking time is directly proportional to the increase of the number of observed hybrid cosmic ray showers. And the importance of these hybrid events is crucial, primarily because of theirs significance in spectrum evaluation, as was described in 3.3.

To evaluate, how actually differs the real observation time with *no Moon* condition and *moonfilter* condition, we have examined the observation dates of FD shifts in 2005. We expected the same duration of each FD shift, but without the *moonfilter* program application we took all the bays with Moon above the horizon as closed. The results of this analysis as shown in Table 4.1 as well as in the Fig. 4.5.

Lunation	**1**	**2**	**3**	**4**	**5**	**6**	**7**	**8**	**9**	**10**	**11**	**12**	**13**
No Moon	12.4	13.6	15.6	21.5	21.0	23.4	22.4	22.4	20.6	17.2	14.9	11.1	10.9
'moonfilter'	14.4	16.0	18.9	25.4	24.9	27.6	26.2	26.4	24.2	20.2	18.2	13.7	13.9

Table 4.1: *Relative observation time per each lunation (synodic month; 29.531 days) according to actual FD schedule for the year 2005.* No Moon *is for observations only with the Moon under the horizon and* 'moonfilter' *is for the observations when the moonfilter program is applied. All values in table are in percent.*

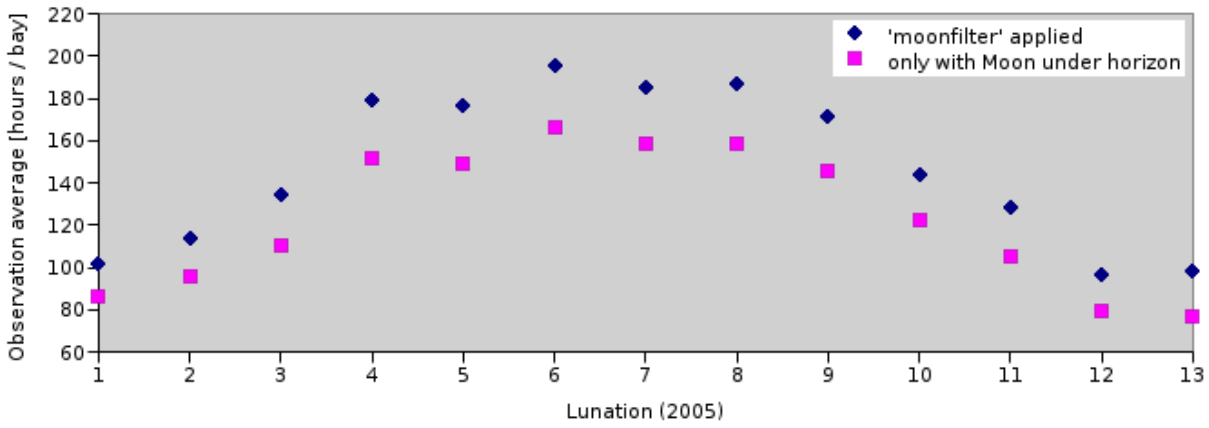

Figure 4.5: *The graph for actual schedule of FD shifts during individual lunations (synodic months) for the year 2005 (the 13th lunation ends on January 6th 2006, however is shown here complete). The vertical axis shows the average number of observation hours during one FD shift (lunation). The difference with* moonfilter *program applied and without it could be clearly seen.*

We can summarize that for the period of year 2005 the ideal (with no weather and hardware problems) duty cycle will be 18.3 % with *no Moon* condition and 21.9 % with actually applied *moonfilter* condition. The relative increase of duty cycle is therefore almost 20 %.

We have to mention, that the number of detected showers will increase less than these resulting 20 %. With the Moon on the sky, the sky is brighter, the noise background is higher and whole detector is less sensitive especially to less energetic showers. As it is probably clear, the sky background brightness does not increase linearly with the illuminated Moon fraction. The actual dependence is shown in Fig. 4.6

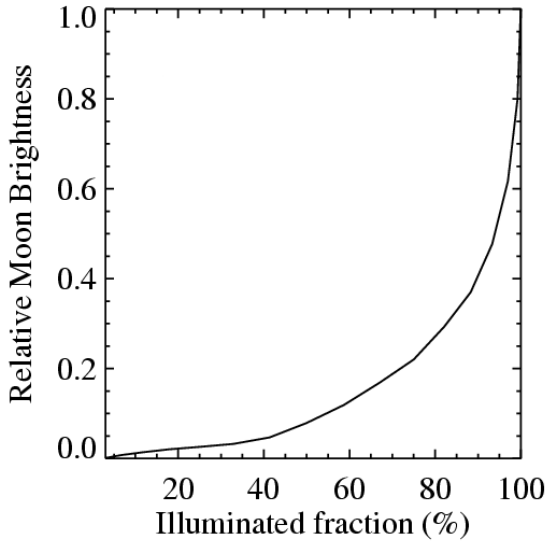

Figure 4.6: *Brightness of the Moon as a function of its illuminated fraction (relative to brightness of the full Moon). From [84].*

The shape of this curve may be quite surprising on the first sight (e.g. only $\sim 15\%$ of full Moon brightness for the 50% illuminated fraction). However, the Moon brightness depends not only on the part of the surface of the Moon which is illuminated, but also on the phase angle what explains this unexpected fact. For small lunar phases the incidence angle of solar rays with respect to lunar surface is very oblique contrary to the geometry of full Moon phase when the incident light is reflected almost perpendicularly to the lunar surface, in the direction to the observer.

Still, the half illuminated Moon increases the sky background by a factor of about 3. According to simulations of [84] this results in non-observability of less energetic showers (up to 10^{19} eV), however the trigger for the most energetic showers (around $\sim 10^{20}$ eV) will be still 100 % efficient. These theoretical expectations are further complicated by fact that during not absolutely pristine nights, when some cloud cover is present, the moving clouds can scatter the Moon light and unfortunately also successfully trigger the FD camera. The number of such false events grows with the illuminated fraction and hopefully will be removed by applying some software restrictions in future. Currently, the maximum allowed illumination of the Moon amounts to 50–60 % of the full Moon illumination because for higher values of lunar illumination the database is dominated by these noise events.

4.4 FD background data

At the very beginning of the Auger Project it was decided to construct the first two prototype telescopes of the Fluorescence Detector. The Head Electronics used in the first

two prototypes [66] comprised the biasing network and a novel optical feedback system that allowed reading the very slowly varying signal left by a star when it enters into the field of view (FOV) of a pixel. All 880 units were equipped with the *current monitor* [17]. On June 25, 2001 the first signal of Vega (Alpha Lyrae), shown in Fig. 4.7, was clearly seen by the telescope at Los Leones [3, 67].

After demonstrating the capability of the telescopes to be sensitive to even dim stars in the UV region, we incorporated a low-cost solution that returns the variance of the baseline fluctuation, which is proportional to the sky background light, that comprises also star signals.

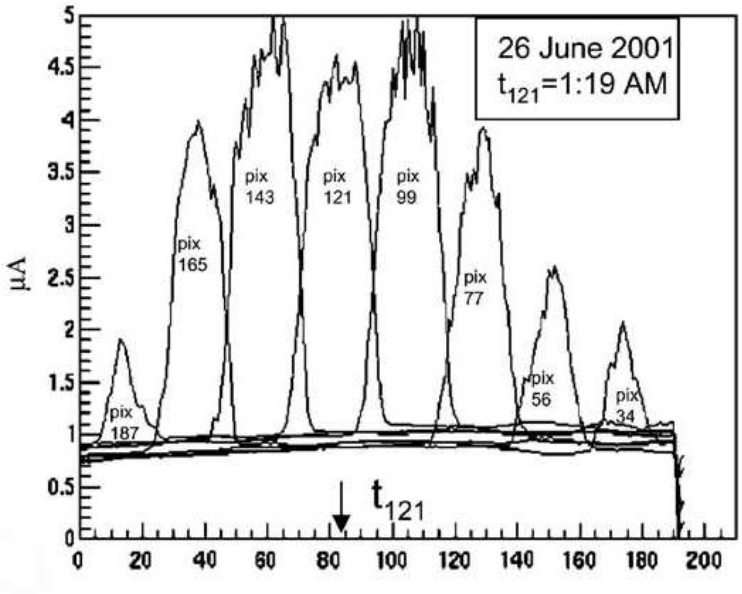

Figure 4.7: *Signals of current monitor (μA) for adjacent pixels vs. time generated by the transit of α Lyrae (Vega) in their FOV. The mean time of Vega's signal in the pixel* 121*, t_{121}, is indicated. The sampling time is 20 s.*

The measurement of background light level, which is currently implemented for Auger FD detectors, was extensively described in [155] (with further details given in [173]). Therefore, we will limit ourselves only to short description here.

The method of DC current monitoring is based on statistical evaluation of measurements of variance σ^2. Because the incoming light flux is Poissonian (see discussion in [155]), the amplitude of signal fluctuations are directly proportional to the intensity of signal itself. So, the signal variance sampled each 100 ns is recorded and then from 65535 ($2^{16} - 1$; due to the size of electronic buffer) such variance values average is computed, which could then be stored. It is clear, that using such approach we are doing very fast photometric measurements of stars — each integration is only 6.5 ms long. This statistical evaluation is done in parallel by 4 FPGA logic boards, each FPGA is handling 6 indepen-

dent camera channels[3] — one after another. Therefore we are potentially able to have 6.5 ms star photometry every ∼39 ms (6 * 6.5 ms = 39 ms). However, for practical purposes the value for each pixel (e.g. "photometric" image of whole 440 pixel camera) is generally stored every 30 seconds.

The sky photon background flux can be directly derived from ADC variances σ^2 [70]. First we have to subtract the electronic noise, using the data that were taken with closed shutters before each nightly run:

$$[\sigma^2]^{sky} = [\sigma^2]^{measured} - [\sigma^2]^{electronic} \tag{4.1}$$

Then we can convert sky background variance from ADC counts to photoelectrons:

$$\sigma^2_{photoelectrons} = [\sigma^2]^{sky}/A_G^2, \tag{4.2}$$

where A_G is the absolute gain (ADC counts per photoelectron). Individual pixels are calibrated using special device called *drum calibrator*, as it is described in detail below within secction 4.6. This method provides a conversion between ADC counts and photons at the telescope diaphragm for each pixel. In terms of these calibration constants C_{FD}, the absolute gain is:

$$A_G = \frac{1}{C_{FD}.f.Q}, \tag{4.3}$$

where Q is the PMT quantum efficiency (0.29 in given spectral range) and f the overall telescope optical factor. This factor includes the optical filter transmission F, the corrector ring lens transmission L (for telescopes with such a lens), the mirror reflectivity R, the mercedes (light collector) efficiency M and the camera shadow factor S, derived from ray tracing simulations; example values for the bay 4 at Los Leones are also shown:

$$f = F.L.R.M.S = 0.83 \times 0.9 \times 0.9 \times 0.93 \times 0.79 = 0.494 \tag{4.4}$$

Having σ^2_{phe} we can convert sky background variance to photoelectrons:

$$n_{phe} = \frac{\sigma^2_{phe}}{1 + V_G}, \tag{4.5}$$

where V_G is the PMT gain variance factor. V_G, which describes the non-poissonian effects induced by the PMT gain chain, is derived in PMT testing operations and from the manufacturer data sheets. It can be reasonably assumed equal for all PMTs, especially after *drum calibration* (see section 4.6).

Finally, we can convert the photoelectrons to photon flux Φ_γ:

$$\Phi_\gamma = \frac{n_{phe}}{Q.f.A.\Delta t}, \tag{4.6}$$

where A is the pixel aperture (being 7.7 m^2deg^2 for the bays equipped with corrector ring and 4.6 m^2deg^2 for those without corrector ring), Q and f were already defined above. Δt is the sampling time, in case of our detector it is 100 ns.

[3]It means that we have $4 \times 6 = 24$ channels for each camera. There are 22 channels for camera rows and 2 virtual channels.

4.4.1 FD background analysis

There is also another approach which could be applied for obtaining of FD background values [71] and this is the analysis of event data files itself. The whole camera is read out every time when any T3 event is detected and the result is stored. Usually, the number of shower pixels comprises only very small fraction of the whole camera and during the night it appears on different randomly distributed places. Therefore, these real event data records could be used also for separate alternative statistic analysis of FD background or these data could be combined with the above described dedicated FD background data.

A stand-alone code has been developed to monitor the FD background signal and the detector status for any data acquisition night for all mirrors and telescope sites. The program can process the background signal in the FD data runs event by event and/or the special ASCII background files (as mentioned above). The output consists of ROOT files that can be then analyzed off-line.

For each event in the FD data runs, the algorithm extracts the pixel information, including their ADC traces. For each trace, the mean value (pedestal) and the variance are obtained. For further analysis only non-shower pixels (that means only pixels not triggered by FLT logic) are used while for the special background measurements all pixels in the camera are considered. The results of such analysis can help in classifying the nights according to the data taking conditions, just looking at the variances. The nights can be easily classified into several basic types, as shown in Fig. 4.8. A systematic investigation for all data taking nights in 2004 has been performed so far and more automatic version of this analysis is planned.

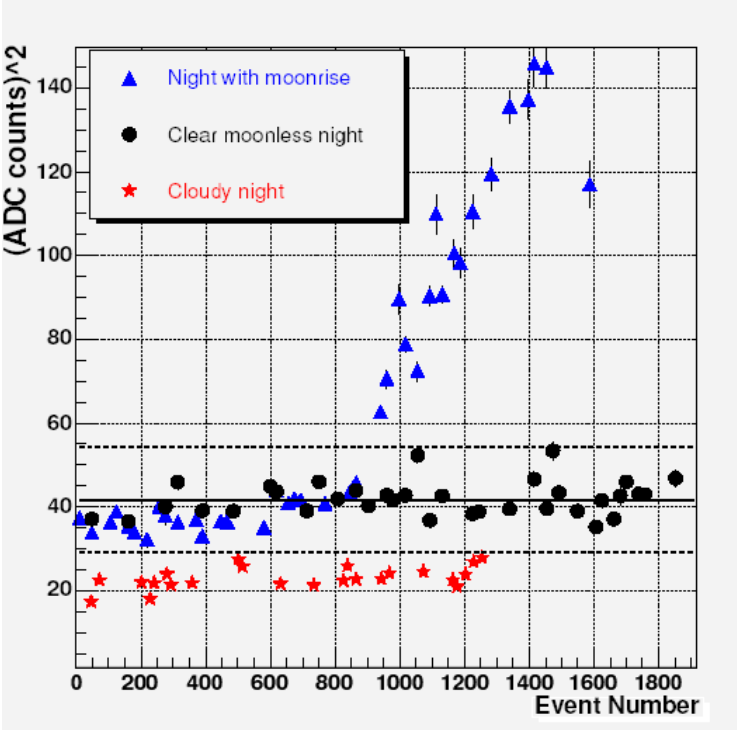

Figure 4.8: *Variances vs. event number for three typical categories of data taking nights: i) (triangles) night with moonrise; ii) (circles) clear moonless night; iii) (stars) cloudy night. Each point is the average value of the variance taken over all noise pixels in telescope 4 at Los Leones. The continuous line is the mean value over the whole night for clear moonless conditions, the dashed lines indicate* $\pm 1\sigma$*. From [71].*

Local background variations can be studied also by plotting the photon flux for each pixel. The most evident feature emerging from this analysis is a systematic up-down effect in the camera illumination. This effect is shown in Figure 4.9, where the sky background flux is shown as a function of elevation and azimuth angles respectively for telescope 4 at Los Leones. Each marker refers to an individual run during the analysis period. A similar behavior is found for all telescopes anlyzed so far, for Los Leones and Coihueco sites. This behavior is in qualitative agreement with astronomical models for sky background brightness, as described eg. in [109]. The increase of brightness with elevation is expected, the surprising and not-yet explained fact is that the brightness is not decreasing for the elevations above 25°, the curve only flattens in this region. The models generally expect maximum brightness for elevations between 20°–25° and then slight decrease.

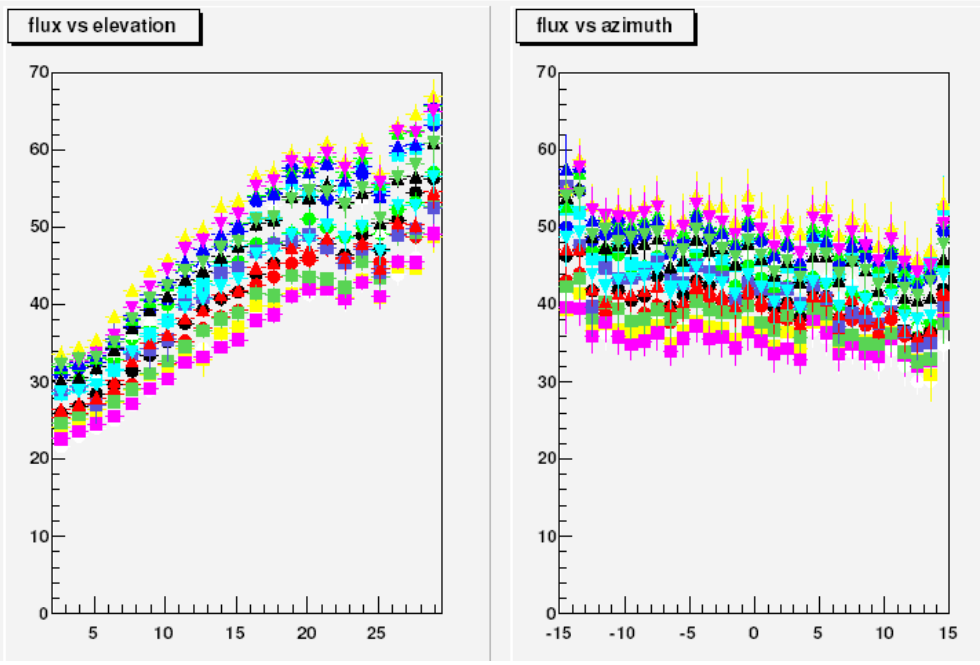

Figure 4.9: *Sky background flux as a function of elevation (left) and azimuth (right) angles for telescope 4 at Los Leones. Each marker refers to an individual night. From [70].*

4.5 Telescope pointing

In this section we describe how to accurately determine the absolute pointing of the fluorescence detector (FD) telescopes of the Pierre Auger Observatory. For this purpose we used data acquired during regular observation periods in 2004. We processed these data using different algorithms for extraction of signals left by stars traversing the field of view of the FD telescopes. We analyzed these signals using two independent methods and obtained compatible sets of pointing directions. Our aim here was to provide a reliable and precise method to check and monitor the absolute telescope's pointing and its long-term stability during the whole life of the project, estimated to be about 20 years. The knowledge of the precise absolute pointing of the telescopes is essential eg. for the improvement of the hybrid angular resolution, which is one of the unpatiently awaited key innovative features of the whole Pierre Auger project.

This section presents a slightly modified version of the paper prepared for NIM (Nuclear Instruments and Methods) A Journal [85], where the author of this thesis is one of the two main authors. The original contribution of the author of this thesis was also published separately as [195].

4.5.1 Two proposed methods

Two methods to deal with the telescope pointing quest were devised recently. First method automatically searches for the star signals in the data. When such signal is found then first the source star is specified. Then the derived central time[4] of the detected signal is identified with the computed position of the star closest to the pixel center. The possible difference of computed and found time is identified as the pixel offset. From many star transits through the given pixel the average offset of this pixel is derived, and finally, from the average offsets of individual pixels the overall offset of the camera is determined. This method we call *the single pixel method*.

The second method is somewhat different. We try to optimize the whole trajectory of bright star across the camera and to identify the time of transits of this star between pixels. Then we look for time differences between expected (computed) times of transit (with some given offset of the whole camera) and between transit times found in data. We go through the matrix of all possible camera center offsets (in some range in azimuthal coordinates) and then we select the optimum offset — with least difference between expected and identified times of transits.

The typical trajectory of a star consists of about 20 transits between pixels and the whole star track is optimized at once. Many (~ 100) such tracks are analyzed and optimized for each camera. The resulting offset of the given camera is then finally calculated as the weighted average of these found offsets. This second method we call *star track optimization method*.

More detailed description of both methods follows below.

4.5.2 Single pixel method

After the first tests of a code that we developed to calculate the telescope's pointing [67], we reviewed the procedure and arrived to a more accurate and reliable method.

The logical scheme of our procedure can be summarized basically on the next three steps:

1. Search for signals in the baseline variance data;
2. Find the stars that give origin to the signals found in (1) to establish the absolute pointing of each single pixel;
3. Determine the pointing of the telescope's optical axis using the reconstructed pixels pointing calculated in (2).

The steps (1) and (2) are repeated for all the nights of the period under analysis (January 2004 — October 2004 in this case) while the step (3) is done only once, at the end of the period of data taking, when the pointing of each pixel has already been determined. In the following paragraphs each step of the procedure will be described.

[4]More precisely the time for the middle of the signal plateau is identified and obtained from background data.

Search for star signals in the baseline variance data

The sky background light varies from night to night and, in a single night it may change within a few hours. To overcome this inconvenience we have implemented two different methods: the Time-Over-Threshold (TOT) and the Slew-Rate (SR) algorithm. As the spot size fixed by the Schmidt optics is 0.5°, 1/3 the pixel size (1.5°), the FD pixel signal is ideally a trapezoidal current pulse whose rise and fall times are about 1/3 the flat top. Our aim is to extract the signals from the variance data and find their central time, i.e. the middle time of its plateau. In Fig. 4.10 an ideal signal shape is shown, to be compared with the real signals of Vega in Fig. 4.7.

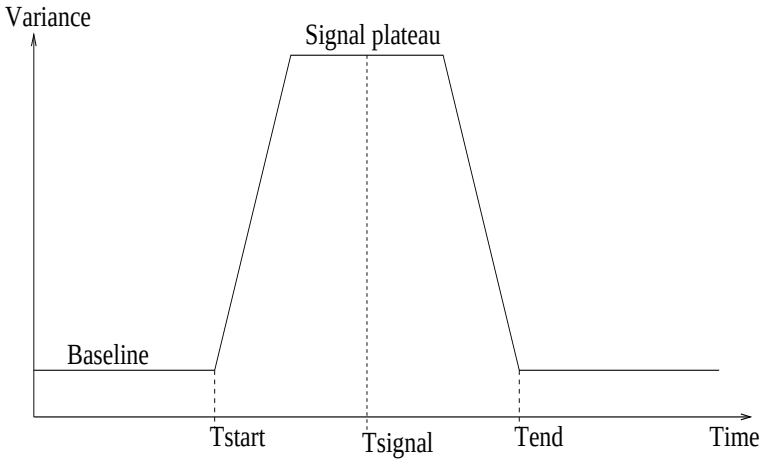

Figure 4.10: *Ideal signal shape. After identifying a star's signal in the variance data, a time T_{signal} is associated to it.*

In the TOT method we first calculate the mean value of the variance baseline, $\bar{v}$, and its RMS value, σ, in a time window of 2 *hrs*. If a star enters into a pixel's FOV, the background noise and the variance of this pixel will increase in a time range of 4 *min.* to 15 *min.* depending on the star declination. Therefore, if a set of variance points is $v_i > \bar{v} + 3\,\sigma$ in this typical time range, a signal is identified and the pixel center is assumed to be pointing to the star direction at time T_{signal}. The absolute pointing direction of each pixel is obtained transforming the equatorial coordinates of the star, right ascension and declination, at T_{signal} to the local coordinate system, elevation and azimuth [111].

The second method, the Slew Rate algorithm (SR), used to extract signals from variance data is a sort of a derivative method. In fact we calculate the increment of the variance between two separated points, $\delta = \Delta v/\Delta t = (v_i - v_j) / (t_i - t_j)$ every 4 *samplings points* (2 *minutes*) during the whole night. A positive and a negative consecutive value of δ, within 4 *min.* to 15 *min.*, will therefore correspond to the leading and trailing edges of a star signal. As for the first method, if a star signal is found, the pixel center is assumed to be pointing to the star direction at time T_{signal}.
A schematic plot of the two methods is shown in Fig. 4.11 in the ideal signal case, while

in Fig. 4.12 the real case is shown. The variance signal in Fig. 4.12(a) has been converted into a number of photons at the diaphragm using the conversion constants obtained with drum calibration.

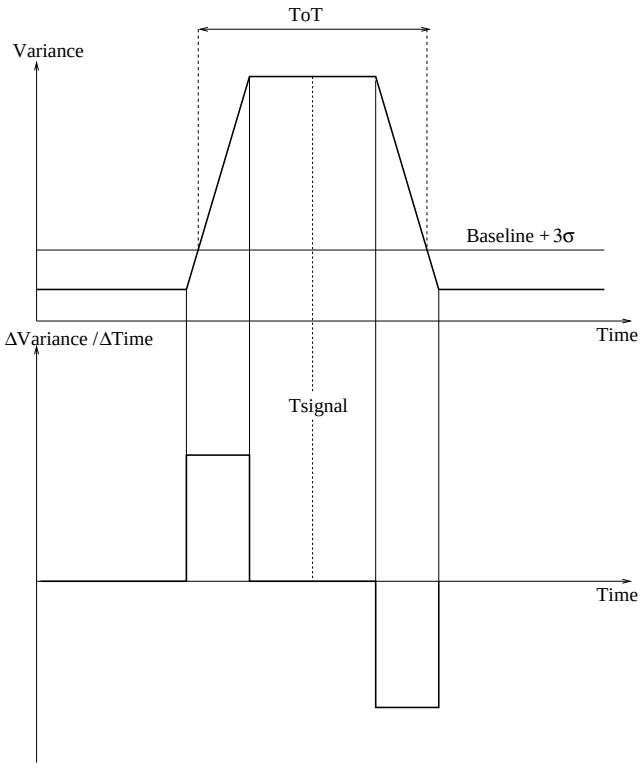

Figure 4.11: *Time-over-Threshold (ToT) scheme above, and Slew-Rate (SR) scheme below.*

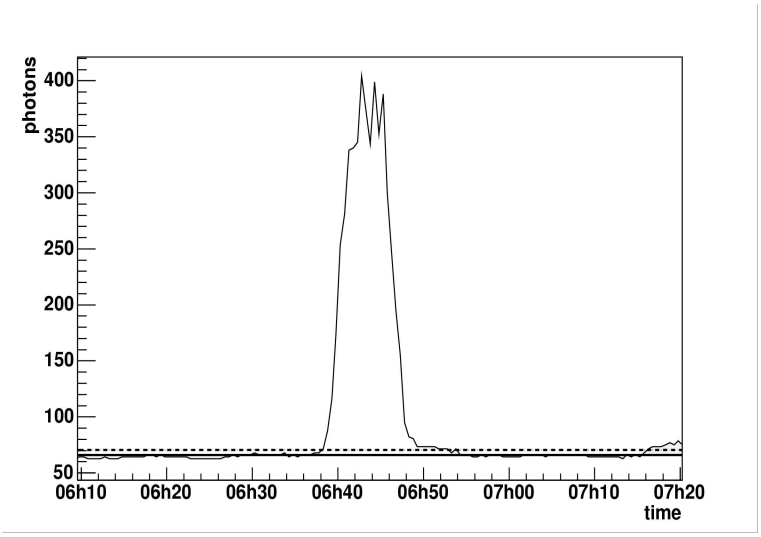

(a)

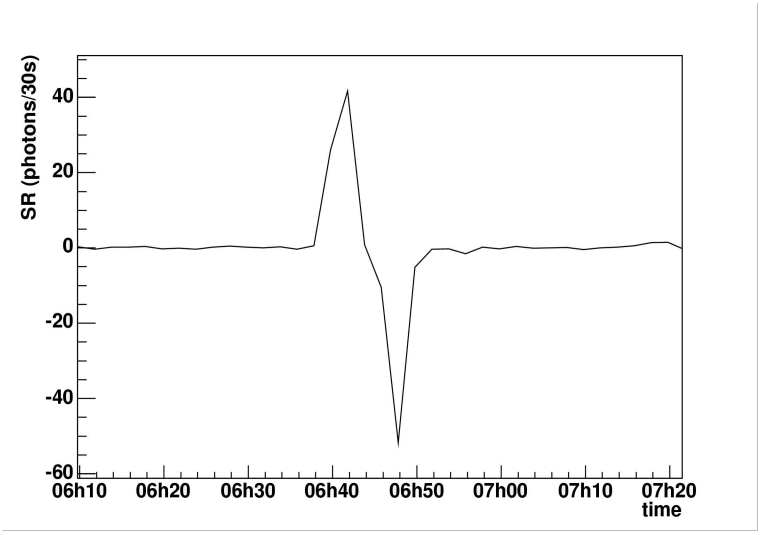

(b)

Figure 4.12: *Los Leones, telescope* 4*, pixel* 77*,* 22 *June* 2004 *(UTAle): signal of Alpha Lyrae. 4.12(a) The signal of Alpha Lyrae is shown; the variance signal has been converted in number of photons at the diaphragm using the conversion constants obtained with the drum calibration; the solid line indicates the mean value of the background noise, the dashed line indicates the mean value* + 3σ *of the background noise. 4.12(b) The increment of the signal of Alpha Lyrae is plotted; the leading and trailing edges of the signal are clearly identified by a positive and a negative slew rate.*

These two methods are complementary in the sense that their efficiency depends on the signal shape and the background trend. The first method works better than the second one if the baseline is highly variable but it is worse for small signals. As shown in Fig. 4.12 both methods work fine for high and clear signals.

For this part of analysis we use a UBV Photometry of Bright Stars catalogue [147] that includes 3777 stars with U magnitude brighter than $U_{mag} = 8$. Because of the presence of the UV filter at each telescope's aperture, we take into consideration only those stars bright enough in U spectral band. We defined $U_{mag} = 3$ as the U magnitude of the faintest star to be accepted. In Fig. 4.13 the number of star signals identified as a function of U magnitude shows that we are sensitive also to fainter stars.

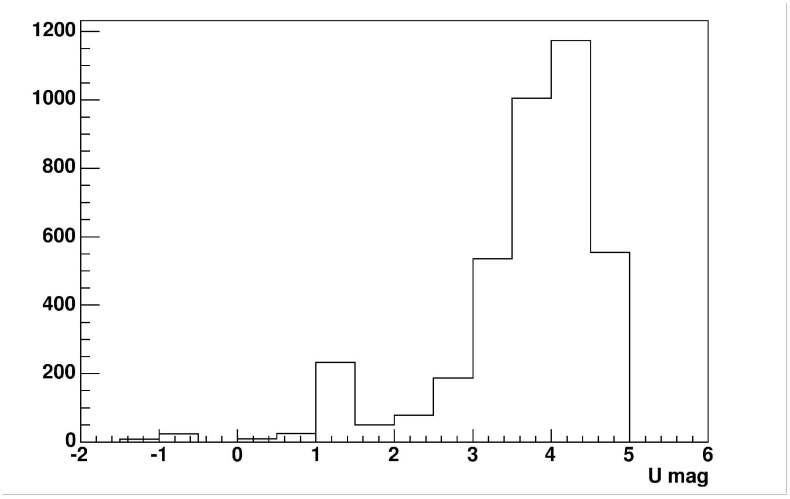

Figure 4.13: *Histogram of star signals identified as a function of U magnitude for the telescope* 1 *at Los Leones.*

When the observation time is long, many signals could be found in a single pixel. Therefore we will have as many pixel's pointing estimations as signals found. The mean value and its statistical error can be calculated from these estimations. The precision in the knowledge of each pixel's pointing will depend on the statistics of stars signals found in each pixel. An example is given in Fig. 4.14 and Fig. 4.15.

Besides the statistical error, we have to consider the systematic error due to the the sampling time equal to 30 s. This produces an uncertainty of 0.125° in determination of the star angular position and, as a consequence, in determination of the pointing of a single pixel. The total error, given by the sum of the squares of statistical and systematic errors and dominated by the latter, was propagated to obtain the uncertainty in the determination of the camera optical axis.

The procedure described here is repeated to determine the pointing of all pixels where at least one signal has been found.

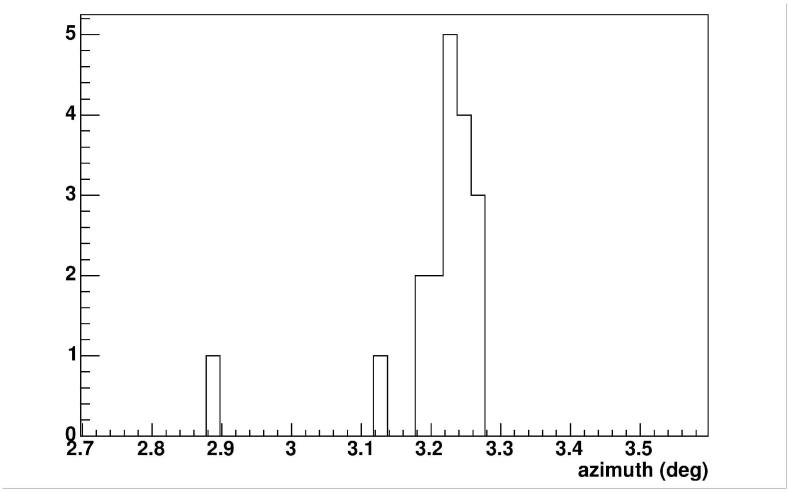

Figure 4.14: *Los Leones, telescope* 2*. The histogram shows the values of the reconstructed azimuth angles for pixel* 388 *from stars signals.*

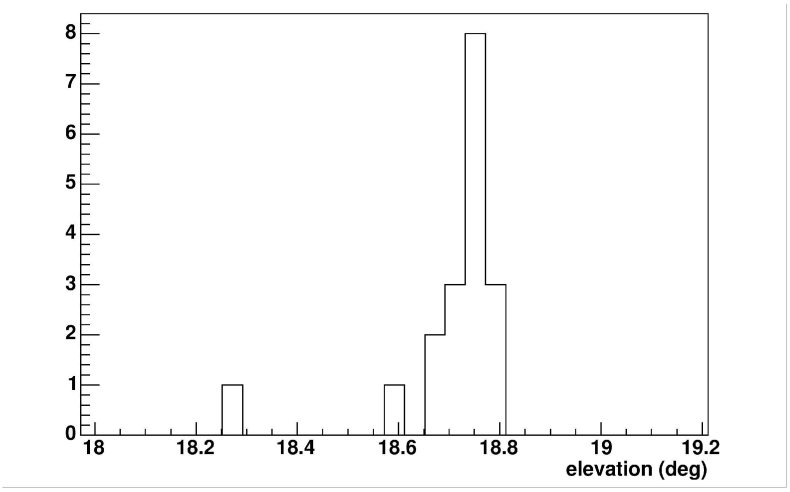

Figure 4.15: *Los Leones, telescope* 2*. The histogram shows the values of the reconstructed elevation angles for pixel* 388 *from stars signals.*

Determination of the camera pointing

As explained in the previous section, after the determination of the pointing of each pixel we are in condition to calculate the pointing of the camera axis simply by inverting the

formulas given originally by [110]:

$$\delta_{j,i} = \arcsin\left(\sin\left(\alpha_j + \alpha_m\right) \cdot \cos\beta_i\right), \tag{4.7}$$

$$\phi_{j,i} = \arcsin\left(\frac{\sin\beta_i}{\cos\delta_{j,i}}\right) + \phi_m, \tag{4.8}$$

where α_m and ϕ_m are the elevation and azimuth angles of the telescope's optical axis in the local coordinate system, $\delta_{j,i}$ and $\phi_{j,i}$ are the elevation and azimuth angles in the sky of the pixel (j,i) and (α_j, β_i) are the angular direction of the pixel (j,i) in the coordinate system centered in the camera (Fig. 4.16).

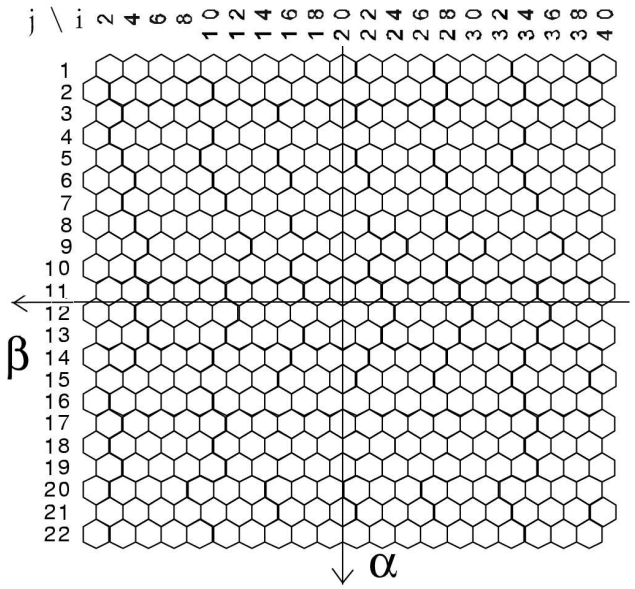

Figure 4.16: 22×20 *pixel matrix shown on the coordinate system centered on the camera* (α, β).

As not all the pixel directions were established with the same number of signals, we have determined, for each telescope, the minimum number of signals (in a single pixel) that minimize the error in the determination of the pointing of the camera axis. In Fig. 4.17 we have plotted the error in the determination of the azimuth optical axis angle for telescope 4 at Los Leones as a function of the minimum number of signals required to use a pixel in our calculations of the camera pointing. As can be seen in Fig. 4.17, a minimum in the error occurs at around 3 signals. In other words, if only pixels with at least 3 signals are used to calculate the azimuth angle of optical axis of the telescope, the error is minimized. The same occurs for the elevation angle. In fact, if the minimum number of signals required is too low (for instance 2), the uncertainty in the knowledge of the directions of the pixels

will lead to a low precision in the determination of the pointing of the camera axis. On the other hand, if the minimum number of signals required is too high (for instance 10), the pixel directions will be known with great accuracy but with detriment of the statistics. Therefore a compromise between high statistics and high precision in the directions of the pixels is needed. This is reached with a minimum number of signals equal to 3 for telescope 4 at Los Leones.

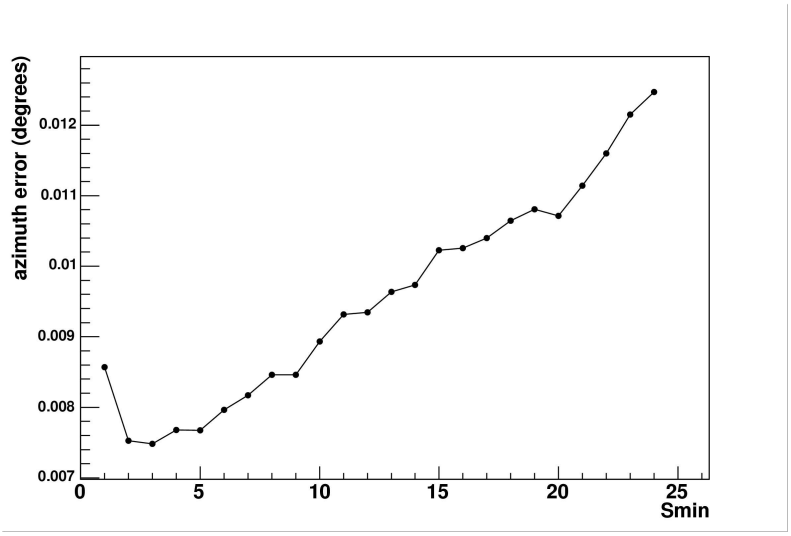

Figure 4.17: *Error Minimization. The plot shows the error in the determination of the azimuth optical axis angle for bay* 4 *at Los Leones as a function of the minimum amount of signals* S_{min} *required for each pixel to be used in the analysis.*

As an example, in Fig. 4.19 and Fig. 4.18, the histograms of reconstructed values of azimuth and elevation angles of telescope 4 at Los Leones and 3 at Coihueco are shown.

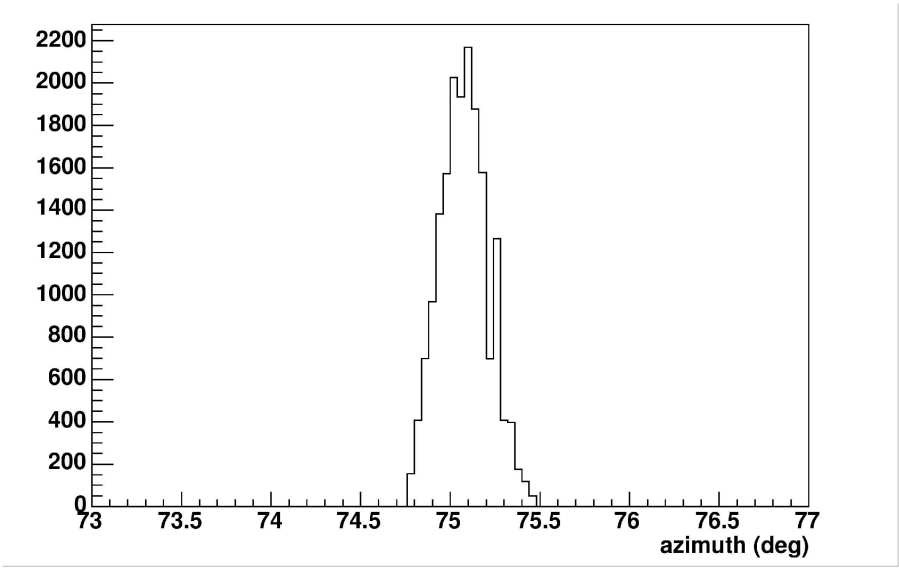

Figure 4.18: Los Leones, telescope 4. Histogram of the reconstructed values of azimuth angle of the telescope optical axis.

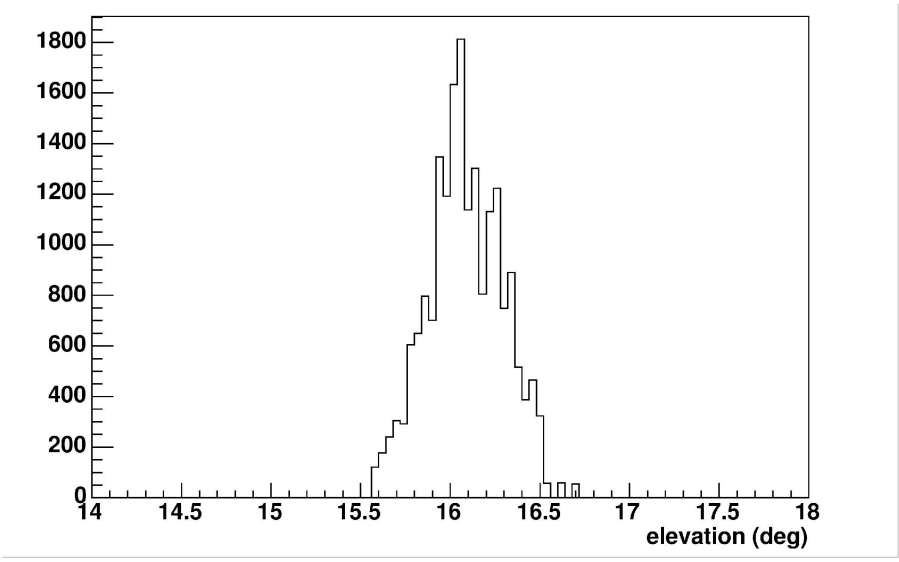

Figure 4.19: Coihueco, telescope 3. Histogram of the reconstructed values of elevation angle of the telescope optical axis.

Pointing results

The procedure described in the previous section has been applied to calculate the pointing of all the telescopes of the fluorescence detector although not all of them were installed at the very same time. After July 2004 the detector started to operate with 12 telescopes, 6 in the Optical Station of Los Leones and 6 in Coihueco. Since April of 2005 also the telescopes of the optical station at Los Morados have been installed. Therefore in this work the pointing was reconstructed with different amount of data, proportional to the time each telescope acquired data (Table 4.2 and 4.3). We have analyzed data from January to October 2004.

Table 4.2: *Los Leones: the rate of signals identified. The rate of those signals are shown for all the telescopes at Los Leones for the whole period analyzed (January – October 2004). The total number of nights and the corresponding total number of hours analyzed are shown in columns* 2 *and* 3. *The total number of signals identified and the number of stars analyzed are shown in columns* 5 *and* 7.

Los Leones: rate of stars signals identified						
Telescope	number of nights	number of hours	hours per night	number of signals	rate (signals/hour)	number of stars
1	70	388.233	5.55	3181	8.19	61
2	71	406.925	5.73	3295	8.10	27
3	119	679.508	5.71	4203	6.19	32
4	110	636.000	5.78	6219	9.78	51
5	109	627.783	5.76	3397	5.41	27
6	115	633.225	5.51	5187	8.19	31

Table 4.3: *Coihueco: the rate of signals identified. The rate of those signals are shown for all the telescopes at Coihueco for the whole period analyzed (January-October 2004). The total number of nights and the corresponding total number of hours analyzed are shown in columns* 2 *and* 3*. The total number of signals identified and the number of stars analyzed are shown in columns* 5 *and* 7*.*

Coihueco: rate of stars signals identified						
Telescope	number of nights	number of hours	hours per night	number of signals	rate (signals/hour)	number of stars
1	34	183.042	5.38	756	4.13	16
2	77	463.133	6.01	1206	2.60	25
3	96	574.917	5.99	9415	16.38	60
4	35	188.725	5.39	2275	12.05	24
5	33	188.225	5.61	3291	17.77	25
6	31	164.283	5.30	997	6.07	24

In this period telescopes 3 to 6 at Los Leones operated around $\sim$ 9 months while telescopes 1 and 2 operated $\sim 3-5$ months. On the other hand, at Coihueco, telescope 2 and telescope 3 operated around 8 months while the others did it around 3 months in the period analysed. These periods must be reduced because of the duty cycle limited to $\approx$ 10% as data are acquired only in moonless nights or at most accepting a moon quarter. The total number of nights and the corresponding total number of hours analyzed for the optical stations at Los Leones and Coihueco are shown in Tables 4.4 and 4.5. Taking into account the effective observational time, the rate of identified signals varies from $\sim$ 5.4 to $\sim$ 9.8 $signals/hour$ for the optical station at Los Leones, from $\sim$ 2.6 to $\sim$ 17.8 $signals/hour$ for the optical station at Coihueco. If the number of stars passing in the field of view of each telescope during the whole analyzed period is taken into account, the rate of signals varies from $\sim$ 0.13 to $\sim$ 0.30 $signals/(hour \cdot star)$ for the optical station at Los Leones, from $\sim$ 0.10 to $\sim$ 0.71 $signals/(hour \cdot star)$ for the optical station at Coihueco. Looking at the rates of each telescope, it seems that for the optical station at Coihueco the rate of identified signals is higher for the telescopes pointing East. This trend is not confirmed by the rates for the optical station at Los Leones.

The detailed results and their errors are shown in Tables 4.4 and 4.5. The total number of pixels reconstructed is also indicated. Columns 4 and 5 in each table show the difference between the results obtained with our analysis and the pointing values specified in the Offline database, used for the shower reconstruction.

Table 4.4: *Results for Los Leones. Columns* 2 *and* 3 *contain the elevation and azimuth errors in the determination of the optical axis direction while columns* 4 *and* 5 *contain the differences between the reconstructed values and the specified ones. Column* 6 *contains the number of reconstructed pixels.*

Los Leones					
Telescope	$Error_{elev}$ (degrees)	$Error_{az}$ (degrees)	Δ_{elev} (degrees)	Δ_{az} (degrees)	Rec.Pixels
1	0.0115	0.0195	0.0694	-0.0800	307
2	0.0131	0.0186	0.0830	0.0506	297
3	0.0195	0.0158	0.0574	0.0471	287
4	0.0218	0.0075	0.0982	0.0782	358
5	0.0281	0.0091	0.0345	0.0830	270
6	0.0197	0.0148	-0.0375	0.0900	284

Table 4.5: *Results for Coihueco. Columns* 2 *and* 3 *contain the elevation and azimuth errors in the determination of the optical axis direction while columns* 4 *and* 5 *contain the differences between the reconstructed values and the specified ones. Column* 6 *contains the number of reconstructed pixels.*

Coihueco					
Telescope	$Error_{elev}$ (degrees)	$Error_{az}$ (degrees)	Δ_{elev} (degrees)	Δ_{az} (degrees)	Rec.Pixels
1	0.0316	0.0237	0.0169	-0.1349	166
2	0.0254	0.0253	0.0999	0.0420	202
3	0.0113	0.0172	0.0844	0.0569	358
4	0.0152	0.0232	0.3053	0.0490	217
5	0.0143	0.0199	0.1810	0.1053	288
6	0.0237	0.0189	0.2867	0.2732	219

4.5.3 Star track optimization method

Processed data — clear nights selection

Variance background data from the period April 2004 — November 2004 were used for this analysis. We have obtained results for all bays operational during this period — it means for 6 bays of Los Leones and 6 bays of Coihueco. Because Coihueco was fully operational only since June 2004, the choice of suitable nights was more limited than for Los Leones.

It is also worthwhile to mention that the bays 4 and 5 at Los Leones and the bays 3 and 4 at Coihueco were equipped with corrector rings during the analyzed periods. The presence of corrector ring influences not only the level of incident light, but also the shape of star image, as it is discussed below.

We tried not to bias data with star signals diminished or otherwise modified by cloud moving through the studied pixel. Therefore we tried to select only really clear nights without clouds. For this reason we used Adelaide database [140] of cloud camera images and manually selected only completely clear nights from given period. Only 10 nights for Coihueco and 15 nights for Los Leones surpassed this cut.

Schematic description of the method

The analysis program was designed to process automatically the background data. The initial idea was just to select some basic criteria and data file, run the program and directly obtain the offset of the camera. The set of necessary starting criteria (or program input parameters) is rather small, actually within our program we select only the bay analyzed, the magnitude of faintest star, which still has to be tracked, and a number of parameters of camera offset (i.e. x offset, y offset only, eventually also camera rotation.) This third parameter — camera rotation — finally turned out not to be an important one. We processed several nights also with camera rotation parameter and all rotation offsets found were negligible. This agrees well also with camera alignment method, where was possible to measure (and remove) the camera tilt very precisely.

To achieve such goal, the designed method has to be able to:

- Automatically find and select the brightest stars with sufficiently long trajectories across the camera during selected night.
- Read the variance data from background files for each pixel of the analyzed camera, together with timestamp.
- Identify star signals within background data and compare them with computed expected signals.
- And finally — shuffle with the camera center position and try to optimize the found difference between the data and expected signals.

Star catalogue used

We used the Bright Star Catalogue (BSC) [135] as the database. This catalogue contains basic astronomical and astrophysical data for all 9096 stars, which are brighter than 6.5 magnitude. Using available data for each star we computed its magnitude in Johnson's U-band, which has almost the same spectral properties as the filter used in the window of all FDs (Schott MUG-6 filter).

Then we sorted the catalogue according to star brightness in U-band and cut off all unnecessary information. Only the star name, Henry Draper catalogue number, magnitude

in U and V band, right ascension and declination coordinates, values of proper motion of the star and the information about possible star variability were retained.

Such form of the catalogue is then suitable for fast and efficient search for the brightest detectable stars[5] (for the given night and selected camera, as was described above) and provides all information needed from the astronomical point of view.

Observable stars

As described above, the variance analysis allows us to determine the incoming background light flux to individual pixels. The typical level of variance for clear moonless night is of about 20–25 (ADC counts)/100 ns for bay without corrector ring or of about 30–35 (ADC counts)/100 ns for bay equipped with corrector ring. More detailed analysis of this sky background light level is done in [69] (for data from Los Leones prototype telescopes). Here we remark that e.g. from absolute drum calibrations [62] it follows that we have roughly 4 photoelectrons per one ADC count.

When the image of a star is projected on studied pixel, the variance increases. The amplitude of this increase depends on the pixel position on the camera — the lower pixels suffer much more prominent losses due to atmospheric extinction (total airmass X for lowest part of the camera is of about 20, for the uppermost part $X = 2$). If we want to analyze the whole star tracks across the camera, then we have to concentrate on those bright stars, which are visible also in the lower part of the camera. From empirical analysis it follows that for stars fainter than 4^{th} magnitude the signal increase is almost negligible (e.g only about 1 (ADC count)/100 ns for star ϱ Gem ($mag_U = 4.47$) at an altitude of 3.5°).

Therefore we concentrated only on the brightest stars in the sky — the stars which are brighter than 2.0 mag in U filter, which have significant offset from sky background also in lower parts of the camera and which are much less biased by intensity fluctuations (see 4.5.3).

Star positions on the sky

Stars are very suitable sources for camera alignment checks, because their positions on the sky could be determined with very high precision.

From BSC catalogue we know star coordinates in equatorial coordinates, so we used standard coordinate transformations to obtain the horizontal coordinates of stars. Before doing so, we applied the correction for Earth precession (effect up to 0.1° for the analyzed period). The star proper motion has a negligible effect of about 0.001°. The coordinate shift due to precession is described by the following equations:

Correction for right ascension α in arcseconds:

$$\Delta\alpha = 46.125 + 20.04 \sin(\alpha) \tan(\delta) \tag{4.9}$$

[5]There are 6 stars brighter than zero magnitude, 24 stars brighter than the first magnitude and 63 stars brighter than the second magnitude — all in the U band and for the whole sky.

And correction for declination δ in arcseconds:

$$\Delta\delta = 20.04 + \cos(\alpha) \tag{4.10}$$

It is very important to include also the effect of atmospheric refraction, which could result in shift of about 0.3° in height above the horizon for the lowest camera pixels. The refraction is generally dependent on pressure ϱ, on air temperature T, on the altitude of the observation site above the sea level h — and on non-homogeneous layers in atmosphere[6].

There are precise numerical models ofrefraction assesment based e.g. on US standard model of atmosphere, which include also the refraction dependence on the light wavelength. However, for our purposes the most important is the dependence on immediate pressure and temperature, which was not directly available from Auger atmospheric database during the time of data processing. Therefore we have decided to use only the Meeus empirical analytical model [172] of atmospheric refraction with fixed pressure ($p = 860$ millibars) and with temperature T estimated on the basis of calendar date of given observation night (sinus-like function with a maximum reaching 293 K in January and with a minimum at 273 K in July).

The equation describing the change in height above the horizon a (in degrees) follows:

$$\Delta a = [r - 0.06\sin(14.7 + 13)]\,\frac{1}{60}\,\frac{p}{1013}\,\frac{283}{T}, \text{ where} \tag{4.11}$$

$$r = \frac{\sin\theta}{\cos\theta}, \text{ and} \tag{4.12}$$

$$\theta = a + \frac{7.31}{a + 4.4} \tag{4.13}$$

Intensity scintillations

When we observe the signal of star traversing one pixel (for the star image fully contained within this pixel) then we observe also intensity fluctuations of such signal. The amplitude of these fluctuations is roughly ranging from 10 to 20%.

There are two reasons of star intensity fluctuations. The first one is that the photocathodes do not have homogeneous sensitivity across their surfaces. As it is discussed in next paragraph, the angular diameter of one pixel is about 1.5° and the angular diameter of star images is about 0.5°. When the star traverses a pixel, it goes through regions of different cathode sensitivity and signal could vary for up to 20 %.

The second reason is a little bit more delicate. We integrate the signal from the star for 6 ms and this interval agrees well with the fastest major frequency of star scintillation [88]. Star intensity scintillation origins due to fast movement of atmospheric layers especially in heights 12–16 km (the incident wavefront of light from the star is not only tilted[7],

[6] Without direct dedicated measurements we are not able to model the appearance and influence of such layers. Unfortunately, their effect could be rather pronounced, but only for lowest part of the sky, say up to 5 degrees above horizon. In these regions they can increase the overall refraction twice to three times.

[7] This angular displacement results in another famous astronomical phenomena — in the so-called *seeing* — the image of the star is blurred to the disc with diameter much larger than is the canonical resolution of the telescope.

but also curved and therefore focused —or defocused— and so star intensity changes). These intensity scintillations mostly depend on the star altitude (effect increases roughly with third power of secants of distance from zenith and saturates about 20 degrees above horizon) and on the the telescope aperture (effect is roughly inversely proportional to the diameter of the telescope). For our purpose (observation below 30° above horizon with telescope aperture of about 2 meters) we can estimate the effect of scintillation to be 10–15 %.

Star images on the camera

The focal surface of the telescope is spherical and therefore the edge-to-edge setup of individual PMTs was not possible. Moreover, the sensitive photocathode surface of PMT is smaller than its glass envelope and there are also mechanical reasons to leave some gaps between PMTs. The reflective edge-shaped plastic inserts were applied to eliminate the insensitive areas between PMTs. Then almost all the incident light is reflected onto some PMT and the focal surface is continuously covered.

The geometry of the camera was described in detail above in section 4.5.2, including the equations necessary for transformations of alt-azimuthal coordinates to *camera coordinates* and back. The angular size of each PMT is about 1.5° for inscribed circle into PMT hexagon. From this fact we can derive that one star could influence the signal from up to three pixels simultaneously.

Light spots

The shape of the spot is not precisely circular, it is deformed by the shadowing of the camera body, by spherical aberration and by the use of a corrector ring on some telescopes. More precisely, the spot deformation is more prominent for the cameras without a corrector ring. This spot shape deformation could result in shift of spot intensity center of up to 0.1°. It is possible to model this star image displacement and then to include this effect into camera offset evaluation, as it was done within this work.

For the spot shape simulation we have used first the Fortran program [190], which simulates the trajectories of light rays through different parts of the aperture according to the rules of geometrical optics. Because the optical system of the camera is not the ideal one, the sufficient number of rays (about 100 000 in our case) coming from specified direction and covering whole aperture will draw for us the spot shape. We run the program for 440 positions of pixels. For these resulting 440 spot shapes we computed the intensity center of each spot and compared its position with position of pixel center (the direction of pixel center was the original direction of incident light rays). Then we plot the resulting offsets (as is shown on Fig. 4.20). We realized that this behavior could be easily modelled under assumptions that the spot center offset is directly proportional to the distance from the camera center (in camera coordinates, evaluation described in 4.5.2. The shift of spot center in horizontal x-coordinate (where x denotes the angular distance from camera center

in camera coordinates) is (in degrees):

$$\text{With corrector ring: } \Delta x = 1.002x \tag{4.14}$$

$$\text{And without corrector ring: } \Delta x = 1.0033x \tag{4.15}$$

And for vertical y-coordinate is then valid:

$$\text{With corrector ring: } \Delta y = 0.998y \tag{4.16}$$

$$\text{And without corrector ring: } \Delta y = 0.9967y \tag{4.17}$$

The difference between our model and between simulation results is less than 0.01° for the bays with corrector rings and less than 0.02° in case without corrector ring, which we take as acceptable. The model results are again shown on Fig. 4.20.

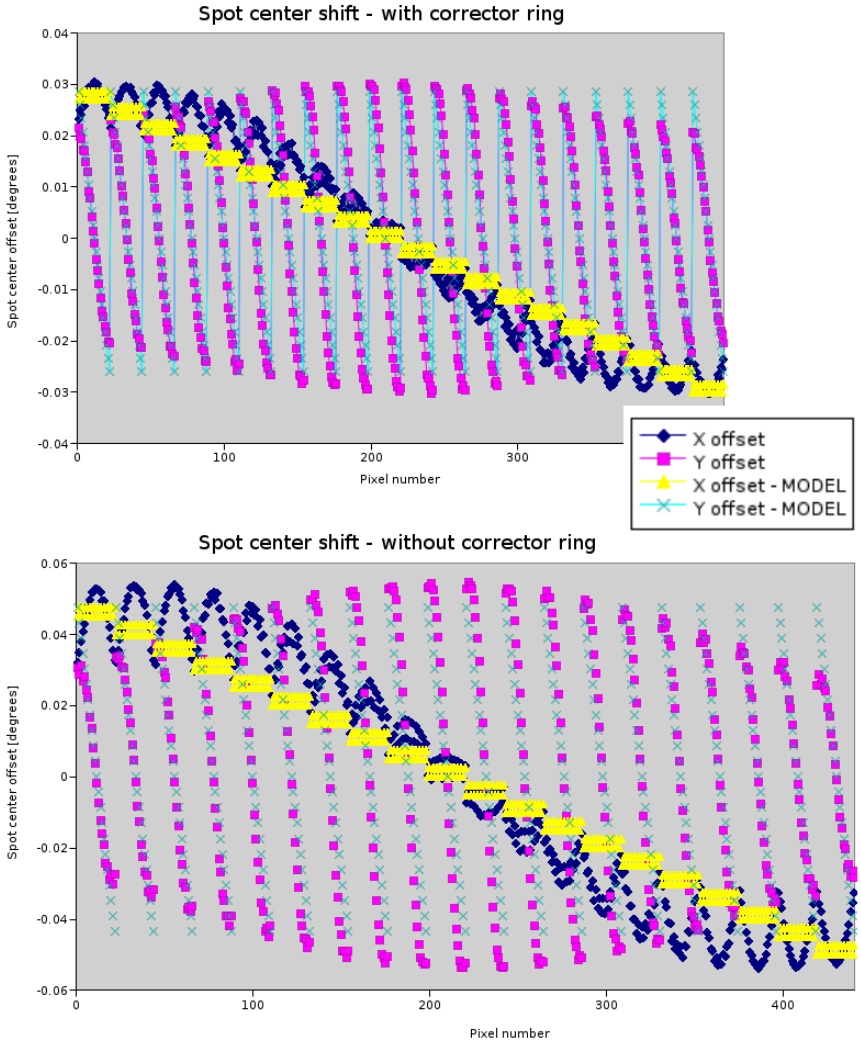

Figure 4.20: *Spot shape results and model*

Star tracks and transits between pixels

We can follow the star passing over the camera and quite easily identify the pixels with increased signals due to the light of a star. In other words, we can plot a star track over the camera. An example of several such star tracks is given in Fig. 4.21.

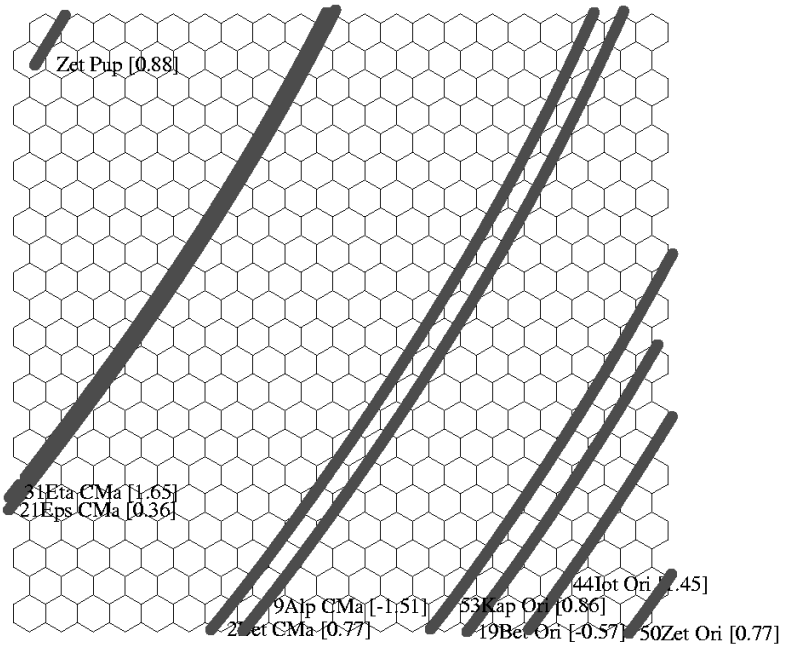

Figure 4.21: *Typical set of star tracks. Imaged tracks are for Los Leones FD camera, bay 1, for the night of November $13^{th}/14^{th}$ (21h UT – 07h UT). Only the stars brighter than 2^{nd} magnitude were plotted.*

Furthermore, we can identify the instants, when the star spot center (SSC) transits from one pixel to next neighboring one. These moments of SSC transit are crucial for our analysis. We expect that before this moment the variance of the first (old) pixel is higher than that of the second (new) pixel and that after this moment the variance of old pixel is lower than variance of new pixel. We can add here that by tracking of SSCs we naturally solve the problem of the cases, when the star image is projected simultaneously to 3 pixels. The SSC as a point everytime transits across the pixel boundary from one specific pixel to another specific (neighboring) pixel.

Knowing the precise position of a given star on the sky and knowing the correction due to SSC offset, we can transform this position to camera coordinates and compute the moment, when the star is crossing the boundary between hexagonal pixels. We can compute such instants for all affected camera pixels — we can identify the times of transits of spot center for the whole star track across the camera.

Star track optimization method

As we described above, we are able to compute the trajectory of SSC across the given FD camera and also to compute the time of transits of this SSC from pixel to pixel.

Furthermore, we are able to identify these transits between pixels in the real background data. In our method we analyze the data from about 180 seconds ahead expected transit to about 180 seconds after expected transit. During this period we check if there is greater variance at least for two consecutive samples on the first ("old") pixel than on the second ("new") pixel. The necessary offset[8] of both signals is at least 1 (ADC count)/100 ns. Such period has to be immediately followed by two consecutive data samples, where the situation is opposite — star already traversed to "new" pixel. So, these two consecutive signals on the new pixel have to be greater at least by 1 (ADC count)/100 ns than the signal in "old" pixel. The star transit is then expected to occur between times of this intensity switch. The exact moment is analytically computed as the crossing of interpolated signals of "old" and "new" pixel (the signal values surrounding the instant of this transit are used for interpolation).

We then have both predicted times of transits and also detected times of transits in the data for the whole track. For these times we can easily calculate $\Sigma\chi^2$ and use it as our main optimization parameter. Having this initial value we can start shuffling with the camera center on the regular grid.

We used shuffling +/- 0.5° around nominal center of the camera on the regular grid with steps of 0.025°. Doing this, we are looking for the least average time offset for the whole track. Of course, during shuffling, we compute again and again new times of transits between pixels — we can even found completely new transits between previously unaffected pixels. As the second parameter we also check the number of transits detected in background data, which of course could be larger than the starting number of detected transits, but should not be much smaller than initial one. Actually, we use condition, which rejects the new resulting shuffled tracks, if the new trajectory would diminish the number of transits by more than 4. The typical results of one star track optimization are shown on Fig. 4.22, where all time differences from shuffling grid are plotted. As it is explained in figure caption, we are looking for some sort of anti-correlations — for regions with low $\Sigma\chi^2$ and high number of pixels of the star track.

[8]The typical offset was generally much greater for the set of chosen bright stars. We tested also different minimal offset values during method development, however we found no significant difference in results, so we used this relaxed version of condition in final implementation, which proved to be only a little more sensitive for signal detection in the lowest parts of the cameras.

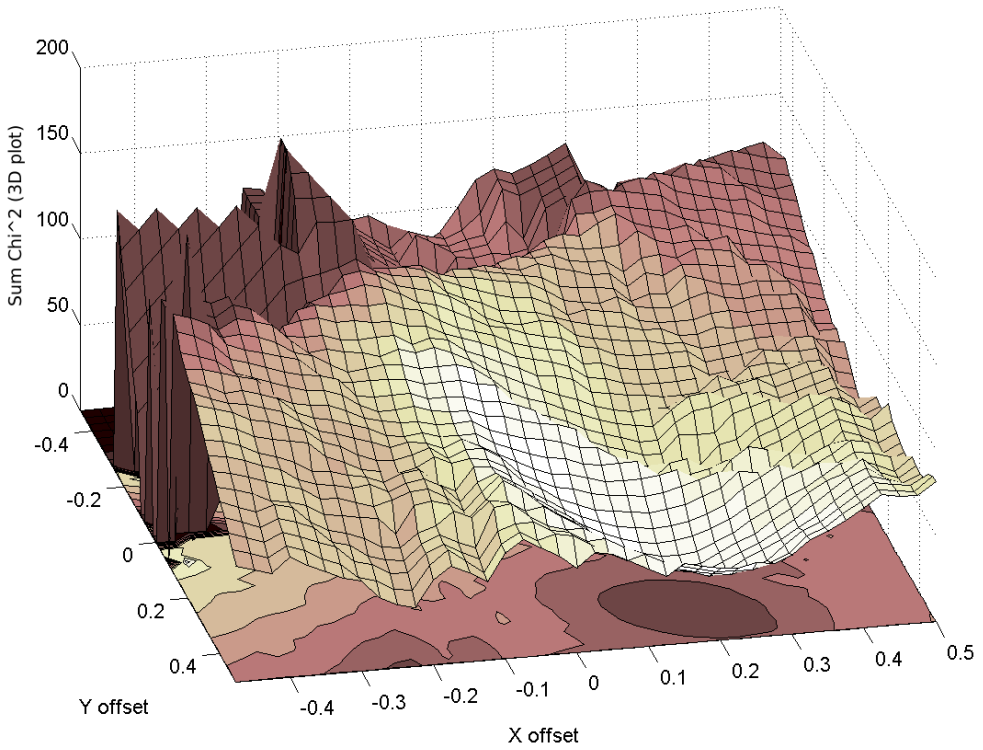

Figure 4.22: *Star track optimization — graph for one chosen star (β Ori). The contour plot on the bottom plane shows that the optimized offset is of about 0.2° on x axis and of about 0.3° for y axis. The darker areas indicate here the regions with smaller differences between detected times of transits and predicted times of transits, lighter areas are for greater time difference. The 3D plot above shows the same thing — deepest valley is for the least difference of time offset. However, the coloring is different — light colors indicate large number of detected star transits, dark colors indicate very low number (or even zero) of successfully detected transits.*

Results

The results of our analysis are summarized in Table 4.6. The final offset of each camera was computed as the weighted average of all optimal offsets associated with successfully identified star tracks for sample of selected nights. The star track was considered as successfully identified if it contained more than 9 transits between pixels. Shorter tracks were not used. The optimized camera offset was computed for each track and as the weight was used the number of detected transits for this optimized track. The statistical error, also shown in following table, was then computed as weighted standard deviation of individual track offsets.

Table 4.6: *The values in the table are in degrees, according to the Auger conventions (elevation increases from horizon ($elevation_{horizon} = 0°$), azimuth increases counter-clockwise from east ($azimuth_{east} = 0°$). The differences of reconstructed (optimized) minus nominal values for the cameras are shown in the tables:*

Los Leones	Bay 1		Bay 2		Bay 3	
	Value	*St.dev.*	*Value*	*St.dev.*	*Value*	*St.dev.*
Azimuth	-0.13	0.07	0.00	0.10	0.07	0.05
Elevation	0.05	0.08	0.06	0.12	-0.03	0.07

Los Leones	Bay 4		Bay 5		Bay 6	
	Value	*St.dev.*	*Value*	*St.dev.*	*Value*	*St.dev.*
Azimuth	0.09	0.06	0.07	0.03	0.10	0.05
Elevation	0.06	0.08	-0.04	0.05	-0.16	0.08

Coihueco	Bay 1		Bay 2		Bay 3	
	Value	*St.dev.*	*Value*	*St.dev.*	*Value*	*St.dev.*
Azimuth	-0.13	0.03	-0.07	0.04	0.04	0.09
Elevation	-0.06	0.05	0.19	0.05	0.15	0.05

Coihueco	Bay 4		Bay 5		Bay 6	
	Value	*St.dev.*	*Value*	*St.dev.*	*Value*	*St.dev.*
Azimuth	0.07	0.07	0.04	0.10	0.22	0.05
Elevation	0.27	0.06	0.17	0.12	0.23	0.03

4.5.4 Comparison of both methods and discussion

The above mentioned results of both methods are in good agreement. All differences are within estimated σ overall error of both methods, as it is discussed below. The actual differences are given in Table 4.7.

Table 4.7: *All values are shown in degrees, according to the Auger conventions (elevation grows from the horizon, azimuth grows CCW from the east), shown are differences of reconstructed minus nominal values. The 'single pixel method' is indicated as 'Single' in the column headers, similarly each value for 'star track optimization method' has 'Track' in the header. The third (boldface) column for each bay contains absolute difference of values for these two methods:*

Los Leones	Bay 1			Bay 2			Bay 3		
	Track	*Single*	*Diff.*	*Track*	*Single*	*Diff.*	*Track*	*Single*	*Diff.*
Azimuth	-0.13	-0.08	**0.05**	0.00	0.05	**0.05**	0.07	0.05	**0.02**
Elevation	0.05	0.07	**0.02**	0.06	0.08	**0.02**	-0.03	0.06	**0.09**

Los Leones	Bay 4			Bay 5			Bay 6		
	Track	*Single*	*Diff.*	*Track*	*Single*	*Diff.*	*Track*	*Single*	*Diff.*
Azimuth	0.09	0.08	**0.01**	0.07	0.08	**0.01**	0.10	0.09	**0.01**
Elevation	0.06	0.10	**0.04**	-0.04	0.03	**0.07**	-0.16	-0.04	**0.12**

Coihueco	Bay 1			Bay 2			Bay 3		
	Track	*Single*	*Diff.*	*Track*	*Single*	*Diff.*	*Track*	*Single*	*Diff.*
Azimuth	-0.13	-0.14	**0.01**	-0.07	0.04	**0.11**	0.04	0.06	**0.02**
Elevation	-0.06	0.02	**0.08**	0.19	0.10	**0.09**	0.15	0.08	**0.07**

Coihueco	Bay 4			Bay 5			Bay 6		
	Track	*Single*	*Diff.*	*Track*	*Single*	*Diff.*	*Track*	*Single*	*Diff.*
Azimuth	0.07	0.05	**0.02**	0.04	0.11	**0.07**	0.22	0.27	**0.05**
Elevation	0.27	0.31	**0.04**	0.17	0.18	**0.01**	0.23	0.29	**0.06**

General considerations

The offsets are generally larger for elevations of the camera than for the azimuthal settings. This is basically what was expected from camera alignment methods. The azimuth measurements are done using two brass reference points on the floor and using plumb line going from the hole in the camera body. The plumb line has to point to the line which connects both brass reference points. The direct camera elevation measurements are done using inclinometer and they are not so precise. During camera alignment also an indirect elevation measurement is used, based on laser distance-meter measurements of camera corners and from the height measurements from the floor. Unfortunately, also these height measurements are not so precise, because the floor is not planar and horizontal to desired precisssion.

There is a simple rule of thumb, which one can use to check roughly the results. For example for Coihueco bay 4 we found the average time difference (between predicted and measured time of transit) of about 80 second. In such a case we can expect 80/(4*60) =

0.3° total offset[9], what generally agrees. Resulting optimized offsets are not precisely zero, but their magnitudes are much reduced compared to the original time offsets. Actually, the resulting offsets are generally about 10–20 seconds, what well agrees with the intrinsic error of the method (10–20 seconds of time offset agrees to less than 0.1° angular offset).

Such estimate of overall error of the method is maybe too rough. The conservative approach will be following: Until we were dealing only with the statistical error and it is quite hard to correctly estimate the systematic error. We think that an estimate of systematic error could outgo from the data sampling period, which is 30 seconds. 30 seconds then agrees with 0.125° star position uncertainty on the sky. So the overall error of the method could be estimated like: $\sqrt{(0.125^\circ)^2 + (0.05^\circ)^2} = 0.13^\circ$, where 0.05° is average statistical error of both methods.

We also tried to estimate how the atmospheric refraction has influenced our results. We processed star track optimization method for this purpose again. During this analysis we omitted the lowest part of the camera (below 10° above the horizon) and we have used only the parts of star tracks in the upper part. However, the results were almost identical (the differences were less than 0.01°) and also the difference of statistical variance was very small.

Analysis of lightcurves

Finally, we would like to present here a simple exercise, which can test the presented method and crosscheck the found results. We can track some bright stars through the given camera and read out the values of variances from pixels, which are closer than 0.5° to the center of the star (it means the values of 1 up to maximum 3 pixels). Than we subtracted the "sky background" value for each pixel. This background was calculated as the average of signals from a given pixel some time before and after the star transit (we generally used averages of 15 minutes before and 15 minutes after the period of time, when the star was traversing the pixel). The sum of corrected signals from all contributing pixels can be then plotted as a function of star altitude.

One would expect, that we will plot — as the star is rising up on the sky — approximately a line slowly growing with the growing altitude. The sum of the signal from all the illuminated pixels (by the spot of the star) has to be almost constant (or slowly growing with altitude); probably there could be some smaller bumps due to influence of reflective plastic inserts or some changes due to sudden changes of atmospheric extinction.

However, such results are not obtained for the original directions of the cameras. This is presented in the upper plot of Fig. 4.23, where an example is plotted for the bay 4 at Coihueco. We can see that for some positions of the star image on the camera we even do not see the correct pixels and consequently we observe almost no signal.

For the optimized position of the camera (lower part of Fig. 4.23) the situation is generally much better, the resulting curve is more or less a straight line. This could be taken as some proof that our results indicate real offsets of camera centers.

[9] A star traverses 15° in one hour or 1° in 4 * 60 = 240 seconds.

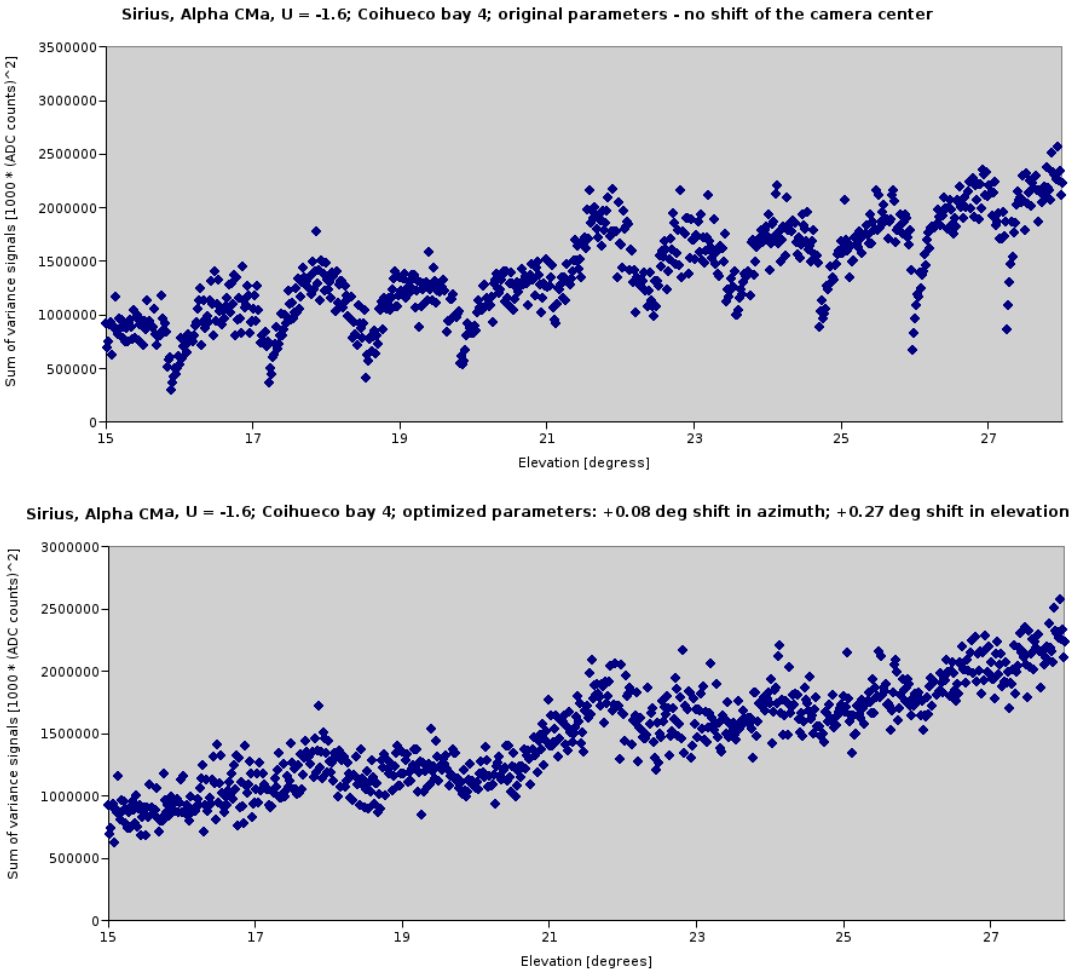

Figure 4.23: *Comparison of lightcurves for original and optimized camera positions of Coihueco bay 4. The data used for the plot are from November 14th 2004 — taken with higher sampling rate 0.2 Hz (instead of ordinary 0.03 Hz sampling rate).*

4.5.5 Summary and conclusions

Another independent check of a telescope pointing could be obtained using laser shots from the Central Laser Facility (CLF). Such analysis was done by two Auger groups. First, the Adelaide working group [45] analyzed the vertical shots for a selected bay — Los Leones bay 4 — and concludes that the telescope pointing is consistent with our star-tracking results. Second, the Prague group made analysis for the inclined laser shots [229], for several selected bays at Coihueco, an example showing the results for Coihueco bay 4 is in Fig. 4.24. As could be clearly seen, the reconstructed shower parameters match much better our values for telescope pointing rather than nominal values.

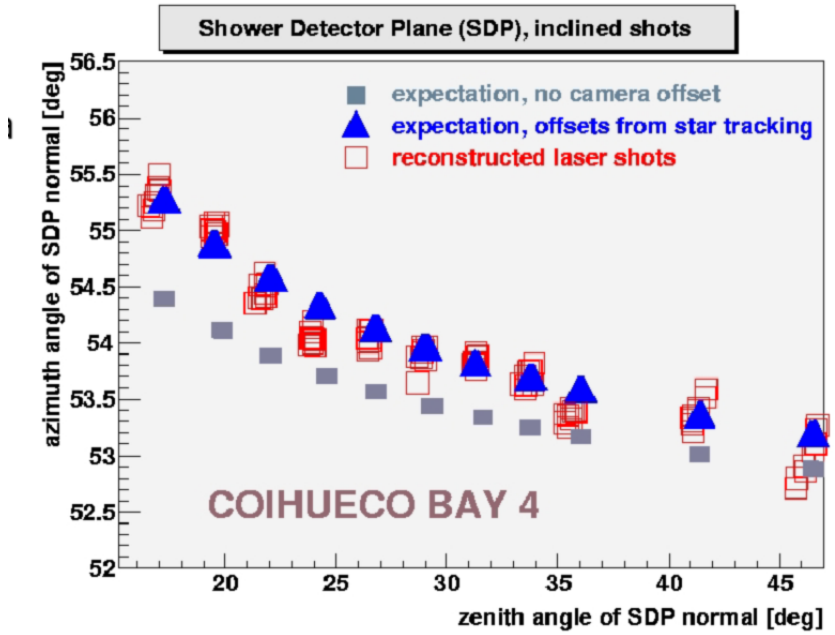

Figure 4.24: *Shower Detector Plane (SDP) for reconstructed inclined laser shots compared with the expectations derived from laser nominal directions. Two expectations are given for: a) no FD camera offsets and b) offsets calculated by star tracking method. From [229].*

We have used star signals to determine the pointing of the optical axis of the fluorescence detector's telescopes of the Pierre Auger Observatory. The differences between our results and the nominal values specified for the FD are less than 18′ and for almost all telescopes are less than the precision of the procedure to determine the pointing of the telescopes, which is 0.1°.

Knowledge of correct pointing directions is essential for the use in the Auger's unique hybrid event reconstructions and for all comparisons with SD geometric reconstructions of those same events. Our methods allow us to go forward with these types of analysis.

Using our above described methods we are now also prepared to monitor easily the long-term stability of measured pointing directions.

4.6 Calibration

4.6.1 Current systematic uncertainties

The signal detected at the FD cameras is converted to the number of 375 nm-equivalent photons arriving at the telescope diaphragm as a function of time. The systematic error in this transformation, which is given as a combination of systematic effects measured by relative and absolute FD calibration, is currently 12 %.

The amount of light emitted at the shower track is calculated using the shower geometry, the known atmospheric conditions, the spectrum of the light and the detector s relative

wavelength response. Using an iterative procedure we take account of the direct and scattered Cherenkov light measured by the FD [182]. The resulting fluorescence light at the shower track is converted to the energy deposited by the shower by applying the expected fluorescence efficiency at each depth. As we mentioned above, the overall uncertainty in the transformation from photons at the detector to emitted fluorescence photons is of the order of 12 %. The application of the fluorescence yield currently includes a systematic uncertainty on the absolute yield of 13 % (see [181]), and systematics related to the pressure (4 %), temperature (5 %) and humidity (5 %).[10]

The integral of the shower energy deposit profile provides a calorimetric measure of the cosmic ray energy. A small correction is made for unseen energy — an energy-dependent correction of 5–15 % with a systematic uncertainty of about 3 %.

All these factors combined together contribute to current overrall systematic error of FD energy estimation of 25 %.

4.6.2 Absolute calibration

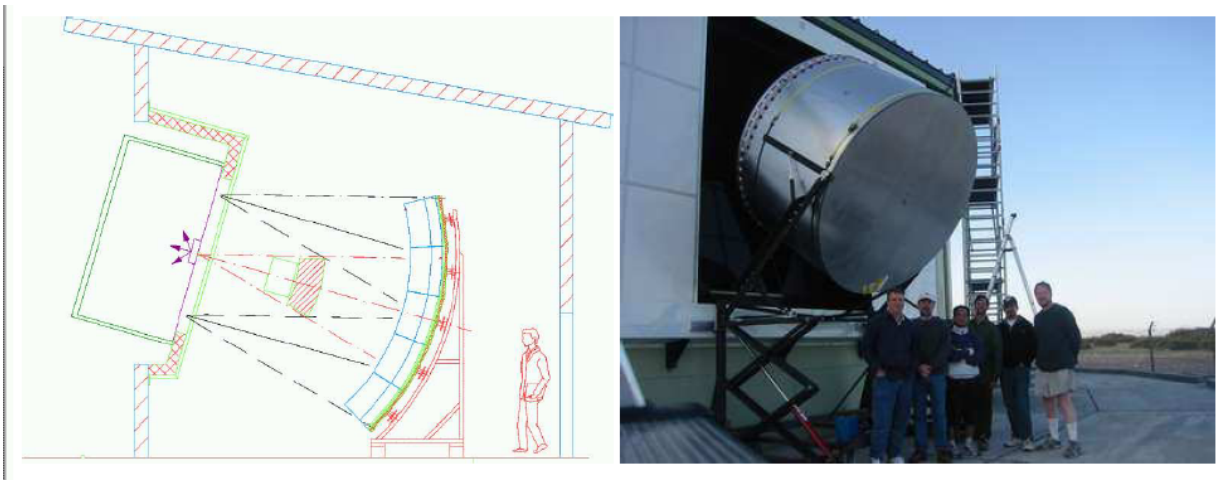

Figure 4.25: *A schematic showing the drum mounted in a telescope aperture, and a picture of the drum being raised into position. From [39].*

To perform an absolute end-to-end calibration of a telescope, a large homogeneous diffuse light source was constructed for use at the front of the telescope diaphragm. This diffuse light source has the shape of a drum, and has a diameter of 2.5 m. The light flux emitted by the drum at the diaphragm is known from laboratory measurements. The ratio of the drum intensity to the observed signal for each PMT gives the required calibration. At present, the precision in the PMT calibration using the drum is about 12 %, and is performed at a single wavelength of 375 nm. The precision will be improved and calibrations will be

[10]For further discussion of these atmospherics factors see chapter 5.

performed at other wavelengths. The drum is also used to adjust gains for uniform response of the pixels. Currently, such absolute calibration is proceeded every three months.

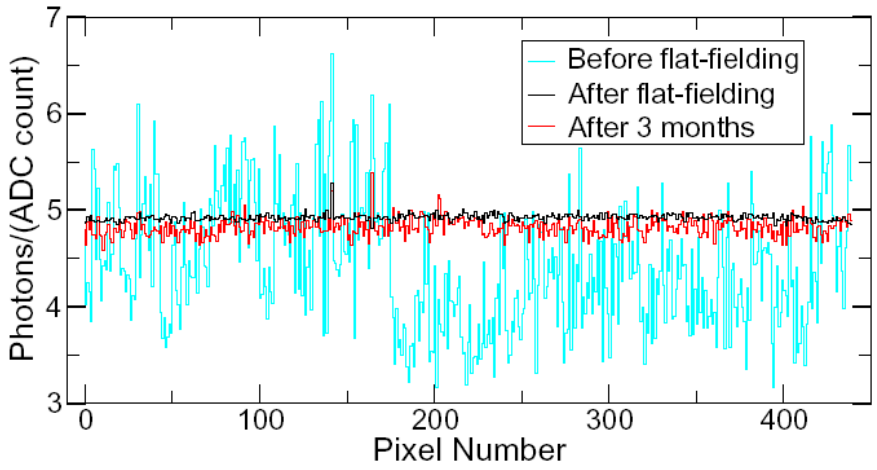

Figure 4.26: *The effects of drum calibration on the 440 pixels of the camera in bay 5 at Los Leones. Blue: as commissioned; Black: immediately after calibration; Red: typical variation seen during next calibration. From [39].*

4.6.3 Relative calibration

Optical fibers bring light signals to three different diffuser groups for each telescope:

- **Calibration A** — The end of the optical fibre is installed at the centre of the mirror to illuminate each camera. For this purpose, optical fibres distribute light from a super-bright LED array (470 nm) to the diffusers which illuminate the cameras in the same FD building simultaneously. Part of the LED light is directed by a fibre to a monitoring photodiode. A LED Calibration Unit (LCU) drives the LED array with programmable current pulses, and records the photodiode signal.

- **Calibration B** — Two xenon flash lamps are coupled to optical fibers to distribute light pulses to different destinations, first of them leads to the each telescope, to the lateral edges of the camera body facing the mirror.

- **Calibration C** — The second xenon lamp light is distributed through optical fibers again to each telescope. The ends of these fibers are now facing two reflecting Tyvek foils glued on the inner side of the telescope shutters. It means, that the light from this flasher has to go through the filter in the aperture first, then reflects from the mirror and finally it is detected by the PMTs of the camera.

Only the results of Calibration A — calibrated LED light measurements were already fully processed and used to estimate systematic errors. Actually, the total charge per pixel is measured with respect to reference measurements made at the time of absolute drum calibrations. This allows the monitoring of short and long term stability, the relative timing between pixels and the relative gain of each pixel.

This obtained relative calibration information is not yet fully incorporated in the reconstruction system. However, the average detector stability has been measured and a corresponding systematic uncertainty of 3 % has been introduced to account for this. This contributes to the overall 12 % systematic uncertainty in the FD calibration.

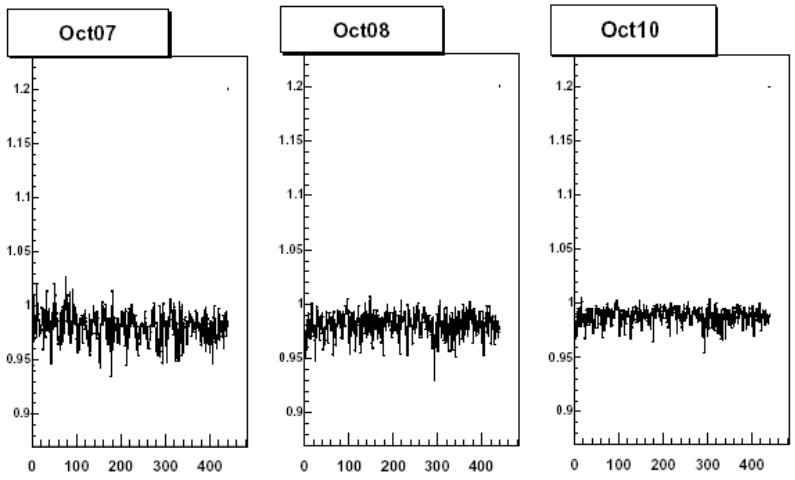

Figure 4.27: *Typical relative calibration constants from calibration A versus the telescope pixel number 1 to 440. The constants fluctuate around 1.0 for all days of the 2004 October shift (October, 7-26). From [15].*

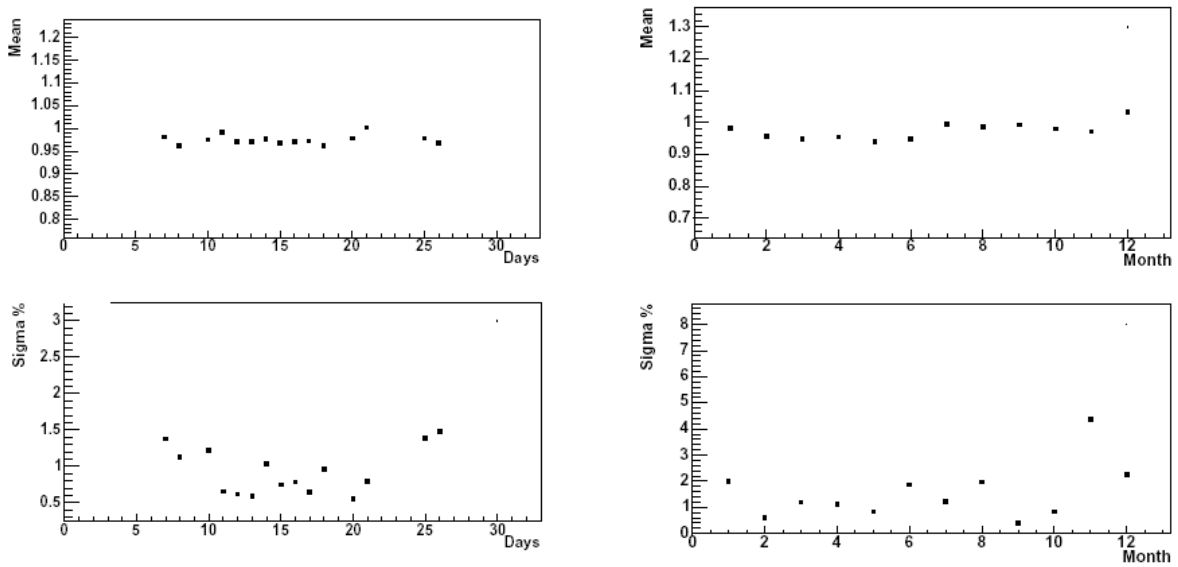

Figure 4.28: Left panels: *Daily averaged relative calibration constants from calibration A for telescope No. 2 in Los Leones during the measuring period in October 2004.* Right panels: *Monthly averaged relative calibration constants from calibration A for telescope No. 4 in Los Leones during the year 2004. From [15].*

4.6.4 Cross-check of the end-to-end calibration

Cross-checks of the FD calibration can be made by reconstructing the energy of laser beams that are fired into the atmosphere from various positions in the SD array. Laser beams are fired to the sky with known geometry and energy. Part of the laser light is scattered by the atmosphere (Rayleigh and aerosol scattering) and this scattered light is detected by the FD telescopes. Using the measured signal and knowledge of the scattering parameters, it is possible to estimate the laser energy for comparison with the real laser energy. The observed difference between the reconstructed energy and the real laser energy is of the order of 10 % to 15 % [19], consistent with the current level of uncertainty in calibrations and knowledge of the atmosphere.

Chapter 5

Atmospheric Monitoring

The calibration of the whole detector is crucial issue. Because the precise energetic reconstruction of cosmic ray showers is one of the main goals of the project, for the usage of fluorescence telescopes we need to know very precisely the immediate status of the atmosphere, especially its extinction — to able to determine how much fluorescence light was lost on its way from the shower to the telescope.

The atmospheric conditions are very variable and have to be carefully monitored all the time and if possible, the measured parameters of atmosphere have to be cross-checked using different methods and different instruments. Within Auger, this task is taken extremely carefully and many independent atmospheric monitoring devices were developed.

The basic instruments, which study the very variable aerosol part of the atmosphere, are CLF (Central Laser Facility) and LIDARs[1]. Furthermore, HAMs (Horizontal Attenuation Monitors) and APFs (Attenuation Phase Function monitors) are working, molecular atmosphere is measured using balloon flights and clouds are detected with infra-red cloud cameras. The most recent addendum to the set of atmospheric monitoring devices are two different star monitors — and one of them is photometric robotic telescope, called FRAM, which was developed by the Czech working group of AUGER project.[2]

Description of the measurement principles, of the hardware and of the software used and of data analysis for individual instruments is provided within next sections.

[1]The word *LIDAR* originated also as an acronym — LIght Detection And Ranging — along two other similar techniques — with sonar (SOund Navigation And Ranging) and with radar (RAdio Detection And Ranging). The latter two words are commonly used written in minuscule letters, not taking into account their origin as an acronym. The history of all these techniques has a comparable length of about half of a century, however, within this work we will still write LIDAR in capital letters.

[2]The second star monitor was developed at the Michigan Technical University in United States as the modified version of full-sky monitor CONCAM [138]. Their sky monitor installed at Los Leones FD site of PAO uses different wide-field camera lens, which provides the field of view of about $100^\circ \times 100^\circ$. This instrument is equipped with single filter — Johnson U filter — and currently works in engineering phase. Thus, so far no scientific data are available as well as no more detailed description of the monitor itself.

5.1 Atmospheric extinction

The term *extinction* means the loss of light in the atmosphere from a directly transmitted beam. Two different mechanisms contribute to extinction: *absorption* and *scattering*. Normally, most of the extinction in the Earth's atmosphere is due to scattering; there is only very small absortion due to molecules of ozone high in the atmosphere, absorption becomes important only when the air is full of smoke (carbon particles) [232]—which is unfortunately quite frequent in Argentinian pampa during brush-fire season.

5.1.1 Scattering

Two kinds of scattering are important: scattering by molecules of air, and scattering by solid particles or liquid droplets suspended in the air. Molecular scattering is usually called Rayleigh scattering, as it was first studied and explained by Lord Rayleigh (John William Strutt, 3$^{\text{rd}}$ Baron Rayleigh) in 1871 [201, 202]. The suspended particles, on the other hand, are collectively known as aerosols, and their contribution is called aerosol scattering. Because aerosol scattering contribution is treated using Mie theory, developed by Gustav Mie in 1908 [174], the alternative name is Mie scattering.

Rayleigh (molecular) scattering

Rayleigh's original paper [201] was intended to show that the blue colour of the sky could be explained as scattering by small particles; but he later realized that the "particles" could well be the molecules of air itself. Assuming that the scatterers are small compared to the wavelength of light, Rayleigh showed that the scattered intensity should be inversely proportional to the fourth power of the wavelength of light, and that this was in good agreement with the spectral distribution of the light of the blue sky. Furthermore, the theory described the polarization, and the variation in intensity with direction, of the scattered light.

A feature of Rayleigh's theory that is often not very much stressed today is that the intensity of the scattering depends on the refractive index of the scattering medium. Because the refractivity of air differs slightly from one, the actual intensity of Rayleigh scattering in air is somewhat steeper than an inverse-fourth-power law, and amounts to about an inverse 4.08-power law across the visible spectrum. Also important is the allowance for anisotropic scattering. The equation for cross section σ in modern notation (see eg. [2]) is then:

$$\sigma = \frac{8\pi^3}{3}\frac{(n^2-1)^2}{N^2\lambda^4}\frac{3(2+\rho_m)}{6-7\rho_m}, \tag{5.1}$$

where n is the index of refraction of air, λ is the wavelength of light, N is the number of scattering particles per unit volume, and ρ_m is the *depolarization factor*. $\rho_m = 0$ for isotropic scattering. The correct value for the air in the wavelength range between 300 and 400 nm seems to be $\rho_m \approx 0.03$, according to recent study of Bucholtz [65].

The normalized Rayleigh differential cross section, or Rayleigh phase function, is given by:

$$\frac{1}{\sigma}\left(\frac{\mathrm{d}\sigma}{\mathrm{d}\Omega}\right) = \frac{3}{16\pi(1+2\gamma)}\left((1+3\gamma)+(1-\gamma)\cos^2\theta\right), \tag{5.2}$$

where $\gamma = \rho_m/(2-\rho_m)$. For isotropic scattering is then $\gamma = 0$. For isotropic scatterers, the Rayleigh scattered light at $\theta = \pi/2$ is fully polarized. This is no longer true for non-zero ρ_m and this is also explaining the name *depolarization factor* for ρ_m.

Mie (aerosol) scattering

Atmospheric aerosols are very diverse. They include tiny grains of mineral dust stirred up from the ground; particles of salt left when droplets of sea spray evaporate; bacteria, pollen grains, mold spores, and other biosol particles; photochemically produced droplets of sulfuric acid and other pollutants; carbon particles produced in fires, and in vehicle exhaust; and many other materials. As most of these are produced at or near ground level, and are washed out of the atmosphere by condensation of cloud droplets on them, followed by precipitation, the aerosols all tend to be concentrated in the lowest part of the atmosphere. An exponential distribution with a *scale height*[3] of about 1.5 km is generally a rough approximation to their vertical distribution.

Because of their diversity, aerosol particles have a wide range of sizes. However, the ones most important for optical scattering turn out to be comparable to the wavelength being scattered, for typical size distributions. Therefore, as the wavelength decreases, we see the smaller particles better. The wavelength dependence of aerosol scattering is almost inversely proportional to the wavelength. (A $\lambda^{-1.2}$ power law is often used.)

Most of the aerosol particles are so weakly absorbing that their extinction is almost entirely due to scattering, rather than absorption. Only carbon particles produced in fires are quite strong absorbers, as we had already mentioned above.

5.1.2 Absorption

Absorption by molecules is sometimes called true absorption, to emphasize its difference from extinction due to scattering; or selective absorption, to emphasize its concentration in narrow spectral bands. The main absorbers in the visible spectrum are ozone (which absorbs in the Chappuis bands, in the orange part of the spectrum), water vapor (several bands in the longer-wavelength regions, noticed mainly under very humid conditions hence the name *rain bands*), and oxygen (which produces Fraunhofer's A and B bands).

[3]The scale height is the height, where the number of particles decreases to $1/e$ of the initial (ground level) value.

5.2 Atmospheric characterization and corrections

The observed light intensity after scattering, I, can be related to the light intensity of the (isotropic) fluorescence source, I_0, as follows[167]:

$$I = I_0.T^m.T^a.(1 + HO).\frac{\mathrm{d}\Omega}{4\pi}, \tag{5.3}$$

where T^m and T^a are the transmission factors for the *molecular* and *aerosol* scattering, HO is a higher order correction (also known as *multiple-scattering* or aureole) and $\mathrm{d}\Omega$ is the solid angle subtended by the observing telescope. Uncertainties in the source light intensity will arise from uncertainties in each of the (correction) factors in the expression. Taking into account only the influence of the atmosphere, as the shower energy is proportional to the fluorescence light signal, the relative uncertainty in the reconstructed shower energy, E, is the same as the combined relative uncertainty in the transmission.

In practice, the Rayleigh scattering related corrections, while large, can be done with precision using cross-sections described above and conventional atmospheric data — the temperature and pressure at the fluorescence detector and the adiabatic model of the atmosphere; or more precisely — using available balloon sounding data.

In contrast the corrections related to Mie scattering, while typically less than the Rayleigh corrections, are *a priori* unknown — because of the high variability of possible scatterers. Thus, most of the atmospheric monitoring is focused on the aerosol (Mie scattering) component.

The analysis of the amount of possible absorption is up to now omitted within existing reconstructions chains (as in Offline framework), although some studies exist (as [204]), how to incorporate the absorption using single scattering albedo (SSA), what is the fraction of scattered photons over all incoming photons that interact with one given atmospheric particle.

5.2.1 Transmission correction

Rayleigh transmission factor T^m, which causes the apparent intensity from a source to decrease exponentially with travel distance through the atmosphere, could be given as:

$$T^m(z, \beta, \lambda) = e^{-\int_0^z \frac{\rho^m(z)\,\mathrm{d}z}{\Lambda^m(\lambda)} \cdot \frac{1}{\sin\beta}}, \tag{5.4}$$

where z is the vertical height of the light source above the fluorescence telescope, $\rho^m(z)$ is the air density and β is elevation angle of the light path. Finally, $\Lambda^m(\lambda)$ is the *Rayleigh (horizontal) extinction length* or *Rayleigh (horizontal) attenuation length.* The relation between Λ^m and between Rayleigh cross-section σ is given as:

$$\Lambda^m = \frac{Molecular\ Weight}{\sigma N_A}, \tag{5.5}$$

where $Molecular\ Weight$ is the weight of one mole of air (28.95 g) and N_A is the Avogadro number. The Λ^m is given in g/cm^2 using 5.1 and 5.5 as:

$$\Lambda(\lambda) = 2874 \left(\frac{\lambda}{400 \text{ nm}} \right)^4 \text{g/cm}^2. \tag{5.6}$$

At PAO site at the altitude $\sim$ 1500 m (using typical air density for this height above sea level) we can convert this horizontal attenuation length to kilometers: $\bar{\Lambda}(\lambda) \sim 18.4$ km at 360 nm (what is an approximate middle of Auger fluorescence detector acceptance).

We can also define *molecular optical depth* — τ^m or OD^m:

$$\tau^m(z, \lambda) = OD^m(z, \lambda) = \int_0^z \frac{\rho(z)\,\mathrm{d}z}{\Lambda^m(\lambda)} \tag{5.7}$$

The remaining part of Rayleigh transmission factor T^m is then full length of the light path — $z/\sin\beta$. The possible further factorization of our basic equation 5.4 into a height dependent part $\int_0^z \rho(z)\mathrm{d}z$, and into a wavelength dependent part $1/\Lambda(\lambda)$, reflects the fact that the composition of the molecular atmosphere is independent of height.

This multiplicative 1-dimensional Rayleigh atmosphere provides a guide to model the multiplicative (Mie) aerosol transmission where we now use $\tilde{\rho}^a(z) = \rho^a(z)/\rho^a(0)$ as the normalized density of aerosols versus altitude. It is typical, but not essential, to parametrize $\tilde{\rho}^a(z)$ as $\tilde{\rho}^a(z) = e^{-z/h_a}$, where h_a is the aerosol (vertical) scale height. $\Lambda^a(\lambda)$ is then in this model the *aerosol extinction or attenuation length* as a function of a wavelength measured at the height of the fluorescence telescopes.

For the *total attenuation length* $\Lambda(\lambda)$ is then valid:

$$\frac{1}{\Lambda(\lambda)} = \frac{1}{\Lambda^m(\lambda)} + \frac{1}{\Lambda^a(\lambda)} \tag{5.8}$$

Finally, we can define also attenuation coefficient α as the optical depth OD at unit length from the relation:

$$OD = \int_0^R \alpha(r)\mathrm{d}r, \tag{5.9}$$

where the r grows along the light path and R is the total distance between light source and observer. If we take α constant then the relation is simple:

$$\alpha = \frac{OD}{R} \tag{5.10}$$

Again, we can define also α_m for *molecular attenuation coefficient* and α_a for the *aerosol attenuation coefficient*. For these it is valid:

$$\alpha = \alpha_m + \alpha_a \tag{5.11}$$

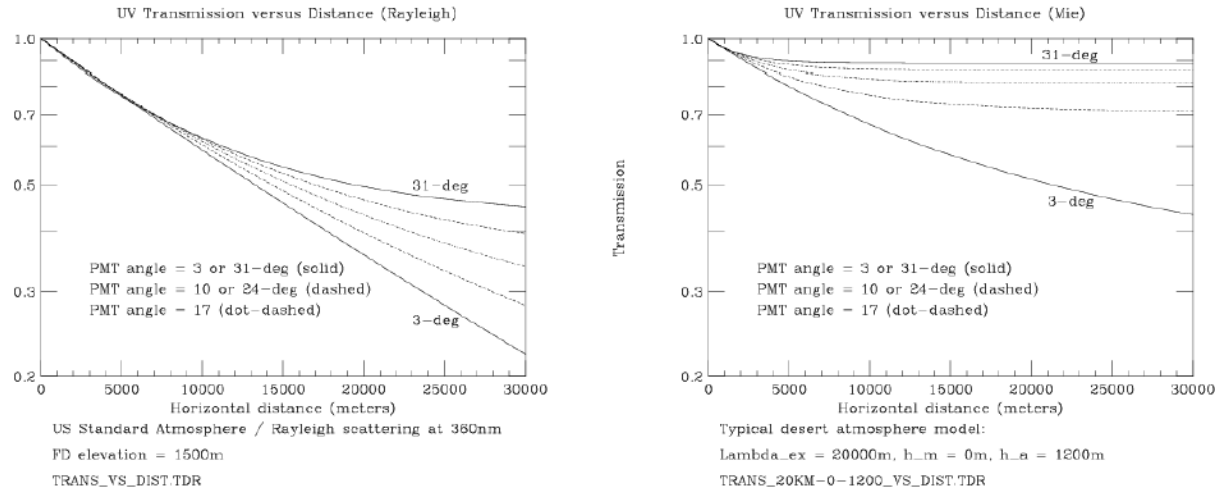

Figure 5.1: Left: *Transmission factor T^m for Rayleigh scattering on the molecular atmosphere. Curves are shown for the Auger FD telescope PMTs' elevation angles ranging from* 3° *to* 31° *above horizon.* Right: *Transmission factor T^a for Mie scattering on aerosols in atmosphere. The aerosols are described by (horizontal) extinction length $\Lambda^a(360\ nm) = 20$ km and an exponential (vertical) scale height $h_a = 1200$ m. Same curves as in the left panel are shown. From [167].*

Representative examples of molecular (Rayleigh) and aerosol (Mie) transmission factors are shown in Fig. 5.1. The transmission factors depend on the elevation angle of the given PMT of the FD telescope, noted before as β , and the horizontal distance of the light source from the fluorescence detector site. The molecular and aerosol transmission curves look different for two reasons: the (horizontal) extinction lengths are slightly different, $\Lambda^m \sim$ 18.4 km versus $\Lambda^a =$ 20 km, and the vertical scale heights are very different, $h^m \sim 7.5$ km versus $h^a = 1.2$ km. While any given air shower may be viewed over a wide range of viewing angles the energy measurement is most sensitive in the direction of shower maximum. In this case fluorescence detector viewing angles, $\beta \approx 10^\circ$, are rather typical.

Implicit in this aerosol model are two assumptions which while true for the molecular atmosphere may not be true for the aerosols. First, that the aerosol vertical variations are much more important than the horizontal variations; i.e. we use a 1-dimensional model (not untypical of the night time atmosphere in large, desert valleys at locations well away from the valley walls). Second, that the vertical profile of the aerosols is the same at all wavelengths in our wavelength interval of interest. Thus we assume that to first order the wavelength dependence is only in the extinction length, $\Lambda^a(\lambda)$.

5.2.2 Extinction in astronomy

Because one of the atmospheric monitoring devices is a typical astronomical instrument—(robotic) photometric telescope FRAM, we will briefly explain here the relation between

the astronomical definition of extinction and between the quantities that we have defined above.

If we omit the effect of instrument properties[4], then the observed star magnitude m_{obs} is given as:

$$m_{obs} = m_{out} + \tilde{\alpha}\tilde{X}, \tag{5.12}$$

where m_{out} is the (tabulated) magnitude of the star outside from the atmosphere, $\tilde{\alpha}$ is the total astronomical attenuation coefficient and $\tilde{X}$ is (astronomical) airmass. Coefficient $\tilde{\alpha}$ is the sum of both molecular and aerosol components: $\tilde{\alpha} = \tilde{\alpha}^m + \tilde{\alpha}^a$ (as it was already similarly defined for the PAO attenuation coefficients in 5.11; note that units are different—$\tilde{\alpha}$ is dimensionless and α is in m^{-1}). By observing we are taking into account the integral volume of air between an observer and a star and we cannot distinguish the Rayleigh and aerosol part of scattering. Astronomical airmass $\tilde{X}$ usually defined as a relative value, with respect to the total mass of air between the observer and star in the zenith (zenith angle $\theta = 0$). Therefore, the resulting airmass $\tilde{X}$ grows with θ roughly as $1/\cos\theta$, or in better approximation as $(1-0.0012\tan^2\theta)\sec^2\theta$. Or, we will obtain precise results for airmass $\tilde{X}$, if we will take into account simultaneously that the Earth surface is curved and that the atmosphere is composed of a number of different layers. Then we can numerically evaluate the airmass $\tilde{X}$ using the properties of these layers from standard atmospheric models (cf. US-StdA — US Standard Atmosphere 1976) or directly from dedicated measurements on site (see balloon sounding 5.5). Finally, using such models it is then easy to convert $\tilde{X}$ to X, where X is the airmass in $\mathrm{g\,cm}^{-2}$ generally used for other applications at PAO.

Again omitting the properties of our instrument we then have for astronomical transmission factor $\tilde{T}$ — for a given star (point source) at a given position[5]:

$$\tilde{T}(\lambda) = 10^{0.4(m_{out}(\lambda)-m_{obs}(\lambda))} \tag{5.13}$$

Such transmission factor $\tilde{T}$ incorporates the convolution of both aerosol and molecular scattering and also the higher order effects. In principle, we are not able to distinguish individual contributions directly from the star observations, however we can try to model e.g. the Rayleigh scattering contribution and to subtract it to obtain the estimate of aerosol contribution. We stress here that $\tilde{T}$ as well as observed magnitude m_{obs} and as well as intrinsic magnitude of any star m_{out} depends non-trivially on the observed wavelength λ. The correct integral transformation of these values is a complex problem during observations using real filters with spectral transmission distribution of non-zero width. Here we generally take the advantage from the measurements using the standard astronomical filter sets — eg. Johnson UBV set or Strömgren uvby set.

[4]For the more detailed treatment of instrument influence and of error estimates of the method see 5.11.1.

[5]Stellar magnitudes were first defined empirically, stars of 1^{st} magnitude being $100\times$ brighter than stars of 6^{th} magnitude. Pogson (1856) established this logarithmic scale of brightnesses mathematically using the relation: $m_2 - m_1 = a\log(E_1/E_2)$, where m_1 and m_2 are stellar magnitudes and E_1 and E_2 observed stellar brightnesses. Constant a is then given from the empirical scale for magnitudes as: $5 = a\log 100$. Therefore factor 0.4 appears in the equation 5.13.

For comparison of other quantities from other monitoring devices we can first convert $\tilde{T}$ to total optical depth OD:

$$OD(\lambda) = -\ln \tilde{T}(\lambda) \tag{5.14}$$

Finally we can obtain *total attenuation length* Λ using evaluated value X in g/cm^2 that is already directly comparable with other instruments:

$$\Lambda(\lambda) = \frac{X}{OD(\lambda)} \tag{5.15}$$

5.2.3 Measured values for the atmospheric database

Atmospheric monitoring data are stored in the dedicated MySQL database. The area of PAO observatory is divided into five regions, four of them are associated with locations of FD eyes and the last one with the location of CLF in the middle of the array. Each region will contain full set of data about molecular and aerosol atmosphere that will be either directly measured or extrapolated from neighboring regions—with respect to presence of specific monitoring device. The data are generated and stored on hourly basis, with exception of cloud cameras that scan FOVs of each FD site every five minutes. Eventually, for events with particularly high energy the more exact atmospheric parameters could be potentially extracted from the raw data of individual devices.

The data for simulation molecular atmosphere are obtained locally at FD sites and at CLF position using weather stations, which measure the temperature, pressure, humidity and wind speed (see 5.4), or using balloon sounding, where we obtain the same values for various atmospheric profiles (see 5.5).

As we stressed above, the aerosol part of the atmosphere is much more variable and is therefore very carefully monitored. Currently, within the Offline framework [188] the aerosol transmission factor T^a is modeled as:

$$T^a = \exp\left[\frac{h_a}{\Lambda^a \cos\theta} \exp\left(\left(\frac{-h_1}{h_a}\right) - \left(\frac{-h_2}{h_a}\right)\right)\right], \tag{5.16}$$

where Λ^a is the aerosol horizontal attenuation length and h_a is the aerosol scale height, as noted above. h_1 and h_2 are the altitudes of an observer and of a light source above the sea level ($h_2 \geq h_1$), respectively, and θ is the zenith angle of the light path. Thus, we need to measure Λ^a and h_a. Both values will be measured using especially LIDARs (see 5.8) and CLF (see 5.7).

Furthermore, we need to estimate the dependence of the aerosol attenuation coefficient α_a on the wavelength λ. This is modeled for the expected power law dependence using the relation:

$$\alpha_a(\lambda) = \alpha_a(355\text{ nm}) \left(\frac{\lambda}{355\text{ nm}}\right)^{\gamma} \tag{5.17}$$

The exponent γ is measured by the HAM monitor (see 5.9) and also by FRAM telescope (see 5.11).

Finally, the aerosol phase function (normalized differential cross section; aerosol equivalent for the Rayleigh phase function defined in 5.2) f^a is currently parametrized by function:

$$f^a(\psi) = \frac{1-g^2}{4\pi}\left(\frac{1}{(1+g^2-2g\mu)^{3/2}} + f\frac{3\mu^2-1}{2(1+g^2)^{3/2}}\right) \tag{5.18}$$

where ψ is a scattering angle, $\mu = \cos\psi$ and f and g are measured adjustable parameters. f and g has to be measured by APF (see 5.10) and by LIDARs (see 5.8).

5.2.4 Possible relative and absolute measurements

All available aerosol atmospheric data are up to now treated and analyzed only as relative measurements—in comparison with carefully selected aerosol-free (Rayleigh) nights. The problem of such selection is that it is made basically by eye—very clear, calm night following some strong precipitations, which have to wash-out all aerosols, is chosen. The reason for such approach is that the used light sources are not easily and precisely calibrated.

For some instruments (CLF and LIDARs) such calibrations of light sources (LIDARs) are realized, however the analysis of the data using these absolute values is more complicated and was not finished yet. With known absolute output of light sources, the Rayleigh contribution then will be modeled and subtracted, and aerosol data will go to database as the absolute values. Some other instruments (especially HAM) have the source not calibrated, and the resulting atmospheric parameters (γ for HAM) then can be biased by the fact that intensity of the source is (strongly) variable and dependent e.g. on the temperature.

In these consequences, astronomical approach to the measurement of astronomical parameters has a great advantage—the sky is full of very well calibrated light sources—thousands of standard stars of different spectral types are available for measurements. Therefore, for example the measurement of wavelength dependence factor γ could be absolute and may be less biased than dedicated HAM measurements.

5.3 Atmospheric simulations

Having ready the models of the atmosphere and database of their parameters, we can try to simulate atmospheric influence on the fundamental parameters of the showers, especially on the energy E of primary particle and the position of the shower maximum X_{max}.

5.3.1 Molecular atmosphere

The relation between atmospheric depth and geometrical altitude is a crucial point in the simulation and reconstruction of EAS and the relation between atmospheric depth and height follows from the air density profile. The data recorded at the site are compared with the US Standard Atmosphere 1976 (US-StdA), which had been commonly used.

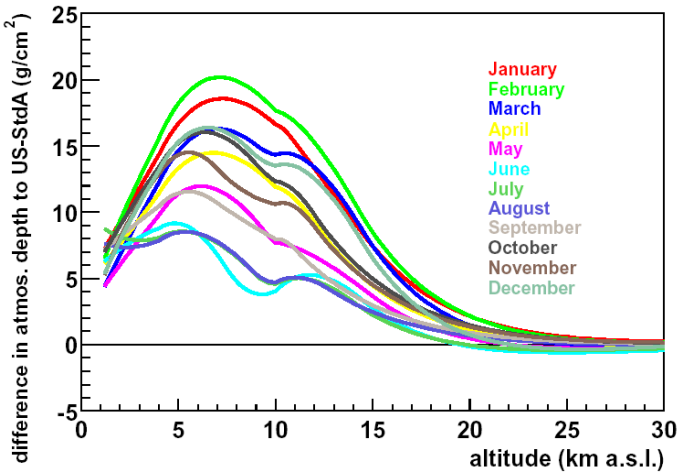

Figure 5.2: *Profiles of atmospheric depth of the Malargüe Monthly Models in difference to the US-StdA. From [61].*

About 2700 hybrid events were analyzed to estimate the resulting difference in the X_{max} position (what is a important factor in distinguishing the composition of CRs) and total deposited energy. During data processing, Malargüe Monthly Models and US-StDA were applied and then the difference was plotted. As could be seen on Fig. 5.3 (right panel), using the Malargüe Models, the average difference in X_{max} is of about -15 g.cm^{-2} (what already has some influence for the determination of chemical composition of detected cosmic ray primaries) and the average change of the reconstructed energy of the primary particle is only 0.7% (Fig. 5.3, left panel). However, the spread of the whole distribution is much larger; individual events could differ in specific cases for more than 5%, so especially the planned dedicated balloon soundings just after observation of particularly energetic events is highly desirable.

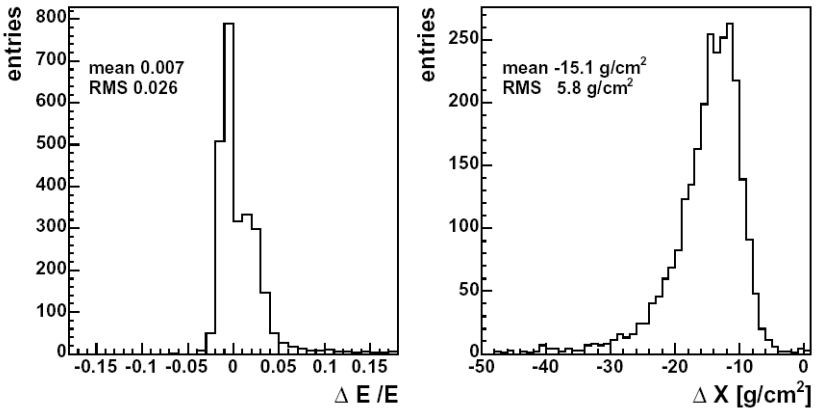

Figure 5.3: *Difference of reconstruction using Malargüe Monthly Models to reconstruction in US-StdA is shown.* Left: *(Relative) primary energy.* Right: *Position of shower maximum. From [61].*

5.3.2 Estimates of aerosol influence

Recently, the influence of the aerosol component was studied [14], using extensive Monte Carlo simulations by the analysis of CORSIKA generated showers. One hundred $10^{19.5}$ eV proton showers and one hundred $10^{19.5}$ eV iron showers with zenith angle $\theta = 37°$ have been used to simulate the FD detector response for different configurations. Five different core locations were used: shower core was fixed in the middle of Los Leones bay 4, at distances from 15 to 25 km in steps of 2.5 km from the fluorescence detector. With this choice of parameters the shower maximum is within the telescope field of view.

In the simulation process the values for horizontal attenuation length Λ^a and aerosol scale height h_a were fixed at: $\Lambda^a = 25$ km and $h_a = 1.5$ km. At each generated core distance, events were analysed using three different aerosol contents:

1. a dirty atmosphere ($\Lambda^a = 15$ km and $h_a = 1.5$ km)
2. the same atmosphere used in the simulation ($\Lambda^a = 25$ km and $h_a = 1.5$ km)
3. an extremely clean atmosphere with virtually no aerosol content (Rayleigh atmosphere; $\Lambda^a = 500$ km and $h_a = 1.5$ km)

For each analysed event, deviations of reconstructed energy and X_{max} with respect to the generated values have been computed. The results have been studied as a function of shower core distance for each atmosphere used in the reconstruction. Two different azimuth angles ϕ were chosen for the simulations, corresponding to the extreme two configurations of shower laying in the vertical plane containing the eye center and the shower core ($\phi = 75°$), and at 90° with respect to that direction ($\phi = 165°$).

We present some results in Fig. 5.4 & Fig. 5.5 below.

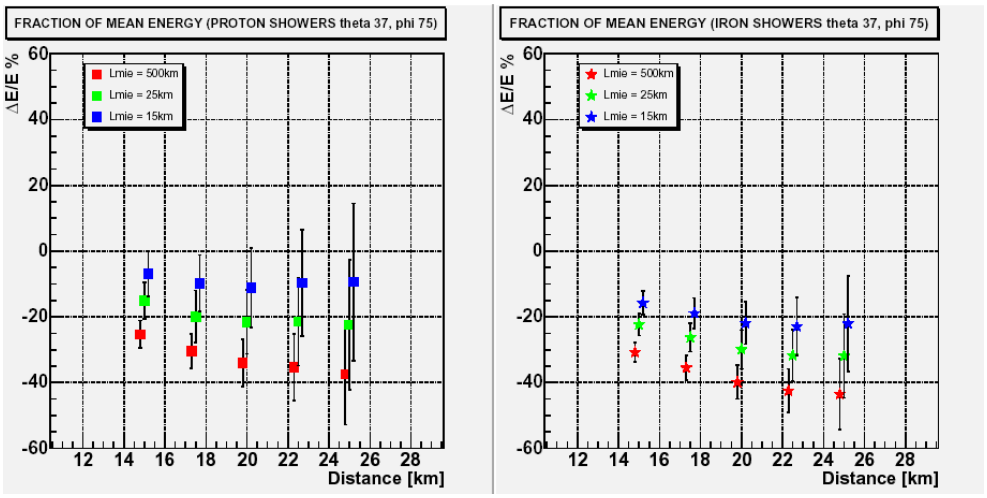

Figure 5.4: *Percentage difference between reconstructed and generated energy E* ($\Delta E/E = (E_{rec} - E_{sim})/E_{sim}$) *versus core distance for protons (left) and iron (right) with the three atmospheres at* $\phi = 75°$. *The spread between points with different atmospheric parameters is of about* $10 - 20$ *%. It is also clear that without accounting the effect of atmopsheric attenuation at all we will be underestimating the shower energy E almost by the factor of 2. From [14].*

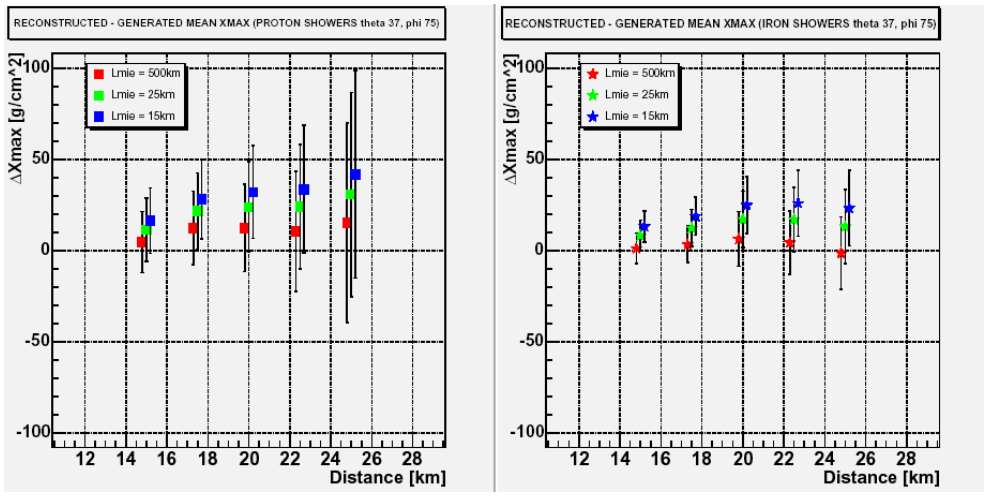

Figure 5.5: *Mean values of* X_{max} *distributions for the versus core distance, for the three atmospheres at* $\phi = 75°$.

We can summarize, that the results of this analysis show that the lack of knowledge of the atmospheric aerosol content produces observable effects on both energy E and shower maximum X_{max} of reconstructed events. A change of the horizontal aerosol attenuation length Λ^a from 25 to 15 km produces an energy shift of about 15 % and a shift in X_{max} of about 10 g/cm^2 for a shower at 20 km from the FD. It is worth noting that such not

negligible variations in the atmospheric transparency have been observed by a preliminary analysis of CLF data even on time scales of a few hours.

5.4 Automatic Weather Stations

Commercial ground-based weather stations record temperature, pressure, relative humidity, and wind data every 5 minutes. Each weather station is connected to the internal Auger network and data are transferred to the central facility.

At completion of the observatory, five stations will be installed. Four of them will be located near to each FD building and the last one in the middle of the array, near to the Central Laser Facility. In the middle of 2005, two stations [74] were already in operation and the data from them are available.

These continuous flowing ground-based data are applied in the calculation of trigger efficiencies of the Cherenkov water tanks, while the atmospheric profiles, measured as it is described in 5.5 are mainly used for simulation and reconstruction of the longitudinal shower development.

5.5 Balloon Sounding

Since August 2002, meteorological radio soundings [61] have been performed during several campaigns near Malargüe, Argentina. The radio probes are launched above the site of the experiment on helium-filled balloons. A set of data is taken about every 20 m during ascent up to 25 km a.s.l. in the average. Despite changing wind conditions, the radiosondes stay mostly directly above the array up to 10 km a.s.l., covering the more interesting part of the profiles for EAS development. More than 100 atmospheric profiles, including data for temperature, pressure, relative humidity, and wind speed and direction, were collected.

Day-night variations are very small in this area. Only temperature variations up to 10 K may occur in the lowest 1000 m above the ground which is roughly at 1400 m above the sea level in our case. The important profile of atmospheric depth hardly changes on day-night time scales. From day to day, the extent of variations is strongly seasonally dependent. During southern summer, the conditions are much more stable than during the winter. At ground, differences in atmospheric depth up to 5 g.cm^{-2} have been found which are related to pressure variations. At higher altitudes, between 6 and 12 km a.s.l., even variations of 10–15 g.cm^{-2} are recorded. Over a period of days, the temperature may change by 15 K. Seasonal effects are, of course, the largest. For individual days, the difference in atmospheric depth between summer and winter can be as large as 20 g.cm^{-2} at the ground and reach approximately 30 g.cm^{-2} at altitudes between 6 and 9 km a.s.l.

5.6 Cloud cameras

Clouds can have very large optical depths and can therefore have a dramatic effect on the scattering and transmission properties of the atmosphere. Although some of the other atmospheric monitors, notably the LIDARs and the CLF, are sensitive to the presence of clouds they do not provide a detailed all-sky map of cloud distributions. This information is collected by the cloud cameras. These consist of finely pixelated infrared cameras (Raytheon model 2000B, 7–14 μm wavelength range) which are sensitive to the temperature differences between the clear sky and clouds. The cameras, with a FOV of $46^\circ \times 35^\circ$, are on steerable mounts so that they can survey the entire sky. It is planned to have one camera per FD site and currently 3 of them are installed at all FD sites which are in operation (Los Leones, Coihueco and Los Morados). The cloud cameras scan the field of view of *its* FD site every 5 minutes, and also generate a full sky scan every 15 minutes.

An analysis effort is underway to provide a clear/cloudy flag for each FD pixel updated every 5 minutes during FD observing periods [74].

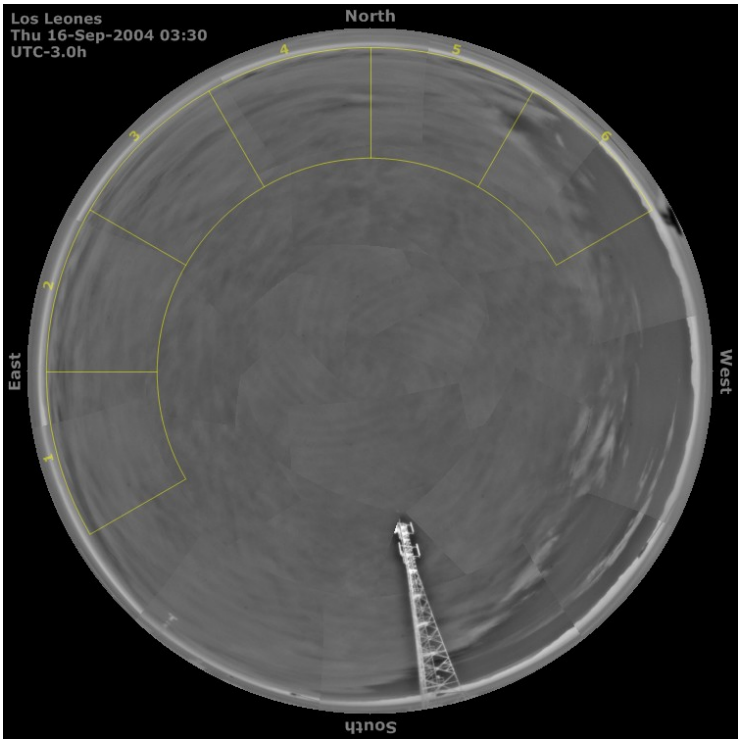

Figure 5.6: *An example of the fullsky mosaic of IR images of the cloud camera. These fullsky images are used as one of the basic sources of weather situation by FD operators during data acquisition. The cloud cover is clearly distinguishable as the lighter parts of the image. The image shows the situation when it is almost overcast, only near southwest horizon is the patch of clear sky.*

5.7 Central Laser Facility

The Central Laser Facility (CLF) provides a *laser test beam* to investigate properties of the atmosphere and the fluorescence detectors. Furthermore, the laser can send light via optical fiber simultaneously to the nearest surface detector tank for hybrid timing analyses. The most recent description of the CLF system could be found in [19], here we will list only the basic properties of the system.

The CLF is located in the middle of the Pierre Auger Observatory SD array, at distances that range from 26 to 39 km from the FDs. This facility is solar powered, housed in a modified shipping container, and operated remotely via microwave Internet link. The facility is unmanned.

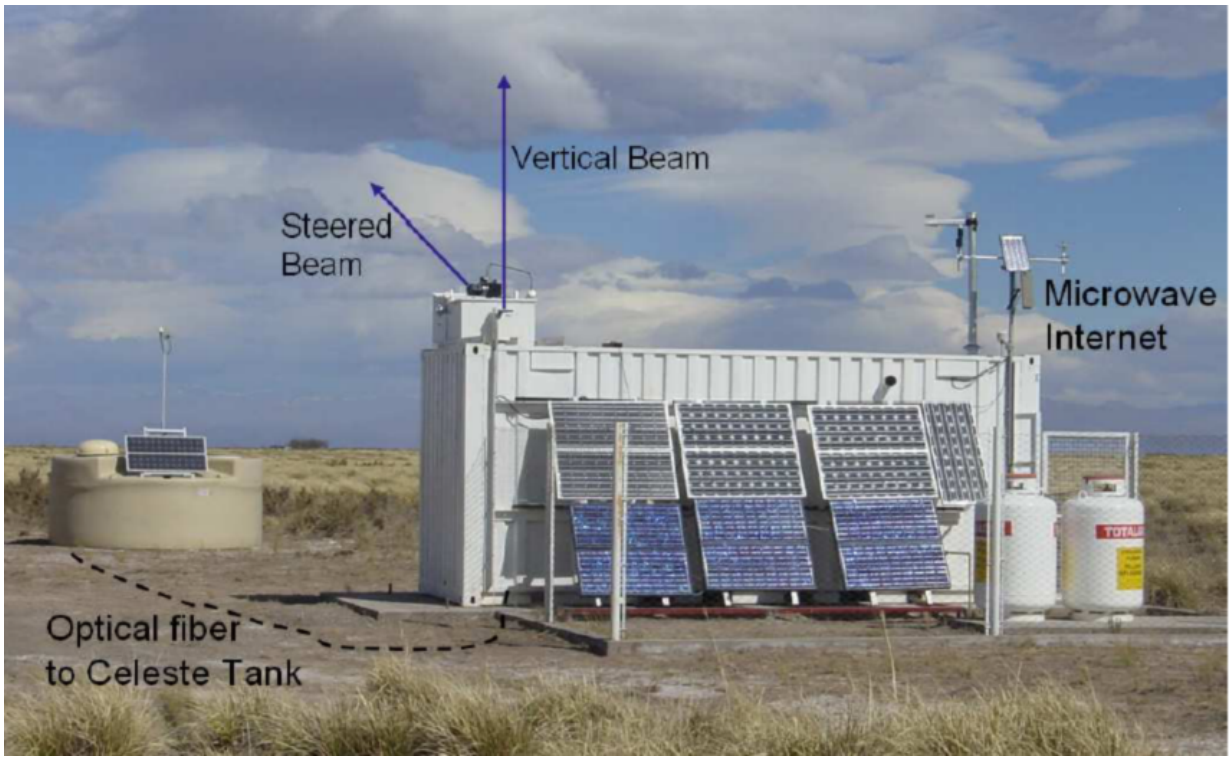

Figure 5.7: *The Central Laser Facility at the southern site of PAO. From [19].*

The CLF tracks recorded by the FD eyes have several similarities to tracks generated by extensive air showers. The laser wavelength of 355 nm is near the middle of the air shower fluorescence spectrum. After accounting for atmospheric effects, the total amount of light scattered out of the beam is proportional to the laser beam energy.

The heart of the system is a frequency tripled YAG laser producing a 7 ns pulsed beam with a maximum energy per pulse of 7 mJ. A *flip mirror* selects between two vertical beam paths. One goes directly to the sky when a simple cover is open. The other enters a mechanism with two mirrors on rotating orthogonal axes that can steer the beam in any

direction above the horizon. A mechanical cover protects the steering apparatus when not in use.

The beams are calibrated and configured with randomized polarization. Depolarizers in each beam path convolve the linearly polarized beam emitted by the laser to an output beam for which the net polarization is within 3% of random. The depolarization of the beam is necessary, because only so is assured the equal scattering in the direction of each FD eye.

The relative energy of each pulse is monitored by a photo-diode detector. A pyroelectic energy probe, installed in March 2005, makes a second relative measurement of the vertical beam energy. The cross-calibration of these two probes is performed several times a year.

The CLF facility also houses a weather station and a radiometric cloud detector. A small computer (PC) monitors the solar power system, collects weather station and cloud detector data, and operates the laser system.

The laser firing time relative to the GPS second is controlled by a programmable timing module. Every shot is tagged to avoid confusion with possible neutrino-generated upward going tracks. A small fraction of the laser light can be injected into the nearest SD water tank (dubbed *Celeste*) via optical fiber. The sky-only shots are recorded by each triggered FD to a special laser file. The sky+Celeste shots are written to the same data stream as air shower candidates together with the corresponding data from the Celeste tank.

Laser operation is conducted from the observatory's central campus only by starting and stopping the control program at the beginning and end of each night of FD operation. Sets of 50 fixed-direction vertical shots are fired every 15 minutes followed by one sky+Celeste shot. Patterns of inclined shots are also fired during two one hour periods each night. This pattern include shots fired at the angle between individual FD eyes and low-energy near-horizontal shots fired over each FD eye.

A fit to the longitudinal profile of vertical tracks recorded by the FDs has been normalized to a clear air profile to generate an hourly database of aerosol optical depth measurements. CLF shots are used in ongoing studies of triggering efficiency, geometrical reconstruction and the details of the FD pixel-pixel response. Sweeps of inclined shots are also used to test the results of FD mirror pointing directions obtained by other methods (as it was mentioned above in 4.5).

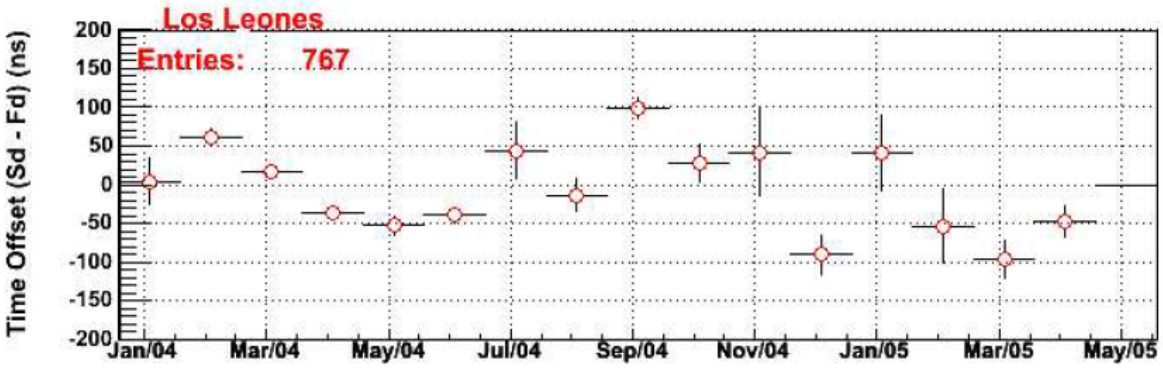

Figure 5.8: *Relative SD-FD time offset (using vertical lasers) for each month since January 2004, as observed by Los Leones FD eye. As the nominal time offset (0 ns in the figure) was taken measured mean offset of 318 ns. This offset is probably due to misalignment of FD telescope as discussed in 4.5. From [10].*

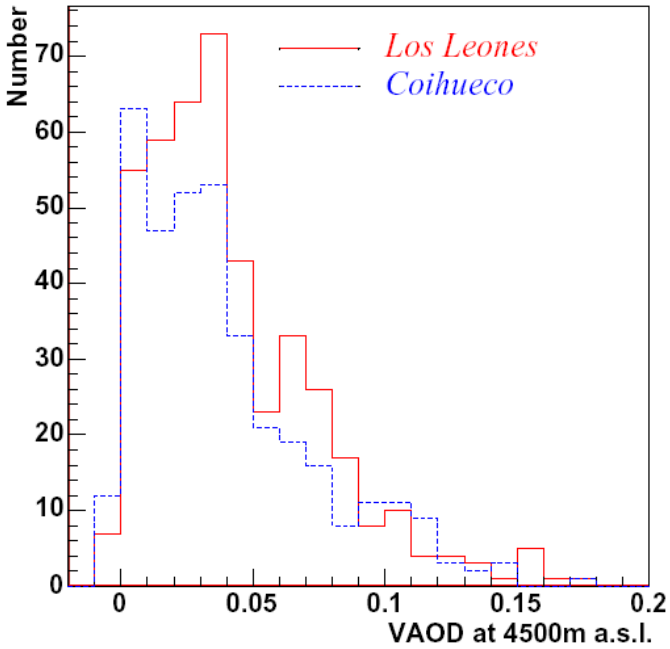

Figure 5.9: *The distribution of VAOD from FD level to 4500 m above sea level (a.s.l) reconstructed from CLF laser shots (January 2004 - February 2005). Note that the distribution slightly differs for the Los Leones FD site and Coihueco FD site. From [74].*

5.8 LIDARs

An elastic backscatter LIDAR will be located near each of the FD sites. Currently two of these LIDARs are operational (Los Leones and Coihueco sites), a third is being built (Los Morados site) and the fourth will be installed when the fourth FD site is completed. These LIDARs detect the elastic backscatter signal from pulsed UV lasers. The backscatter signal is detected by photomultiplier tubes (PMTs) at the foci of three 80 cm diameter parabolic mirrors. The laser and mirrors are mounted on a steering frame that allows the LIDAR to be pointed to almost any direction in the sky.

The PMT signals are recorded by a commercial LIDAR transient digitizer (Licel model TR40-160) with 12 bit resolution at 40 MHz sampling rate. The digitizer has a 16 kilobyte trace length and can also record the arrival times of single photons with a 250 MHz counting system. The dynamic range of the LIDAR systems is increased by repetitive sampling of the laser backscatter signals. To reduce data collection time the laser systems are being upgraded to high repetition-rate lasers. Diode pumped lasers working at the wavelength of 351 nm will be used, the actual type is DC30-351, made by Photonics Industries. The backscatter trace recording rate, limited by the Licel DAQ, is 300 Hz. Within a 2–3 second period the LIDARs can record a good quality backscatter signal at distances in excess of 25 km.

During FD operation the LIDAR systems perform a routine scan of the sky over each FD providing an hourly measurement of aerosol conditions. If an FD detects a cosmic-ray track it can send the shower-detector plane information to its local LIDAR system to request a shoot-the-shower (STS) procedure. The LIDAR software connects to the surface detector (SD) data acquisition system to see if a cluster of tanks triggered at the same time as the FD event. If this is confirmed the LIDAR will interrupt its routine operation and scan the shower-detector plane providing real-time information about the aerosol content of the atmosphere.

As a part of the backscatter LIDAR program a single Raman LIDAR detector has been installed on one of the elastic backscatter LIDARs. This detector measures backscatter light that has been frequency shifted by Raman scattering from atmospheric nitrogen and oxygen. The Raman LIDAR technique allows for a more accurate reconstruction of aerosol transmission, which is limited for elastic backscatter LIDARs by uncertainties in the aerosol backscatter cross-section. Due to the small Raman scattering cross-section this technique requires large numbers of high power laser shots. This would result in an unacceptable level of light pollution if the FDs were operating, so the Raman LIDAR is run during non data-taking periods and will be used to cross-check the accuracy of the vertical average optical depth (and its dependence on altitude) measurements made with the elastic backscatter LIDARs.

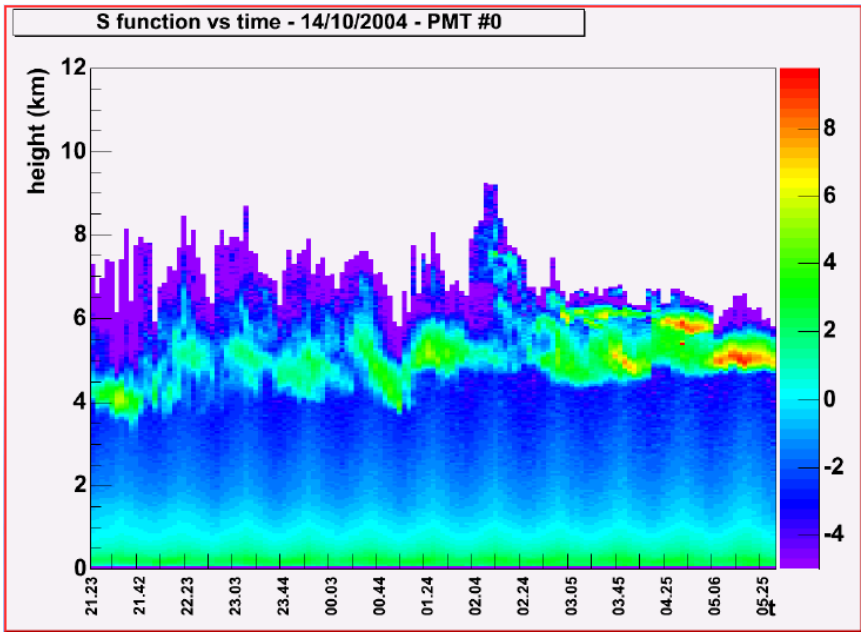

Figure 5.10: *The time evolution of the cloud layer and its height shift could be clearly seen. During the night the layer above LIDAR station at Los Leones rised from 4 to 5 kilometers and became more optically thick. From [177].*

5.9 HAMs

The HAMs measure the attenuation length at near ground level between the FD eyes. Each HAM system consists of a DC light source, located near the one FD eye, and a receiver located at the vicinity of another FD eye. Currently one HAM is operational and monitors the aerosols between the Los Leones and Coihueco FD sites[6]. Two more systems are planned that will monitor other regions of the Pierre Auger Observatory aperture.

The DC light sources emit a broad spectrum of wavelengths including in the 300–400 nm range where the FDs are sensitive. The light detectors consist of UV enhanced CCD arrays (Starlight XPress model MX5-16) at the focus of 15 cm diameter mirrors. A filter wheel in front of the CCD allows for monitoring at different wavelengths (365, 404, 436 and 542 nm). A measurement of the horizontal attenuation length at these wavelengths is made for each hour of FD operation. The principle measurement made by the HAMs is the wavelength dependence of the horizontal attenuation length described by a power law index, γ. The distribution of γ for total attenuation (molecular and aerosol) from measurements made during the period December 2004 until March 2005 is shown in Figure 5.11.

[6]The HAM light source is located about 100 m from the Coihueco FD building and HAM CCD detector is atop the gallery on the roof of Los Leones FD building. The FRAM system is located nearby at Los Leones, so extensive cross-checks measurement between HAM and FRAM are in preparation.

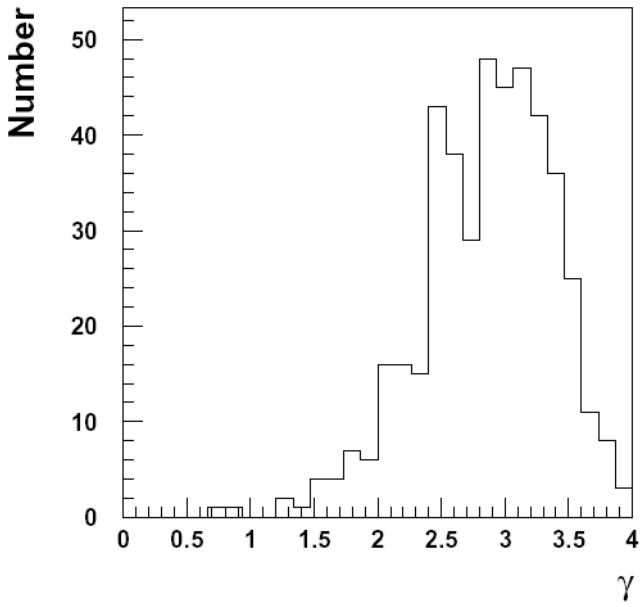

Figure 5.11: *Distribution of the aerosol attenuation wavelength dependence parameter, γ, as measured by the first HAM system. All available hourly results for the analyzed period of part of year 2004 are shown. For a pure molecular atmosphere we would expect γ to be close to 4. From [74].*

5.10 APFs

Cosmic-ray induced EAS generate approximately equal numbers Cherenkov and fluorescence photons over the life of the cascade. The Cherenkov photons are strongly forward beamed, but do contaminate the fluorescence signal directly and through atmospheric scattering. The scattering properties of the molecular atmosphere are well known, but the aerosol scattering properties depend on the specific characteristics of the aerosols.

The Aerosol Phase Function monitors (APFs) [168] are designed to measure the aerosol differential scattering cross-section ($d\sigma/d\Omega$). The measurement is made by firing a horizontal, collimated beam of light from a xenon flashlamp across the front of an FD site. The track that is generated contains a wide range of light scattering angles from the beam (30°–150°). The APFs then include narrow band filters to monitor the wavelength dependence of $d\sigma/d\Omega$.

One APF has been installed at the Coihueco FD eye and has been generating hourly data since September 2004. A second APF is currently being commissioned at the Los Morados FD site.

5.11 FRAM

The name of this device was chosen not only as little ortographically crippled acronym **F**otometric **R**obotic **A**tmospheric **M**onitor[7], but also in honor of pioneering Fridtjof Nansen's polar vessel — FRAM. *Fram* means *onward* in Norwegian.

5.11.1 Basic principles of the method

Figure 5.12: *FRAM telescope and house during sunset at Los Leones site.*

Some stars are very carefully calibrated standard sources. During decades of observations in different astronomical filters also the wavelength dependence was studied and variable and non-variable (standard) stars were distinguished. Finally, based upon these long series of measurements the effects of instrument properties (so called instrument zero-point, M_{zero}) and especially the influence of atmosphere was subtracted and the intensity of incoming light or the star magnitude outside from Earth's atmosphere (m_{out}) was determined. Both from theoretical observations and from various measurements it is well proved that atmospheric influence on the star brightness (for given particular wavelength

[7]In Czech, the acronym is ortographically correct: **FRAM** — **F**otometrický **R**obotický **A**tmosférický **M**onitor.

λ or for given particular astronomical filter) could be expressed as the product of a total mass of air between a star and an observer (airmass; X)[8] and of the extinction coefficient ($\alpha(\lambda)$ or sometimes $k(\lambda)$).[9]

Several catalogues of such standard stars were compiled, for our particular case of FRAM telescope we use *uvby* catalog[10] of bright standard stars by Perry, Olsen & Crawford [186].

Thus, our measurement procedure starts with the selection of a suitable star. If we are able to center this star in the field of view of our photometer and obtain photometric measurements by the set of different filters, then we can continue with the following data reduction:

Knowing precisely the star magnitude outside of atmosphere m_{out} we can either follow the star through different airmasses X and then derive the parameters of following linear equation (5.19) or rather determine the instrument zero-point independently before[11], assume that this zero point is not changing rapidly with time and so be able to evaluate the extinction α directly from any single observation. For a given astronomical filter or a given wavelength it is valid:

$$m_{obs} = m_{out} + M_{zero} + \alpha X \tag{5.19}$$

For the evaluation of airmass X we can use some standard models (e.g. US Standard Atmosphere) or rather straightforwardly the seasonal models of molecular atmosphere for the area of PAO near Malargüe, presented for example in [152].

At this point we wish to remark on the main disadvantage of the method. We are able to measure the influence of all atmospheric layers between an observer (FRAM) on the ground and between a star in the outer space. In contrast, all cosmic ray showers origin in the atmosphere, typically in distances of the order of tens of kilometers from the observer. However, the upper layers of atmosphere, which do not play any role in shower observations, are also of much less importance for star observations. Moreover, these upper parts of atmosphere do not vary as much as the lower layers, where aerosols play essential role. Furthermore, these upper layers are much less dense and so they don't contribute so importantly to overall airmass X between the observer and the star.

[8] Within this section we use X again in astronomical sense, as a relative value. In 5.2.2 we noted this as $\tilde{X}$.

[9] For the relation between astronomically obtained values for the atmosphere and standard PAO atmospheric parameters see 5.2.2. Again in 5.2.2 we noted astronomical parameter as $\tilde{\alpha}$.

[10] The so-called Strømgren *uvby* is one of the standard set of astronomical filters, first published in [216]. Another important set of astronomical filters was introduced by Johnson [146] and is also partially used in FRAM photometer.

[11] During series of initial dedicated observations.

Estimated precision of measurement

On the basis of similar astronomical campaigns[12] we expect that for the first season the expected precision is of about 0.01 magnitude for nightly observation of individual standard star. This first data set will be used for detailed evaluation of instrument zero-point, its wavelength and time dependence. Then, for the next seasons—using this model of our instrument—we can expect that the precision of individual star measurement will be improved up to 0.003 magnitude, what is probably the limit of both of the method and of our instrument.

We know, that shower energy E is directly proportional to the number of emitted fluorescence photons. This amount of emitted light is reduced on its way to the observer due to atmospheric extinction. We can write down simple relation:

$$\frac{\Delta E}{E} = \frac{\Delta I}{I} \propto \frac{\Delta(e^{-m})}{e^{-m}} = \frac{\Delta m e^{-m}}{e^{-m}} = \Delta m, \text{ where} \tag{5.20}$$

ΔE is the energy uncertainty, $\Delta I/I$ is the intensity uncertainty over the intensity of emitted fluorescence light and m is the chosen star magnitude and Δm is again its uncertainty. Therefore, with precision of about 0.01 magnitude in measurement of our star this will give us 1 % precision of energy estimation (taking into account atmospheric extinction only). Unfortunately, this simple statement is not valid, because the extinction is given not only by observed star magnitude, but also by airmass X and airmass depends on the current distribution of density in the atmosphere. We have to add this piece of information using some independent measurement, e.g. the results of balloon soundings measurements or at least use seasonal molecular Malargüe atmosphere model. Furthermore, as we already pointed out, during any star observations we are making integral observation through whole atmopshere. So, anytime we have also to subtract the effect of upper atmospheric layers (of layers, which are behind the cosmic ray shower). This naturally reduces absolute precision of this type of measurement.

Fortunately, as we discussed above, the vast majority of the most variable component of the atmosphere—its aerosol part—is typically distributed in quite low heights above the ground, some 1–2 kilometers above the ground level. Then the shower maximum (X_{max}) for an average shower with energy 10^{19} eV with average zenith angle of $\sim 37°$, is situated above this aerosol layer and we will be almost correctly subtracting only the molecular part, which we know with high precision and which has almost negligible effect (< 1 %) on the energy reconstruction, as it was discussed above in 5.5.

We can describe such estimate in a more general way:

The position of the shower maximum X_{max} is energy dependent and for our estimate we can use both theoretical and experimental data which are shown e.g. in Fig. 2.3. Using the particular model of the atmosphere we can then straightforwardly assign the height h

[12] All such campaigns were done using photoelectric photometers; in particular we use the experience of the observatory of the Astronomical Institute of the Academy of Sciences of the Czech Republic situated at island Hvar, Croatia.

above the ground to the studied X_{max}. For quick reference we present below in Fig. 5.13 the relation between X_{max} and h for the US-StdA model.

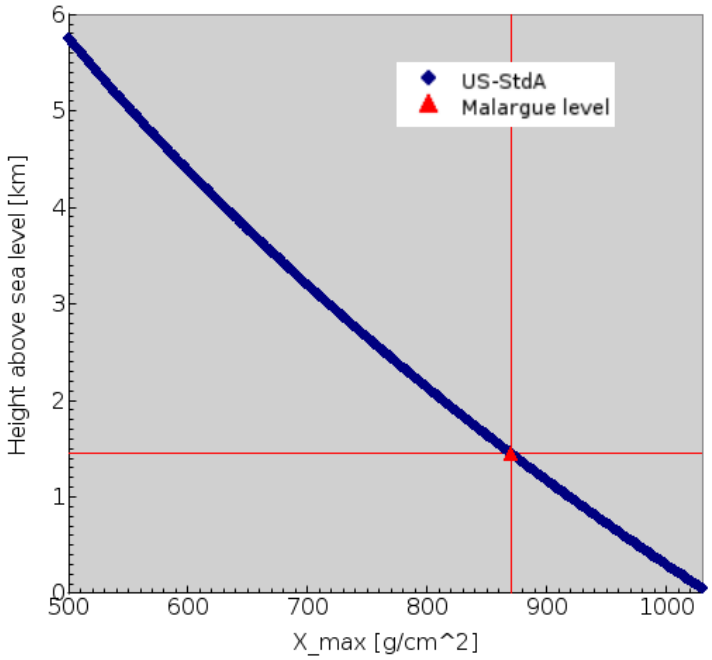

Figure 5.13: *The relevant part of the graph of the relation between position of shower maximum X_{max} and height h above the sea level according to the definition of the US Standard Atmosphere.*

Such evaluation is of course valid only for the vertical shower. To obtain the correct X_{max} for any angle θ, where θ is the zenith angle of incoming shower, we have to use following equation:

$$X_{max}(\theta) = \int \rho(h) \frac{\mathrm{d}h}{\cos\theta} = \frac{1}{\cos\theta} \int \rho(h)\,\mathrm{d}h = \frac{X_{vertical}}{\cos\theta} \tag{5.21}$$

Unfortunately, the shower maximum is closest to the ground for the most interesting showers with the highest energies. But even for such energies of about 10^{20} eV and for the altitude of PAO ($\sim$ 1450 m a.s.l.) the shower maximum lays above critical height of 2 km above the ground for the showers with zenith angles $\theta > 40°$.

Surely, we cannot claim that the aerosols are always limited within the discussed height range and therefore we cannot guarantee at the moment the overall precision of the method without further cross-checks of real photometric data with the other data available from different atmospheric monitoring devices. On the other hand, such cross-checks will be then highly useful also for the verification of the general methodology of the astronomical photometry itself.

Advantage of passive measurement

Finally, we would like to stress here that this astronomical method has one great advantage in comparison with LIDAR measurements. Photometric measurement of standard stars is entirely non-invasive method, producing no light and not-interfering with detections of any (new) showers. The FD detector will detect and will trigger on the discussed laser shots into the field of view (shoot-the-shower method) and therefore there is some chance that during processing of this false trigger FD will miss some new coming showers. To get rid of such bogus data, there is in practice applied a FD veto during the shoot-the-shower LIDAR scan. However, the result is the same — during the duration of this veto we are losing some (quite small) fraction[13] of the showers.

5.11.2 Hardware

The telescope

The primary instrument used is a 20-cm Cassegrain-type (mirror) telescope with an Optec SSP-5 photometer with several customizations, with integrated filter slider (see Table 5.1). Effective telescope focal length is 2970 mm (focal ratio ∼1:15). This system is able to achieve magnitude 9 in 1s integration with signal to noise 100:1, what is a value needed for proper extinction modeling and still offering vast enough stars around the sky.

To make focusing possible, the system is further equipped with an electronic focuser Optec TCF-S. This Crayford-style motorized focuser is installed in secondary Cassegrain focus and bears the photometer on its moving end.

The instrument is equipped with a 45° foldable mirror, originally used for the pointing eyepiece. This eyepiece is substituted by a CCD used for automatic focusing and fine pointing of the photometer when needed. The CCD is StarLight XPress MX7 with a fixed Johnson R-band filter. The 45° mirror is motorized using a simple stepper-motor drive driven by the computer.

Wide-field camera

The secondary instrument is a simple wide-field (WF) camera. This camera provides a direct image of the area being observed, allowing detection of possible disturbing effects (clouds, airplanes) and helping with telescope pointing. Camera consists of a 200 mm/2.8 Carl-Zeiss Sonnar objective and reliable SBIG ST7 camera. The field of view of this device is 85x60 arc minutes. Being equipped with a fixed R_J filter it is able to provide reasonable photometry down to magnitude 10 in a typical 20 s exposure. This photometry may be compared with Tycho catalog to provide an independent single-color extinction model usable for testing the photometric one.

[13] Currently (October 2005), it is about 8 % during FD measurements, but since 2006 it will decrease probably below 3 %.

We also expect that this camera, although not very powerful, will be helpful with providing prompt GRB optical follow-ups in the very short period after the event.[14]

The telescope mount

Mount is a commercially available Losmandy G-11 without any customization. Our mount uses the standard GEMINI GOTO system equipped with two servomotors with relative optical encoders. It provides roughly $20'$ GOTO precision[15], which is possible to be improved to about $5'$ GOTO precision by integrated and learnable pointing model. With slewing speed $5°$ it's able to achieve any position on the sky within one minute.

Telescope dome

Telescope dome is situated on Los Leones observation site (see Fig. 5.12), in the distance approximately 20 meters in front of the bays 2 & 3, below field of view of these bays. Our custom-made laminate (epoxy) dome has square layout with a side size of about 2.5 meters. Laminate walls with steel frames are fastened to the concrete basement. Pyramid-shaped roof is splitted into two halves, which are hydraulically opened. The dome control receives information about the weather from FD Slow Control system and automatically analyzes the situation and opens/closes the doom roof according to specific situation (sunset/sunrise, strong wind over 50 km/h, rain). The telescope itself stands in the middle of the house on concrete pier, which was built as a separate part of basement and is shock-isolated from the rest of the house by styrofoam.

Photometer

Optec SSP-5A is a high-precision stellar photoelectric photometer equipped with a photomultiplier tube (PMT). Light enters the photometer through the 1.25-inch telescope adapter and is directed either to the focusing NF CCD camera or the photomultiplier tube (PMT) by means of a flip-mirror. After a star is centered, the flip-mirror is rotated to allow light to pass through the aperture stop which separates the star from the background. A Fabry lens then projects an image of the primary mirror/lens onto the photocathode of the PMT.

The use of PMT allows us to make very fast measurements of bright stars (for the brightest stars integration only several millisecond long is enough). Furthermore, the photometer produces ASCII pure ASCII/numerical output with values of star brightness, so we can directly process these results and don't have to analyze image like in the case of CCD cameras.

The R6358 PMT option was used, because this version has not only the extended response to about 185 nm, which is due to the special UV transmitting glass used in the

[14] See also Chapter 6.

[15] If we put the request to mount to go to certain position on the sky, then the difference between position where telescope finishes its slewing and the real position of searched object on the sky we call GOTO precision.

Filter position	**Filter name**	λ_{center} [nm]	**Filter FWHM** [nm]	**Note**
0	Dark	—	—	*Dark current monitoring and daytime protection*
1	u	350	38	*Strømgren u*
2	v	411	19	*Strømgren v*
3	b	467	18	*Strømgren b*
4	y	547	23	*Strømgren y*
5	U	355	70	*Johnson U*
6	—	340	7	*Special narrowband filter*
7	—	365	7	*Special narrowband filter*
8	—	394	7	*Special narrowband filter*
9	—	412	7	*Special narrowband filter*
—	R_J	697	190	*Filters used on CCD cameras*

Table 5.1: *FRAM filter characteristics*

tube. Further, the multialkalian material used in the R6358 photocathode surface extends the spectral response from the same 185 nm at the blue end to 830 nm at the red end. A Fabry lens of B270 glass and 2.9 mm center thickness cuts has transmission over 90 % down to 350 nm. At 330 nm it is still almost 80 %, then the transmission lowers to 50 % at 315 nm and to 0 % at 300 nm. However, this small loss of UV transmission near 300 nm does not adversely affect the Johnson's U or Strømgren's *u* filter transformation to the standard system.

The photometer is equipped with motorized 10-position filter slider, which allows us to shift the filters as necessary during observations. The list of all filters and theirs characteristics is available in table 5.1.

CCD cameras

Wide-field camera — SBIG ST7XE

During the first period of the test measurements (April – August 2005) we were using the Starlight XPress camera MX 516. Unfortunately, it proved to be not reliable enough for our observation purposes, because of presence of random noise spikes. These randomly placed and randomly placed spikes were identified with our automatic astrometry software as false stars. Therefore, the catalogue match of observed field of view generally have failed. The frequency of observations of these spikes was increasing with the time and so we replaced the WF camera at the end of August 2005 for the more reliable older type SBIG ST7XE.

For completeness, we present below both descriptions of WF CCD cameras.

Starlight's MX 516 is low-cost and light-weight (about 0.2 kg only) compact CCD camera with USB 1.1 interface. Camera is equipped with Sony ICX055BL SuperHAD chip with resolution of 500 × 290 pixels. Pixel size is 9.8 × 12.6μm, what gives imaging area of 4.9 × 3.6 mm. Non-square shape of pixels was causing problems for astrometry (see

5.11.3), so the images has to be correctly re-scaled before any processing. This chip has low dark current and vertical anti-blooming. There is a thermoelectric cooler to give a CCD temperature of approximately 30 degrees below ambient. The field of view of this system was $85.5' \times 63.8'$.

SBIG ST7XE weights about 0.9 kg and it is connected to the computer via parallel port. The readout of single image is therefore slower and takes about 13 seconds. The imaging CCD chip in the ST-7XE version is the enhanced KAF-0401E CCD from Kodak. The Full Frame Resolution is 765×510 pixels at $9 \times 9\mu$m, what gives imaging area of 6.9×4.6 mm. The resulting field of view is $120.7' \times 80.6'$. The camera is equipped with electromechanical exposure shutter, which is available to make exposures ranging from 0.12 s to 3600 s with 10 ms resolution. Camera is cooled with single stage thermoelectric active fan. It is possible to achieve typically 45°C below ambient temperature.

Both types of cameras were/are connected through standard M42 thread barrel to ordinary camera lens — to Sonnar 200 mm/2.8 lens. The R_J filter is installed between camera chip and camera lens.

Narrow-field camera — StarlightXpress MX 716

Starlight's MX 716 is the product from the same line as just described MX 516. The principle of small compact camera with thermoelectric cooling system is the same, camera is again communicating with main computer using USB 1.1 interface, only another chip with better resolution was used. The Sony ICX249AL EXview CCD chip with ultra low dark current and vertical anti-blooming and with image format 752×580 pixels was used. The pixel size is in this case almost square, $8.6 \times 8.3\mu$m, so the imaging area of this CCD is 6.47 mm (horizontal)$\times$ 4.83 mm (vertical). The camera is attached to the FRAM system behind the flip-mirror of photometer, so it is using the image from main Cassegrain telescope. Due to Cassegrain system speed (1:15), the field of view of this NF camera is relatively small — only about $7.5' \times 5.5'$. Again, camera is equipped with standard astronomical R_J filter to be able to obtain calibrated measurements.

As we recognized during the tests of the system, this camera has problem with interlacing of image during readout. The odd and even lines are generally shifted — final image is not composed correctly, individual star images have visible strips. This fact appeared to be fundamental problem in obtaining of automatic astrometry from this camera[16], because the stripped stars were identified as multiple star images and were not matched with star catalog. This problem was solved only very recently by a script, that is analyzing and correctly transforming images. Just recently, we were able to have first images with astrometry also from this NF camera. However, this camera still remains as the auxiliary device only, which allows to us to check, whether our centering algorithm is working properly (we need to have a star in $1'$ field of view of photometer), and which allows us to focus the main telescope, using TCF-S focuser.

[16]This camera was planned to be used as WF camera, because of its better quantum efficiency and better resolution.

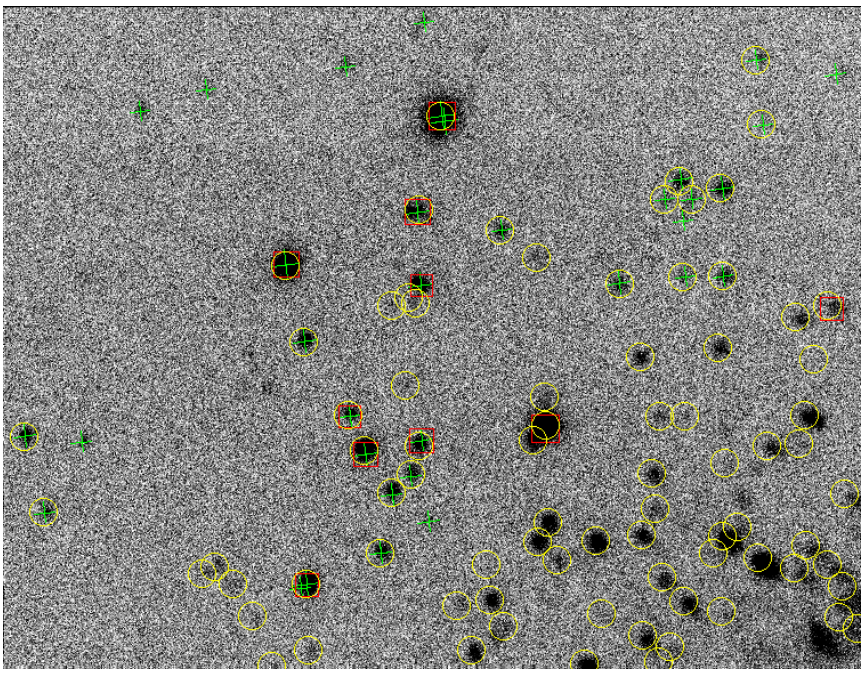

Figure 5.14: *Region near globular cluster M4 from our NF camera. The identified stars are crossed. This is one of our first images from NF camera with astrometry. The globular cluster itself is situated in the lower right corner — because of its density, no stars are identified near the core of this cluster. See also figure from WF camera (Fig. 5.15) and the description in section 5.11.3.*

5.11.3 Software

The system is driven by RTS2 software package. It is a package developed under open-source license in collaboration with robotic-telescope teams of BART [143] and BOOTES [72]. This modular, database based complex package is focused to allow fully robotic control of complete observatory, for example as described above in section 5.11.2.

RTS2 provides abstraction layers allowing the operator to separate device maintenance, planning, task execution, data pipelines and archiving and develop them as separate, though interacting tasks. From bottom this is represented by device daemons, taking care of mount, CCD cameras, mirror etc. Devices are accessed by target executor, performing all the actions needed to obtain requested observation. Executor at it's end invokes the image-reduction pipeline, to analyze the image on background.

The scheduler, staying rather aside of all the single task stuff, performs task selection based on maximum merit selection algorithm.

Target information for scheduler, observation records, image info including the obtained WCS/astrometrical info and photometry are stored in the SQL database, allowing (for example) simple and fast position lookups.

Image astrometry

The CCD images pass through image processing pipeline to perform dark subtraction, flat-fielding, star detection, field registration, precise WCS (World Coordinate System; `http://fits.gsfc.nasa.gov/fits_wcs.html`) astrometrical solution (typical RMS stays around 1/10 of pixel), give rough photometric calibration (simple fit against a single-color catalog) and search for new objects. Obtained information (apart of image header) is stored in the database.

This practically means that we *wire-up* the coordinate grid on the image; what is highly useful: such a link between (x, y) on the image and (α, δ) is an essential step for further analysis (photometry, new objects), an operator may later load such an image into the viewer and draw the catalog over it, it makes archiving quite simple and last, but not least, it allows us to perform telescope feedback.

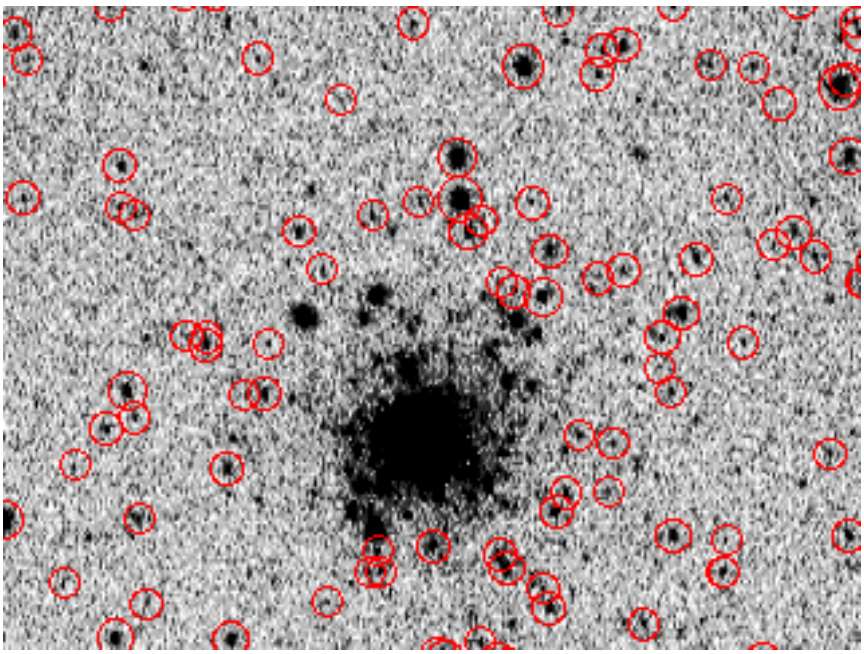

Figure 5.15: *Region around globular cluster M4 as an example of WF camera (MX 5) image with astrometry. The red circles around stars indicate theirs catalog positions. The cluster itself is so dense that individual star position are not catalogued.*

Telescope pointing

After successful image astrometry we precisely know, where the telescope is pointing, so then the telescope may actually be "told" where it is pointing. The mount precision is typically about an order of magnitude worse, than is the precision of our obtained astrometric information. However, the use of this pointing information is essential for any successful photometric observations. As mentioned above, the mount precision without any modeling is in order of tenths of angular minutes (with mount parameter modeling

about $\sim 5'$), but we need to have given star centered with precision of some fractions of angular minute (FOV of photometer is only $1'$). Knowing the precise pointing direction of the telescope, the photometer centering is then an easy job, because $1'$ corresponds to 6 pixels of WF camera and local corrections of mount position easily allow to center the studied star with subpixel precision.

5.11.4 FRAM observations

The system is capable of observing in different regimes.

Wide-field CCD observation

The simplest observing possibility is plain imaging with the WF camera. Although it is not primarily meant as an instrument for observation with direct scientific use, but rather as an engineering device to provide pointing information, there is a range of direct applications of data from this device.

Having a field of view $120' \times 64'$, the WF CCD camera covers most of the standard photometric fields on one shot, achieving similar photometric precision as the photomultiplier. However, as it does not exchange filters and uses only R_J filter, this application is limited to main model testing only (e.g. to compare the fluctuations of zero point with results given by main photometric observations).

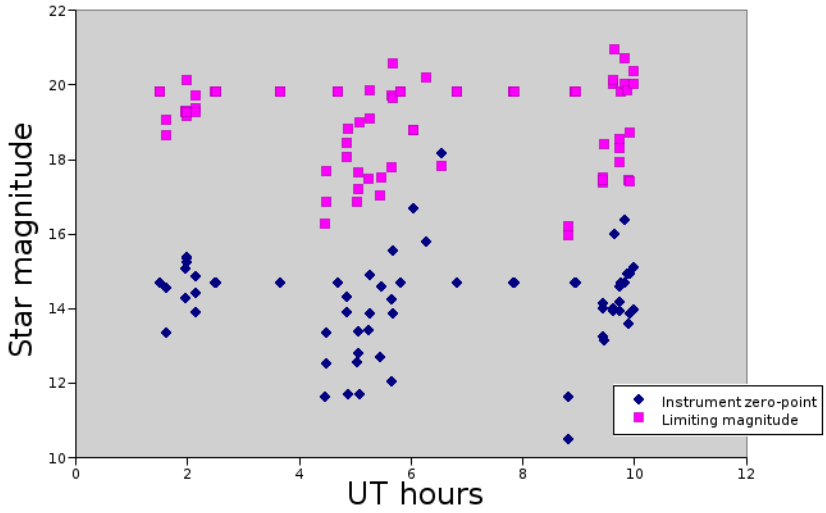

Figure 5.16: *Some rather illustrative and preliminary example of some direct WF camera image analysis for the night of May 14th, 2005. The image shows time dependence of both limiting magnitude of camera images and evaluated instrument zero-point from these images. No correction for the angular height above the horizon was made. However, three periods of strong fluctuations of these values are clearly visible. This particular night had very variable cloud cover and these fluctuating periods coincide with dense cloud cover above Los Leones site.*

Another interesting application of this simple observing technique is the prompt Gamma-Ray Bursts (GRB) optical transients (OT) follow-up observation. Although the period of potential OT visibility is very short for this particular device (minutes), the possible detection would be very welcome.

Main goal — photoelectric photometry

FRAM is primarily designed to provide the atmospheric extinction model with the maximum possible precision. The data for this model are collected by the photometer with the help of both CCDs. As was described above, the observations objects are suitable selected bright standard stars (generally brighter than 9th magnitude) from photometric catalogue [186].

The target cycle in this case begins with a slew to the position followed by a short WF camera exposure to check the pointing accuracy. The position of the photometer aperture within WF camera's image is well known, so if the initial pointing is not satisfactory the correction could be made. Also this image serves as a test of atmospheric conditions: target may be canceled, if the conditions are not fine (clouds or fog resulting in no image astrometry).

After having checked that the star of interest is within the aperture, the photometer does one sequence of measurements per filter of interest. Each sequence typically consists of thirty one-second integrations to obtain the value and its sigma in each filter. Simultaneously with the sequence, the WF camera takes the exposure. In this way pointing may be improved in real-time, the simultaneous measurement in R-filter is obtained and also it is later possible to judge (manually) queer points, if such points are eventually found within photometer data.

Altogether, this sequence gives measurements in N filters, plus N+1 CCD images in R_J.

Narrow-field CCD observation

Although the narrow-field imaging CCD is supposed to provide only focusing, pointing and centering aid, it may be used to provide scientific imaging, if needed. The NF camera images will potentially have better angular resolution and better magnitude limit for observations of any faint objects.

Special target observations

We plan or already test a set of special observations, which will allow us especially to compare our measurements with other Auger atmospheric monitoring devices.

HAM observations

The Horizontal Attenuation Monitor (HAM) uses continuously radiating Mg-Xe HID lamp situated near Coihueco building. This lamp is observed using small CCD camera with

custom mirror objective and filter wheel from the roof of Los Leones FD building (distance of about 50 kilometers). We can observe HAM lamp also with FRAM, using both our CCD cameras and photometer. Especially for cross-check tests of HAM observations we equipped FRAM with four narrowband interferometric filters with wavelengths 340, 365, 394 and 412 nm.

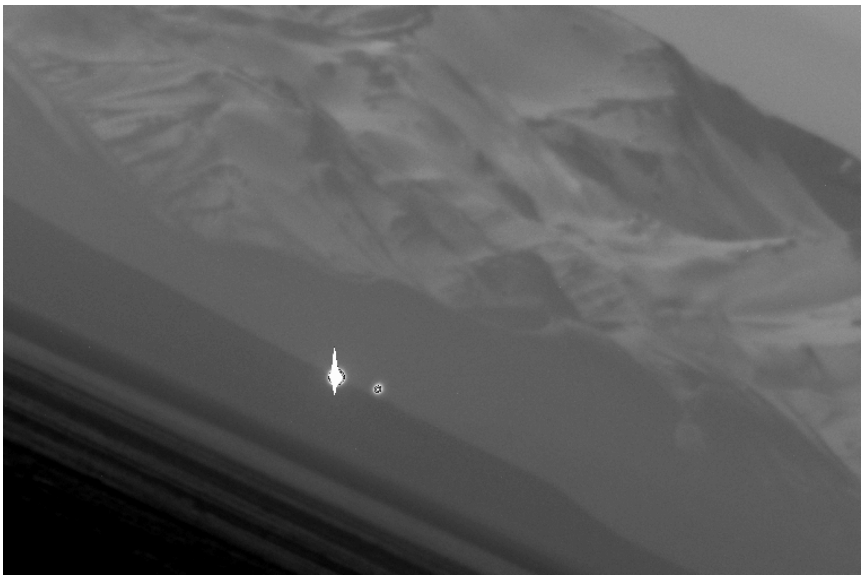

Figure 5.17: *WF CCD camera (SBIG ST7) observation under moonlight (illuminated fraction of the Moon surface was about 50 %). The brightest source on the image is HAM itself, the fainter source to the right are two red light bulbs on the Coihueco communication tower. The Coihueco ridge and pampa (lower left corner) are also visible.*

The hourly automatic observations of the HAM light source started during October 2005. For the HAM observations it is used specific astrometric algorithm, which will be later used also for *NF camera guiding* (for the description see 6.3). The brightest light source is identified within the image and then centered to the desired position on the WF camera, using iterative procedure. When such center position is achieved, the photometer flux is checked and observation script started. Currently, we took one NF camera image with 10 s exposure and 10 3 s integrations per each of 8 available filters — Strömgren filter y could not be used, because the flux from HAM source is saturating our photometer. The ultimate result of these observations is to obtain the independent values for the γ coefficient of the aerosol attenuation wavelength dependence (see 5.9).

Only very preliminary results are available (see Fig. 5.18), but if the succesfull acquisition of data of this type will continue, then we will immediately try to cross-check our data with data from regular HAM analysis and start to transfer our results to the atmospheric database of PAO.

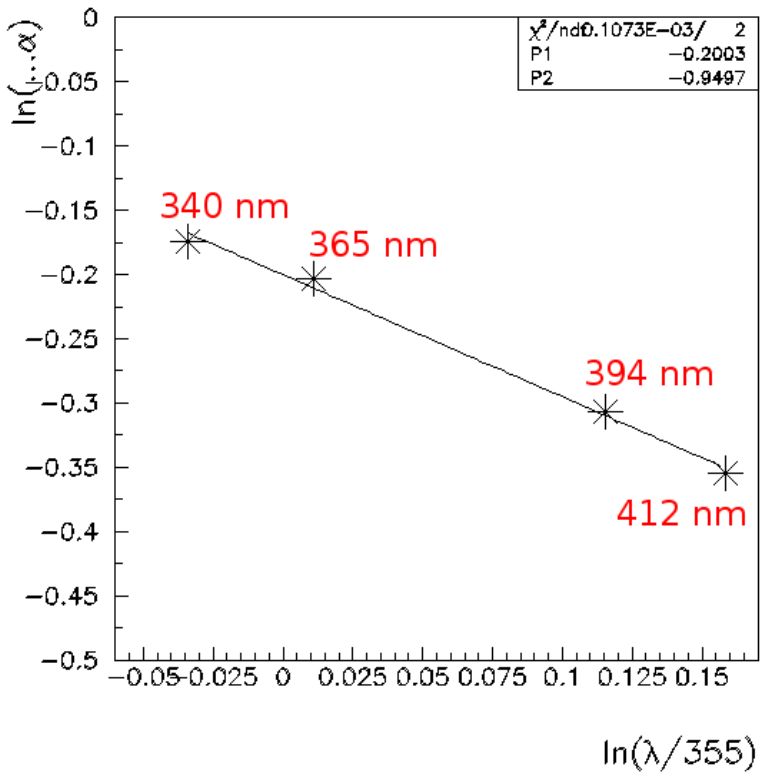

Figure 5.18: *A log-log plot and fit to the measured of HAM lamp light intensity in four of our narrowband filters. The resulting γ factor is -0.9. This plot presents only very preliminary results, because no calibration with respect to* pure Rayleigh night *or using cross-check with HAM detector has been done yet.*

Comparison with FD background data

The images of brightest stars are observable also directly from the background variance data of FD telescope. This fact was recently used for the check of absolute pointing of the telescopes. However, we can also directly monitor the star brightness as it rises in the field of view of given camera. Available background variance data are very short ($\sim$ 6 ms) photometric integrations of star brightness in filter, which is almost identical with astronomical Johnson U filter (the FD filter window is from Schott MUG-6 and it has almost the same spectral properties as Johnson U filter). FRAM photometer is equipped also with Johnson U and simultaneous millisecond observations of these bright stars could be quite easily planned.

Preliminary studies were already done as could be seen in Fig. 5.19. It is evident that the resulting spread of the FD background data is rather large, however the trend of the CLF results seems to be followed. Anyway, more extensive studies are definitely needed

to reliably establish the potential precision of this method and its usefulness as well as the cross-check data from the FRAM photometer.

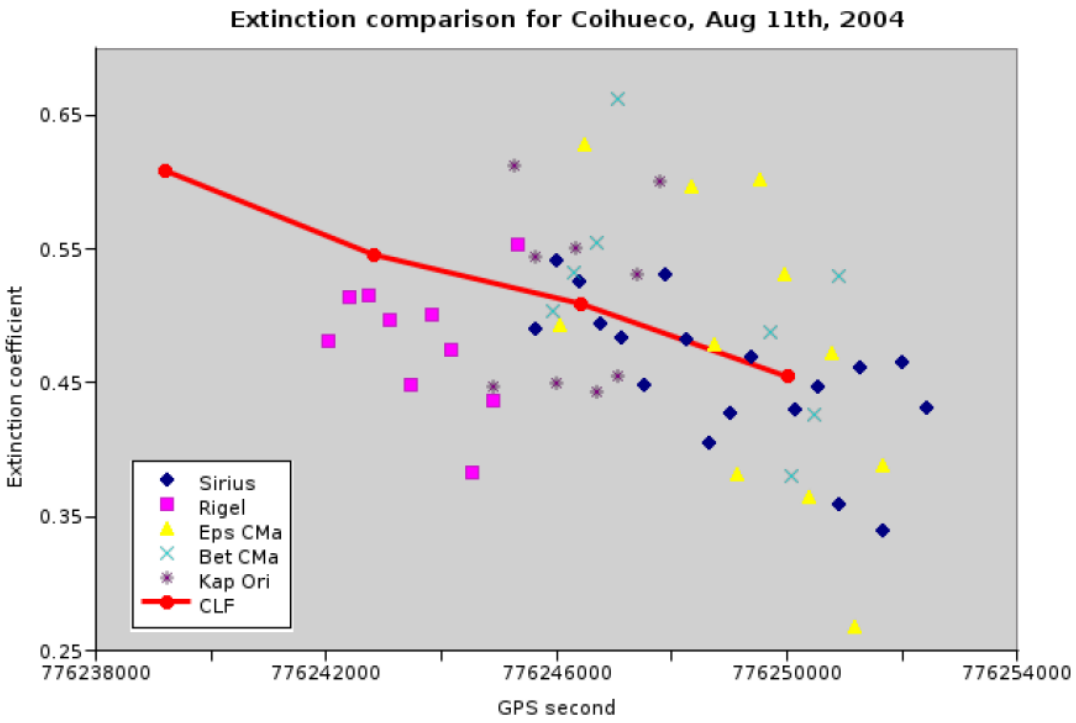

Figure 5.19: *U-band extinction coefficient comparison for Coihueco site, night of August 11th, 2004. The combined data for the brightest stars from different bays were used, relatively compared to the hourly results of analysis of CLF laser shots.*

"Shoot-the-shower" (STS)-like observations

When the suitable T3 selection and overall (STS) algorithm will be tested by LIDAR team, we can employ this observation mode also for FRAM. We can make fast and dedicated observations of the sky in the direction of just observed particularly interesting shower and then give not only "usual" wavelength dependence of extinction, derived from observations of nearest standard stars, but also e.g. magnitude limit from wide-field camera observations or test our CCD images for the presence of clouds, etc.

5.11.5 Data processing and analysis

For the obtained photometric data we plan to use automatic processing chain, with `HEC22` photometric reduction program as the most important element. Program `HEC22` is designed for an automatic multi-night reduction of photoelectric observations, their stable transformation into extinction-free instrumental and standard magnitudes, and data archiving.

All-sky as well as differential photometry of many different stars can be treated by the program. For the general background of the adopted strategy of data reduction and transformation, we can refer to work [125]. Basically, the transformation coefficients between the observed and extinction-free magnitudes determined separately for each night of observations include the first-order extinction coefficients and a possibility to model time variations of the linear extinction coefficients via polynomials up to 5^{th} degree.

We expect to finally produce for each observation night a table with hourly atmospheric extinction coefficients for different wavelengths (different filter used). Such table will allow us to go through (at least relative) comparison with the data from many different atmospheric monitoring devices, as it was discussed above in 5.2.4.

5.11.6 Summary and outlook

The FRAM system was installed on Los Leones FD observation site during March and April 2005. During May 2005 robotic operation of the telescope was tested and some hideous problems associated with mount programming were solved. In August 2005 the WF CCD camera was replaced.

During September 2005 another mechanical problem was identified—the unsufficient rigidity of the WF camera attachment to the main telescope. The pointing direction of this camera changes by $10'$ between looking at the zenit and at the horizon (with respect to the pointing direction of the main telescope).

This problem will be solved during November 2005, when the old attachment will be replaced with a new one. Because of these problems we have concentrated ourselves to the HAM light source comparison observations only.

We also plan to install an upgrade during this planned next stay, when instead of currently used motorized flip-on mirror we will install dichroic fixed hot mirror, which will speed up all observations and increase the mechanical reliability of the whole instrument.

The reliability of other parts seems to be good (e.g. roof works in automatic mode without any failure since installation in April 2005, the selection algorithm of bright photometric stars was improved and tested to select the stars with suitable airmass).

Chapter 6

Future prospects

6.1 FD observations under Moon

As it was described above, the employment of the *moonfilter* program potentially increases the FD measurement time by $\sim$ 20%. However, current status of program integration within data acquisition procedures is still rather unsatisfactory. The members of FD data taking crew have to take care of opening/closing the affected bays bays in proper time. This fact somewhat decreases the effectiveness of *moonfilter* usage, because human operators can sometimes forgot to open the bay when it is again possible or, what is worse, they also can forgot to close the bay and then — because of the Moon's quite small angular dimensions — it can endanger the exposed phototubes[1] or at least to shorten theirs lifetime due to this un-necessary intense light flux.

Therefore, we plan to integrate *moonfilter* program into the slow control software. It will check, whether the given bay is running (PMT high voltage is on) and if yes, then it will automatically operate only the bay shutter in times predicted by software. It is not necessary to change the status of any other part of the equipment or to stop DAQ for the given bay, because with closed shutter there will appear no T3 triggers and so there will be also no stored nonsense data.

We plan to start with this integration already during November 2005, and we expect to have it finished before the end of the year 2005.

6.2 FD background data

During the FD background data processing, when the main aim was to correctly evaluate the precise telesope pointing, was developed the set of software tools which allow us to try to dig some further information from this very voluminous sets of data.

[1] The photomultipliers will not be destroyed by such unwanted exposition. Electronic control system is installed and the high voltage will trip at the exposed camera part and then this camera segment will be switched off.

The main purpose of this further analysis is to obtain some cross-check information about the immediate status of the atmosphere. The advantage is that in such a case we will have the data directly from the observation site, for the light which went through the real FD telescope aperture and which was detected bu the real FD camera. Thus, such measurement will not be biased by the systematic uncertainties of different instrument or by the systematic uncertainties of the FD calibration.

However, the FD background data are not primarily dedicated for such type of analysis, so we can expect probably only rough estimates of basic values. We can for example check the presence of the clouds on the given part of the camera by checking the appropriate images of bright stars or we can check the star visibility in general or just simply estimate the average variance and from it deduce the likelihood of the presence of a cloud cover.

Furthermore, we can try to detect the faintest star on the camera (e.g. 3σ above the noise level with taking into account the altitudinal dependence of the background intensity) and then try to correlate such dependence with other known atmospheric parameters.

Or, probable the most straightforward method is to estimate the extinction itself (in Johnson U band, which spectral transmission curve agrees well with the transmission curve of the aperture M-UG 6 filter) by the observations of bright stars and by analysis of theirs changing magnitude with their growing/decreasing altitude. Preliminary studies were already done as could be seen above in Fig. 5.19.

6.3 FRAM

Probably the largest amount of future work can be associated with our robotic telescope FRAM. This is because of the recent date of the instrument installation, which was March 2005. The telescope works still in its testing phase, with some maintenance and upgrades planned for the November 2005. Since October 2005 it automatically measures the HAM lamp light source and the data are stored for the subsequent analysis and Auger amospheric database filling.

During this stay at the observatory site the faulty wide-field camera attachment will be replaced by more rigid one and the flip-on mirror will be substituted by non-moving dichroic hot mirror. Because of the properties of hot mirror the WF camera filter will be also replaced — R filter will be substituted by I filter. These setup changes will allow us to take the data more reliably. The motorized flip mirror was sometimes stuck in the middle of its rotation during southern winter months and the installation of fixed mirror naturally solves this problem. Moreover, with this semitransparent mirror we will be able to take the data simultaneously with both photometer and narrow-field camera and so significantly speed-up the measurement procedure of single star and increase the nightly statistics.

Finally, the most important upgrade associated with this semitransparent mirror installation will be the possibility of direct photometer *guiding* using immediately processed images from the narrow-field camera. The studied image of a bright star will be identified in the image from narrow-field camera and then continuously centered using finest tele-

scope movements to the projected coordinates of the center of the photometer field of view in these NF camera images. Therefore, the position of any studied star in the middle of the photometer FOV will be assured and controlled during longer expositions.

We would like to mention here two probably the most important categories of additional observations, which will enrich the portfolio of FRAM observed targets and will prove the instruments' multifunctionality.

6.3.1 Variable stars

In contrast with the situation at the northern hemisphere, the databases of observations of variable stars on the southern sky are far from completeness. Many of the world's most modern and largest telescopes was recently installed on the southern hemishere with Chile as one of their favourite locations. However, these huge perfect observatories have specific programs which rarely contain the variable stars observations and therefore still quite significant lacks of observations even of bright variable stars still exist.

Such observations could be easily incorporated into FRAM observation schedule, starting with specially selected interesting types of target stars. To give an actual example, the observation of V1007 Sco is planned just after the regular observation of photometric targets will be established.

6.3.2 Optical transients of GRBs

The software system for all telescope operations — *RTS2 system* was developed especially for the search of optical transients of gamma-ray bursts. RTS2 system uses also robotic telescope BART, located at Ondrejov site of Czech Astronomical Institute or the set of BOOTES telescopes in Spain, which very recently succeeded in observations of optical transients of two rare short-duration bursts.

This system was significantly modified to achieve FRAM main aims in atmospheric monitoring, however it is still very easy to activate special observation mode of optical transients observations. The main computer of the system then receives the alerts about potential bursts via network and then makes the images of the given part of the sky region.

The test observations of optical transients was already successfully done. In fact, we even were able establish some unique upper magnitude limits of potential optical transient of GRB 050820B. The actual results of this observation could be seen in Fig. 6.1 and were published as GRB Coordinates Network Circular Service note [145].

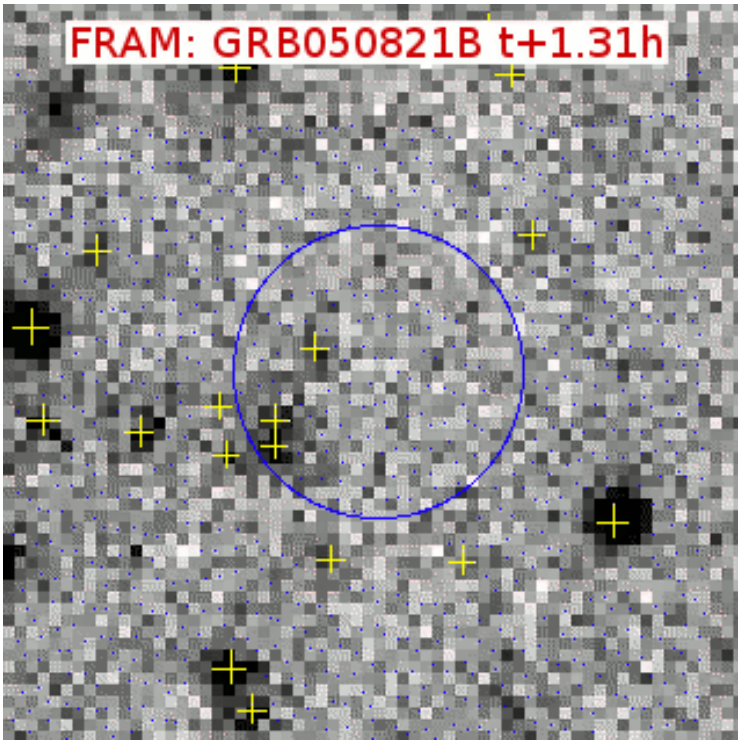

Figure 6.1: *Our telescope FRAM has observed the field of GRB050820B in semi-automatic mode starting 1.31h after the GRB onset. No new optical source is detected within the uncertainity region given by [99] GCN3840 (Fenimore et. al.). The 3-sigma limit of three coadded exposures is R=15.3 magnitude. Figure from [145].*

Chapter 7

Summary

The review of the principles of observations of the extremely energetic cosmic rays, as well as the description of the design and function of Pierre Auger observatory were presented within this thesis, when a special attention is given to the fluorescence part of the current world-largest cosmic-ray detector located in the Argentinian pampa.

Four major author's original contributions were presented in this review.

Firstly, the influence of Galactic magnetic field on cosmic ray propagation was studied alongside with some statistical analysis of resulting observed spatial distribution of these particles (see section 2.10). Results of this analysis were published separately in [193] (Astronomy & Astrophysics Journal) and in [194] (Moriond conference proceedings).

Secondly, the special code was developed [71] to allow the FD observations with the Moon above horizon (see section 4.3). Application of this code led to the relative increase of FD data taking time of about 20 %.

Thirdly, the fluorescence detector background data were used to obtain detailed analysed of exact telescopes pointing directions (see sections 4.4 & 4.5). These results were published as the Auger Project Technical GAP note [195], then briefly presented in August 2005 during 29^{th}ICRC conference in India [19] and are prepared to be submitted as a separate article in Nuclear Instruments and Methods Journal [85]. It is planned that the developed program tools for the background data analysis can be applied in near future also for at least rough independent check of U-band extinction time dependence and other comparisons of atmospheric quality.

Fourthly, the robotic photometer FRAM was designed and built at PAO site, which will primarily monitor the immediate atmospheric extinction (see chapter 5, especially section 5.11). This telescope is still in its testing phase, however after planned changes of its setup in very near future (end of year 2005) it seems that it could be very useful instrument also for additional purposes—e.g. for variable star observations and for observations of optical transients of GRBs.

Appendix A

FRAM maintenance manual

This maintenance manual was written for the Argentinian technicians who are responsible for the basic maintenance of all the monitoring instruments of the Pierre Auger Observatory. The manual was slightly modified before its insertion as an appendix of this thesis — all personal contacts and sensitive information (passwords) were removed. Main purpose of inclusion of this appendix to the thesis is to present the simplicity of basic operations with telescope system and the easiness of its common maintenance.

A.1 Introduction

FRAM is a robotic photometric telescope for atmospheric monitoring, located at the Los Leones site. It sits in a small white laminate house in front of the main building. Be careful everytime, when entering the house! Telescope could be just behind the doors... Open the doors really slowly and carefully!

A.2 Computers

There are three computers operatinf all parts of the FRAM system. Two of the computers are situated in the rack. 'fram' computer has removed cover. Its power button is removed from the front side and is hidden within computer. You can find power button on the end of the red/white wire. 'framphot' computer is slightly smaller and with cover.

192.168.12.35	framsbig.fd-leones.augernet	(SBIG ST7 CCD camera)
192.168.12.42	framcam.fd-leones.augernet	(IP camera)
192.168.12.43	fram.fd-leones.augernet	(main computer)
192.168.12.44	framphot.fd-leones augernet	(photometer readout)

Keyboard and monitor in the house are connected to the last of the computers, to 'framsbig' computer, which stands besides the rack. When some software maintenance will be necessary, then you have to ssh to 'fram' first.

There are free ethernet cables connected to the D-Link switch in the house, so you can use your notebook and ssh to any of the FRAM computers.

A.3 RTS2 software package

RTS2 software package is essential for the FRAM system operation. It's a rather complex package containing several programs servicing the roof and the telescope with it's cameras and other devices.

A.3.1 *rts2-mon*

The main control panel of RTS2 is a program called *rts2-mon*. It displays status of connected devices and allows for a limited control over them. After running the program (for best results in a full-screen xterm), you get a screen divided into three basic parts: in the top right corner, there's a main status display, together with attached clients. Under this goes the log of current traffic over the communication channel. The rest of the screen contains the device widgets, showing independently each devicemost important status values. There's the telescope (T0), photomultiplier (PHOT), two CCD cameras (C0, C1), focuser (F0), terciary mirror (M0) and the roof (DOME).

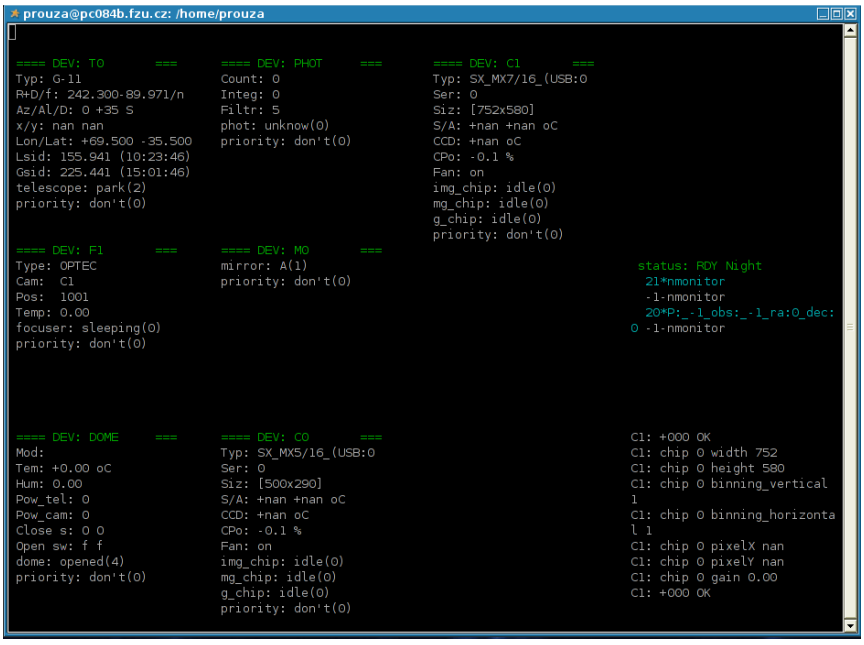

Figure A.1: *rts2-mon of FRAM telescope system*

While running the monitor, user may use the basic control keys:

- `<F2> OFF` Switch all rts2 system to off state. This means there will be neither observation, nor any steps to get ready to observation and all devices will be at their lowest power consumption level possible. Roof will stay closed all night. Telescope will stay parked and so on. This state is expected to be used especially if something gets wrong.
- `<F3> STANDBY` This switches the system to standby mode. That means there is everything being carried out as if the actual observation should run, but something (typically weather) prevents it from the actual work. The DOME device has built-in handling of this state so it switches to STANDBY temporarily when unacceptable weather is reported. Manually switching to this state is typically caused by longer predicted period of bad weather. However, it's not fully recommended as people DO forget and it might cause the system not to observe unnecesarilly by forgetting to switch it back ON (this really happened).
- `<F4> ON` Switch everything ON. Typically the system should be in this state. It takes care about itself, so it is pretty safe to leave it like that, unless really needed.
- `<F5> UPDATE` (back in rts2-mon) this requests all devices to re-send their info to the monitor. Replies may take few seconds tocome, depending on the system load. Pressing F5 again will not speed it up.
- `<F10> EXIT` Exit from the monitor.

There are several things one can do with the monitor. Apart of the basic possibility of recognizing that some device does not respond and needs to be checked (later), there's a possibility to give the devices commands. The list of commands possibly usable while maintaining the system follows:

`priority <n>` set up priority of this monitor on the system. Upon start-up, monitor has none (-1) priority. To perform any of the following actions it needs the highest priority within the system (the highest priority client claims the devices). Priority of the other clients may be seen in the main status tab (top-right corner).

Priority is needed to do anything from the following:

`{device}.{action} [parameters]`

Generic way of requesting anything from a given device. The device name is in green on top of it's widget. Actions vary and depend on the device type. Type and number of parameters depend on the device and action. All the following commands are not commands by itself but rather examples of this generic formula. `device.help` writes (into the system log, so read fast) the list of available command.

- `T0.park` Asks telescope to slew to the parking position and rest. Useful if the telescope is suspected to have lost it's position as it moves to a known, well-defined position on the mount which is simple to check.

- `T0.move <ra> <dec>` This sends the telescope to the given astronomical coordinates. T0.move 0 -90 should send the telescope to the south pole which is just another way of checking if it knows where it is pointing (very near to the telescope parking position).
- `DOME.close` Closes the roof (but normally it will open again within 15 minutes, if it does not know about any reason why to stay closed (weather, system state).
- `DOME.open` Opens the roof if possible (won't open if weather does not permit that). Note the dome driver will close the roof if it thinks it should be closed within 15 minutes.

A.3.2 Startup script

RTS2 consists of several programs running on background, invisibly to the user. Although there's a way of handling them separately, it requires a lot of experience to do that. The statup script provides an easy and efficient way of handling the system restarts in the case of some failure. Currently, subsystem restart is supported:

```
/etc/init.d/rts2 restart
```

together with `start` and `stop` (which are used while boot up/shutdown). This action restarts all devices including the roof, which implies certain period of bad weather, blocking the roof for at least 15 minutes. Apart of that, there should be no limitation of use of this script.

A.4 Hydraulic roof

Like other parts of the system, also the roof is operated through rts2 system. `/usr/local/bin/rts2-dome-fram` is the roof daemon. The system shouldn't run without this part (the crash of this part should result in reboot of whole fram computer). The restart of rts2-system, as described above, should result also in closing of the roof.

In case of emergency you can use also as root@fram in directory /root/demo:

```
./demo z    for closing
./demo o    for opening
```

If the roof doesn't close even after *rts2restart* or using *./demo* program, please check:

- if the roof transformer (black metal box) is connected to power (230V plug)
- open the black box and check — if the red diode is on and if the all fuses inside are on — and if the serial port connector is properly attached (besides of red diode)

If the roof behaves strangely (e.g. one part opening, one part closing, fuse in the black box going out during the closing procedure, strange sound of hydraulic engine, but nothing happening, etc.), please check if all the wires are properly connected to the electronic board in the black box and on the valves. There is a spare electronic board in the wooden case in the house. Please, contact us, if it appears necessary to remove the board.

There is unfortunately no way, how to close roof mechanically without removal of hydraulic oil. In case of absolute emergency and danger of damage of the system — disconnect the hydraulic hoses from engine, try to catch the hydraulic oil into some vessel and then you can close the roof manually. Roof is quite heavy, probably two or three people are necessary to close it. Please, fix then two roof pieces together using some rope (without hydraulics — there is no force holding roof halves together). If possible, inform us before doing this.

If it is not possible to close the cover and the equipment inside is endangered, please use at least the plastic sheet, which is under the wooden case. Cover the telescope and computers. Many thanks.

A.5 Telescope and its parking

The description of equatorial mount of the telescope is below, for telescope parking are important RA and DEC clutch knobs.

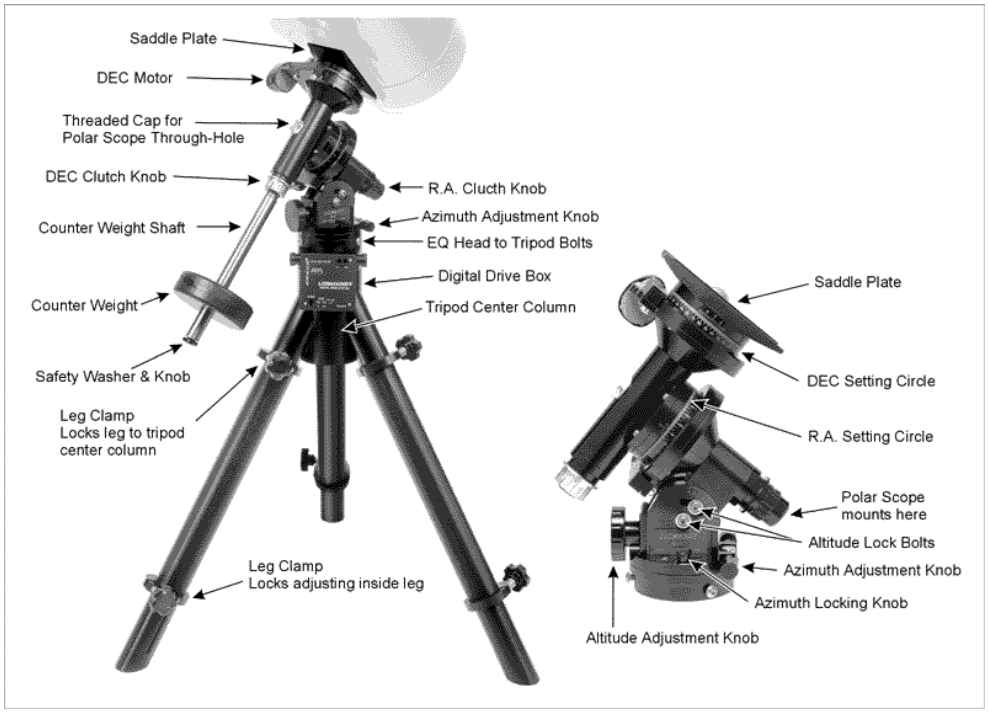

Figure A.2: *The Losmandy G-11 mount and description of its parts*

Unfortunately, telescope has no absolute sensor. So, from time, if something goes wrong telescope, could lose its alignment with stars on the sky. The only way how to correct this situation is *to park the telescope*. There are yellow stripes of tape on both telescope axis — on the declination axis (upper one, by the telescope) and on the right-ascension axis (lower one, by the telescope pier).

Each stripe is splitted to three pieces — the piece on the middle ring is loose — you can align it first with the upper part of the stripe, by turning the ring (setting circle) by finger before parking.

A.5.1 Parking procedure

1. switch off the main GEMINI box (black box fixed on the telescope pier, power switch has red LED inside) (if it is night-time and telescope could possibly move, unplug RS-232 connection from GEMINI first - not very probably during daily maintenance...)

2. release clutches on both axis

3. very gently(!) and slowly move the telescope manually to the parking position - as precisely as you can (see below if you cannot achieve sufficient precision manually). *There are black pencil lines in the middle of yellow tape stripes — the line should be really continuous one — going from upper through middle to the bottom part.*

4. tighten knobs of clutches again

5. switch on main GEMINI box and take GEMINI hand controller (see image below for hand controller)

6. GEMINI will start with some 'booting' message (what type of Gemini memory is used...) and then the message will appear: *Warm restart? :*

   Then there are four buttons in the upper part of hand controller - in rectangular pattern. You have to press once the bottom one - then the message has to change[1] to *Warm start? :*

   Confirm this by pressing right button.

   GEMINI then will say *Warm started at ...* and that's it...(when really properly aligned! if not — continue with steps below.)

7. If not properly and exactly parked manually... After warm start you can use these four buttons on hand controller also for precision movement of the mount — the upper and bottom button moves declination axis of the telescope, the left and right

[1] If not then repeat pressing the bottom button for the *warm start* message. There is also third option — *cold start*. Warm restart means that the telescope was restarted on its previous position (not the case during parking), *warm start* — no change of location, but telescope was parked — our case; finally — cold start is with the change of location and time — it deletes the alignment model. So please when parking use warm start option only.

button moves the right ascension axis. The mount will move very slowly, so you can easily align the lines on the stripes.

When the mount will be perfectly aligned, then switch off GEMINI again and go again for *warm start* as described above. (Finally the real parking position was reached.)

Figure A.3: *Main GEMINI box (left) and hand controller (right)*

A.6 Photometer reset

Photometer (Optec SSP 5A) hangs on the end of the main telescope. From time to time, very bright star or rather HAM calibration source may cause photometer to overflow. In this case the red diode (OV) continuously shines. In such case it is necessary to switch photometer just off and after some seconds then on. The switch is to the left from the diode.

Since end of June 2005 we have also possibility to restart the photometer remotely. Anyway, you will be asked, if this case will appear.

A.7 Spare parts

There is a wooden box with some spare parts located within the house (by the left wall). Some spare parts are in the box — e.g. spare electronic board for hydraulic roof, spare electric valve for hydraulics, spare telescope motor. There is also eyepiece for the telescope, set of special Allen keys, etc.

You will be probably asked, if something will have to be exchanged. But it is good to know.

Appendix B

Example of *moonfilter* output

An example of the text output of *moonfilter* program, which is printed every lunation for the purposes of the FD operators. The one below is for the whole 12th lunation in 2005. Only the *important* times are shown — so are dubbed the times, when some operator activity is needed. Actually, the start and end of the dark period (astronomical twilight), the Moon rise/set and times of opening/closing of any shutters of any FD site are shown. The table contains the date and local time, the Moon altitude and azimuth, its illuminated fraction and magnitude, the estimated level of the FD background brightness and status of individual bays (in this order).

```
*** MOONFILTER *** Program for Moon filtering during FD DAQ; PAO Malargue
Starting date is 23.11.2005.

*** Next night *** [o - open; X - close]                  Los Leones    Coihueco      Los Morados
Date        Time      Alt.   Az.     Frac.  Mag.   Var.   1 2 3 4 5 6   1 2 3 4 5 6   1 2 3 4 5 6
23.11.2005  22:13:00  -----  ------  -----  -----    20   o o o o o o   o o o o o o   o o o o o o
24.11.2005  02:39:00   0.06   16.00  0.472  -10.0    20   o X o o o o   o o o o X o   o o o o o o
24.11.2005  03:41:00  11.72   25.07  0.468  -10.0    89   o X X o o o   o o o o X o   o o o o o o
24.11.2005  04:00:00  15.14   28.12  0.467  -10.0   107   o X X o o o   o o o o X X   o o o o o o
24.11.2005  04:37:00  21.34   34.37  0.464  -10.0   131   o X X o o o   o o o o X X   o o o o o o

*** Next night *** [o - open; X - close]                  Los Leones    Coihueco      Los Morados
Date        Time      Alt.   Az.     Frac.  Mag.   Var.   1 2 3 4 5 6   1 2 3 4 5 6   1 2 3 4 5 6
24.11.2005  22:14:00  -----  ------  -----  -----    20   o o o o o o   o o o o o o   o o o o o o
25.11.2005  03:03:00   0.12    9.31  0.377   -9.5    20   o X o o o o   o o o o X o   o o o o o o
25.11.2005  04:36:00  17.88   22.94  0.371   -9.5    85   o X o o o o   o o o o X o   o o o o o o

*** Next night *** [o - open; X - close]                  Los Leones    Coihueco      Los Morados
Date        Time      Alt.   Az.     Frac.  Mag.   Var.   1 2 3 4 5 6   1 2 3 4 5 6   1 2 3 4 5 6
25.11.2005  22:15:00  -----  ------  -----  -----    20   o o o o o o   o o o o o o   o o o o o o
26.11.2005  03:26:00   0.15    2.24  0.285   -9.0    20   X X o o o o   o o o X X o   o o o o o o
26.11.2005  03:47:00   4.36    5.14  0.284   -9.0    26   o X o o o o   o o o X X o   o o o o o o
26.11.2005  04:08:00   8.55    8.08  0.282   -9.0    39   o X o o o o   o o o o X o   o o o o o o
26.11.2005  04:35:00  13.70   11.84  0.281   -9.0    53   o X o o o o   o o o o X o   o o o o o o

*** Next night *** [o - open; X - close]                  Los Leones    Coihueco      Los Morados
Date        Time      Alt.   Az.     Frac.  Mag.   Var.   1 2 3 4 5 6   1 2 3 4 5 6   1 2 3 4 5 6
26.11.2005  22:17:00  -----  ------  -----  -----    20   o o o o o o   o o o o o o   o o o o o o
27.11.2005  03:49:00   0.08  354.93  0.199   -8.4    20   X o o o o o   o o o X o o   o o o o o o
27.11.2005  03:50:00   0.28  355.07  0.199   -8.4    20   X X o o o o   o o o X o o   o o o o o o
27.11.2005  04:12:00   4.69  358.06  0.198   -8.4    24   X X o o o o   o o o X X o   o o o o o o
27.11.2005  04:35:00   9.10    1.07  0.197   -8.4    32   X X o o o o   o o o X X o   o o o o o o
```

```
*** Next night *** [o - open; X - close]                Los Leones    Coihueco      Los Morados
Date        Time      Alt.   Az.     Frac.  Mag.   Var.  1 2 3 4 5 6   1 2 3 4 5 6   1 2 3 4 5 6
27.11.2005  22:18:00  -----  ------  -----  -----    20  o o o o o o   o o o o o o   o o o o o o
28.11.2005  04:14:00   0.05  347.66  0.124   -7.6    20  X o o o o o   o o o X o o   o o o o o o
28.11.2005  04:34:00   3.79  350.22  0.123   -7.6    21  X o o o o o   o o o X o o   o o o o o o

*** Next night *** [o - open; X - close]                Los Leones    Coihueco      Los Morados
Date        Time      Alt.   Az.     Frac.  Mag.   Var.  1 2 3 4 5 6   1 2 3 4 5 6   1 2 3 4 5 6
28.11.2005  22:19:00  -----  ------  -----  -----    20  o o o o o o   o o o o o o   o o o o o o
29.11.2005  04:33:00  -----  ------  -----  -----    20  o o o o o o   o o o o o o   o o o o o o

*** Next night *** [o - open; X - close]                Los Leones    Coihueco      Los Morados
Date        Time      Alt.   Az.     Frac.  Mag.   Var.  1 2 3 4 5 6   1 2 3 4 5 6   1 2 3 4 5 6
29.11.2005  22:20:00  -----  ------  -----  -----    20  o o o o o o   o o o o o o   o o o o o o
30.11.2005  04:33:00  -----  ------  -----  -----    20  o o o o o o   o o o o o o   o o o o o o

*** Next night *** [o - open; X - close]                Los Leones    Coihueco      Los Morados
Date        Time      Alt.   Az.     Frac.  Mag.   Var.  1 2 3 4 5 6   1 2 3 4 5 6   1 2 3 4 5 6
30.11.2005  22:22:00  -----  ------  -----  -----    20  o o o o o o   o o o o o o   o o o o o o
 1.12.2005  04:32:00  -----  ------  -----  -----    20  o o o o o o   o o o o o o   o o o o o o

*** Next night *** [o - open; X - close]                Los Leones    Coihueco      Los Morados
Date        Time      Alt.   Az.     Frac.  Mag.   Var.  1 2 3 4 5 6   1 2 3 4 5 6   1 2 3 4 5 6
 1.12.2005  22:23:00  -----  ------  -----  -----    20  o o o o o o   o o o o o o   o o o o o o
 2.12.2005  04:32:00  -----  ------  -----  -----    20  o o o o o o   o o o o o o   o o o o o o

*** Next night *** [o - open; X - close]                Los Leones    Coihueco      Los Morados
Date        Time      Alt.   Az.     Frac.  Mag.   Var.  1 2 3 4 5 6   1 2 3 4 5 6   1 2 3 4 5 6
 2.12.2005  22:24:00  -----  ------  -----  -----    20  o o o o o o   o o o o o o   o o o o o o
 3.12.2005  04:32:00  -----  ------  -----  -----    20  o o o o o o   o o o o o o   o o o o o o

*** Next night *** [o - open; X - close]                Los Leones    Coihueco      Los Morados
Date        Time      Alt.   Az.     Frac.  Mag.   Var.  1 2 3 4 5 6   1 2 3 4 5 6   1 2 3 4 5 6
 3.12.2005  22:25:00   8.04  207.68  0.079   -7.0    23  o o o o o o   o o o o o o   o o o o X X
 3.12.2005  23:13:00  -----  ------  -----  -----    20  o o o o o o   o o o o o o   o o o o o o
 4.12.2005  04:31:00  -----  ------  -----  -----    20  o o o o o o   o o o o o o   o o o o o o

*** Next night *** [o - open; X - close]                Los Leones    Coihueco      Los Morados
Date        Time      Alt.   Az.     Frac.  Mag.   Var.  1 2 3 4 5 6   1 2 3 4 5 6   1 2 3 4 5 6
 4.12.2005  22:26:00  17.68  198.19  0.152   -8.0    38  o o o o o o   o o o o o o   o o o o X o
 4.12.2005  23:23:00   7.22  205.01  0.156   -8.0    27  o o o o o o   o o o o o o   o o o o X X
 5.12.2005  00:05:00  -----  ------  -----  -----    20  o o o o o o   o o o o o o   o o o o o o
 5.12.2005  04:31:00  -----  ------  -----  -----    20  o o o o o o   o o o o o o   o o o o o o

*** Next night *** [o - open; X - close]                Los Leones    Coihueco      Los Morados
Date        Time      Alt.   Az.     Frac.  Mag.   Var.  1 2 3 4 5 6   1 2 3 4 5 6   1 2 3 4 5 6
 5.12.2005  22:27:00  26.59  187.39  0.245   -8.7    68  o o o o o o   o o o o o o   o o o o X o
 6.12.2005  00:47:00  -----  ------  -----  -----    20  o o o o o o   o o o o o o   o o o o o o
 6.12.2005  04:31:00  -----  ------  -----  -----    20  o o o o o o   o o o o o o   o o o o o o

*** Next night *** [o - open; X - close]                Los Leones    Coihueco      Los Morados
Date        Time      Alt.   Az.     Frac.  Mag.   Var.  1 2 3 4 5 6   1 2 3 4 5 6   1 2 3 4 5 6
 6.12.2005  22:29:00  34.12  174.85  0.350   -9.4   118  o o o o o o   o o o o o o   o o o X o o
 6.12.2005  22:31:00  33.72  175.14  0.351   -9.4   118  o o o o o o   o o o o o o   o o o X X o
 6.12.2005  23:44:00  19.20  185.06  0.356   -9.4    96  o o o o o o   o o o o o o   o o o o X o
 7.12.2005  01:23:00  -----  ------  -----  -----    20  o o o o o o   o o o o o o   o o o o o o
 7.12.2005  04:30:00  -----  ------  -----  -----    20  o o o o o o   o o o o o o   o o o o o o

*** Next night *** [o - open; X - close]                Los Leones    Coihueco      Los Morados
Date        Time      Alt.   Az.     Frac.  Mag.   Var.  1 2 3 4 5 6   1 2 3 4 5 6   1 2 3 4 5 6
 7.12.2005  22:30:00  40.06  159.87  0.463  -10.0   191  o o o o o o   o o o o o o   o o o o o o
 7.12.2005  22:47:00  36.83  163.05  0.464  -10.0   188  o o o o o o   o o o o o o   o o o X o o
 8.12.2005  00:03:00  21.92  175.07  0.470  -10.0   156  o o o o o o   o o o o o o   o o o X X o
 8.12.2005  01:16:00   7.33  185.03  0.476  -10.0    66  o o o o o o   o o o o o o   o o o o X o
 8.12.2005  01:53:00  -----  ------  -----  -----    20  o o o o o o   o o o o o o   o o o o o o
 8.12.2005  04:30:00  -----  ------  -----  -----    20  o o o o o o   o o o o o o   o o o o o o
```

Bibliography

[1] Abbasi R.U. et al. (The HiRes Collaboration), 2005, Phys.Lett. B619, 271 (also Preprint astro-ph/0501317)

[2] Abendschein A. & Matthews J.A.J., 2003, Auger Technical GAP Note 2003–059

[3] Abraham J., ..., Prouza M., ... (The Auger Collaboration), 2004, Nuclear Instruments and Methods, A 523 2004, 50

[4] Abu-Zayyad T. et al., 2000, Phys. Rev. Lett. 84, 4276

[5] Afanasiev B.N. et al., 1993, in Nagano M. (ed.) Proceedings of the Tokyo Workshop on Techniques for the Study of the Extremely High Energy Cosmic Rays, 35

[6] Aharonian F.A., Cronin J.W., 1994, Phys. Rev. D 50, 1892

[7] Ahn E.-J., Medina-Tanco G., Biermann P., Stanev T., 1999, Preprint astro-ph/9911123

[8] Allard D. et al. for the Auger Collaboration, 2005, Proceedings of the 29th International Cosmic Ray Conference Pune, HE1.4, usa-lhenry-yvon-I-abs1-he14-poster

[9] Allard D. et al. for the Auger Collaboration, 2005, Proceedings of the 29th International Cosmic Ray Conference Pune, HE1.4, fra-parizot-E-abs1-he14-poster

[10] Allison P. et al. for the Auger Collaboration, 2005, Proceedings of the 29th International Cosmic Ray Conference Pune, HE1.4, usa-covault-C-abs2-he15-poster

[11] Alvarez-Muñiz J., Engel R. & Stanev T., 2002, ApJ 572, 185

[12] Ambrosio M. et al., 2001, IEEE Transactions on Nuclear Science 48, 400

[13] Apanasenko A.V., Sukhadolskaya V.A., Derbina V.A. et al., 2001, Astroparticle Physics 16, 13

[14] Aramo C. et al., 2005, Auger Technical GAP Note 2005–027

[15] Aramo C. et al. for the Auger Collaboration, 2005, Proceedings of the 29th International Cosmic Ray Conference Pune, HE1.5, ita-insolia-A-abs1-he15-poster

[16] Arciprete F. et al. (The AIRFLY Collaboration), 2005, Proceedings of the 29th International Cosmic Ray Conference Pune, HE1.4, cze-bohacova-M-abs1-he14-poster

[17] Argiró S., Camin D. V., Destro M., Guérard C. K., 1999, Nuclear Instruments and Methods, **A435** (1999) pp. 484-489.

[18] Argiró S. et al. for the Auger Collaboration, 2005, Proceedings of the 29th International Cosmic Ray Conference Pune, HE1.5, usa-paul-T-abs1-he15-poster

[19] Arqueros F. et al. for the Auger Collaboration, 2005, Proceedings of the 29th International Cosmic Ray Conference Pune, HE1.5, usa-malek-M-abs1-he15-poster

[20] The Ashra Collaboration, `http://www.icrr.u-tokyo.ac.jp/~ashra/index-e.html`

[21] The Auger Collaboration, 2004, Technical Design Report, draft, pp. 1-491
(For the Auger Collaboration authors list please see:
`http://www.auger.org/admin/ICRC_2005_Author_List.pdf`*)*

[22] The Auger Collaboration, 2005, Proceedings of the 29th International Cosmic Ray Conference Pune, HE1.4, arg-bertou-X-abs1-he14-oral

[23] The Auger Collaboration, 2005, Proceedings of the 29th International Cosmic Ray Conference Pune, HE1.4, fra-revenu-B-abs1-he14-oral

[24] The Auger Collaboration, 2005, Proceedings of the 29th International Cosmic Ray Conference Pune, HE1.4, usa-sommers-P-abs1-he14-oral

[25] The Auger Collaboration, 2005, Proceedings of the 29th International Cosmic Ray Conference Pune, HE1.4, ger-risse-M-abs2-he14-oral

[26] The Auger Collaboration, 2005, Proceedings of the 29th International Cosmic Ray Conference Pune, HE1.4, usa-mostafa-M-abs1-he14-oral

[27] The Auger Collaboration, 2005, Proceedings of the 29th International Cosmic Ray Conference Pune, HE1.4, aus-bellido-J-abs1-he14-oral

[28] The Auger Collaboration, 2005, Proceedings of the 29th International Cosmic Ray Conference Pune, HE1.4, bra-bonifazi-C-abs1-he14-oral

[29] The Auger Collaboration, 2005, Proceedings of the 29th International Cosmic Ray Conference Pune, HE1.4, fra-letessier-selvon-A-abs1-he14-oral

[30] The Auger Collaboration, 2005, Proceedings of the 29th International Cosmic Ray Conference Pune, HE1.4, ita-ghia-P-abs1-he14-oral

[31] Auger P., Maze R., 1938, C. R. Acad. Sci. Ser. B 207, 228

[32] Auger P., 1945, What are Cosmic Rays?, University of Chicago Press

[33] The Auger Collaboration, 1997, The Pierre Auger Observatory Design Report, Fermilab

[34] The Auger Project Official Website, 2005, `http://www.auger.org/admin`

[35] Axford W.I. et al., 1977, in Proceedings of the 15th International Cosmic Ray Conference, Plovdiv, Vol. 11, 132

[36] Axford W.I., 1994, Ap& SS 90, 937

[37] Baltrusaitis R. M., Cady R. et al., 1985, Nucl. Instrum. Methods Phys. Res. A 240, 410

[38] Bassi P., Clark G., Rossi B., 1953, Phys. Rev. 92, 441

[39] Bauleo P. et al. for the Auger Collaboration, 2005, Proceedings of the 29th International Cosmic Ray Conference Pune, HE1.5, arg-rovero-AC-abs1-he15-poster

[40] Beck R., Brandenburg A., Moss D., Shukurov A., Sokoloff D., 1995, NORDITA preprint 95/67 A

[41] Beck R., Brandenburg A., Moss D., Shukurov A. & Sokoloff D., 1996, ARA& A 34, 155

[42] Beck R., 2000, Preprint astro-ph/0012402

[43] Beck R., 2001, Space Science Reviews 99 (1), 243

[44] Bellido J.A. et al. for the Auger Collaboration, 2005, Proceedings of the 29th International Cosmic Ray Conference Pune, HE1.5, ta-petrera-S-abs1-he15-poster

[45] Bellido J. et al., 2005, Pierre Auger Project Technical GAP note 2005–016

[46] Berezinsky V.S., Grigoreva S.I., 1988, A&A 199, 1

[47] Berezinsky V. et al. (The EUSO Collaboration), Proceedings of the 29th International Cosmic Ray Conference Pune, HE1.5, ger-teshima-M-abs1-HE15-poster

[48] Berezinsky V., Gazizov A.Z., Grigorieva S.I., 2002, Preprint astro-ph/0204357

[49] Berezinsky V.S., Preprint hep-ph/9802351

[50] Bergman D. R. (The HiRes Collaboration), Proceedings of the 29th International Cosmic Ray Conference Pune, HE1.4, usa-bergman-D-he14-poster

[51] Bertou X., Boratav M., Selvon-Letessier A., 2000, Preprint astro-ph/0001516

[52] Bhattacharjee P., Sigl G., 2000, Phys. Rep. 327, 110

[53] Billoir P., Letessier-Selvon A., 2000, Preprint astro-ph/0001427

[54] Bird D.J. et al., 1994, ApJ 424, 491

[55] Bird D.J. et al., 1995, ApJ 441, 144

[56] Blasi P., Epstein R.I., Olinto A.V., 2000, ApJ 533, L123

[57] Blumenthal G.R., 1970, Phys. Rev. D 1, 1596

[58] Boháčová M., 1999, Diploma Thesis, Charles University Prague

[59] Boldt E., Ghosh P., 1999, Mon. Not. R. Astron. Soc. 307, 491

[60] Borreani G. et al., 2001, IEEE Transactions on Nuclear Science 48 ,406

[61] Blü mer J. et al. for the Auger Collaboration, Proceedings of the 29th International Cosmic Ray Conference Pune, HE1.4, ger-keilhauer-B-abs2-he14-poster

[62] Brack J., Meyhandan R.& Hofman G., 2002, Pierre Auger Project Technical GAP note 2002–033.

[63] Brunetti M.T., Codino A., 2000, ApJ 528, 789

[64] Bunner A. N., 1964, PhD Thesis.

[65] Bucholtz A., 1995, Appl. Opt. 34, 2765

[66] Camin D. V. et al., 1999, Pierre Auger Technical GAP note 1999–043

[67] Camin D. V. et al., 2004, IEEE Transactions on Nuclear Science 51, 3034

[68] Capdevielle J.N. et al., 1992, Kernforschungzentrum Karlsruhe preprint KfK 4998

[69] Caruso R.& Petrera S., 2004, GAP note, 2004–072.

[70] Caruso R. et al. for the Auger Collaboration, 2005, Proceedings of the 29th International Cosmic Ray Conference Pune, HE1.5, ita-petrera-S-abs2-he15-poster

[71] Caruso R. et al. for the Auger Collaboration, 2005, Proceedings of the 29th International Cosmic Ray Conference Pune, HE1.5, ita-rodriguezmartino-J-abs1-he15-poster

[72] Castro-Tirado A.J. et al., 2005, `http://laeff.esa.es/BOOTES/ing/index.html`

[73] Catalogue of Highest Energy Cosmic Rays, 1980, World Data Center for Cosmic Rays, Institute of Physical and Chemical Research, Itabashi, Tokyo, Japan

[74] Cester R. et al. for the Auger Collaboration, 2005, Proceedings of the 29th International Cosmic Ray Conference Pune, HE1.4, usa-roberts-M-abs1-he15-poster

[75] Chudakov A. E., Suga K. et al., 1962, Laboratorio de Fisica Cosmic de la Universidad Mayor de San Andreas, La Paz, Bolivia, 2, pp. XLIX.

[76] Coleman S., Glashow S.L., 1999, Phys. Rev. D 59, 116008

[77] Committee on the Physics of the Universe, National Research Council, 2003, Connecting Quarks with the Cosmos: Eleven Science Questions for the New Century, The National Academies Press

[78] Compton A.H., 1933, Phys. Rev. 43, 387

[79] Cordero A. et al., 1996, Auger Technical Gap Note 1996–039

[80] Cowsik R., Rajalakshmi G., Sreekantan B.V., 1999, in: Nagano M. (ed.) Proceedings of the 26th International Cosmic Ray Conference, Salt Lake City, HE 5.3.09

[81] Cronin J.W., 1992, Nucl. Phys. B. (Proc. Suppl.) 28B, 213

[82] Cronin J.W., 1999, Rev. Mod. Phys. 71, S165

[83] Dar A., 2000, Preprint astro-ph/0006013

[84] Dawson B.R. & Smith A.G.K., 1997, Proc. Int. Symp. on Extremely High Energy Cosmic Rays (University of Tokyo)

[85] De Donato C. et al., 2005, to be submitted to Nucl. Inst. Methods A

[86] Delvaille J., Kendzicrski F., Greisen K., 1962, Journal of the Physical Society of Japan, 17, 76 Supplement A-III, Proceedings of the International Conference on Cosmic Rays and the Earth Storm, held 5-15 September, 1961 in Kyoto. Volume II1: Cosmic Rays. Published by the Physical Society of Japan, 1962.

[87] De Marzo C.N., 1998, in: Krizmanic J.F., Ormes J.F., Streitmatter R.E. (eds.) Proceesdings of Workshop on Observing Giant Cosmic Ray Air Showers from $> 10^{20}$ eV Particles from Space, AIP Conf. Proc. No. 433, 87

[88] Dravins D., Lindegren L.& Mezey E., 1997, Publications of Astronomical Society of the Pacific, Vol. 109, pp. 173–207, 1997.

[89] Drechser H.J. et al., 2001, Phys. Rep. 350, 93

[90] Elbert J.W., Sommers P., 1995, ApJ 441, 151

[91] Ellis J., 2000, Preprint astro-ph/0010474

[92] Elstner D., Meinel R., Beck R., 1992, A& AS 94, 587

[93] Enge H. A., 1966, Introduction to nuclear physics, Addison-Wesley Publishing Co.

[94] Engelmann J.J. et al. , 1990, A & A 223, 96

[95] Farrar G.R., 1996, Phys. Rev. Lett. 76, 4111

[96] Farrar G.R., Piran T., 1999, Preprint New York University 99-XX

[97] Fasso A., Ferrari A., Sala P.R., 2001, Proceedings of the MonteCarlo 2000 Conference, Lisbon, October 23–26 2000, A. Kling, F. Barao, M. Nakagawa, L. Tavora, P. Vaz eds., Springer-Verlag Berlin, 159-164

[98] Fasso A., Ferrari A., Sala P.R., 2001, Proceedings of the MonteCarlo 2000 Conference, Lisbon, October 23–26 2000, A. Kling, F. Barao, M. Nakagawa, L. Tavora, P. Vaz eds., Springer-Verlag Berlin, p. 955-960

[99] Fenimore M. et al., 2005, GRB Coordinates Network Circular Service, 3840, 1

[100] Fermi E., 1949, Phys. Rev. 75, 1169

[101] Fesefeldt F., 1985, Report PITHA-85/02, RWTH Achen

[102] Finley C.B., Westerhoff S., 2004, Astroparticle Physics 21, 359

[103] Finley C.B., Westerhoff S. (The Hires Collaboration), 2005, Proceedings of the 29th International Cosmic Ray Conference Pune, HE1.4, usa-finley-C-abs1-he14-oral

[104] Fletcher R.S. et al. , 1994, Phys. Rev. D 50, 5710

[105] Gaisser T.K., 1990, Cosmic Rays and Particle Physics, Cambridge University Press

[106] Gaisser T.K., 2000, Preprint astro-ph/0011525

[107] Gaisser T.K., 2001, AIP Conference Proceedings 558, 27

[108] Garcia-Munoz M. et al., 1987, ApJS 64, 269

[109] Garstang R.H., 1989, Publications of the Astronomical Society of the Pacific 101, 326

[110] Giller M. et al., 2000, Auger Technical Gap Note 2000–032

[111] Girdwood L. & Kubánek P., 2005, `http://libnova.sourceforge.net`

[112] Gorbunov D. et al., 2004, JETP Lett. 80, 145

[113] Green D.A., 2001, A Catalogue of Galactic Supernova Remnants, `http://www.mrao.cam.ac.uk/surveys/snrs/`

[114] Greisen K., 1956, in: Wilson J.G. (ed.) Progress in Cosmic Ray Physics III, 3

[115] Greisen K., 1960, Annual Review of Nuclear and Particle Science, **10** (1960), pp. 63-108.

[116] Greisen K., 1966, Phys. Rev. Lett. 16, 748

[117] Han J.L., Qiao G.J., 1994, A & A 288, 759

[118] Han J.L., Manchester R.N., Qiao G.J., 1999, Mon. Not. R. Astron. Soc. 306, 371

[119] Han J.L., 2002, AIP Conference Proceedings 609, 96

[120] Han J.L., Manchester R.N., Lyne A.G. & Qiao G.J., 2002, ApJ 570, L17

[121] Hara T., Kawaguchi S., Mikamo S., Nagano M., Suga K., Tanahashi G., Uchino K., Akiyama H., 1970, Acta Phys. Acad. Sci. Hung. 29, Suppl. 3, 361

[122] Harari D., Mollerach S., Roulet E., 2000, Preprint astro-ph/0010068 v2

[123] Harari D., Mollerach S., Roulet E., 2000, AIP Conference Proceedings 566, 289

[124] Harari D., Mollerach S., Roulet E. & Sánchez F., 2002, The Journal of High Energy Physics 03, 045

[125] Harmanec P., Horn J., Juza K., 1994, A&AS, 104, 121

[126] Haungs A., 2003, J. Phys. G: Nucl. Part. Phys. 29, 809 (also Preprint astro-ph/0212481 v1)

[127] Hayashida N. et al., 2000, Preprint astro-ph/0008102

[128] Hess V., 1912, Physik. Zeitschr. 13, 1084

[129] Hill C.T., Schramm D.N., 1985, Phys. Rev. D 31, 564

[130] Hillas A.M., 1968, Can. J. Phys. 46, S623

[131] Hillas A.M., 1970, Acta Phys. Acad. Sci. Hung. 29, Suppl. 3, 355

[132] Hillas A.M. et al., 1971, in Proceedings of the 12th International Cosmic Ray Conference, Hobart, Vol. 3, 1001

[133] Hillas A.M., 1985, in: Proceedings of the 19th International Cosmic Ray Conference, La Jolla, Vol. 1, 155

[134] Hiltner W.A., 1949, ApJ 109, 471

[135] Hoffleit D.& Warren W. H. Jr., 1991, Astronomical Data Center, NSSDC/ADC, 1991.

[136] Hörandel J.R., 2003, Astroparticle Physics 19, 193 (also Preprint astro-ph/0210453 v1)

[137] http://www.elsevier.com/wps/find/journaldescription.cws_ _home/523319/description#description

[138] http://www.nightskylive.com

[139] http://www.isiknowledge.com/portal.cgi?DestApp=JCR

[140] http://www.physics.adelaide.edu.au/astrophysics/

[141] http://www.iop.org/EJ/journal/JCAP

[142] Hrabovský M., Palatka M., Schová nek P., Grygar J., Řídký J., Soukup L., 1999, Auger Technical GAP Note 1999–025

[143] Hudec R. et al.: http://lascaux.asu.cas.cz

[144] Hughes R. H., Philpot J. L., Fan C. Y., 1961, Physical Review, 123, 2084

[145] Jelínek M., Prouza M. et al., 2005, GRB Coordinates Network Circular Service, 3854, 1

[146] Johnson H.L., Morgan W.W., Astrophysical Journal 117, 313 (1953).

[147] Johnson H.L. et al., 1966, Commun. Lunar & Planet. Lab. 4, 99, Table 9

[148] Kakimoto F. et al., 1996, Nuclear Instruments and Methods in Physics Research A 372, 527

[149] Kalmykov N.N., Ostapchenko S.S and Pavlov A.I., 1997, Nucl. Phys. Proc Suppl. B 52, 17

[150] Karakula S., Osborne J.L., Roberts E., Tkaczyk W., 1972, J. Phys. A 5, 904

[151] Kawai H. et al. (The Telescope Array Collaboration), Proceedings of the 29th International Cosmic Ray Conference Pune, HE1.5, jap-fukushima-M-abs1-HE15-oral

[152] Keilhauer B. et al., Pierre Auger Technical GAP note 2003–107 or GAP note 2005–021

[153] Kewley L.J., Clay R.W., Dawson B.R., 1996, Astropart. Phys. 5, 69

[154] Klages H.O. et al., 1997, Nucl. Phys. B (Proc. Suppl.) 52 B, 92

[155] Kleifges M., Menshikov A., Tcherniakhovski D.& Gemmeke H., 2003, IEEE Trans. Nucl. Sci, Vol. 50, No. 4, pp. 1204–1207, 2003.

[156] Kronberg P.P., 1994, Rep. Prog. Phys. 57, 325

[157] Lawrence M.A., Reid R.J.O., Watson A.A., 1991, J. Phys. G 17, 733

[158] Lee A.A., Clay R.W., 1995, J. Phys. G 21, 1743

[159] Lemaître G., Vallarta M.S., 1933, Phys. Rev. 43, 87

[160] Lemoine M., Sigl G., Olinto A.V., Schramm D., 1997, ApJ 486, L115

[161] Linsley J., 1963, Phys. Rev. Lett. 10, 146

[162] Linsley J., 1979, in Filed Committee Report, "Call for Projects and Ideas in High Energy Astrophysics for the 1980s", National Science Foundation, unpublished

[163] Linsley J., 1986, J. Phys. G 12, 51

[164] Linsley J., Scarsi L., 1962, Phys. Rev. 128, 2384

[165] Linsley J., Scarsi L., Rossi B., 1961, Phys. Rev. Lett. 6, 458

[166] Longair M.S., 1992, High Energy Astrophysics, Cambridge University Press

[167] Matthews J.A.J. & Clay R. for the Pierre Auger Collaboration, 2001, in Proc. 27th ICRC (Hamburg)

[168] Matthews J.A.J. & Mostafa M., 2003, in Proc. 28th ICRC (Tsukuba), 873

[169] Matthiae G., Privitera P., 1999, Auger Technical Gap Note 1999-01

[170] Medina-Tanco G., 1998, ApJ Lett. 495, L79

[171] Medina Tanco G.A., de Gouveia dal Pino E.M., Horvath J.E., 1998, ApJ 492, 200

[172] Meeus A., 1998, Astronomical algorithms, Willman-Bell, 1998.

[173] Menshikov A., Kleifges M.& Gemmeke H., 2003, IEEE Trans. Nucl. Sci, Vol. 50, No. 4, 1208

[174] Mie G., 1908, Annalen der Physik 25, 377

[175] Millikan R.A., Cameron G.H., 1928, Phys. Rev. 32, 53

[176] Murthy P.V.R., Wolfendale A.V., 1993, Gamma-ray astronomy, Cambridge University Press

[177] Mussa R. & Sequieros G., 2005, private communciation

[178] Nagano M. et al., 1992, J. Phys. G 18, 423

[179] Nagano M., Watson A.A., 2000, Rev. Mod. Phys. 72, 689

[180] Nagano M. et al., 2000, Astropart. Phys. 13, 277

[181] Nagano M. et al., 2003, Astroparticle Physics 20, 293 (also Preprint astro-ph/0303193)

[182] Nerling F. et. al. for the Auger Collaboration, 2005, Proceedings of the 29th International Cosmic Ray Conference Pune, HE1.4, ger-nerling-F-abs2-he14-poster

[183] Olinto A.V., 2000, Preprint astro-ph/0011106

[184] O'Neill S., Olinto A., Blasi P., Proceedings of ICRC 2001, Section OG 1.3, Paper No. 6890 (also Preprint astro-ph/0108401)

[185] Penzias A.A., Wilson R.W., 1965, ApJ 205, 638

[186] Perry C.L., Olsen E.H., Crawford D.L., 1987, Astron. Soc. Pacific 99, 1184

[187] Porter N.A., 1960, Nuovo Cimento 16, 958

[188] Prado L. Jr., 2003, Auger Technical GAP Note 2003-084

[189] Pravdin M.I. et al., 1999, in: Nagano M. (ed.) Proceedings of the 26th International Cosmic Ray Conference, Salt Lake City, OG 1.3.14

[190] Privitera P. & Facal san Luis P., 2001, priv. comm.

[191] Protheroe J.R., 1998, Preprint of the University of Adelaide, Australia, ADP-AT-98-9

[192] Prouza M., 2001, Diploma Thesis, Charles University, Faculty of Mathematics and Physics, Prague

[193] Prouza M., Šmída R., 2003, Astron. & Astrophys. 410, 1

[194] Prouza M., 2004, Proceedings of the XXXIXth Rencontres de Moriond, La Thuile, Italy — Exploring the Universe, 441

[195] Prouza M. et al., 2005, Pierre Auger Project GAP note 2005–041

[196] Prouza M., Jelínek M., 2005, Pierre Auger Project GAP note, to be submitted.

[197] Ptuskin V.S., Rogovaya S.I., Zirakashvili V.N. et al., 1993, A & A 268, 726

[198] Puget J.-L., Stecker F.W., Bredekamp J.H., 1976, ApJ 205, 638

[199] Rand R.J., Kulkarni S.R., 1989, ApJ 343, 760

[200] Ranft J. 1995, Phys. Rev. D 51, 64

[201] Rayleigh, 1871, Phil. Mag, 41, 107

[202] Rayleigh, 1899, Scientific Papers, Cambridge University Press, Vol. I, 87

[203] Risse M. et al., 2005, Proceedings of the 29th International Cosmic Ray Conference Pune, HE1.4, ger-risse-M-abs1-he14-poster

[204] Roberts M.D., 2004, Auger Technical GAP note 2004–048

[205] Ryu D., Kang. H., Biermann P.L., 1998, Preprint astro-ph/9803275

[206] Sakaki N. et al., 1997, in: Proceedings of the 25th International Cosmic Ray Conference, Durban, Vol. 5, 217

[207] Sasaki M. et al. (The ASHRA Collaboration), Proceedings of the 29th International Cosmic Ray Conference Pune, HE1.5, jap-sasaki-M-abs1-HE15-oral

[208] Scarsi L. (The EUSO Collaboration), Proceedings of the 29th International Cosmic Ray Conference Pune, HE1.5, ita-scarsi-L-abs1-HE15-oral

[209] Sciutto S.J., 1999, Preprint astro-ph/9905185

[210] Sommers P., Elbert J.W., 1995, ApJ 441, 151

[211] Stanev T., Biermann P., Lloyd-Evans J., Rachen J., Watson A.A., 1995, Phys. Rev. Lett. 75, 3056

[212] Stanev T., 1997, ApJ 479, 290

[213] Stecker F.W., Salamon M.H., 1999, ApJ 512, 521

[214] Stecker F.W., 2001, Preprint astro-ph/0101072 v2

[215] Streitmatter R.E., 1998, in: Krizmanic J.F., Ormes J.F., Streitmatter R.E. (eds.) Proceedings of Workshop on Observing Giant Cosmic Ray Air Showers from $> 10^{20}$ eV Particles from Space, AIP Conf. Proc. No. 433, 95

[216] Strømgren B., Vistas in Astron. 2, 1336 (1956).

[217] Suga K., Chudakov A.E., 1962, in: Escobar I. (ed.) Proceedings of 5th Interamerican Seminar on Cosmic Rays, Laboratorio de Fisica Cosmic del Universidad Mayor de San Andres, La Paz, Bolivia, Vol. 2, p. XLIX

[218] Swordy S.P., Müller D., Meyer P. et al., 1990, ApJ 349, 625

[219] Swordy S.P, 1997, Scientific American, January 1997.

[220] Takahara F., 1996, in: Nagano M. (ed.) Proceedings of the International Symposium on Extremely High Energy Cosmic Rays: Astrophysics and Future Observations, Institute of Cosmic Ray Research, University of Tokyo, Tokyo, Japan, 61

[221] Takahashi, 1998, Nuclear Physics B (Proceedings Supplement) 60B, 83

[222] Takeda M et al., 1998, Phys. Rev. Lett. 81, 1163

[223] Takeda M. et al., 1999, ApJ 522, 225

[224] Takeda M. et al., 1999, in: Nagano M. (ed.) Proceedings of the 26th International Cosmic Ray Conference, Salt Lake City, Vol. 3, p. 252

[225] Takeda M. et al., 2003, Astropart.Phys. 19, 447 (also Preprint astro-ph/0209422)

[226] Telescope Array Design Report, 1998, Institute of Cosmic Ray Research, Univeristy of Tokyo, Tokyo, Japan

[227] Tinyakov P.G. & Tkachev I.I., 2002, Astroparticle Physics 18, 165

[228] Torres D.F. & Anchordoqui L.A., 2004, Rept.Prog.Phys. 67, 1663 (also Preprint astro-ph/0402371)

[229] Trá vníček P., 2005, priv. comm.

[230] Uchihori Y. et al., 1996, in: Nagano M. (ed.) Proceedings of the International Symposium on Extremely High Energy Cosmic Rays: Astrophysics and Future Observations, Institute of Cosmic Ray Research, University of Tokyo, Tokyo, Japan, 50

[231] Uchihori Y. et al., 2000, Astropart. Phys. 13, 151

[232] Young A.T. et al., 1997, Appl. Opt. 36, 2689

[233] Wainscoat R.J. et al., 1992, ApJS 83, 111

[234] Watson A.A., 1992, Nucl. Phys. B (Proc. Suppl.) 28, 3

[235] Waxman E., 1995, Phys. Rev. Lett. 75, 386

[236] Weiler T.J., 1999, Vanderbilt University Preprint VAND-TH-9-99

[237] Westerhoff S., Finley C.B for the HiRes Collaboration, 2005, Proceedings of the 29th International Cosmic Ray Conference Pune, HE1.4, usa-westerhoff-S-abs1-he14-oral

[238] Widrow L.M., 2002, Reviews of Modern Physics 74, 775 (also Preprint astro-ph/0207240 v1)

[239] Wiebel-Sooth B., Biermann P.L. & Meyer H., 1994, A & A 330, 389

[240] Winn M.M. et al., 1986, J. Phys. G 12, 653

[241] Wolfendale A.W., Wibig T., 1999, in: Nagano M. (ed.) Proceedings of the 26th International Cosmic Ray Conference, Salt Lake City, OG 1.3.01

[242] Yoshida S., Teshima M., 1993, Prog. Theor. Phys. 89, 833

[243] Yoshida S., Dai H., 1998, J. Phys. G 24, 905

[244] Zatsepin G.T. & Kuzmin V.A., 1966, Zh. Eksp. Theor. Fiz. (Pisma Red.) 4, 114